Physik-Department
Technische Universität München

Microbeam Radiation Therapy at a Compact Synchrotron X-ray Source

Karin Burger

PhD Thesis

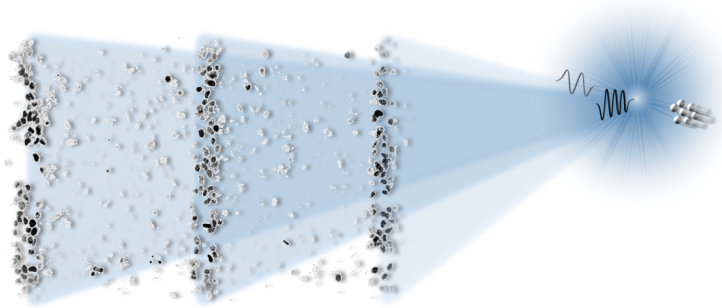

November 2017

Supervisors:
Prof. Dr. Jan J. Wilkens
Prof. Dr. Franz Pfeiffer

Technische Universität München

Klinik und Poliklinik für RadioOnkologie und Strahlentherapie,
Advanced Technologies in Radiation Therapy, Prof. Jan J. Wilkens

Physik-Department, Lehrstuhl für Biomedizinische Physik, Prof. Franz Pfeiffer

Microbeam Radiation Therapy at a Compact Synchrotron X-ray Source

Karin Maria Burger

Vollständiger Abdruck der von der Fakultät für Physik der Technischen Universität München zur Erlangung des akademischen Grades eines

Doktors der Naturwissenschaften (Dr. rer. nat.)

genehmigten Dissertation.

Vorsitzender:	Prof. Dr. Martin Zacharias
Prüfer der Dissertation:	1. Prof. Dr. Jan J. Wilkens
	2. Prof. Dr. Reinhard Kienberger

Die Dissertation wurde am 15.11.2017 bei der Technischen Universität München eingereicht und durch die Fakultät für Physik am 11.12.2017 angenommen.

Abstract

"La radiothérapie est à la fois le fruit le plus inattendu et le plus précieux de la découverte de Röntgen."

Freely translated:
"Radiotherapy is simultaneously both the most unexpected and the most precious fruit of the discovery of Röntgen."

Docteur Antoine Béclère, 1906 [1]

X-ray microbeam radiation therapy (MRT) is suggested to widen the 'therapeutic window' that opens between tumor control and normal tissue damage using a geometrical redistribution of the dose. In the last two to three decades, this radiation therapy concept has been developed from in-vitro to in-vivo studies towards its clinical application. However, high requirements on X-ray flux and beam collimation restrict its application to large-scale, cost-intensive synchrotron sources which hampers routine patient treatment.
This thesis presents different approaches for microbeam radiation therapy at compact, cost-efficient X-ray sources. To apply radiation therapy with such sources, a dedicated dosimetry is developed considering the unusual radiation physics compared to clinical practice. A change of the source parameters can considerably influence radiation-induced biological effects. Therefore, DNA damage, cell survival, tumor growth, and effects on vascular structures are studied by microbeam irradiations in-vitro and in-vivo in contrast to conventional treatment.
Microbeam irradiations were performed using on the one hand a conventional rotating anode X-ray tube, and on the other hand a unique compact synchrotron based on inverse Compton scattering, the MuCLS. Microplanar beam patterns were produced with optical grids of different materials and periodicities with the goal of optimizing microbeam geometry. In this context, the characterization of relatively fine beam widths of a few micrometer was required, for which a variety of dosimetric options was investigated.
The feasibility of microbeam radiation therapy at compact X-ray sources was demonstrated successfully with the following results:

- A dedicated microbeam setup for in-vitro and in-vivo experiments was installed and characterized at the MuCLS.
- In-vitro experiments suggest a higher cell survival and therewith a sparing effect for skin using microbeams compared to conventional, homogeneous irradiations. Additionally, less cytogenetic damage is caused by MRT which can be related to a lower risk for second cancer development.
- With a tumor-bearing mouse model, a comparison of tumor growth delay induced after microbeam or homogeneous irradiation was performed. Moreover, histological analysis and X-ray computed tomography was established

to study the tumor ex-vivo in two and three dimension. No significant tumor growth delay can be stated after microbeam irradiation with respect to non-irradiated tumors so far using the MuCLS. Increasing the microbeam dose, for example, might allow to achieve a tumoricidal effect of MRT at the MuCLS in the future. Preliminary results from tumor analysis ex-vivo suggest that the developed methods are well suited to further explain the radiation-induced effects.

The here achieved developments and results of microbeam applications at compact, cost-efficient X-ray sources constitute a significant contribution to and an important advancement of research on microbeam radiation therapy. This might be especially useful for the realization of microbeam radiation therapy at other compact X-ray sources currently under development, thereby supporting the progress of this promising technique towards clinical applicability.

Zusammenfassung

„La radiothérapie est à la fois le fruit le plus inattendu et le plus précieux de la découverte de Röntgen.“

Frei übersetzt:
„Die Strahlentherapie ist zugleich die unerwartetste, wie auch die kostbarste Frucht der Entdeckung Röntgen's.“

Docteur Antoine Béclère, 1906 [1]

Bisherige Untersuchungen zur Röntgen-Mikrostrahltherapie, basierend auf einer geometrischen Umverteilung der Dosis, weisen auf eine Weitung des sogenannten „therapeutischen Fensters“ hin, welches sich zwischen Tumorkontrolle und Schonung des Normalgewebes aufspannt. Dieses Strahlentherapiekonzept wurde in den letzten zwanzig bis dreißig Jahren von in-vitro zu in-vivo Studien in Richtung klinischer Anwendung weiterentwickelt. Jedoch können die hohen Anforderungen an Röntgenfluss, sowie Strahlkollimierung fast nur an kostspieligen Synchrotron-Großforschungsanlagen erfüllt werden und erschweren somit eine zukünftige, routinemäßige Behandlung von Patienten.
In dieser Doktorarbeit sollen verschiedene Ansätze zur Mikrostrahltherapie an kompakten und kosteneffizienteren Röntgenquellen aufgezeigt werden. Die strahlentherapeutische Nutzung solcher Quellen erfordert das Überdenken von Strahlenphysik im Vergleich zu herkömmlichen Geräten und die damit verbundene Entwicklung eines geeigneten Dosimetriekonzepts. Des Weiteren beeinflusst eine Änderung der Quellparameter maßgeblich die strahlenbiologischen Effekte. Daher wurden im Verlauf dieser Arbeit Strahlenschäden an DNS, Zellüberleben, Tumorwachstum, sowie Einfluss auf Gefäßstrukturen nach Bestrahlung mit Mikrometer-breiten Kanälen im Vergleich zu konventioneller, homogener Bestrahlung in-vitro und in-vivo untersucht.
Als Röntgenquellen dienten eine Laborquelle mit Drehanode, sowie eine bislang einzigartige kompakte Synchrotronquelle, welche auf dem Prinzip von inverser Compton-Streuung basiert, die Munich Compact Light Source (MuCLS). Mit dem Ziel, die Strahlengeometrie zu optimieren, wurden mikroplanare Bestrahlungsmuster unterschiedlicher Geometrie getestet, welche durch verschiedene Kollimatoren erzeugt wurden. Für besonders feine Mikrokanalbreiten im Bereich weniger Mikrometer wurden außerdem verschiedene Dosimetrieoptionen untersucht.
Die erfolgreiche Umsetzung der Mikrokanalbestrahlung an kompakten Röntgenquellen erzielte folgende Ergebnisse:

- An der MuCLS wurde ein Aufbau für in-vitro und in-vivo Mikrokanalbestrahlungen entwickelt und charakterisiert.
- Experimente in-vitro zeigten ein höheres Zellüberleben nach Mikrokanalbestrahlung im Vergleich zu konventioneller Bestrahlung, woraus auf eine Schonung des Normalgewebes geschlossen werden kann. Des Weiteren wurde

geringerer zytogenetischer Schaden verursacht, welcher im Allgemeinen mit einem niedrigeren Risiko für die Entwicklung eines Zweittumors einhergeht.

- An einem tumortragenden Mausmodell wurde Tumorwachstumverzögerung nach Mikrokanal- und homogener Bestrahlung gemessen. Außerdem wurden Methoden zur histologischen Analyse und Röntgencomputertomographie etabliert, um die Tumoren ex-vivo in zwei und drei Dimensionen zu untersuchen. Bislang führte Mikrokanalbestrahlung an der MuCLS zu keiner signifikanten Tumorwachstumsverzögerung im Vergleich zu nicht bestrahlten Entitäten. Beispielsweise könnte eine zukünftige Erhöhung der Dosis bei Mikrokanalbestrahlung eine gesteigerte Schädigung des Tumors mit gleichzeitiger Schonung des Normalgewebes erzielen.

  Erste Ergebnisse der Tumoranalyse ex-vivo weisen auf eine gute Eignung der verwendeten Methoden zur Erklärung strahleninduzierte Effekte hin.

Die in dieser Arbeit aufgezeigten Entwicklungen und Ergebnisse zur Anwendung von Mikrokanalbestrahlung mit kompakten, kostengünstigen Röntgenquellen stellen einen wesentlichen Beitrag zur und eine bedeutende Weiterentwicklung der Forschung an Mikrokanalstrahlentherapie dar. Dies könnte ebenfalls für die Durchführung von Mikrokanalstrahlentherapie an weiteren kompakten Röntgenquellen nützlich sein, welche sich derzeit noch in Entwicklung befinden, damit diese vielversprechende Technik ihren Fortgang in Richtung klinischer Anwendbarkeit nehmen kann.

Contents

1. Introduction

Cancer is still one of the leading causes of human death. Thanks to reduced tobacco consumption, and advances in cancer prevention, early detection, and treatment, the cancer death rate is constantly decreasing since the 1990's [2]. However, with increasing life expectancy, the probability of cancer development for an individual person rises. This involves a higher demand of personalized therapeutic concepts with age, in particular, considering the risk of a second cancer that can develop several decades following primary radiation therapy treatment (e.g. for breast cancer, 30 years after primary cancer diagnosis, there is a – not forcedly radiation-induced – 21% cumulative incidence of second cancer [3]).
Nowadays, cancer treatment can fall back on four main pillars: surgery to resect the malignant tissue where possible, chemotherapy to hinder cell division and thus tumor growth, immunotherapy to re-activate and improve killer cells against the tumor, and radiation therapy to destroy tumorous tissue by irreparable DNA double-strand breaks. Second cancer development is dependent on many different parameters which render systematic studies difficult. Apart from significant risk factors such as environmental exposure, lifestyle, genetic predisposition etc., the treatment of primary cancers can influence second cancer development. On the one hand, chemotherapy applying cytotoxic agents might be the root even of non-hematologic second cancers. On the other hand, radiotherapy with its ionizing radiation is estimated to cause up to 10% of all second cancers [4]. Despite this low number, a (radiotherapy) treatment should not be the root of a new disease. Hence, it is important to reduce second cancer development which especially affects the radiotherapeutic treatment of primary cancer in the childhood. Coming back to Dr Béclère's words, radiation therapy, the most unexpected fruit of Röntgen's discovery of the X-rays in 1895, will only stay so precious if it is applied in a prudent and conscious manner.

To address this issue, various radiation therapy concepts have been developed in the last decades. Implemented in the early 2000's, intensity-modulated radiation therapy is nowadays available in clinical routine as it clearly improved conformity of the planned dose distribution to the tumor target volume compared to conventional uniform X-ray beams [5]. Moreover, after first clinical treatments in 1990, proton and heavy ion therapy expanded as it permits to treat distinct, well-localized tumors using the so-called Spread-out Bragg-peak to reduce normal tissue damage [6]. Yet, this method developed slowly due to high space requirements and operational costs of cyclotrons or synchrotrons needed to accelerate the particles to MeV energies and among others due to the necessity of a dedicated therapy

planning system. Today, ion beam therapy can also be combined with intensity modulation. Retrospective studies to confirm the hypothesis of a lower risk of second tumor development using ion beams are still rare [7].

We can not only vary the intensity and the type of radiation but also its spatial distribution. Already in 1909, Alban Köhler proposed the so-called *grid therapy* for faster skin regeneration and prevention of necrosis by placing a mm-sized grid of lead on the patient's skin before X-ray irradiation [8]. His approach considered that a broad source size or multiple, neighboring sources with smaller focal spot sizes will lead to homogeneous coverage of the tumor situated at several mm distance behind the grid. About 50 years later, Zeman *et al.* [9] discovered that a 1 millimeter-sized deuteron beam with an entrance dose of 140 Gy causes total necrosis in mice brains whereas the application of a 25 µm beam using the same dose does not yield any effect up to 240 days after irradiation. Only at doses as high as 4000 Gy, neurons were eradicated in the microbeam path while still leaving an intact brain matrix behind. Exemplary histological images from this study are shown in Fig. 1.1. Later studies found that the damaged vasculature after microbeam irradiation had possibly been repaired by neighboring, non-irradiated endothelial cells migrating into the irradiated areas (e.g. [10]).

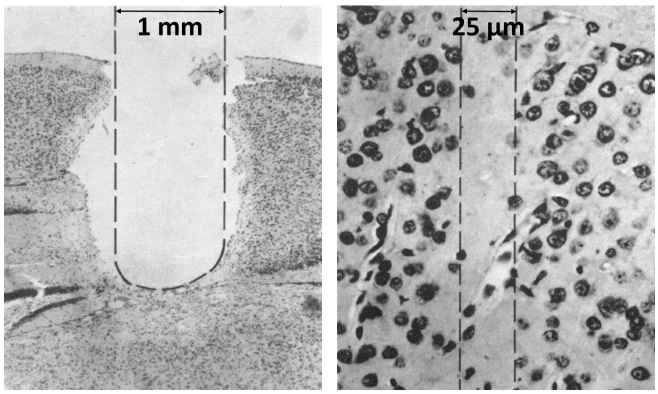

Figure 1.1.: *Histological sections from a deuteron-irradiated mouse brain. (a) 120 days after irradiation with 280 Gy in a 1 mm wide beam: a cystic cavity can be observed. (b) 24 days after irradiation with 4000 Gy in a 25 µm wide beam: neurons are lost but the vein at the lower center of the track seems intact. The beam tracks are indicated with dashed lines. (Adapted from [11].)*

Based on Köhler's grid therapy and Zeman's and Curtis' discovery, a radiation therapy concept called microbeam radiation therapy (MRT) was developed in the 1990's [12, 13]. In these first experiments, planar microbeams were created from quasi-parallel synchrotron X-rays with a beam width varying between 25 and 100 µm and a center-to-center spacing of up to 400 µm applying doses from several hundred to a few thousand Gray. This combined the skin sparing effect of the

grid therapy by Köhler with the high dose tolerance of normal tissue to sub-mm beam sizes seen by Curtis *et al.* Until today, a threshold beam size for tissue tolerance – if there is any – remains unknown [14], especially considering its dose dependency. As the chosen beam parameters for MRT entail high sensitivity for motion blur, fast and precise dose delivery is needed. Extremely high dose rates (8-16 kGy/s [15]) and a collimated X-ray beam with about 100 keV mean energy could only be delivered by third-generation synchrotrons with several hundred meters circumference. This is why until today, most of the research on MRT has been performed at large-scale synchrotrons [16, 17].

With the finding that in addition to normal tissue sparing, high-dose microbeams lead to lower tumor tolerance in contrast to the normal tissue [18–20], the interest in MRT as a clinical radiation therapy concept is growing [17, 21–24]. Many in-vitro and in-vivo studies have investigated the radiobiological effect of MRT ranging from gene expression, bystander and abscopal effects, and DNA repair mechanisms on the cellular level [25–28] to a rather macroscopic perspective of vascular damage, tumor growth delay, and overall survival aiming for human trials [19, 29–31]. Even if in the last years, patient treatment at the European Synchrotron Radiation Facility (ESRF) in Grenoble, France became feasible, yet, a routine treatment of patients is not practicable for technical, safety, and budget reasons. The construction costs of the ESRF, for example, sum up to about one billion US-dollars [32] and its annual budget accumulates to roughly 90 million Euros [33].

The apparent need of laboratory-sized and cost-efficient systems – for MRT as well as for imaging techniques requiring coherent X-rays – led to a variety of new X-ray sources.
Mainly for imaging and structural studies, X-ray free-electron lasers with still more than 100 m in length can deliver coherent, femtosecond-pulsed X-rays with very high brightness. Restricted to wavelengths of about 0.1 nm, i.e. an X-ray energy of 12.4 keV, these systems are not appropriate for MRT. This exclusion criterion also holds true for liquid metal-jet X-ray tubes that deliver monochromatic X-rays with a flux exceeding that of rotating anode tubes by more than one order of magnitude as they support higher electron-beam power. The X-ray energy depends on the K-edge of the metal alloy yielding commercially available X-ray sources of up to 25 keV (Indium alloy) [34, 35]. For MRT, due to the large cone-angle of these source, the microbeam pattern cannot be maintained within the tissue at a reasonably short source-to-sample distance.
In the 2000's, a carbon-nanotube X-ray source array was implemented at the University of North Carolina (UNC, Chapel Hill, NC, USA) that is well suited for micro-computed tomography and for MRT [36–38]. Electron beams from parallel carbon nanotube field emission cathode arrays are focused onto a narrow line focusing track on the anode to generate X-rays with an energy spectrum up to 100 kVp. A dose rate of about 1 Gy/min was reported using large microbeams.

Almost in parallel, studies on laser-electron storage rings were conducted seeking to reduce the size of synchrotron X-ray sources [39,40]. Following the high demand of a compact and brilliant source for low energy X-ray imaging, e.g. to resolve protein structures, Lyncean Technologies Inc. constructed a Compact Light Source (CLS) using inverse Compton scattering of low-energy laser photons by high-energetic electrons. With this laser undulator instead of a permanent magnet undulator, a lower electron energy compared to large-scale synchrotrons is sufficient to achieve keV X-rays. Since 2015, the first commercially sold system, the Munich Compact Light Source (MuCLS) with a footprint of $5 \times 3\,\mathrm{m}^2$ is installed at the Munich School of Bioengineering of the Technical University of Munich (TUM) in Garching, Germany. With X-ray energies up to 35 keV and a flux of up to 3.3×10^{10} ph/s [41,42], it can be applied, for example, for propagation-based, high-resolution phase-contrast computed tomography, grating-based phase-contrast and dark-field imaging and as well for preclinical studies of MRT in-vitro and in-vivo with small animals. With the prospect of even higher X-ray flux and thus dose rate by machine upgrades and the prospect of possible X-ray energies up to 200 keV involving further machine development, the MuCLS is an X-ray source with future clinical relevance for MRT.
Similar compact synchrotron sources based on inverse Compton scattering have been built. However, they do not reach laboratory-size or cost-efficiency, e.g. because of superconducting linear accelerators, and can often not deliver relevant keV X-ray energies for MRT (cf. [43] and others listed in [44]). Compact and brilliant X-ray sources dedicated to MRT are under construction, like the *ThomX* in France [45] or a rotating-anode approach with one-dimensional spatial confinement of the electrons [46,47].

In the present thesis, first MRT experiments at the MuCLS are shown based on the results from technical, dosimetric, and radiobiological studies. From beam characterization through to in-vitro, and up to in-vivo irradiations, the potential of this promising radiation therapy technique at a compact synchrotron is investigated and additional insight into the radiobiological mechanisms of MRT compared to conventional, homogeneous irradiations is given.
Following this introduction, background information on microbeam radiation therapy and the MuCLS with respect to physics, chemistry, and biology is provided in chapter 2. Generic methods of data acquisition and analysis used throughout the subsequently presented experiments are explained in chapter 3. Chapter 4 comprises the evaluation of various approaches for high-resolution dosimetry to facilitate the investigation of relatively small microbeam widths. Experimental studies with microbeam irradiations in-vitro and in-vivo are described in chapter 5, which is divided into four subchapters. First, in subchapter 5.1, the applicability of small microbeam widths is investigated qualitatively at a rotating anode X-ray tube by staining radiation-induced DNA double-strand breaks. Secondly, setup components and dosimetric methods for MRT studies at the MuCLS are introduced and evaluated in subchapter 5.2. Thirdly, using the MuCLS, microbeam

irradiations of normal tissue cells are explored quantitatively applying a typical microbeam geometry (subchapter 5.3). For this purpose, clonogenic cell survival, and chromosome aberrations are analyzed after microbeam, homogeneous, and sham irradiation. Finally, a tumor growth delay study of xenografts in the mouse ear in-vivo is presented in subchapter 5.4. This includes – for improved understanding of the results on tumor growth delay – tumor analysis ex-vivo in two and three dimensions applying dedicated staining protocols and imaging techniques. Chapter 6 concludes this thesis with a short summary of microbeam radiation therapy at compact X-ray sources including an outlook on future projects.

2. Fundamental principles

This chapter seeks to inform the reader about the background important to understand the motivation and outcome of the research presented subsequently. This includes an introduction to microbeam radiation therapy (MRT) as a therapeutic concept regarding physics, dosimetry, and biology. Moreover, the working principle and setup of the Munich Compact Light Source (MuCLS) are presented with focus on the specific settings used for MRT experiments.

2.1. Microbeam Radiation Therapy as a therapeutic concept

MRT strives to widen the therapeutic window, which opens between tumor control and normal tissue sparing [48]. This section starts with a short motivation why and in which cases MRT could be useful (section 2.1.1). Thereafter, in section 2.1.2, its technical requirements concerning X-ray source, and microbeam creation are explained. Following the description of dose deposition by X-ray interaction with matter and the consequent radiation-induced biological effects in section 2.1.3, dosimetric methods relevant to MRT are introduced in section 2.1.4. The final summary of the challenges that MRT faces nowadays yields the motivation for this thesis and future research on MRT (section 2.1.5).

While MRT is also applied with other types of ionizing radiation, such as protons [49–53], the present work focuses only on X-ray irradiations. This separation is important as ion beam irradiations use the skin sparing effect of MRT but ions have different scattering properties. Upon interaction with matter, the ion impact through secondary particles is known to cause a homogeneous dose distribution at the tumor in contrast to X-ray MRT, which is commonly applied with a collimated, keV X-ray beam that maintains the microbeam pattern through the tumor tissue. Details on the interaction of X-rays with matter and the homogeneous tumor coverage using X-ray MRT will be given below.

Historically, one of the first tissues to be treated with microbeams was the brain, which showed high tolerance to extreme peak doses (in the 1960's, [11]). In 1998, Laissue *et al.* demonstrated the ablation of rat gliosarcoma using MRT [54]. As a consequence, many subsequent research studies on MRT focused at – often radioresistant – brain tumors like glioblastoma multiform (GBM) with low overall survival (about 12 months, cf. [55, 56]). This was motivated by several factors.

On the one hand, the high peak dose might allow to overcome radioresistance, on the other hand, the concept of MRT foresees a single radiotherapy session instead of the conventional, fractionated treatment over 6 weeks. Especially treatment of malignant hindbrain neoplasm in children has been proposed due to its shallower position compared to adults [57] and the high importance to avoid neurological sequelae during child growth [21, 31].
Additionally to tumor treatment, Pouyatos *et al.* observed in a proof-of-concept study that precise microbeam irradiation of brain structures that can generate seizures in absence epilepsy allowed to suppress seizure initiation [58]. Furthermore, MRT treatment of Parkinson's disease or chronic pain has been suggested [14, 15, 20]. Meanwhile, sparing of normal tissue by the dose redistribution into microbeams could be a complementary benefit to reduce side effects and second tumor development, as discussed in the introduction.

2.1.1. Rationale – microbeam geometry and X-ray energy

In X-ray MRT, spatially fractionated, high-dose beamlets are used to spare healthy tissue from radiation damage while achieving tumor control. In the following, tumor treatment with MRT is discussed in the context of microbeam geometry and X-ray energy.
As described earlier, normal tissue exhibits an extremely high tolerance to radiation doses when the irradiated volume is small. A specific geometry is required to make use of this so-called *dose volume effect*. Typically, the beam width ranges from 25 to 100 µm with a maximum dose in the *peak*. The individual beams are spaced by 200 to 400 µm representing the *valley*. These beams can be either cylindrical or microplanar produced by absorbing structures in the beam path. Due to easier fabrication processes of the structures, microplanar beams are commonly used. Exemplarily, an ideal transmission pattern is presented in Fig. 2.1 with 50 µm wide microbeams separated by valleys of 300 µm (i.e. a *center-to-center spacing* or *period* of 350 µm).
The valley dose must not exceed the tolerance dose of the normal tissue. This is a crucial aspect as scattering contributions from the peaks increase the valley dose – the more the larger the microbeam array is, with a maximum dose in the center. As most of the dose is deposited by secondary electrons having a range that scales with the X-ray energy, MeV photons are too energetic to maintain the microbeam pattern. The electron range can be considered similar to the penetration depth for low Z (atomic number) materials like water. Fig. 2.2 shows the energy dependence of the electron range in water following [59, 60] for an energy range up to 50 keV. With 25 keV of kinetic energy, the electron reaches a penetration depth of about 13 µm whereas the electron can travel more than 40 µm with 50 keV. Hence, to maintain the microbeam pattern within the tissue and to achieve a high peak-to-valley dose ratio (PVDR), the X-ray energy must be low. As a trade-off, many synchrotron studies on MRT have been performed with mean energies of about 100 keV instead of the commonly therapeutic X-ray energies in the MeV range.

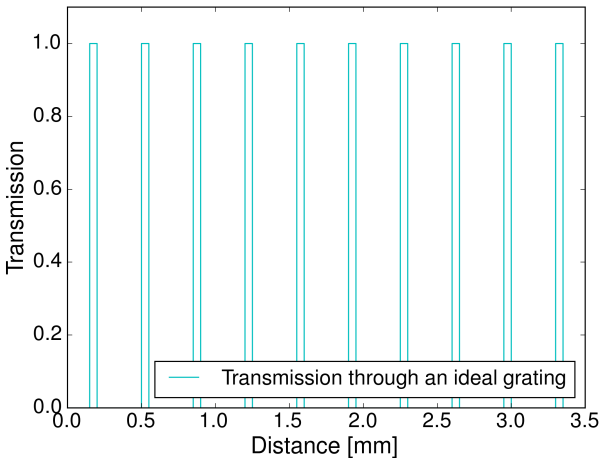

Figure 2.1.: *Transmission of X-rays through an ideal grating. 50 µm wide microbeams with transmission = 1 in the peak and a beam spacing of 300 µm with transmission = 0 in the valley are produced.*

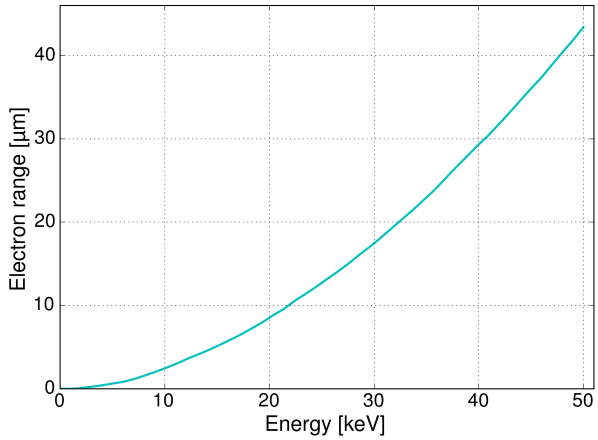

Figure 2.2.: *Range of electrons in water (H_2O) for energies up to 50 keV. Data is based on [59, 60].*

However, due to the reduced penetration depth of lower energetic X-rays, treatment of deeper situated tumors becomes challenging. As an example, 84% of a 100 keV X-ray beam are transmitted through 1 cm of water and roughly 71% through 1 cm of cortical bone.

The influence of the X-ray energy is demonstrated by a simulation of dose distribution in water in Fig. 2.3 applying a microbeam array with beam widths of 50 µm. The microbeam period was varied from 100 µm in Fig. 2.3 (a) to 350 µm in Fig. 2.3 (b). The smaller spacing in Fig. 2.3 (a) was chosen to better visualize the difference of the curves and to highlight the importance of a sufficiently large peak spacing. The larger spacing in Fig. 2.3 (b) corresponds to a typical microbeam geometry. In both figures, three different energy configurations are compared: the

ESRF spectrum of the beamline ID17 (here denoted as *ESRF spectrum*) with a mean energy of 100 keV in blue, the 25 keV MuCLS spectrum in green, and a hypothetical MuCLS spectrum with a peak energy at 50 keV in red (the ESRF spectrum is shown in Appendix A.1, the 25 keV spectrum of the MuCLS in chapter 5.2.2). The corresponding dose distributions were obtained through adjoint Monte-Carlo simulations using Geant4 as described in [61] assuming ideal conditions (point-like X-ray source, ideal microbeam pattern as in Fig. 2.1, homogeneous medium). The profiles are taken from the center of a quadratic field containing 7 microbeams, i.e. $700 \times 700\,\mu m^2$ or $2450 \times 2450\,\mu m^2$ to account for scattering contributions from neighboring microbeams. We integrated contributions from the surface of the water volume to a depth of 1 mm.

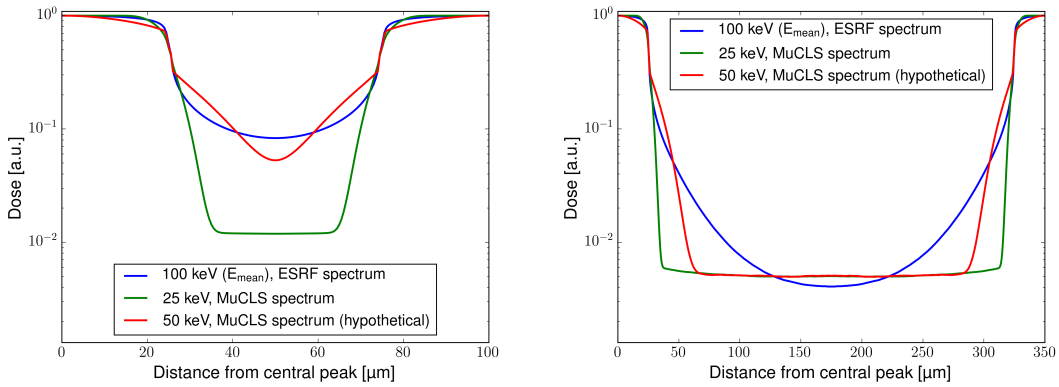

Figure 2.3.: *Simulation of dose distribution in water along the distance from the central peak for a microbeam width of 50 µm. In (a) with a period of 100 µm, in (b) with a period of 350 µm. The blue curve shows the result for the ESRF spectrum with 100 keV mean energy, the green curve for the MuCLS spectrum of the 25 keV configuration, and the red curve for a hypothetical MuCLS spectrum of 50 keV. Please note the logarithmic scale on the vertical axis.*

The dose distributions demonstrate the benefit of even lower energies than 100 keV as a significantly higher peak-to-valley dose ratio (PVDR) value can be achieved with the MuCLS spectrum at 25 keV in Fig. 2.3 (a) compared to the ESRF spectrum (E_{mean}=100 keV), cf. Fig. 2.3 (a). In Fig. 2.3 (b), the larger spacing permits for similar PVDR values but the edge sharpness of the microbeam is clearly enhanced towards lower energies. The photoelectric process becomes dominant below 30 keV in water, leading to isotropic emission of the photoelectron in contrast to the forward directed Compton scattering (for details on X-ray interaction with matter, see section 2.1.3.a), and thus a blurring of the pattern. In the case of 25 keV, the penetration depth of secondary electrons is still low (cf. 2.2) yielding a quite steep dose fall-off at the microbeam edge. The transition from photoelectric to Compton effect is visible in the dose pattern of the 50 keV spectrum (red curve). In this energy range, the photoelectric absorption and the larger penetration depth

of secondary electrons than for 25 keV add up to a significantly broadened peak. In the blue curve using the ESRF spectrum, the larger energy range from roughly 40 to 200 keV leads to a smoothed dose pattern such that individual effects cannot be distinguished. Here, the larger microbeam spacing results in a lower minimum of the valley dose as forward directed scattering from the Compton effect is predominant. The application of lower energies suggests an improvement of normal tissue sparing and could allow for higher peak doses to treat radioresistant tumors, if sufficient flux is available. Moreover, a smaller center-to-center spacing can be realized with higher PVDR without reaching the normal tissue threshold dose. Thus, tumor coverage can be improved. However, the penetration depth of X-rays decreases with energy. Therefore, the investigation of lower energies for the application of MRT at superficial targets could be of interest.

Conventionally, a treatment plan prescribes a homogeneous coverage of the tumor. In most cases, this is achieved by several individually shaped beams from different angles around the patient that overlap in the tumorous region. This is why also for MRT so-called *interlacing* or *crossfiring* schemes have been developed [14, 62, 63] that foresee the application of microplanar beams from different directions. As shown in Fig. 2.4, interlaced microbeams are composed of orthogonal, non-intersecting microplanar arrays with plane distances that are a multiple of the plane width (e.g. 3).

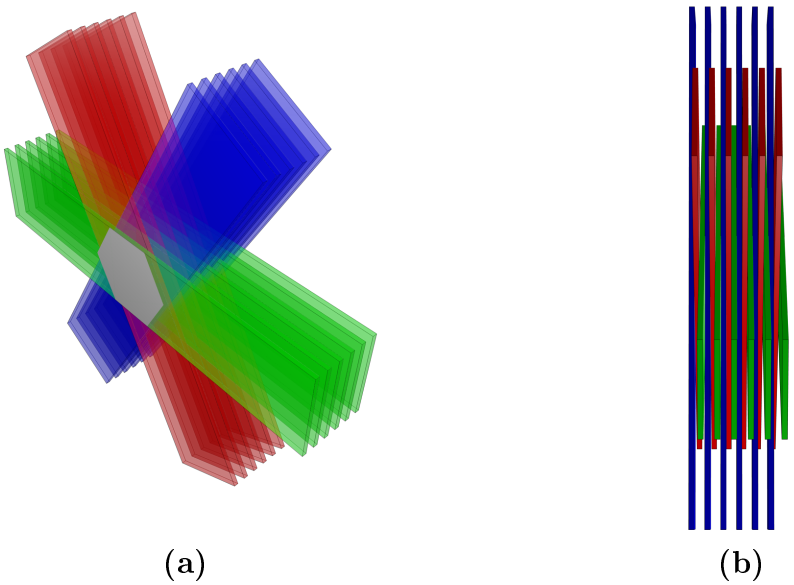

Figure 2.4.: *Schematic representation of the interlacing geometry for homogeneous tumor coverage (a) in 3D view, and (b) in side view. Arrays of microplanar beams from three different angles (red, green, and blue planes) create a homogeneous target region in their center (marked in gray).*

Accordingly, the tumor is irradiated with several (e.g. 3) arrays from different

azimuthal angles such that the space between the planes of one array is partially or completely filled with the planes of the other arrays. With the high doses applied in MRT, total necrosis of the homogeneously irradiated tumorous tissue can be achieved while normal tissue is spared. However, patient positioning must be very precise including the rotation of the patient for each irradiation angle. Thus, a highly accurate patient positioning system together with image guidance is required [23, 64].
Following the higher therapeutic index measured after MRT irradiation compared to homogeneous irradiation [15], a homogeneous tumor coverage might not be necessary. The tumorous vasculature shows similar structures as immature vasculature of normal tissue which comes along with a less efficient repair mechanism [19]. Consequently, one array of spatially separated high dose beamlets might be sufficient to achieve tumor control and the complex interlacing scheme can be avoided. However, the microbeam geometry becomes crucial as the center-to-center spacing needs to be sufficiently large to achieve a lower valley dose and, thereby, a sparing effect in the normal tissue but at the same time the spacing should be small enough as the tumor must be substantially damaged.

2.1.2. Physical Requirements

To apply MRT, a dedicated X-ray source, an optical or mechanical device to create the microplanar array, a sample or patient positioning system, and a dosimetry setup are essential.

2.1.2.a. X-ray sources for MRT

As discussed above, the X-ray source has to generate an almost parallel beam with very high photon flux to maintain a collimated beam and achieve a high dose rate. Moreover, the energy should not exceed 200 keV.
These criteria can be fulfilled at third generation synchrotron sources like the National Synchrotron Light Source (NSLS[1]) or the ESRF, where most of the research on MRT has been performed so far. To achieve such X-ray beams, electrons are accelerated and bunched in a large-scale radiofrequency accelerator and transported into a storage ring of several hundred meters circumference, where they are kept on a circular orbit by strong magnets. At straight sections in the storage ring, undulator structures or wigglers create an alternating magnetic field in which the electrons are deviated. During radial acceleration, the electron bunches release energy in the form of X-ray photons in tangential direction with a small beam divergence. These X-rays are extracted from the storage ring into tangentially placed beamlines and can be further modified by X-ray optical devices. For MRT experiments at the beamline ID17 of the ESRF, for example, a *white* wiggler spectrum of 50 to 600 keV X-rays with a mean energy of 100 keV is achieved by filtering and

[1] NSLS, Upton, NY, USA

absorbing elements to remove energies below 50 keV and to reduce the dose rate if required. As stated earlier, the dose rate at the ESRF reaches up to 16 kGy/s [24]. Due to infrastructure and maintenance costs of these large-scale machines, a compact X-ray source for MRT is highly desirable. Thus, testing the applicability of MRT at current laboratory X-ray tubes is a logical consequence. For imaging, tube voltages ranging from 20 to 200 keV are commercially available. Here, the cooling of the anode restricts the electron current and, accordingly, the X-ray flux. Using a rotating anode system yet allows for a flux of up to 1×10^9 ph/s. A more recent technique that replaces the solid anode by a liquid metal jet leads to a further increase in flux by about one order of magnitude [65]. However, their energy range is limited by the specific metal alloys used to produce the liquid metal jet. For MRT, due to the large cone-angle of these source, penumbral blurring leads to a reduced PVDR at reasonably short source-to-sample distances. Consequently, a rotating anode system remains the most appropriate source to test MRT in laboratories. In this thesis, first cell experiments demonstrate the possibilities and challenges of MRT at a rotating anode X-ray tube.

Up to now, the dose rate at today's rotating anode X-ray tubes does not reach clinically relevant values, such that synchrotron sources are still required for MRT. In the last years, to minimize space and construction as well as maintenance costs, compact and brilliant X-ray sources are emerging. For example, using plasma acceleration instead of radiofrequency accelerators, smaller X-ray sources can be realized [66, 67]. Even if such systems nowadays can be operated in the hard X-ray regime (up to 200 keV), these sources are pulsed and therefore not suited for MRT (e.g. 1 pulse/40 seconds [67]). Also other compact and brilliant X-ray sources exist that unfortunately cannot be applied to MRT due to limitations in X-ray beam properties and hence will not be further discussed here [44]. A new approach to construct a laboratory-sized X-ray source with a small focal spot yielding high brilliance has been proposed recently [46,47]. Following the simulated specifications, it would be well-suited for MRT experiments.

At the University of North Carolina[2], a carbon-nanotube based X-ray source array produces field emitted electrons that are focused by specific lenses to a long and narrow focusing track on the anode [38, 68]. Today, this machine has been commercialized by a startup company[3]. MRT studies in-vitro and in-vivo have been demonstrated at this X-ray source with a mean energy of 60 keV [37, 38, 64, 69]. Being under development, a prototype machine shall provide anode voltages up to 160 kVp at 30 mA and estimated dose values of 6000 Gy/min [38]. However, only one microbeam is formed by a collimator, such that the sample irradiation is performed in a step-and-shoot manner [70]. For a beam width of 280 µm (rather minibeam than microbeam) and a center-to-center distance of 900 µm with a PVDR of 16, an average dose rate of 1.2 Gy/min was reported [64]. With the help of magnetic resonance imaging (MRI) and physiological gating, the high risk of motion blur due to the low dose rate can be reduced. While further research

[2]University of North Carolina, Chapel Hill, NC, USA
[3]XinRay Systems, Xintek Inc., Morrisville, NC, USA

and improvements with respect to stability and dose rate seem to be required, it presents one of the approaches towards MRT at a compact X-ray generator.
Ultimately, compact synchrotron sources using inverse Compton scattering constitute alternative X-ray sources for MRT. While a variety of these sources are either still large and thus not clinically relevant, still under construction, or under development [43, 45], the first commercially available Compact Light Source (CLS) based on inverse Compton scattering by Lyncean Technologies Inc.[4] is operated since 2015 at the Munich School of BioEngineering at the TUM (Garching, Germany). This source bridges the gap between standard laboratory X-ray tubes and large-scale synchrotron facilities. With a flux of up to 3.3×10^{10} ph/s and a brilliance of more than 0.6×10^{10} ph/s/mm^2/mrad^2/0.1% bandwidth at 35 keV, the Munich Compact Light Source (MuCLS) is at least one order of magnitude brighter than rotating anode X-ray tubes (cf. [65] for brilliance parameters of laboratory sources including optics). Additionally, it delivers almost monochromatic X-rays tunable from 15 to 35 keV with an energy bandwidth of 3 to 6% (full width at half maximum (FWHM)). The monochromaticity is important for several imaging applications but it means as well that for MRT no additional absorbers are necessary to modify the spectrum. Moreover, a circular beam profile with a diameter from 7 to 60 mm is accessible such that translation in vertical direction for full sample irradiation is not required. This is a benefit in contrast to the highly asymmetric beam profiles at large synchrotron facilities (e.g. beam size for MRT at the ESRF: 40×1 mm^2 [16]). Due to the low X-ray energies, the MuCLS is well suited for preclinical MRT experiments, both in-vitro (cells and tissues) and in-vivo (small animals). Further details on the working principle of this machine can be found in section 2.2. Future upgrades of this prototype machine will reduce the irradiation time considerably by enhancing the flux. Moreover, design adaptations on the electron injection and storage ring as well as the laser cavity can enable energy upscaling to beyond 100 keV to reach a clinically relevant X-ray energy.

2.1.2.b. Creation of microbeam pattern

In most MRT studies, an absorbing structure is used to create the microbeam pattern. Such multislit collimators or gratings need to be precisely fabricated with a thickness that allows for full absorption of the X-ray beam at the applied X-ray energy. A variation of several micrometers on the grid pattern might be negligible in the experiment. Simulating the dose with Monte Carlo models and understanding the radiobiological effects, however, relies on a well-known setup geometry that is preferably simple. This holds true especially when using interlacing schemes for homogeneous tumor coverage.

Existing collimator designs. Several collimator designs have been investigated for MRT applying 100 keV X-rays [17, 71]. For the most recent collimator at the ESRF, a wire cutting technique was applied to create microbeam slit widths down

[4] Lyncean Technologies Inc., Fremont, CA, USA

to 70 µm in 8 mm thick solid tungsten carbide [17]. The beam width is adjustable by two subsequent identical collimators. Due to the high dose rate at the ESRF, the temperature of the tungsten carbide rises and therefore oxidation processes can occur. This is avoided by placing the collimators in a nitrogen gas environment. For larger microbeam widths, a single collimator can also be built by highly precise mechanical stacking of tungsten carbide plates in a pre-structured tungsten carbide block. A simpler approach consists of stacking alternating plates of tungsten (valley) and polyimide (peak) [72], which will reduce the dose rate due to X-ray absorption by the polyimide. The advantage is that the microbeam width can be easily reduced to 25 µm. As a reminder, for smaller microbeam widths, scattering-related blurring of the microbeam peak is reduced and a higher PVDR can be maintained.
Compared to the collimator design of the ESRF, MRT setup at the carbon-nanotube based X-ray source array consists of two parallel blocks of tungsten carbide to create a single microbeam. Hence, stepping of the irradiation target is required to apply an array of microbeams.

Collimator for the MuCLS. As the MuCLS was operated at 25 keV for MRT experiments, a 200 µm thick plate of tungsten is sufficient to absorb almost 100% of the X-rays. Due to a sufficiently low dose rate, the heating of the tungsten plate becomes negligible. Thus, a $1 \times 1\,\mathrm{cm}^2$ tungsten slit array (plate area: $1.2 \times 1.2\,\mathrm{cm}^2$) in air was produced by laser-micromachining (Laser Micromachining Ltd. (LML), United Kingdom) with a slit width of 50 µm and a center-to-center spacing of 350 µm. A photograph of the tungsten slit array is shown in Fig. 2.5.

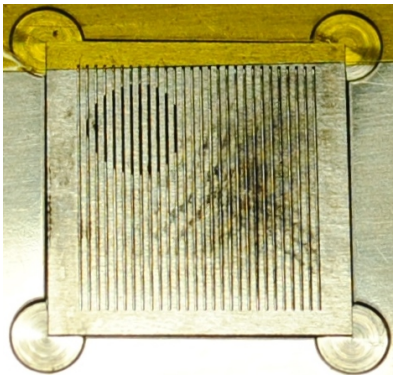

Figure 2.5.: *Photograph of the laser-micromachined tungsten slit array with 50 µm slit size and 350 µm center-to-center spacing used at the MuCLS.*

The fabrication process was specified to result in a maximum taper of 10 µm at each side of the slit which would only slightly blur the ideal grating pattern (see Fig. 2.6).
Characterization of the tungsten slit array is shown in chapter 5.2.

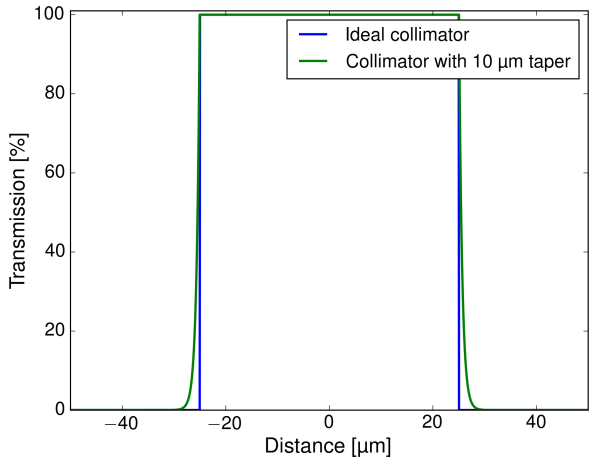

Figure 2.6.: *Microbeam pattern produced by tungsten slit array for a single slit. The blue curve shows the ideal pattern without taper, the green curve considers a taper of 10 µm at each side of the slit. In both cases, the energy spectrum of the MuCLS at 25 keV peak energy was used.*

Optimization of microbeam geometry. The importance to optimize microbeam geometry is highlighted by Fig. 2.7, which shows simulations of the dose deposition in water resulting from microbeams with a width of 5, 10, 25, and 50 µm with a period of 100 µm. As X-ray spectra, the 25 keV configuration of the MuCLS and the ESRF spectrum with 100 keV mean energy were used. The small center-to-center spacing was chosen for visualization purposes (see Appendix A.2 for results with 350 µm period). Simulations were performed as described in section 2.1.1.

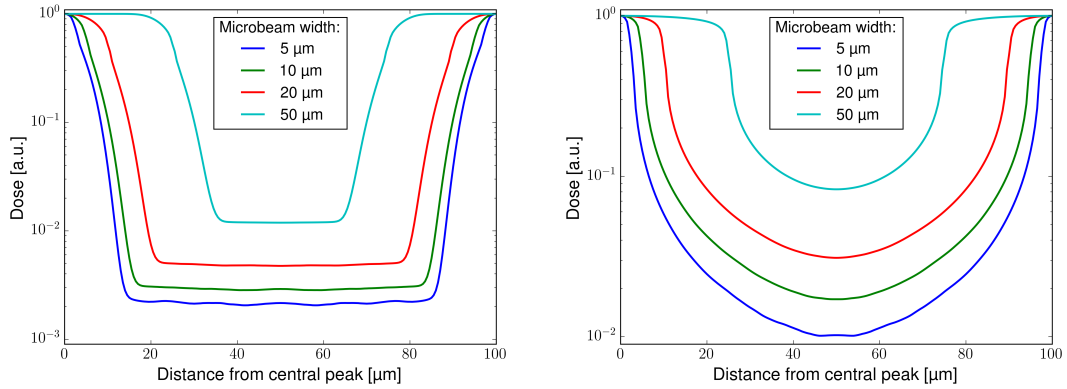

Figure 2.7.: *Simulation of dose distribution in water along the distance from the central peak for microbeam widths of 5, 10, 20, and 50 µm with a period of 100 µm using the MuCLS spectrum of the 25 keV configuration in (a) and the ESRF spectrum of 100 keV mean energy in (b).*

The valley dose clearly increases with the beam's diameter such that large beams will reach the tolerance threshold of normal tissue more rapidly than smaller ones. This holds not only true using the 25 keV configuration of the MuCLS as shown in Fig. 2.7 (a) but also for the ESRF spectrum as presented in Fig. 2.7 (b). Exploring the radiobiological effect of MRT towards smaller microbeam widths, i.e. below 50 µm, might therefore open new possibilities in microbeam treatment.

Absorption gratings by LIGA fabrication. To achieve microbeams of widths below 10 µm, absorption gratings were used in the here-shown experiments, mainly fabricated by the Karlsruhe Institute of Technology[5]. The LIGA process[6] is applied to fabricate such gratings. For this purpose, masks produced by photolithography are electroplated in a bath of the desired absorber material, most commonly gold (Au). The structure is supported by a silicon wafer of 200 to 500 µm thickness or similar material, such that additional absorption needs to be considered. The photoresist structure might be stripped if possible. As high aspect ratios (about 100 or higher, depending on the X-ray energy) of grating height to line width are required for sufficient X-ray absorption, grating periods below 10 µm are mostly made with additional stabilizing structures – so-called bridge or sunray layouts (e.g. [73]). Such bridges in the resist are visible as interruptions in the grating lines, see Fig. 2.8 (a). For MRT experiments, the sunray layout, in Fig. 2.8 (b), or continuous lines are therefore highly preferred. For the sunray layout, the stabilizing structures are not added together with the absorbing lines by top irradiation of the resist but by an additional irradiation with a slanted beam. Thus, the line pattern is not fully interrupted in contrast to the bridge layout.
The duty cycle describes the ratio of slit width to the width of absorbing structure. For most gratings, it equals 0.5, as used in grating-based absorption imaging. Thus, the slit width is half the grating period.
Experiments using the here-shown grating layouts can be found in chapters 4 and 5.

2.1.3. Radiation-induced biological effects

This section shall provide an insight into biological effects induced by X-ray radiation in cells and tissue, specifically with regard to MRT. As a basic prerequisite, X-ray interaction with matter is discussed in the following. For simplification, atomic structures will be explained using the Bohr model.

2.1.3.a. X-ray interaction with matter – dose deposition

The subsequent explanation seeks to identify the X-rays interaction processes which are used for beam shaping and characterization and, in particular, those

[5] KIT, Karlsruhe, Germany
[6] LIGA is a German acronym for the steps of the process: Lithographie, Galvanoformung und Abformung (Lithography, Electroplating, and Molding)
[7] Carl Zeiss Microscopy, Pleasanton, CA, USA

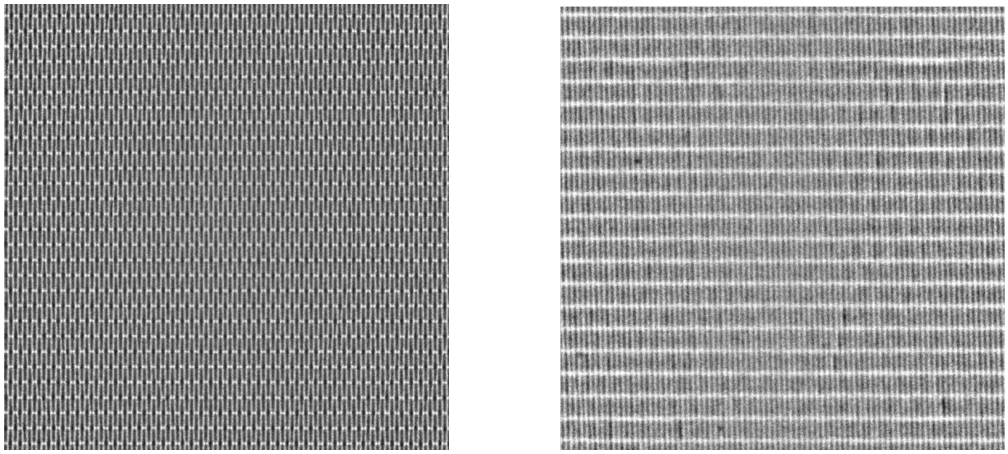

(a) **(b)**

Figure 2.8.: *Radiographic images of vertically aligned gratings taken with an X-ray microtomography system (Zeiss Xradia 500 Versa system[7]). (a) Grating with bridge design. Grating lines are fully interrupted in horizontal direction due to stabilizing bridges in the mask. (b) Grating with sunray layout. Only partial interruption is caused by the stabilizing sunray structures.*

which are responsible for dose deposition in the irradiated material.

When X-ray photons interact with matter, the following fundamental processes can occur on the atomic scale (for the energy range relevant in this thesis): *elastic* (Rayleigh or Thomson scattering) and *inelastic* scattering (Compton effect), and the photoelectric effect. Their combination leads to the macroscopically observable effects of absorption and refraction, which are described by the complex refractive index of the respective material. While absorption reduces the intensity of the photons, refraction (and reflection as a special case) cause a change in beam direction. With a complex refractive index of slightly less than unity, total external reflection of X-rays takes place only at grazing incidence, limited by the critical angle. This has to be taken into account in the production of X-ray optics for beam collimation and focusing, for example.
Dose is deposited when energy of the X-ray photon is transferred to the target material. X-ray photons rarely contribute directly to ionizations but transfer their kinetic energy to so-called *secondary electrons* after a few scattering events. Considering absorption in the hard X-ray regime below 100 keV, Compton and the photoelectric effect are the major contributors to X-ray absorption.

Compton effect. The Compton effect describes the inelastic collision of an incident photon with an electron upon which the photon is scattered with reduced energy (discussed respectively for inverse Compton scattering in section 2.2.2). Under the assumption of a free electron at rest, the Compton scattering cross section is directly proportional to the atomic mass density, and hereby to the atomic

number Z, and scales inversely with the X-ray energy E. With lower X-ray energies, the scattering process becomes more elastic and approaches, with respect to the photon energy, the classical limit of Thomson scattering. Further interaction processes can be triggered by the Compton scattered secondary electron and the X-ray photon, respectively.

Photoelectric effect. In the case of photoelectric absorption, the X-ray energy transferred upon collision allows to release secondary electrons, which distribute the kinetic energy by ionization or excitation of atoms while decelerating. The secondary electrons arise from the photoelectric effect as follows:
An atom absorbs the incoming X-ray photon and subsequently emits a core electron with the transferred energy reduced by the binding energy of the electron. The vacancy created in the atomic shell can be re-filled by an electron from a higher-lying orbit. The energy gain of this electron resulting from the lower binding energy of the core orbit is released in form of a characteristic X-ray photon – so-called X-ray fluorescence (XRF) –, or is used to expel another electron from the atom, an Auger electron. XRF can, for instance, be used for beam characterization or intensity measurements. The emitted core electron – defined as *secondary electron* in the context of radiation therapy – deposits energy by ionization or excitation of atoms within a so-called range depending on its kinetic energy as shown in section 2.1.1.
For photoelectric absorption, the differential cross section is dependent on the atomic number Z with $\sim Z^4$, and the X-ray energy E with $\sim 1/E^3$. The absorption cross section is discontinuous at the absorption edges, where the energy of the X-ray photon corresponds exactly to the binding energy of an electron in a certain orbit. Consequently, photoelectric absorption becomes dominant for high Z materials at low X-ray energies.

Intensity loss and dose deposition. The contributions from the different absorption processes are contained in the material-dependent absorption coefficient μ, which is directly proportional to the total absorption cross section and the atomic mass density. Fig. 2.9 shows the mass attenuation coefficient μ/ρ with density ρ of water in the energy range from 1 to 150 keV separately for coherent (Thomson) scattering in red, incoherent (Compton) scattering in orange, and for photoelectric absorption in green. The combination of these scattering contributions yields the total attenuation (cyan). Excluding coherent scattering does only marginally influence the total attenuation (blue).
This representation shows that in the energy range of several tens of keV – relevant for this thesis –, Compton and photoelectric effect are the main contributors to X-ray absorption in water.
Using Beer-Lambert's law, we can calculate the intensity I transmitted through a homogeneous material (constant μ) of thickness Δz assuming an initial intensity I_0:

$$I = I_0 e^{-\mu \Delta z}, \tag{2.1}$$

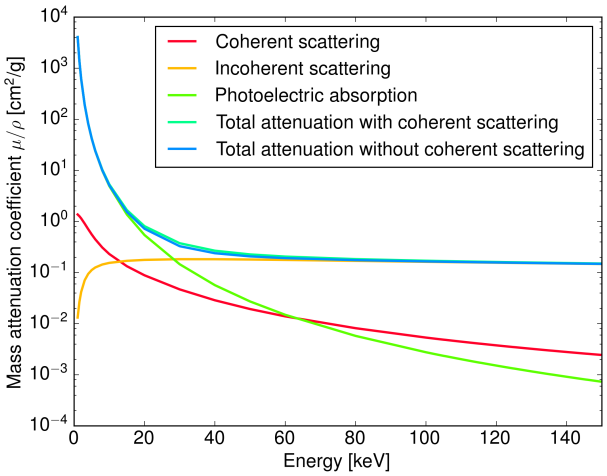

Figure 2.9.: *Mass attenuation coefficient of water for the energy range from 1 to 150 keV. Note the logarithmic scale. The contributions from coherent and incoherent scattering are presented in red and orange, respectively. Photoelectric absorption is shown in green. The cyan and blue curves represent the total attenuation including or excluding coherent scattering. Data retrieved from [74].*

which corresponds to an intensity loss of $1-{}^{I}/_{I_0} = 1-\exp(-\mu\Delta z)$. In the monochromatic case, the intensity loss with respect to an initial photon number N is related to the dose D, i.e. the energy per mass, deposited in a material of volume $A \cdot \Delta z$ with density ρ via:

$$D = \frac{N(1-\exp(-\mu\Delta z))}{A\Delta z\rho}E. \tag{2.2}$$

For small Δz, such as cell monolayers ($\sim$10 µm thick), the Taylor expansion of the exponential function $\exp(x)$ can be approximated to $1-x$, yielding:

$$D = \frac{N}{A}\frac{\mu}{\rho}E \tag{2.3}$$

that extends in the polychromatic case to:

$$D = \frac{N}{A}\int_{E_{\min}}^{E_{\max}} \omega(E)\frac{\mu(E)}{\rho}EdE, \tag{2.4}$$

where $\omega(E)$ is the differential energy spectrum describing the energy dependent number of photons with $\int_{E_{\min}}^{E_{\max}} \omega(E)dE = 1$. The ratio N/A is also referred to as *fluence*. The SI-unit of absorbed dose is joule per kilogram (J/kg) called Gray (Gy), i.e. 1 Gy= 1 J/kg, superseding the former unit rad. Note the capital letter in *Gray* to avoid confusion with the color *gray*.

Using the absorption coefficient μ might lead to an overestimation of the dose as energy losses in radiative processes, for example, are not considered. As described

above, dose in the here-considered energy range is mainly deposited by secondary electrons.
To account for the X-ray energy that is transferred to kinetic energy of charged particles during interactions, and the possible loss of this energy in radiative processes in the target material, the mass energy absorption coefficient μ_{en}/ρ has been introduced [75].
With this correction, the dose calculation can be adjusted to:

$$D = \frac{N}{A} \int_{E_{\min}}^{E_{\max}} \omega(E) \frac{\mu_{en}(E)}{\rho} E dE, \tag{2.5}$$

In Fig. 2.10, the mass energy absorption coefficient of water, $\mu_{\mathrm{en,H_2O}}/\rho_{\mathrm{H_2O}}$, is shown over the energy range relevant for the 25 keV configuration of the MuCLS (retrieved from [76]).

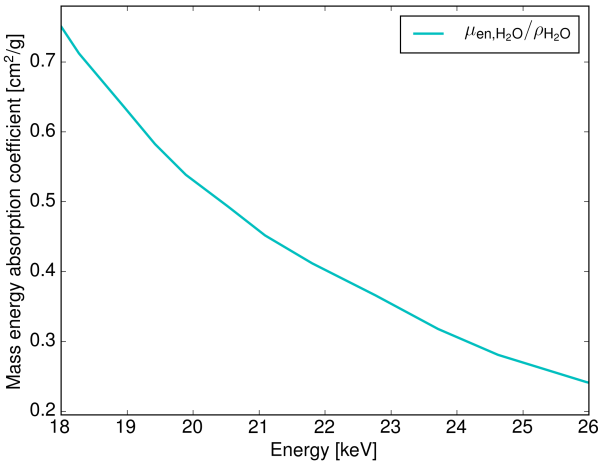

Figure 2.10.: *Mass energy absorption coefficient of water for the energy range of the 25 keV configuration at the MuCLS. Data retrieved from [76].*

From 18 to 26 keV, the absorption cross section decreases remarkably. In this energy range, the application of higher energies leads to a reduced dose deposition in water. This aspect needs to be considered when choosing the optimal energy for microbeam irradiations at the MuCLS.
It should be noted that the dose calculation in Eq. (2.5) is only a good estimate for homogeneous and thin materials as used throughout this thesis. More accurate results can be achieved by Monte Carlo simulations using the cross sections of the scattering and absorption processes and including setup geometry as well as tissue composition. The development of such calculations specifically for MRT at the MuCLS is on-going work of the research group Advanced Technologies for Radiation Therapy[8], which will allow for more complex irradiation dosimetry in the future.

[8]Department of Radiation Oncology, Klinikum rechts der Isar, TUM, Munich, Germany

2.1.3.b. Biological effects

In this section, the above described interaction of X-rays with matter as a physical process is now related to the biological radiation response via the according chemical reactions. On the molecular level, the ionization and excitation of atoms and molecules can lead to bond breakage, e.g. directly in the genetic material, the deoxyribonucleic acid (DNA) or to the creation of highly reactive radicals via radiolysis or to mutation of molecules like amino acids. These molecular variations are either repaired – including misrepair –, or might cause cell death via different pathways. Thus, subcellular damage can occur, e.g. chromosome aberrations or leakage of the cell membrane and, on cellular level, the probability for cancerous cell mutations increases.

Radiation damage at cellular and subcellular level. As DNA, located in the cell nucleus, is the most radiosensitive part of a cell, we will focus on the radiation effect at this specific site, following [77]. Subsequent to ionization, direct and indirect DNA damage can be observed, which is schematically represented in Fig. 2.11.

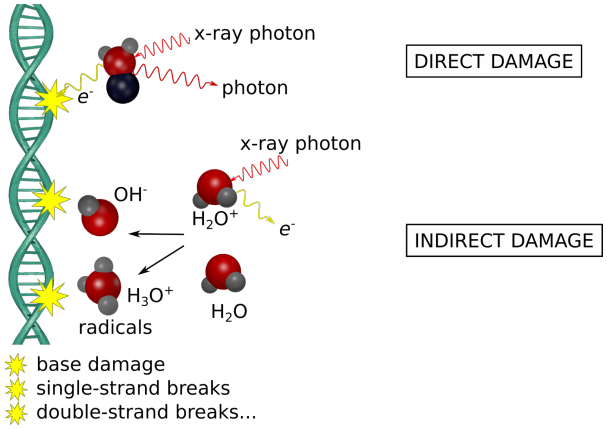

Figure 2.11.: *Schematic drawing of direct and indirect DNA damage.*

In the direct case, an electron e^- of, for example, a water molecule in proximity to the DNA is hit by an incoming X-ray photon (assuming an X-ray energy above the binding energy of the electron), which leads to ionization of H_2O to H_2O^+:

$$H_2O \rightarrow H_2O^+ + e^-. \tag{2.6}$$

Collision of the secondary electron with molecules of the DNA can lead to their ionization or excitation causing DNA damage.
The indirect effect implies that a water molecule outside of the DNA is radicalized and reacts with another water molecule to

$$H_2O + H_2O^+ \rightarrow H_3O^+ + OH^-. \tag{2.7}$$

Subsequent chemical reactions of the ionized radical H_2O^+ (Eq. (2.6)) or the free hydroxyl radical OH^- (Eq. (2.7)) lead to breaks of covalently bound molecules and thus to biological damages. Additionally, radiolysis can take place with the formation of hydrogen peroxide H_2O_2 by the hydroxyl radical OH^- and the superoxide radical HO_2 via

$$e^- + H_2O \rightarrow H_2O^- \rightarrow H + OH^-, \tag{2.8}$$

followed by

$$H + O_2 \rightarrow HO_2. \tag{2.9}$$

Hydrogen peroxide is then built by:

$$H + 2OH^- \rightarrow H_2O_2. \tag{2.10}$$

Both hydrogen peroxide and superoxide are highly reactive and thus can produce oxidative damage in the cell.
Such DNA damages in the dose range up to 100 Gy include single strand breaks and double-strand breaks (DSBs) (above $\sim$0.2 Gy), DNA-DNA or protein-DNA crosslinks, and base mutations in the nucleotide. Mechanisms like excision repair, homologous recombination, and nonhomologous end joining allow to repair these damages but may fail, especially in severe cases, e.g. a locally high concentration of DNA DSBs.
As a final consequence of permanent DNA damage, the cell can trigger its death via apoptosis, or the cell might loose its capability of reproduction, which is desired in tumor treatment. Lasting damages can be mutations, deletions, insertions, and aberrations, which should be reduced to a minimum when irradiating the normal tissue surrounding the tumor. Different assays, e.g. colony forming or chromosome aberration tests, allow to study these damages. Details on the radiation effects investigated in this thesis and on the according experimental procedures for the tests will be given in chapter 3.
Damages occurring on other subcellular units than the cell nucleus, like proteins or mitochondria, are rarely effecting the cell functionality as they are regenerative and exist in manifold copies. In-vitro studies have shown an increase in permeability of the cell membrane above $\sim$30 Gy [18, 78]. If the membrane is destroyed, uncontrolled cell death occurs – so-called *necrosis*.

Radiation damage – intercellular and vascular response. On the intercellular level, due to cell signaling, also neighboring non-irradiated cells can be affected in the same way as irradiated cells and even undergo apoptosis. This *bystander effect* has been investigated for various irradiation conditions and can occur already at very low X-ray doses [25–27, 79, 80]. Even so-called *abscopal effects*, i.e. effects in remote organs, and inter-animal signaling have been observed [28, 81]. Whether bystander or other distant effects are beneficial or undesirable is still an open question [81].
With increasing dose, for example in the case of high-dose microbeams, the mem-

brane of vascular structures might not only be permeabilized but can as well become disrupted and the microvascular length can be reduced [82]. Therefore, the vascular system has to create new pathways to supply the cut-off cells. As tumorous vasculature is thought to be immature in contrast to normal tissue, this process might fail in tumors and the shortage facilitates tumor control [18–20, 63]. Therefore, the difference in vascular repair between normal and tumorous tissue seen after MRT treatment is suggested to broaden the therapeutic window.

Microbeam-specific radiation effects. Several studies have sought to explain the biological mechanisms post microbeam irradiation and proposed a separation of the reaction into the dose volume effect and a microbeam specific effect. As a reminder, the dose volume effect describes the increasing tolerance to higher radiation doses when reducing the relative irradiated volume [80]. The microbeam-specific effect relates to a fast tissue recovery, which can be selective for mature and immature (tumorous) tissue, as seen, for example, in the repair of microvasculature at the chorio-allantoic membrane of chick embryos in ovo [19, 83, 84].
To discuss normal tissue sparing after MRT, we may separate the microbeam pattern in three regions: the valleys, the peaks, and the transition zones. Cells directly hit by X-rays, i.e. in the peak areas, are lethally damaged. With microbeam widths at the size of cells, the space of endothelial cells eradicated by irradiation has been shown to be filled by neighboring surviving cells that extend their cytoplasm into the gaps [80]. The consequent reduction of local edema contributes to tissue sparing – and thus to the dose volume effect – using MRT compared to conventional treatment. Lasting damage can be caused at the tails of the microbeams, due to scattering or bystander effects, for example. In the valleys, the X-ray dose of the tails sums up and reaches its maximum in the center of the array but should be kept below the normal tissue tolerance dose. Hence, this region largely contributes to normal tissue sparing implying, for example, a lower risk of skin ulcerations [85].

As such a large variety of parameters can influence the therapeutic effect of MRT, the radiobiological mechanism has not yet been fully understood and is moreover subject to changes in PVDR and microbeam geometry.

Relative biological effectiveness. For comparison of different studies, a common measure is needed. In order to express the absorbed dose leading to the same biological effect when using a certain radiation quality with respect to a reference radiation (IAEA), the term relative biological effectiveness (RBE) was introduced. The International Atomic Energy Agency defines the RBE as follows [86]:

> "A relative measure of the effectiveness of different radiation types at inducing a specified health effect, expressed as the inverse ratio of the absorbed doses of two different radiation types that would produce the same degree of a defined biological endpoint."

It is commonly used to compare the radiation damage caused by protons and heavy ions with respect to X-rays, or Cobalt-60. Thereby, we consider that X-rays produce a considerably higher number of single strand breaks per cell and Gray but, for example, α-radiation results in a larger number of double-strand breaks, which are more complex to repair. In X-ray MRT, the particle type remains unchanged, however, the dose is geometrically redistributed. For this purpose, the RBE throughout this thesis is defined as:

$$\mathrm{RBE} = \left.\frac{\text{Homogeneous dose}}{\text{Microbeam dose}}\right|_{\text{same effect}}. \tag{2.11}$$

2.1.4. Dosimetric considerations

To compare MRT with homogeneous irradiations and moreover MRT research performed at different setups, the applied dose must be defined. Research on parameter optimization for MRT is still ongoing such that a standardized MRT treatment procedure including dosimetry has not yet been established.
Historically in radiation oncology, the X-ray dose prescribed to treat a tumor is given as *dose-to-water* instead of a more specific *dose-to-medium*. Dose values prescribed by medical doctors nowadays are based on the knowledge and experiences of the last century with respect to dose-to-water. In a simplified picture, tumors are treated conventionally with doses of 60-80 Gy (dose-to-water) given in fractions of 2 Gy over about 6 weeks. As mentioned above, MRT treatment is supposed to be given in a single session and moreover, is used with valley doses of a few Gray and peak doses of several hundreds of Gray. Thus, a more intuitive convention for MRT would be to use a conversion factor for its relative biological effectiveness with respect to conventional treatment. For this purpose, several studies have sought to define a biologically equivalent dose (e.g. [87–89]). The big challenge at the current stage is that there is neither a uniform microbeam width or center-to-center spacing, nor an optimal PVDR, nor an agreement on the best range of the valley dose so far.
Therefore, it is important for every MRT research project to well determine the energy spectrum of the X-ray source and the microbeam pattern with the peak and valley doses such that comparability is guaranteed. The energy spectrum can be measured with spectral detectors as will be shown later on. As introduced in section 2.1.1, microbeams are created by multislit collimators or absorption gratings, which need to be well characterized for microbeam dosimetry.

In the process of dose determination for MRT, three main challenges have to be addressed. First, using beams of several micrometers in diameter requires dedicated dosimetric systems that allow for sufficient resolution of the microbeam pattern. Secondly, a large sensitivity range is necessary due to the strong variations between valley and peak dose. A third condition arises if the X-ray flux is varying over time: online, i.e. live dosimetry has to be performed.

Different options for dosimetric measurements exist that differ in accuracy but also in applicability depending on setup complexity and beam parameters.

Calorimetry

Graphite or water calorimetry is considered to be the most accurate system to determine dose-to-water with a possible relative standard uncertainty of 0.5-1% [90]. Here, the heat load deposited by the X-rays is measured and converted into dose, knowing the specific heat capacity and heat defect of the material. For MRT, the integrated dose could be measured with standard calorimeters but a single microbeam might not lead to a measurable temperature change. Therefore, a future system with a smaller graphite core shall increase sensitivity [91].

Ionization chambers

As a secondary standard system, calibrated ionization chambers allow for dose determination within 3-5% uncertainty. In such a chamber, a high voltage between anode and cathode creates an electric field such that free electrons and ions separated by incident X-ray radiation reach the electrodes before recombination occurs. For example, free-air ionization chambers can be employed, with a slightly higher dose uncertainty due to recombination and electron loss corrections at high dose rates. Yet, their aperture might limit the beam size and vice versa [91]. When using unconventional X-ray sources, errors in dose might increase as irradiation conditions deviate from calibration conditions, e.g. by using a different energy spectrum.
In conclusion, with calorimetry and ionization chambers, a broad beam can be well characterized.

2D and 3D water-equivalent dosimeters

However, to scan a microbeam and determine its dose profile, higher resolution systems are required. This can be achieved in two or three dimensions by radiochromic films, polymers or gels that are additionally water equivalent to avoid uncertainties by converting to dose-to-water. In principal, the interaction of X-rays with the dosimetric material causes a change in optical density that is subsequently resolved by appropriate imaging techniques. The dosimeters have to be calibrated within the desired dose range and energy spectrum with respect to a calibrated ionization chamber to determine the dose from the optical density. Especially, radiochromic film dosimetry can achieve a high resolution when read-out with a modified microscope instead of a conventional transmission scanner but is also subject to noise and film inhomogeneities [92]. Yet, this method lacks the aspect of online dosimetry. While being promising candidates for three-dimensional and online dose determination with high resolution, gel dosimeters like Presage®[9]

[9]Presage, Skillman, NJ, USA

still require investigations on reproducibility and dose rate dependency as well as improvement of homogeneity [15]. With a dose range of 10 to 500 Gy, these dosimeters are not applicable for the studies presented in the following. While deviating by 30% in absolute dose from Monte Carlo simulations, such gel dosimeters can still be used for positioning, e.g. in the case of interlacing beam geometry [93].

Silicon strip detectors

Specifically designed for MRT, silicon strip detectors permit fast readout and resolution as high as 10 µm. However, the energy-dependence of silicon in the relevant energy range is strong compared to the absorption coefficient of water. The sensitivity ranges from 10 to 50 000 Gy, which does not cover the full range of the MuCLS experiments. Moreover, the calibration of these detectors to achieve absolute dose values remains challenging [15, 94].

Single crystal diamond detector

Livingstone *et al.* proposed to scan the beam profile with a microDiamond detector[10], which has a cylindrical active volume with a radius of 1.1 mm and a thickness of 1 µm [95]. Using the thickness as resolution limit, the detector can be stepped through the microbeam to measure the beam profile. Similar as for ionization chambers, the detector has to be well calibrated to the applied energy spectrum. While a microDiamond detector might allow to resolve the microbeam pattern, online dosimetry of the full irradiation field cannot be performed.

Fluorescent nuclear track detectors

As another approach, fluorescent nuclear track detectors shall be mentioned [96, 97]. Generally used for the detection of neutrons and heavy charged particles, these wafers of fluorescent aluminum oxide single crystals (doped with carbon and magnesium: Al_2O_3:C,Mg) have been tested to successfully resolve microbeams with 0.6 µm resolution in a dose range from 0.005 to 50 Gy [98]. After irradiation, the detectors can be read out with laser scanning fluorescence confocal microscopy. Up to now, large dose uncertainties mainly stem from variations of detector sensitivity depending on the concentration of the fluorescent color centers of each detector.

The presented methods seek for clinical applicability with dose uncertainties on the order of 3%. For the first research experiments on MRT at the MuCLS with cells or small animals, larger deviations of the dose of up to 20% are acceptable. Moreover, the radiation effect in the new parameter space offered by the MuCLS is not comparable to existing studies. Using doses of hundreds of mGy to tens of Gy, the detector must exhibit an appropriate dose sensitivity. When using cells in a monolayer, the low absorption allows for X-ray detection behind the cells

[10] PTW, Freiburg, Germany

with a photon-counting detector. Knowing the X-ray spectrum and the absorbing elements along the beam path, permits to convert photon counts into dose (cf. Eq. (2.5)). For small animal experiments, a simple scintillation counter in front of the target that is calibrated with the photon counting detector is sufficient to deduce the dose online. To further evaluate possibilities of high-resolution dosimetry, radiochromic films and ion track detectors were tested, see chapter 4. Details on the dosimetry setup at the MuCLS and the according calculations can be found in chapter 5.2.

2.1.5. Challenges and prospects

Summarizing the main aspects of this chapter, MRT is a promising candidate to further widen the therapeutic window for tumor treatment, especially in children, but as well for epilepsy and other brain diseases. One of the main drawbacks of this method is the low penetration depth of keV photons compared to conventional therapy using MeV energies with a consequently higher absorption, i.e. larger dose deposition, in dense tissue like the skull. Moreover, when superposing the scattering contributions of each microbeam, the valley dose, with its maximum in the center of the microbeam array, rises with increasing field sizes and might reach the normal tissue tolerance dose. This restricts the treatable tumor size to a few centimeters and deteriorates the PVDR. Technical difficulties in absolute dose determination are still to be solved. However, as the MRT concept and effect is different to known conventional treatment and doses, the absolute dose might not be the most relevant factor. Similarly, the creation of the microbeam pattern mainly requires high accuracy to allow for comparison to other setups, and when interlacing schemes are used. While a non-ideal grating yielding larger microbeam tails will reduce the normal tissue sparing, it is not clear if the dose effect of these tails in tumorous tissue might be beneficial in MRT. If thereby higher tumor control is achieved, maybe interlacing schemes for homogeneous tumor coverage could be avoided. Due to the complexity of the radiobiological response, the MRT effect has still not been fully understood. Additionally, the variation of parameters like the X-ray energy, the peak dose and the microbeam geometry alter the tissue's reaction. Highly challenging is the patient positioning system including rotation of the patient at large-scale synchrotron facilities. While the time scale of single irradiations is on the order of few ms, the irradiation from multiple ports might take longer, and therefore positional changes could occur. The most elegant solution would be a rotating source around the patient as in conventional therapy. Even if compact synchrotron X-ray sources based on inverse Compton scattering are small enough for rotation, their laser cavity systems are extremely sensitive with respect to movements. However, they provide patient safety and beamline scheduling more readily than large-scale synchrotron facilities (e.g. due to multiple beamlines in parallel use) and, in particular, they provide an extended beam in horizontal and vertical direction. Thus, motion blur due to stepping can be avoided.
In conclusion, the radiobiological response to MRT still requires investigation,

especially with regard to the unexplored parameter space of MRT that becomes available with a compact synchrotron X-ray source like the MuCLS. This implies the study of lower peak doses to approach more clinically used values, as well as smaller microbeam sizes towards the size of the cell nucleus to reduce the valley dose.

2.2. The Munich Compact Light Source – a compact synchrotron X-ray source using inverse Compton scattering

Several approaches to achieve clinically affordable and room-sized synchrotron X-ray sources have been highlighted in the previous chapter. The CLS using inverse Compton scattering was constructed and commercialized by Lyncean Technologies Inc. in Fremont, CA, USA. Since 2015, this machine with a size of about $5 \times 3\,\mathrm{m}^2$ is in operation at the TUM in Garching, Germany. The concept of inverse Compton scattering allows to tune the X-ray energy via the electron energy and to reduce the storage ring size significantly as lower electron energies than at large-scale synchrotron facilities are sufficient to produce X-rays in the keV range. To enable comparison of the MuCLS performance with other X-ray sources, three characteristic figures of merit, brilliance, emittance, and coherence length are introduced below (section 2.2.1). In the following section, 2.2.2, the concept of inverse Compton scattering and its translation to X-ray production for a compact synchrotron source are described. Subsequently, basic components and parameters of the MuCLS are discussed in section 2.2.3, relevant to the MRT experiments shown in this thesis.

2.2.1. Figures of merit

Specific beam properties can be well compared by brilliance, emittance, and coherence introduced in the following.

Brilliance. The brilliance analyzes the performance of an X-ray source by [99]:

$$B = \frac{\Phi}{\Omega \cdot A \cdot \Delta E/E} = \left[\frac{\text{photons}}{\text{s} \cdot \text{mrad}^2 \cdot \text{mm}^2 \cdot 0.1\%\text{BW}}\right], \tag{2.12}$$

with respect to photon flux Φ = photons/s per source area A (i.e. *fluence rate*). Beam collimation is given by the solid angle Ω, which is proportional to the divergence angle θ with $\Omega \approx 4\pi\frac{\theta}{4}$. The energy spread is given in units of 0.1% relative bandwidth $\text{BW} = \Delta E/E_{\text{peak}}$ with X-ray peak energy E_{peak}.

Emittance. The confinement of a beam in space and momentum is described by the product of source size σ and angular divergence σ', named *emittance* with [99]:

$$\epsilon_x = \sigma_x \cdot \sigma'_x \tag{2.13}$$

$$\epsilon_y = \sigma_y \cdot \sigma'_y, \tag{2.14}$$

Here, horizontal and vertical source size are given as standard deviations σ_x and σ_y of the Gaussian beam profile – the same applies to the divergence. The emittance of a synchrotron X-ray source is obtained by convolution of electron beam emittance and photon beam emittance.
Consequently, in case of the MuCLS, the brilliance, which is inversely proportional to the emittance, can only be increased by reducing the electron beam emittance. This implies a smaller X-ray energy bandwidth, which is desirable but can lead to a less homogeneous beam profile (see section 2.2.3 below).
Following Heisenberg's uncertainty relation, the X-ray source size cannot be smaller than the size determined by the diffraction limit, such that the emittance is limited to $\epsilon_{min} = 4\pi/\lambda$. This results in an upper limit for the brilliance.

Coherence length. The coherence properties of a source can be described by introducing *transverse* and *longitudinal* coherence lengths. For the explanation of both properties, the wave picture is used [99].
The transverse (or spatial) coherence length considers (electromagnetic) waves with different propagation directions and describes the distance for which the waves' phases at two points of the resulting wavefield are no longer correlated. It decreases for larger source sizes but increases with the distance of the observer to the source and with the wavelength.
In contrast, the longitudinal (or temporal) coherence length depends on the degree of monochromaticity of waves with the same propagation direction. It is a measure for the distance from the source where the waves are out of phase by 180°.
At the MuCLS, a high longitudinal coherence compared to conventional X-ray tubes and synchrotron sources without monochromator can be expected. The transverse coherence length of the source is – despite the small source size – relatively short as the experimental setups are installed only a few meters away from the source (at 4 m from the source, the transverse coherence length reaches about 1.7 µm, following [100]).

2.2.2. Inverse Compton scattering

Inverse Compton scattering describes the generation of X-rays at the MuCLS using the particle picture: a relativistic electron transfers energy to an infrared laser photon upon collision. Neglecting the recoil energy of the electron and assuming head-on collision followed by back-scattering of the X-ray photon, the conservation of momenta allows to calculate the X-ray energy E (for a detailed derivation,

see [40]):

$$E \approx 4\gamma^2 E_l, \tag{2.15}$$

where the laser energy is $E_l = hc/\lambda_l$ with the laser wavelength λ_l. The Lorentz factor γ describes the ratio of the electron energy to its rest energy with $\gamma = E_e/m_0c^2$. Due to the proportionality of $E \propto E_e^2$, a variable electron energy permits access to a large range of X-ray energies.
To understand the reduction in storage ring size, let us consider the wave picture. At the CLS, the electromagnetic field of the counterpropagating laser pulse acts on the electrons like the magnetic field created by permanent magnet undulators at large-scale synchrotron sources. The term *laser undulator* results from this analogy. Under the same conditions as stated for Eq. (2.15), the fundamental wavelength λ_1 of an undulator is given by:

$$\lambda_1 = \frac{\lambda_u}{2\gamma^2}\left(1 + \frac{K^2}{2}\right). \tag{2.16}$$

K represents the undulator parameter, which is dependent on the maximum magnetic flux density and the undulator period λ_u. In case of a permanent magnet undulator, λ_u is in the range of a few centimeters fixed by the size of the permanent magnets. In contrast, using a laser undulator, λ_u is dictated by the laser wavelength with $\lambda_u = \lambda_l/2$ in the micrometer range (for the electron velocity approximating the speed of light [99]). From Eq. (2.16), it becomes obvious that one can already obtain X-ray energies ($\propto 1/\lambda_1$) with a laser undulator for electron energies ($\propto \gamma$) which are 100 times smaller than at large synchrotrons. Correspondingly, a smaller storage ring size is sufficient, from which compact synchrotron systems like the MuCLS benefit.
Note that the intensity and energy distribution of the X-rays is dependent on the scattering angle θ between incident electron beam and X-ray beam. Unlike in the simplified picture of head-on collision above, the design of the MuCLS requires a slightly slanted collision of electron beam and laser pulse. The according scattering cross section can be deduced from the Klein-Nishina formula and is shown for the MuCLS in the next section.

2.2.3. Setup and operation of the MuCLS

Components. A photograph of the MuCLS is shown in Fig. 2.12. At the MuCLS, X-rays are generated by almost head-on collision of highly relativistic electrons with infrared laser photons. For this purpose, electrons are produced by a radiofrequency photocathode gun and reach energies of 25-45 MeV in a linear accelerator, which consists of three high power microwave acceleration cavities (waveguides visible as copper structures in Fig. 2.12 (a)). The electrons are transferred into a storage ring of 4.6 m circumference, where they circulate with approximately 65 MHz being re-bunched by a radiofrequency cavity. At a rate of 25 Hz, a new electron bunch is injected replacing the old bunch that is dumped. The

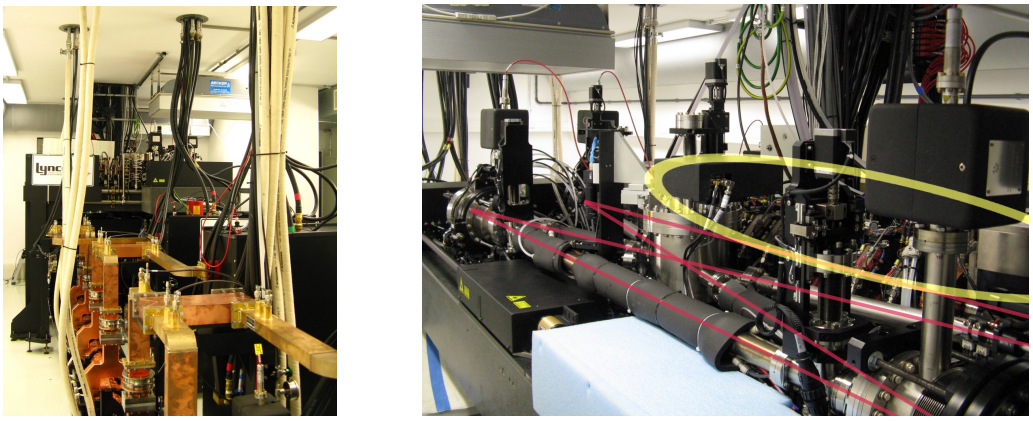

(a) (b)

Figure 2.12.: *Photographs of the MuCLS as installed at the Munich School of BioEngineering, TUM, Garching, Germany. (a) Side view of the accelerator structures including the waveguides (copper). The optical table with electron storage ring and infrared laser cavity can be seen in the back. (b) View onto optical table with a sketch that highlights the laser photon path in red in the bow-tie cavity and the electron path in the storage ring in yellow.*

infrared photons of (λ_l=1064 nm) are produced by a mode-locked Nd:YAG laser and enhanced in a high finesse bow-tie laser cavity, which shares one of the straight sections with the electron storage ring (see Fig. 2.12 (b)). Two laser pulses travel in the cavity with a length of 9.2 m at half the rate as the electron bunch in the storage ring to ensure collision with ∼65 MHz. At the interaction point, the beam waist of both bunches is focused down to less than $50\times50\,\mu m^2$. The beam divergence angle and with this, the final energy bandwidth are determined by a thinned region in one of the four high-reflectivity mirrors that transmits the X-rays. From here, the X-rays emerge with an opening angle of the cone beam of 4 mrad. In Fig. 2.13, the simulated intensity distribution and the normalized differential cross section are shown over the scattering angle θ for the 25 keV configuration with an electron energy of 37.5 MeV (adapted from [101]). The cut-off angle of ±2 mrad is indicated by red dashed lines, showing a quite homogeneous intensity distribution of the final beam profile under the assumption that the emittance of the electron beam is zero (cf. Fig. 2.13 (b)). In reality, the electrons at the MuCLS inherit a finite emittance, which means that they have a spread in position and momentum. This results in an even more homogeneous X-ray beam with respect to intensity and energy. Tuning the electron energy between 25 and 45 MeV enables the choice of different almost monoenergetic X-ray spectra with maximum energies E_{peak} between 15 and 35 keV offering an intrinsic bandwidth (BW) of $\Delta E/E_{\text{peak}}$ between 3 and 6%.

Infrastructure. The entire machine is located in a cave radiation-shielded by a 30 cm wall made of heavy concrete and 50 cm of electric furnace slag [41]. The

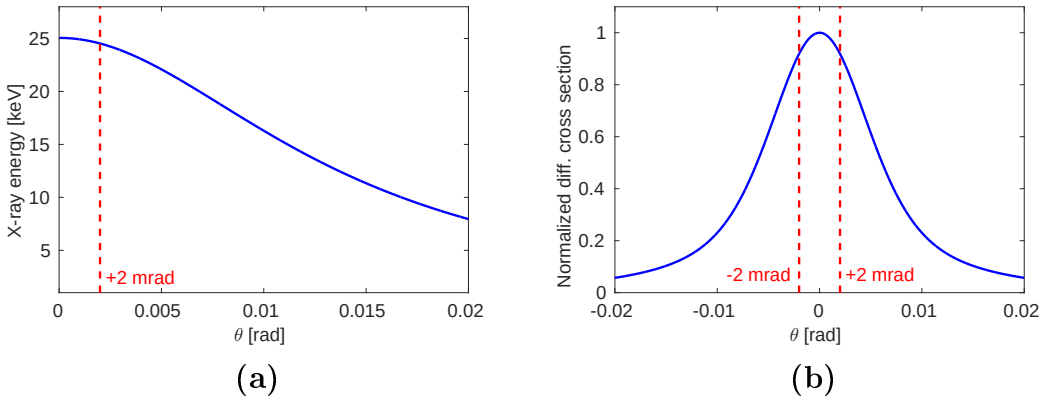

Figure 2.13.: *Energy and intensity distribution of the X-rays produced by inverse Compton scattering at the MuCLS. (a) The X-ray energy is depicted with respect to the scattering angle θ. (b) The angular intensity distribution is shown via the normalized differential cross section. In both graphics, red dashed lines indicate the cut-off angle at ± 2 mrad (adapted from [101]).*

X-rays exit the system through a beryllium window. The X-rays pass through the cave wall into the experimental hutches in vacuum-pumped beampipes covered by thin polyester foils to maintain the highest flux possible up to the setup position. Different endstations are available ranging from high-resolution, propagation-based phase-contrast imaging, and microbeam irradiations in the near hutch at 3 to 8 m from the source, to grating-based phase-contrast mammography and tensor tomography in the far hutch (at about 15 to 17 m source distance). Beam sizes between ∼7 mm (cave) and 60 mm (far hutch) are available.

Operation and operational challenges. Only the main aspects about the operation of the MuCLS are mentioned in the following to give insight into time and safety precautions necessary for MRT experiments in-vitro and especially, in-vivo. For more details, please refer to [42]. Time estimates can vary depending on the machine status (magnets on/off, energy change etc.).

- Chillers must provide sufficient cooling for magnets and modulators. Because of the large heat load, problems can occur if the external temperature is too high.
- For effective extraction of electrons, the photocathode in the evacuated radiofrequency electron gun must be clean. Contamination of the cathode, e.g. due to vacuum leaks, can cause the electron charge to drop continuously until the cathode is cleaned again with a UV laser. This process takes 10 to 15 min.
- The electrons are accelerated and bunched in radiofrequency waves generated by three klystrons, which are driven by solid-state modulators. After ramping the modulators to the desired RF output power levels, it takes about

20-30 min until the RF phases in the accelerator structures have stabilized. The occurrence of interlocks in these systems – possibly due to communication errors or arcing – can lead to failure of electron beam acceleration. In the rare case of several subsequent interlocks, slow re-ramping often allows to restore their operability (20 to 30 min).

- Shape and energy of the electron beam are optimized for injection into the storage ring using a screen inserted after the linear accelerator structures. This can take on the order of 10 min. The worse the injection efficiency, the higher the energy that is deposited in the kicker magnet, which regulates the bunch refreshment. As the kicker magnet system contains radiosensitive parts, these components – distributed on 'kicker cards' – may fail from time to time, requiring spare parts. Naturally, the probability of a kicker card failure rises with increasing energy. A broken kicker card has to be exchanged, which takes on the order of 2 hours. This includes a shutdown of the magnets, waiting time because of activation of parts of the kicker, card exchange, and re-ramping of the klystrons. With the improved kicker card diagnosis tool installed in spring 2017, the broken card can be identified much more quickly such that the time for card removal and re-insertion is reduced from 30 min to about 5 to 15 min.

- If the electron beam fulfills all requirements, it is injected at a low charge and stored. The injection efficiency is further improved by adjusting horizontal, vertical, and longitudinal injection while increasing the charge to the desired level (200 to 300 pC).

- The infrared laser delivers a TEM_{00} mode, which is further amplified in a set of solid-state amplifiers. Subsequently, the laser has to be locked to the passive enhancement cavity (Pound-Drever Hall locking [102]) with the goal of storing as much laser power as possible. Depending on temperature and alignment, about 15 to 20 min might be necessary.

- Subsequently, the cavity has to be locked to the reference frequency of 65 MHz to synchronize the laser pulses with the electron beam.

- Now, X-rays can be produced, which are observed on a photon counting detector in the second experimental hutch (see section 5.2.1). With a knife edge, parameters like source size and position are determined. The flux is estimated from a fully illuminated region of interest. Thus, the collision of electron beam and laser pulses can be optimized in time and space to minimize the source size, reduce inhomogeneities, and maximize the X-ray flux. Depending on the demand of the experiment, the tuning time can take between 15 and 40 min.

As first experiments on MRT were already performed in the commissioning phase of the MuCLS, cell irradiations shown in this thesis were performed within the

cave (2015-mid 2016). For exchange of the samples, this requires a shutdown and subsequent re-ramping of the klystrons. Additionally, the alarm sounding during the safety search of the cave might cause unlocking of the laser from the cavity. The small animal setup (built end of 2016) was located in the near experimental hutch. For microbeam irradiations, the 25 keV energy configuration was chosen to optimize dose rate and flux stability. All source parameters given in Table 2.1 and in the following chapters refer solely to this configuration (see [42] for more details). Due to interventions in the system from April 2015 to February 2017, during which the here-shown experiments were performed, several parameters are given in an interval. The *total flux* of 1×10^{10} ph/s corresponds to the average flux at 25 keV measured in a stability scan over 3 hours [41]. Following the most recent upgrade of the laser system in March 2017, a flux of 3.3×10^{10} ph/s at 35 keV can be achieved nowadays.

Table 2.1.: Parameters of the MuCLS for the 25 keV configuration. *Values refer to measurements from April 2015 to February 2016 (partly from [41]).*

Brilliance*	0.6 to 0.8×10^{10}
Total flux	1×10^{10} ph/s
Source size	39×36 to $50 \times 50\,\mu m^2$
Cone angle	4 mrad
Bandwidth	3.6 to 4%

*in units of: $^{ph}/_{(s\,mm^2\,mrad^2\,0.1\%BW)}$

3. Experimental methods and data analysis

In the following, general methods used for data acquisition and analysis are presented. This includes experimental procedures to assess different types of radiobiological responses, tools and methods for dosimetry, and software information. Setup-specific methods requiring (further) development and characterization will be explained in the respective chapter later on.

3.1. Experimental evaluation of radiation-induced damage

To better understand the sparing effect of MRT in-vitro, cell survival after irradiation is of high interest, which has been investigated in just a few MRT studies up to now [88]. Moreover, as mentioned in the introduction, a radiation therapy concept – especially when focusing at children – needs to avoid second tumor induction where possible. Therefore, radiation-induced non-lethal cytogenetic damage, which can lead to cancerous cell mutations, should be low. Achieving meaningful statistics on non-lethal aberrations like translocations is, however, cumbersome. With the knowledge that lethal damages occur in parallel to non-lethal ones, the more straight-forward investigation of lethal chromosome aberrations was chosen here. In order to verify the dose distribution visually, γ-H2AX or 53BP1 assays marking DNA double-strand breaks (DSBs) were performed at the different irradiation setups. Before the individual protocols are presented, the cell holder design is introduced, used for all cell experiments.

3.1.1. Cell holder design

At the experimental setups described in the respective chapters later on, X-ray source and detector are placed on a horizontal axis, i.e. the beam is travelling horizontally. Hence, standard cell irradiation in a petri dish is not feasible but the cells must be positioned vertically in the beam with enough humidity to avoid dehydration. For this purpose, a cell holder was constructed previously [103] that consists of three stainless steel plates between which 6 µm thin Mylar foils are stretched and clamped, see Fig. 3.1.
A circular aperture in the plates assures beam transmission for irradiation and dosimetry. Here, the cells are seeded using specific cylindrical chambers with

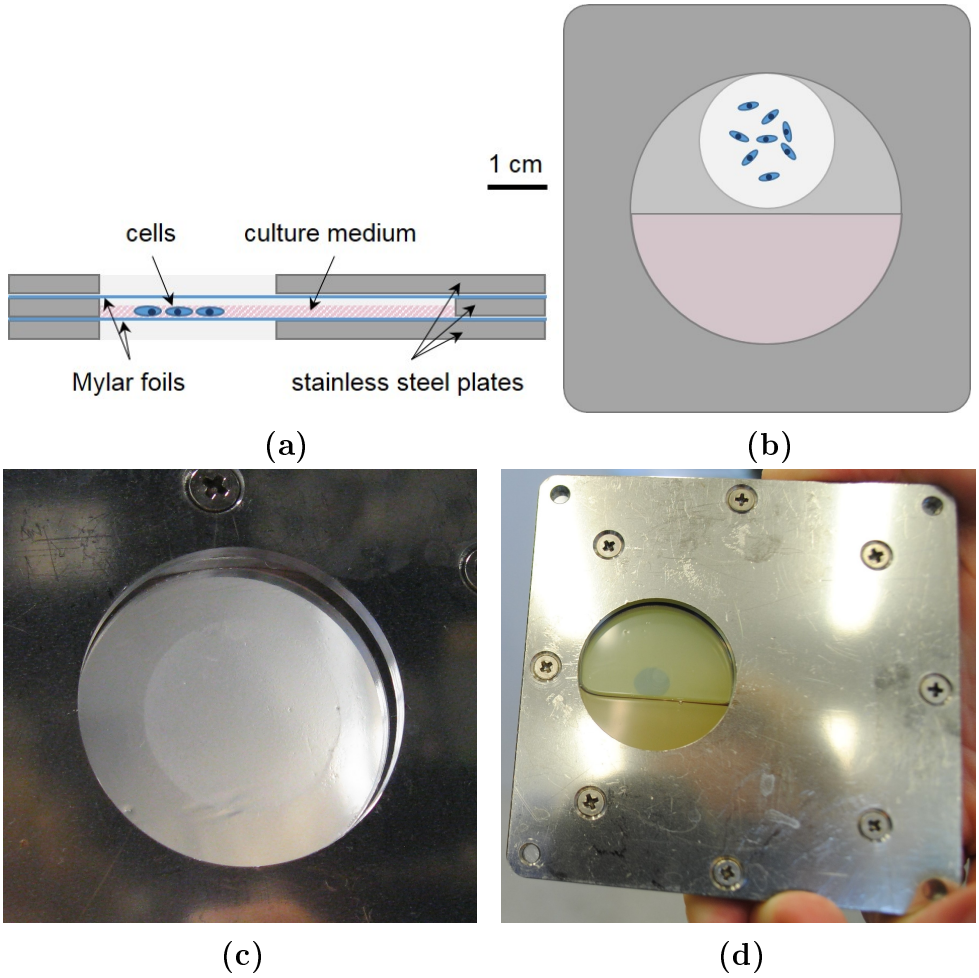

Figure 3.1.: *Design of the cell holder and cell distribution. (a) Schematic drawing of the side view at the center of the cell holder. Between the stainless steel plates, Mylar foils are stretched. The cells adhere to one foil and are covered with culture medium and the second foil. The medium is held in the space below the aperture when the holder is in upright position. (b) Drawing of the front view of the upright positioned cell holder with removed cover (second stainless steel plate). (c) Photograph of the aperture on the cell holder with cells extending over the full open field (whitish area). (d) Photograph of the cell holder tilted sideways to demonstrate the presence of culture medium. Here, the cells are only seeded in a centric circular area of about 4 mm diameter (whitish spot in the center). To visualize the X-ray beam hitting the cells, a radiochromic film (yellow) was attached behind the holder. The darker spot in the center shows the irradiated area.*

different diameters [104]. They can either occupy the entire aperture with more than 2 cm diameter, cf. Fig. 3.1 (c), or only a few mm in the center, see Fig. 3.1 (d). On the inner side of one of the stainless steel plates, the aperture is extended to offer a reservoir for the cell medium. Thus, medium is only available to the cells in horizontal position but ensures a humid atmosphere when the cell holder is placed upright (cf. Fig. 3.1 (b)). The Mylar foils are pre-treated with Cell-Tak

extracted from common mussels to improve cell adhesion (Cell-Tak Cell and Tissue Adhesive[1]).

3.1.2. γ-H2AX assay and 53BP1 staining

As stated above, the γ-H2AX assay as well as the staining of the repair protein 53BP1 allow to visualize DNA double-strand breaks with immunofluorescence microscopy.

γ-H2AX assay

With the γ-H2AX assay, DNA DSBs can be visualized via immunofluorescence microscopy. Two main repair mechanisms are initiated in the case of a DSB, homologous recombination and non-homologous end-joining. Both repair pathways include phosphorylation of neighboring H2AX histones to γ-H2AX. These H2AX histones from the H2A protein family are located in the eukaryotic cell nucleus as part of a histone octamer around which the DNA is wound. Within seconds following a DSB, the H2AX phosphorylation takes place. Adding anti-γ-H2AX antibody after irradiation labeled with fluorescent secondary antibody permits to detect the DNA DSBs in the cell nucleus. The corresponding γ-H2AX foci increase in number linearly with the absorbed dose [105] but, using standard imaging techniques, a too high concentration of foci will hamper the resolution of individual foci. The time point of maximal occurrence for highest foci intensity is cell line dependent. Almost exclusively, cells in G1 phase are subject to DNA damage. Non-specific binding of the antibodies or staining of mitotic cells [106] can lead to background fluorescence such that non-irradiated control measurements or, preferably, sham irradiations are crucial.

53BP1 staining

An early step in the DSB repair pathway is the recruitment of the 53BP1 protein at the DNA DSB site for ATM activation. 53BP1 can be stained by according antibodies and fluorescent dye as above. Depending on the concentration of 53BP1 in the cell and the number of DSBs induced, the signal intensity of 53BP1 foci might not increase linearly with dose due to a competition effect arising from the limited pool size [107]. A combinatorial staining of the two DNA DSB markers, γ-H2AX and 53BP1, is used in this work to further improve detection of DSBs and exclude spontaneous foci.

Protocol

For both staining procedures, we applied the same cell handling following Schmid *et al.* [108]. Cells were incubated in humidified atmosphere containing 5% CO_2 and 95% air at 37 °C unless stated otherwise.

[1] Corning Inc., Corning, NY, USA

HeLa cells from a cervical cancer cell line [109], most commonly used in scientific research, were grown in tissue culture flasks with RPMI 1640 medium supplemented with 10% fetal calf serum, 100 units of penicillin and 20 µg of streptomycin per ml of culture medium. In a few cases, Chinese hamster ovary (CHO-K1) cells were used instead of HeLa cells. Two weeks before irradiation, a frozen aliquot of cells was thawed and passaged 3 to 4 times. One day before irradiation, the cells were trypsinized, and seeded in a concentration of about 300 000 cells per cylindrical chamber onto the pretreated carrier foil (see above) to achieve a confluence of roughly 70%. Then, the cells were incubated, individually covered by a lid of a tissue culture dish. As during irradiation at room temperature repair mechanisms are rarely initiated, the cells were incubated post irradiation for another 10 to 30 min (if not stated otherwise in the respective experimental chapter, a standard incubation time of 30 min was used). Subsequently, the cells were fixed with 2% paraformaldehyde and then permeabilized in three subsequent 5 min washing steps in phosphate-buffered saline (PBS) + 0.15% TritonX-100[2]. For γ-H2AX staining, monoclonal mouse anti-γ-H2AX antibody (Anti-phospho-Histone H2A.X (Ser139) Antibody, clone JBW301[3]) diluted 1:350 in PBS was added to the irradiated cells and left at 4 °C overnight. After removal of unbound antibody by several washing and re-blocking steps, goat-F(ab')2-anti-mouse antibody, Alexa488 labelled (green fluorescence) or goat anti-mouse antibody, Alexa 568 labelled (orange-red fluorescence) was applied as secondary antibody (Invitrogen, Waltham, MA, USA). In the case of 53BP1 staining, a polyclonal rabbit antibody[4] served as primary antibody and either goat anti-rabbit Alexa 488[5] (green fluorescence) or goat anti-rabbit Alexa 555[5] (red fluorescence) as secondary antibodies. Finally, DNA was stained with DAPI (4',6-diamidino-2-phenylindole) and a cover slip was mounted with a drop of Vectashield[6] onto the cells. The thus fixed Mylar foil was cut around the cell area with a soldering iron to minimize wrinkle formation.

Data evaluation

Microscopic γ-H2AX foci were immunolocalized and images were acquired using epifluorescence sectioning microscopy (Axiovert 200 M including AxioCamMRm or AxioImager M2 including AxioCamMR3[7]) with various magnification factors from a 10x Plan objective for overview scans to a 63x oil immersion objective for individual foci discrimination in singular cells.

[2] *former* Sigma-Aldrich, *now* Merck KGaA, Darmstadt, Germany
[3] Upstate Biotechnology Inc., Lake Placid, NY, USA
[4] Novus, Littleton, CO, USA
[5] Invitrogen, Waltham, MA, USA
[6] Vector Laboratories, Burlingam, CA, USA
[7] Carl Zeiss Microscopy GmbH, Jena, Germany

3.1.3. Colony forming assay

The gold standard method to determine the overall cell survival after irradiation is the colony forming assay. In this thesis, the aim is to determine the survival rate of irradiated relative to control (sham irradiated) cells for both MRT and homogeneous irradiation geometry. A non-cancerous cell line is appropriate in order to use cell monolayers as a simplified model for normal (skin) tissue. Therefore, the robust CHO-K1 cell line was chosen with a well-established protocol for clonogenic cell survival studies. As radiosensitivity is specific to each cell line, quantitative results given in this thesis might not be valid for other cell lines but can indicate a certain trend.

Protocol

Two weeks before the experiment, a frozen aliquot of cells was thawed. Monolayer cultures were grown in RPMI-1640 medium supplemented with 10% fetal calf serum, 100 units of penicillin, 100 µg of streptomycin per ml of culture medium, 2 mM L-glutamine, and 1 mM sodium pyruvate. As the preparations took place at the Klinikum rechts der Isar, TUM in Munich, Germany, but irradiations were performed at the TUM in Garching, Germany, cells were transported to the irradiation site at least one day before the experiment to allow for acclimatization. Four hours prior to irradiation, the cells were seeded on the carrier foil and incubated (humidified atmosphere with 5% CO_2 and 95% air at 37 °C). All experiments for colony formation were performed at the MuCLS at a short source distance (in the cave) implying an X-ray beam size of 7 mm diameter. To assure complete coverage of the cells with the available beam size, the seeding area was restricted to a centered circle of about 4 mm (cf. Fig. 3.2). For irradiation, the cell chambers were

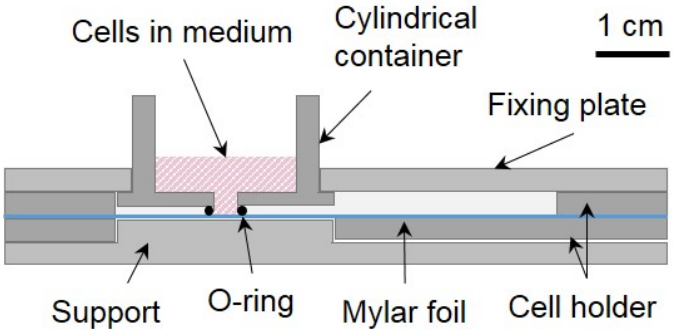

Figure 3.2.: *Schematic drawing of the cylindrical chamber placed on top of the Mylar cell carrier foil to restrict the seeding area to the desired field within the aperture of the cell holder. The cover plate was removed for seeding (compare to Fig. 3.1).*

positioned upright at room temperature (18 to 26 °C) for standard irradiations up to 30 min and at maximum up to one hour (with additional proof of cell vitality). Afterwards, the cells were detached from the Mylar foil by trypsinization, counted,

and reseeded in irradiation-dependent concentrations into 12-well plates. For irradiation doses and geometries resulting in lower cell survival, a higher concentration of reseeded cells is necessary to achieve a statistically relevant number of evaluable colonies. After 5 days of incubation, the colonies were fixed with methanol for 5 min, and stained with 0.1% crystal violet for 2 min. Colonies, defined by at least 50 cells per colony, were counted automatically with a Bioreader (BIO-SYS GmbH, Karben, Germany) using identical settings for each experiment.

Data evaluation

Taking into account the number of seeded cells, the survival rate of the X-ray irradiated samples was determined with respect to the plating efficiency of the sham irradiated samples. Following the linear-quadratic regression model for the survival fraction S that depends on the dose D with $S = \exp(-(\alpha D + \beta D^2))$, the corresponding sensitivity coefficients α and β were determined for both, the homogeneously irradiated cells as reference data, and the MRT treated cells (according to ref. [110]). A non-linear least-square fit was applied to the data weighted with the number of contributing replicates. From the resulting survival curve, the relative biological effectiveness (RBE) was calculated, described in Eq. (2.11).

3.1.4. Chromosome aberration test

To verify radiation-induced cytogenetic damage, the biodosimetric gold standard consists in the investigation of dicentric chromosome aberrations [111]. In parallel, other aberrations like acentric fragments, centric rings, and micronuclei are produced as explained in the following (selected aberrations are depicted in Fig. 3.3).

Dicentrics. A chromosome is visible in metaphase as two identical sister-chromatids attached at a centromere. Following a DSB in each of two chromosomes, the parts are possibly misrepaired to a dicentric containing both centromeres and an acentric fragment with the terminal ends only. Their occurrence rate allows to determine radiation doses with an accuracy of a few 100 mGy [112].

Acentric fragments. From the excess fragments of a dicentric chromosome, acentric fragments can be formed. Additionally, acentric fragments result from DSBs in the chromatids of one chromosome, or from the formation of centric rings. As acentric fragments appear more frequently than dicentrics, their background rate is higher, and thus the number of acentric fragments per cell is more error-prone.

Centric rings. A centric ring is formed from a single chromatid which lost its terminal ends by DSBs but maintained the centromere. The remaining ends are excess fragments that can form an acentric fragment as described above. The centric ring rate in an untreated cell is very low, which allows for quantitative analysis

following irradiation. However, the probability of radiation-induced centric rings is not as high as in the case of dicentrics.

Micronuclei. For completeness, micronuclei shall be shortly introduced. In the mitotic phase, chromosome fragments might form a nucleus separate from the daughter cells. Such *micronuclei* can also result from lagging chromosomes at an anaphase due to mitotic spindle damage. As micronuclei detection is straight-forward and fast, the cytokinesis blocked micronuclei assay is a common method in radiation biology studies but it exhibits a larger uncertainty in background frequencies than dicentrics (e.g. [113]). Therefore, micronuclei tests were not performed within this thesis.
Fig. 3.3 shows chromosomes in a human metaphase cell including dicentrics, centric rings, and acentric or access fragments. These structural aberrations are mostly

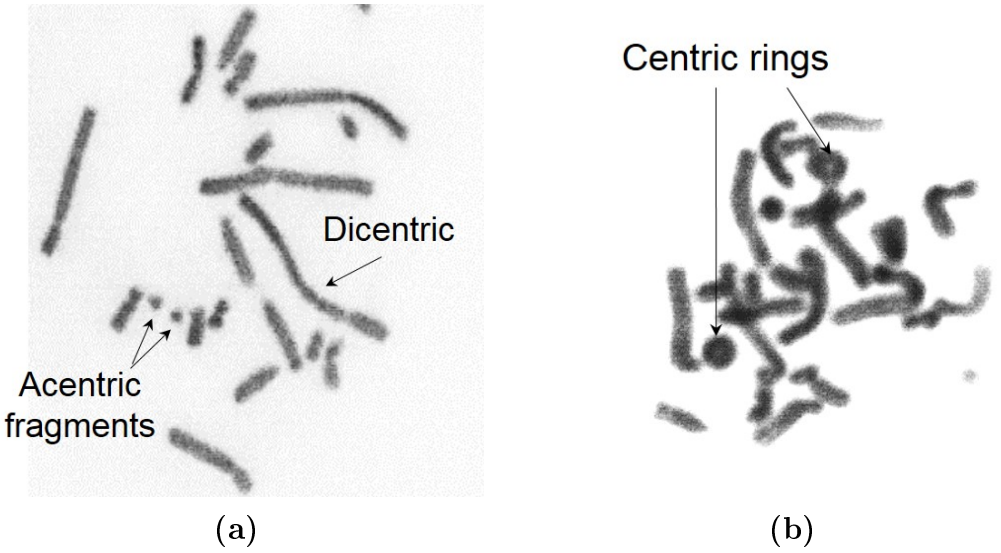

Figure 3.3.: *Microscopic images of chromosomes in a metaphase cell (A_L cell line). Arrows indicate a dicentric chromosome and acentric fragments in (a) and centric rings in (b). (Images courtesy of Prof. Dr. Ernst Schmid[8] and PD Dr. Thomas E. Schmid[9].)*

unstable, i.e. potentially lethal to the cell [114]. To extrapolate the probability of second cancer development from cytogenetic damage, the stable damages like translocations are important indicators. As the translocation rate increases with the number of dicentrics, indirect information on second cancer probability can be drawn from lethal aberrations [115,116]. Due to the complex evaluation of translocations, good statistics can be more easily achieved studying dicentric chromosome aberrations. Furthermore, Gascoigne *et al.* showed that inactivated (non-lethal) dicentrics can lead to additional DNA damage and genomic instability [117].

[8]Institute for Cell Biology, LMU, Munich, Germany
[9]Department of Radiation Oncology, Klinikum rechts der Isar, TUM, Munich, Germany

The automation of the counting process for aberrations as well as translocations is still subject to development. Commercially available systems provide full automation for micronuclei counting and supporting automated counting for dicentrics, for example (e.g. Metafer[8]).
Consequently, to achieve high accuracy, dicentrics and centric rings (and acentric fragments) were manually evaluated with a microscope by a blinded, experienced experimenter (Prof. Dr. Ernst Schmid[9]).

Protocol

Radiation-induced chromosome aberrations were analyzed in individual cells of a monolayer culture in the A_L cell line established for this purpose [49, 118]. These cells provide a standard set of CHO-K1 chromosomes with an additional single human chromosome 11. The same growing procedure and handling before irradiation was applied as described for the CHO-K1 cells. Immediately after irradiation, the cells were trypsinized and re-seeded in 4 ml RPMI-1640 medium supplemented with 10% fetal calf serum and antibiotics (penicillin/streptomycin) and incubated for 24 h at 37 °C in a humidified atmosphere of 5% CO_2 in air. Colcemid at a concentration of 0.03 µg/ml was added to the cultures 4 h after irradiation. The presence of colcemid allowed to synchronize cycling A_L cells which were at G1 phase of the cell cycle during irradiation [49]. The cultures were centrifuged, the supernatant removed and replaced by a hypotonic potassium chloride solution of 0.075 M at 37 °C for 10 min. The cells were fixed with a 3:1 ratio of methanol to glacial acetic acid. Aliquots of fixative were added dropwise to each sample and air dried. Subsequently, cells were stained with 2% of acetic Orcein for 10 min. Thereby, the cytoplasm of the cells is preserved and chromosome loss can be avoided. Chromosome preparation was performed according to the standardized laboratory procedure described by the IAEA for human lymphocytes [111, 119].

Data evaluation

The radiation-induced cytogenetic damage was assessed via the yield of dicentrics and centric rings per metaphase cell. For each irradiation geometry, a non-linear least-square approximation was used to fit the following linear-quadratic model (implementation, cf. colony forming assay, section 3.1.3) to the data for dicentrics and centric rings: dicentrics/cell $= \alpha D + \beta D^2 + c$. With regard to the very specific dose points chosen for evaluation, the fit must be kept stable. For a very low number of aberrations in the sham group, the offset value c to account for dicentrics in non-irradiated samples was set to zero, described as reasonable assumption in [111]. Additionally, the β-value was set to zero if no quadratic relation was manifest in the cytogenetic damage with dose leading to non-convergence of the fit.

[8] MetaSystems Hard & Software GmbH, Mannheim, Germany
[9] Institute for Cell Biology, LMU, Munich, Germany

3.2. Dosimetry – methods and analysis

3.2.1. Spectral analysis

In order to apply the appropriate dosimetric method, the spectrum of the X-ray source is required. Among others, this holds true for the choice of ionization chambers, and radiochromic films, described below. Moreover, with known energy spectrum, the relative biological effectiveness (RBE) of the radiation quality can be estimated with respect to reference data.

Source spectra shown in this thesis were recorded with one of the following two spectrum analyzers: Amptek X-123[10] or KETEK AXAS-D[11]. For this purpose, the detector was placed in the direct beam. Only in case of XRF measurements, the detector was positioned 90° to the beam direction.

For the Amptek detector, an external lead collimator allows to additionally narrow the acceptance angle reducing scattered radiation. However, characteristic X-rays emitted from the lead collimator might alter the measured spectrum. Attenuating slabs of polymethylmethacrylat (PMMA) or aluminum (Al) prevent saturation of the detector. These were positioned at sufficient distance to the detector to avoid undesired scattering contributions. Both spectrum analyzers convert incident X-rays to electrons via photoelectric absorption by a silicon (Si) photodiode with energy-dependent efficiency (Amptek: Si P|N 500 µm, Ketek: Si drift 450 µm). Gain and peaking time were optimized to choose energy resolution, and furthermore, to reduce pile-up at high energies and electronic noise at low energies. A multichannel analyzer sorts the pre-amplified and shaped pulse by amplitude for the desired energy range with a resolution at 5.9 keV of 145 to 260 eV for the Amptek and a minimum resolution of 133 eV for the Ketek detector. Calibration of these channels is performed via the characteristic K_α and K_β lines of different materials (e.g. lead (Pb) and copper (Cu)) in a separate calibration scan with equivalent settings inserting a dedicated calibration phantom in the beam path. A linear fit to the available calibration data yields the channel-to-energy conversion. To obtain the source spectrum, the measured spectrum has to be corrected for detector efficiency and for all absorbing elements along the beam path between source and detector. The energy-dependent efficiency was determined via the Beer-Lambert law (chapter 2.1.3.a, Eq. (2.1)) using the photoelectric absorption coefficient of Si tabulated at the National Institute for Standards and Technology (NIST[12]) [76]. Correction for possible absorbing elements is further described in the respective experimental chapter.

[10] AMPTEK, Inc., Bedford, MA, USA
[11] KETEK, Munich, Germany
[12] NIST, Gaithersburg, MD, USA

3.2.2. Ionization chamber dosimetry

Ionization chambers were used in this thesis to directly measure the dose rate of the X-ray beam or to calibrate radiochromic films.
Their working principle is shortly described in section 2.1.4. For this work, soft X-ray chambers were used with active areas below 2 cm in diameter. As these are calibrated for different radiation qualities (energy spectrum, filter) by PTW[13] under standard conditions with respect to air temperature and pressure, according correction factors, k_Q and $k_{T,p}$, need to be considered. With an electrometer, a voltage is applied to the ionization chamber to extract the electrons liberated by radiation-induced ionization of atoms. The measured charge can be converted into dose-to-water D_{raw} by a chamber specific factor $N_{D,w}$ given in Gy/C. The corrected dose value D is thus obtained as follows:

$$D = k_Q \cdot k_{T,p} \cdot D_{raw}, \tag{3.1}$$

with k_Q close to 1, deviating in the second decimal place, and

$$k_{T,p} = \frac{T_0}{p_0} \cdot \frac{p_m}{T_m}. \tag{3.2}$$

T_0 and p_0 correspond to normal air temperature and pressure conditions used for calibration of the ionization chamber. The measured temperature, T_m, was monitored at the setup position during the experiment with a standard thermometer. The measured pressure, p_m, was determined either by a digital barometer or a barometric sensor from a mobile phone. As an estimate, pressure values were also taken from the Oskar-von-Miller tower of the Meteorological Institute[14]. To reduce statistical errors, a mean dose value of at least three individual measurements was determined in each case.

In this thesis, mainly a thin window plane parallel chamber for soft X-rays was used (Type 23342, PTW). The most relevant parameters are given in Table 3.1. Importantly, the ionization chamber has to be placed in a homogeneous field of at least $1 \times 1\,\mathrm{cm}^2$. If, for example, the measured dose is to be compared with the dose calculated from a photon-counting detector, following Eq. (2.5), the field size must be large enough to fit both detectors without mutual influence.
The applied dose increases if absorbing material is surrounding the irradiated object, e.g. because of backscattered photons. Therefore, the irradiation geometry of the experimental setup needs to be considered for absolute dosimetry measurements. For some applications, the ionization chamber was placed in a solid water phantom composed of a 2 cm thick slab of Standard Grade Solid Water[15] with a cavity for the ionization chamber.

[13] PTW, Freiburg, Germany
[14] LMU, Garching, Germany
[15] Gammex, Middleton, WI, USA

Table 3.1.: Parameters of the ionization chamber.

Type	23342
Entrance window	0.03 mm PE
Sensitive volume	$0.02\,\mathrm{cm}^2$
Energy range	8-35 keV
Field size	min. $1 \times 1\,\mathrm{cm}^2$
Dose range (to water)	[50...300] mGy/min
Temperature range (air)	[291.2...297.2] K
Pressure range (air)	[950... − 1050] hPa
Air humidity	[40...60]%
$N_{D,w}$	$1.158 \cdot 10^9$ Gy/C
TW50*,†	1.005 ± 0.033
TW30*,‡	1.000 ± 0.033
T_0	293.2 K
p_0	1013.2 hPa

*Radiation quality is named *TW* and combined with the peak acceleration voltage (in kVp) applied at the electrode of the source used for the calibration measurement (50 kVp or 30 kVp).
†TW50 implies a 1 mm thick aluminum filter.
‡TW30 implies a 0.5 mm thick aluminum filter.

3.2.3. Film dosimetry

Radiochromic film dosimetry was applied for absolute dose determination and visualization of irradiation patterns. The resolution limit of different film types is investigated in chapter 4. Here, the standard handling is described.

Before absolute dosimetry can be performed, a calibration curve has to be taken for every film batch with the same, or similar irradiation settings as used for the calibration of the ionization chamber and the actual experiment (e.g. energy spectrum, and dose range). For this purpose, the soft ionization chamber was employed, described in the previous section. Depending on the experiment, the appropriate correction factors were applied: 1.00 for 30 kVp with 0.5 mm Al (TW30), or 1.005 for 50 kVp with 1 mm Al (TW50), given with 3.3% uncertainty each. As a minimum dose rate, i.e. electron current from the radiation-induced ionization of air, is required for the sensitivity range of the electrometer, and as the sensitive volume has to be entirely in the field of view, film calibration could not be effected at the MuCLS. Instead, the energy spectrum of a commercial irradiation system (RS225[16]) was adjusted to mimic most accurately the MuCLS spectrum. The energy dependence of EBT3 films in the range from 30 to 50 kVp was assumed to be lower than 5%, which was confirmed in a comparison study of 30, 50, and 70 kVp

[16]Gulmay Medical Ltd., Surrey, UK

calibration curves by Theresa Urban[17] [120].

In most cases, the calibration curve shown in Fig. 3.4 was applied, which was acquired as follows:
Films were calibrated for twelve dose values from 0 to 30 Gy operating the RS225 at 30 kVp X-rays, 15 mA, with filter 'no. 3' at 23.6 °C, and 942.2 mbar. The ionization chamber was placed in a $20 \times 20 \times 2\,\mathrm{cm}^3$ solid water phantom directly below the film. After more than 24 hours post irradiation, the films were scanned with a warmed-up flatbed scanner (Epson Perfection V700 Photo[18]) with 48-bit color depth one after each other at the same position on the scanning area, and with the same dpi setting to avoid readout artifacts. The red channel of each film was evaluated for the mean value of a homogeneous region of interest. The net optical density, OD, can then be calculated from the mean value of the irradiated film normalized to the unirradiated reference film by:

$$OD = \log_{10}\left(\frac{\text{Reference}}{\text{Irradiated film}}\right) \tag{3.3}$$

Different fit functions are available to model the change in optical density with dose. Compared to a formerly used polynomial function with $D = a_0 OD + a_1 OD^{a_2}$ including the fitting parameters a_0, a_1, and a_2, the rational function with $OD = a + b/(D - c)$ is preferable as it is more stable for higher dose values, consistent with the dose-dependent film behavior, and invertible [121]:

$$D = b(OD - a) + c. \tag{3.4}$$

Here, the fitting parameters resulting from non-linear least-square fitting are denoted by a, b, and c. For dose values above 20 Gy, the green channel was evaluated additionally to the red one due to its higher sensitivity in this dose range.

With 50 µm wide microbeams, the scanner resolution of 20 µm is not sufficient for absolute dosimetry (possibilities for high resolution dosimetry are discussed in chapter 4). Therefore, with this protocol, only homogeneously irradiated films were evaluated quantitatively. For the actual experiment, the self-developing films were irradiated and a new reference film was included, which was handled similarly to the irradiated ones except for X-ray exposure. The scanning procedure was performed as above. Subsequently, the dose values were obtained via Eq. (3.4) using the fitting parameters of the calibration curve. A discussion of uncertainties in absolute dose arising in film dosimetry can be found in chapter 4.1.

[17] Department of Radiation Oncology, Klinikum rechts der Isar, TUM, Munich, Germany
[18] Epson, Seiko Epson Corporation, Japan

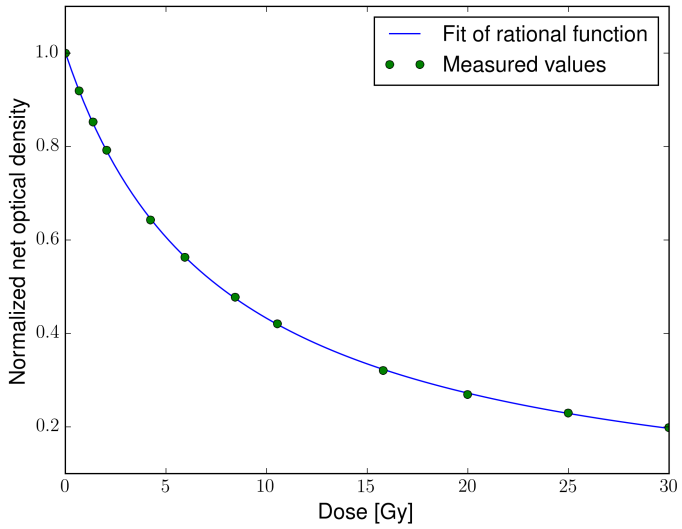

Figure 3.4.: *Calibration curve for EBT3 film dosimetry.*

3.2.4. Statistical analysis of radiation-induced effects and dosimetric measurements

Radiation-induced effects

For both, the in vitro and the in vivo study, error calculations were performed to analyze the significance of the observed effects, namely, the survival fraction measured by the colony-forming assay, the cytogenetic damage resulting from the chromosome aberration test, and the tumor growth delay determined in tumor-bearing mice. In all cases, the standard error of the mean (SEM) was calculated to account for the number of evaluated colonies, cytogenetic damage, or relative tumor volumes of each replicate x with respect to the mean $\bar{x}$:

$$\mathrm{SEM} = \frac{\mathrm{SD}}{\sqrt{n}} = \frac{1}{\sqrt{n}} \sqrt{\frac{\sum_{i=1}^{n} (x_i - \bar{x})^2}{n-1}}. \tag{3.5}$$

Here, SD describes the sample standard deviation. In rare cases where replicates are considered individually, the population's standard deviation is used, which reduces the denominator of the sample standard deviation (SD) with $\sqrt{n-1}$ to $\sqrt{n}$. As the cell handling for colony formation and the measurement of tumor sizes with a caliper leads to various statistical errors, both data sets were assumed to be normally distributed within a confidence interval of 68%. From the Student's t-distribution [122], the according t-factor is determined for the respective degrees of freedom df, related to the number of replicates n with: $df = n-1$. Consequently, the standard error of the mean (SEM) was corrected with this t-factor. In contrast, the chromosome aberration test can be performed with very high accuracy, so

small dose fluctuations can be distinguished. Hence, no additional correction is necessary. To determine the SEM of the RBE, errors of fit parameters from the dose effect curves were propagated using Gaussian error propagation.

Dosimetric measurements

Regarding the errors in dosimetry, SDs are given for each replicate (cell sample or tumor) based on statistical errors (cf. Eq. (3.5)). Of course, systematic errors occur in dose calculation that might arise from the determination of air absorption along the beampath, or the inaccuracy of absorption coefficients necessary for spectrum analysis and dose calculation leading to an error in absolute dose. However, as homogeneous and MRT irradiation data are compared which were obtained with identical dose calculation methods, systematic errors cancel out. Statistical errors result, for example, from the choice of regions of interest on the photon-counting detector, or the manual timing of the X-ray shutter, and thus can differ from sample to sample.

3.3. Software for data acquisition and data analysis

The acquisition of experimental data using a specific device was mostly performed with the manufacturer's software. For motor and detector control, mainly the scientific software *spec* was employed [123]. Dedicated programming code was developed using the Python programming language [124] to process the measured data either simultaneously to the experiment or following data acquisition. Mainly the NumPy and the SciPy package [125, 126] served for data analysis, and the Matplotlib package [127] for data visualization. Partially, the written programs include in-house developed modules of the Chair of Biomedical Physics (TUM). For segmentation of microscopic images, the image analysis software *CellProfiler* was used [128].

4. High-resolution dosimetry for MRT at lab-sized X-ray sources

As discussed in chapter 2, MRT requires microbeams with a high peak dose and a sharp lateral dose falloff to a low valley dose. However, the optimal microbeam geometry with respect to beam width and peak-to-peak distance is still unknown. Thus, it is of high interest to investigate the performance of MRT while varying the microbeam pattern from the minibeam scale down to the nanometer range, i.e. below cell size. While a wide number of publications address minibeam geometries with beam widths above 100 µm (e.g. [129–131]), the lower limit of microbeam widths and their potential for MRT has rarely been studied [29, 59]. Therefore, in this thesis, irradiation fields were analyzed applying microbeam widths smaller than 50 µm towards a few micrometers while at the same time microbeam width and spacing were assimilated. Such a fine microbeam pattern can only be characterized with detection methods providing correspondingly high resolution. While X-rays can be recorded with photon-counting detectors, for example, their resolution is limited by the pixel size, which ranges from 50 to about 200 µm and their efficiency is highly energy-dependent. To overcome these limitations and to extend the range of dosimetric procedures for MRT presented in chapter 2.1.4, four different approaches were reviewed:

- **radiochromic film dosimetry** (section 4.1): this method allows to directly measure dose-to-water as radiochromic films are composed of water-equivalent material. This is particularly useful for dose determination in biological experiments with e.g. cells, which mainly consist of water. For specific film types, resolution below 10 µm has been reported [92].

- **nuclear track detectors** (section 4.2): they offer high resolution when read out with microscopic methods and have shown to be sensitive to X-rays in a previous study [132]. To determine the dose, an adequate calibration system has to be established.

- **a high-resolution camera system** (section 4.3): high-resolution imaging can be peformed using a camera with CMOS or CCD sensor offering a pixel size on the order of a few micrometers, together with a scintillator for conversion of X-rays to visible light and magnifying objectives. Also for this

method, the dose has to be determined indirectly by quantification of the measured intensity.

- **X-ray fluorescence** (section 4.4): A spectral detector records the signal from an X-ray fluorescent material, which is stepped through the beam to rasterscan the microbeam pattern. To the first order, resolution is limited by the size of the fluorescent material. Dosimetry would require calibration of the recorded intensity values.

As a general measure for resolution and contrast of an imaging system, the modulation transfer function (MTF) was determined if applicable. The spatial frequency where the MTF is 10% (*short:* 10% MTF) was chosen as comparative figure. It should be noted that the 10% MTF describes the detectability of dose differences, i.e. relative and not absolute dose values. To determine the MTF, either a sharp edge or a narrow slit was imaged with the respective detection method. From this image, a line profile over the edge, a so-called *edge spread function*, has to be analyzed. To reduce noise, several edge spread functions were taken from a region of interest (ROI) and aligned mutually before computing the mean. Differentiation yields the line spread function to which a Gaussian fit was applied. The one-dimensional Fourier transform of the fitted curve was normalized to calculate the resolution at 10% MTF in line pairs per millimeter, lp/mm. This frequency $\nu_{10\%}$ corresponds to a feature size of $\frac{1}{2}\nu_{10\%}$ in real space (for more details, refer to [133]).

4.1. Resolution of conventional radiochromic films

This section on radiochromic film dosimetry for MRT shows how good (film) resolution can and has to be. Therefore, two aspects were investigated: what is the resolution limit of the employed films, and how do microbeam dose profiles look like if they are produced by fine-structured absorption gratings – in experiment and simulation.

The resolution of standard radiochromic films was tested using self-developing EBT films (EBT2, EBT3, and EBT-XD) and XRQA2 films[1]. The advantage of radiochromic films for dosimetry is their water-equivalence such that we can directly observe the microbeam dose pattern if their resolution is high enough. The film types were chosen to match the dose range available at our setups. In general, the films consist of an active layer of several micrometer thickness covered by polyester material. The active layer contains microcrystalline lithium salt (LiPCDA) undergoing polymerization when hit by ionizing radiation, which results in a change in optical density. The LiPCDA molecules are aligned as 10 to 50 µm

[1] Ashland, Bridgewater, NJ, USA

long hair-like elements [134]. Their resolution limit as stated by the manufacturer assuming standard film scanning is 25 µm or less.

4.1.1. Flatbed scanner

Before the resolution of the films can be determined, the performance of the film readout needs investigation. The typical procedure for film readout is described in chapter 3.2.3. Briefly, films were read with a warmed-up flatbed scanner (Epson Perfection V700 Photo[2]) at least 24 hours after irradiation. To minimize negative influence on resolution, scanning direction and position of the films were kept constant. Note that the following results refer to the specified nominal resolution of the scanner with 4800 dpi for films scanned in reflection and 6400 dpi in transmission instead of the maximum resolution with 12600 dpi, which is based on image postprocessing by interpolation.
To measure the resolution limit of the scanning method, the 10% MTF was determined from edge irradiation of an XRQA2 film (introduced below). The highest scanning accuracy was found to be 1200 dpi (in reflection) in contrast to the abovementioned specifications of 4800 dpi. Hence, the film scanner limits the resolution to about 21.2 µm. This observation was verified for the transmission scans performed with EBT films shown later on.

4.1.2. XRQA2 film

For low dose measurements between 1 mGy and 200 mGy at low X-ray energies, XRQA2 films were characterized. These films are non-symmetric and semiopaque such that scanning was performed in reflection. Unfortunately, dosimetry with this film type exhibits an experimental uncertainty (e.g. scan reproducibility, film and scanner nonuniformity) which increases from a few percent at 75 dpi to already 5% at 150 dpi and 6-7% at 300 dpi [135].
To analyze its resolution limit – specified by the manufacturer as larger than 5000 dpi (∼5 µm) – films were positioned directly behind a resolution pattern (assembly of gold structures, manufactured by former Xradia[3] and irradiated with an X-ray microtomography system at 30 kVp and 1 W (Zeiss Xradia Versa 500 system[4]). Radiographic images of the resolution pattern show an overview in Fig. 4.1 (a) and, in more detail, the investigated ROI in Fig. 4.1 (b).
Bartzsch *et al.* [92] proposed microscopic film readout to overcome the scanner limitation. Consequently, microscopic images were acquired at a Zeiss microscope (Axioskop 2[5]) with a 5-fold magnifying objective (0.42 µm/px) focusing in the plane of the active layer of the film, see Figs. 4.1 (c) and 4.1 (d). From the resolution pattern, the line pairs in the lower left column of Fig. 4.1 (c) correspond

[2]Epson, Seiko Epson Corporation, Suwa, Nagano, Japan
[3]*former* Xradia Inc., Pleasanton, CA, USA
[4]Carl Zeiss Microscopy, Pleasanton, CA, USA
[5]Carl Zeiss Microscopy GmbH, Germany

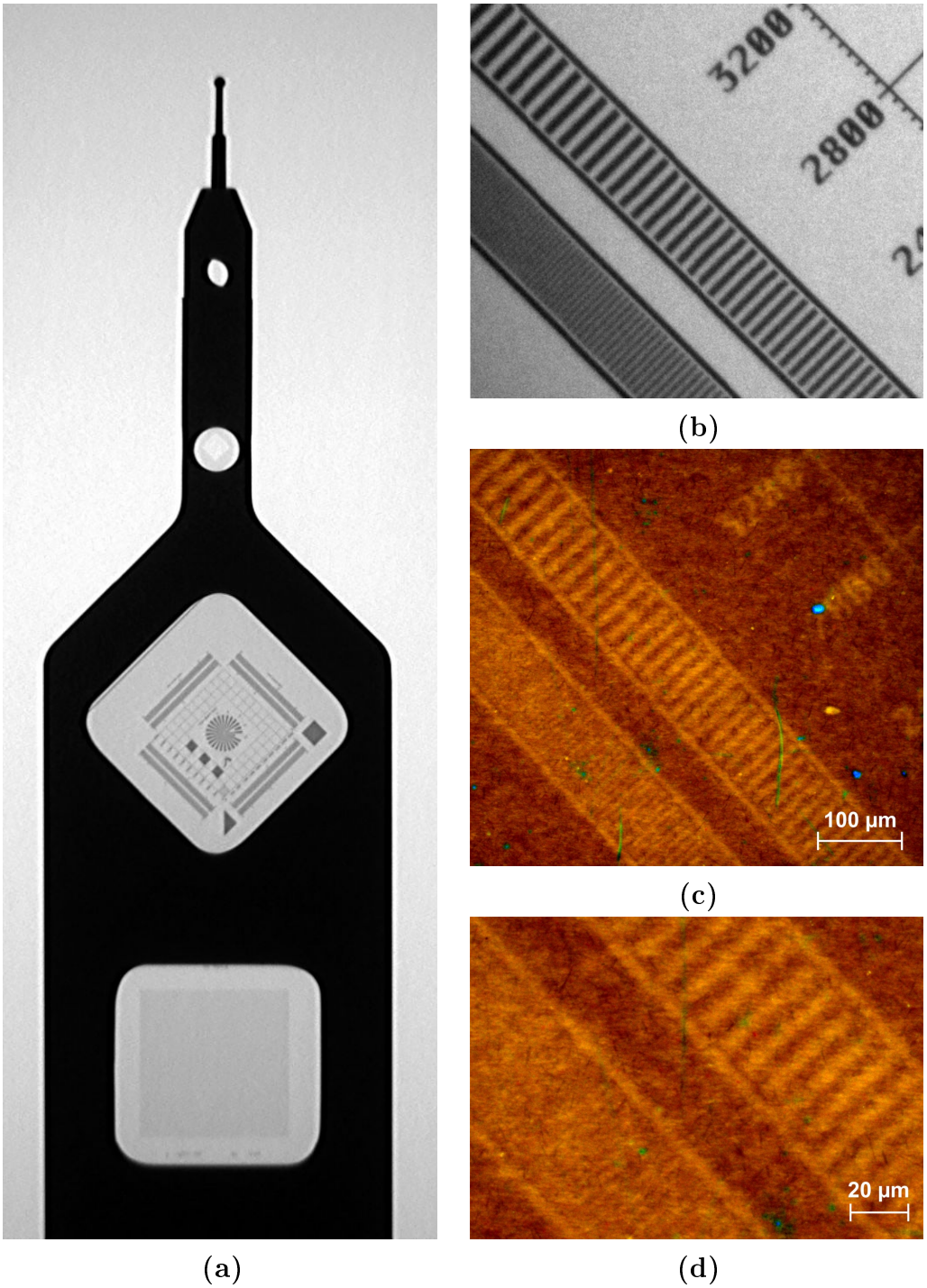

Figure 4.1.: *Xradia resolution pattern. (a) shows the entire phantom imaged at 40 kVp with a 0.39x objective. (b) A region of interest from a radiograph taken with 4-fold magnification objective (1.6 µm effective pixel size). The line pair in the column left to the number '2800' corresponds to a resolution of 24 µm. The second column to the left depicts line pairs requiring resolution below ∼15 µm. (c) Irradiated XRQA2 film imaged with a microscope (5-fold magnification). The resolution pattern was placed in front of the film, applying 30 kVp X-rays at the Xradia Versa XRM. Region of interest as in (b). (d) Detailed view of (c) to visualize the line pair pattern and the structure of the film material.*

to a resolution below 15 µm but can hardly be distinguished. Especially for this film type, fiber structures from the film material, visible in the enlarged image in Fig. 4.1 (d), limit the resolution to around 15 µm. Therefore, spatially-resolved microbeam dosimetry for microbeam widths on the order of a few micrometers cannot be performed. Moreover, this film type was reported to be energy dependent [135], which might hinder absolute dosimetry if calibration is not performed with the same energy spectrum.
In conclusion, a resolution in the range from 15 to 20 µm is achievable with XRQA2 films. However, clear feature separation is obstructed by the composition of the film material such that, for example, PVDR determination of microbeams below 20 µm will not be feasible.

4.1.3. EBT film

4.1.3.a. Film properties

EBT films are transparent and thus allow scanning in transmission mode. As experiments were performed at the time of the market launch of the EBT3 film, in this chapter both the EBT2 and its successor, the EBT3 film, are investigated. EBT2 films are built asymmetrically with a dynamic dose range of 0.1 to 10 Gy and are subject to larger inhomogeneities as well as energy-dependence compared to the symmetrically composed EBT3 films with a dynamic dose range from 0.1 to 20 Gy [136]. However, component and thickness of the active layer of the two films are almost equivalent, such that comparable resolution can be expected (28-30 µm LiPCDA layer). Yet, the frequent appearance of Newton rings in EBT2 films when scanning these films as demonstrated in Fig. 4.2 (a) can hamper high resolution. EBT3 films are specifically laminated with an anti-Newton ring coating to avoid this issue. For these reasons, the optical density modulation of the EBT2 film was investigated by eye only, whereas further quantitative analysis was performed using the EBT3 film.
As MRT requires a large dynamic dose range because of the high difference in peak and valley dose, a more recently developed EBT-XD film for a dynamic dose range from 0.1 to 60 Gy was investigated additionally. Even without microscopic readout, large grains or even grain clusters discernible in the scanned radiochromic film in Fig. 4.2 (b) indicate that film resolution is potentially limited by film inhomogeneity, resulting in statistic dose errors. This observation is in accordance with the study of Bartzsch *et al.* [92], who identified the crystal size on the order of 2 µm and the statistic noise as limiting factor of radiochromic film resolution. The authors measured a resolution of 5 µm, yet limited to one dimension. While with HD-810 and HD-V2 (Gafchromic films[6]) different film types appropriate for higher energies and doses were used, these films are made of similar material as EBT films so, in the subsequent study on EBT films, a similar limitation of resolution quality could be expected.

[6]ISP (Nuclear Associates), Wayne, NJ, USA

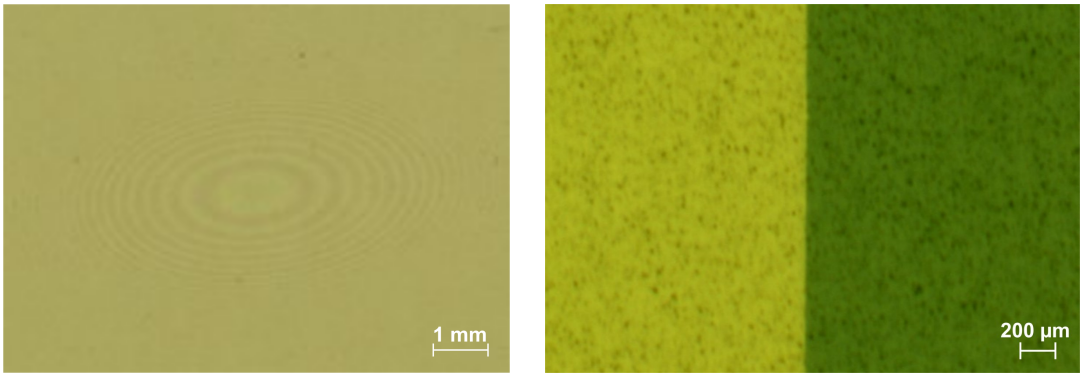

Figure 4.2.: *(a) EBT2 film showing Newton rings. (b) EBT-XD film irradiated with a partly transparent edge. Film scanning was performed using a flatbed scanner at 600 dpi for (a) and 6400 dpi for (b), respectively. To enhance the feature visibility in (b), brightness, and contrast were optimized for this thesis but not for quantitative analysis of the edge.*

4.1.3.b. Experimental methods

As explained for the XRQA2 film above, changing the dpi settings can influence the experimental uncertainty and hereby, the resulting dose value. To further investigate the dpi dependence in film scanning, a ROI on an irradiated EBT film was scanned with a resolution between 600 and 4800 dpi. The mean value of the ROI was evaluated yielding deviations of 1.5% with trend to higher pixel values for increasing dpi. To reduce such errors, films that were compared with each other were always scanned with the same dpi setting.

For quantitative determination of EBT film resolution, films were edge-irradiated for MTF evaluation using a highly absorbing tungsten alloy piece of about $4 \times 2 \times 0.5\,\mathrm{cm}^3$ (Densimet®[7]), or using a tungsten slit array of 50 µm slit size spaced by 300 µm described in chapter 2.1.2.b. After irradiation, films were read out with a flatbed scanner (described above) and/or microscope (Axio Imager M2[8]) to determine the resolution limit of the film. As the optical density of EBT films increases with dose, the film appears darker with higher absorbed dose.
To apply a fine-structured microbeam pattern on radiochromic films and study the resulting dose profile, gold (Au) absorption gratings of few micrometer pitch were used (tabulated as *grating 20* and *grating 10* in chapter 5.1). Grating 20 offers a period of 20.29 µm period with a duty cycle of 0.66, and a Au height of 70 µm (microbeam width: 6.8 µm, absorbing Au structure: 13.2 µm). Grating 10 is a 10 µm period grating of 150 µm high Au structures with 0.5 duty cycle based on bridge layout (for details on the grating design, see chapter 2.1.2.b).

[7] Plansee Composite Materials GmbH, Lechbruck am See, Germany
[8] Carl Zeiss Microscopy GmbH, Jena, Germany

For film irradiation, the absorbing structures were placed directly in front of the EBT film. X-rays were applied using a rotating anode X-ray tube at 50 kVp or the MuCLS at 25 keV (for more details on the setup, see chapter 5). Accurate positioning of the X-ray absorbers was verified with a photon counting detector, and penumbral blurring due to the finite source size was minimized to below 1 µm.

4.1.3.c. Experimental results

First, the edge irradiated EBT-XD film shown in Fig. 4.2 (b) will be further analyzed. The MTF obtained from the summed edge profiles yielded a resolution of 45 lp/mm, i.e. features down to 22 µm are resolvable. As this value corresponds to the resolution of the flatbed scanner measured above (section 4.1.1), the film resolution might still be higher. Hence, the film was scanned with a microscope using 40-fold magnification objective (0.16 µm/px), yielding the stitched image in Fig. 4.3 (a). Next to the image, in Fig. 4.3 (b), the corresponding line spread function – i.e. the derivative of the summed edge profiles – is shown. Due to the illumination setting of the microscope, scattered light might have influenced the right tail of the line spread function. Therefore, the left tail of the line spread function was evaluated as representative for the transition from non-irradiated to irradiated area. With a Gaussian fit to this part of the function, the resolution of the film is determined to 10.75 µm (at 10% MTF).

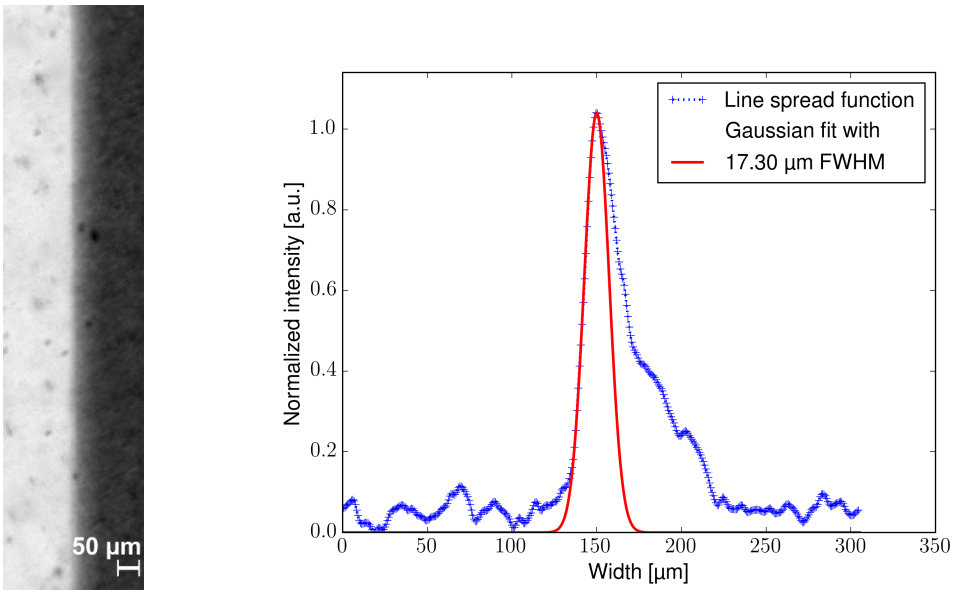

(a) (b)

Figure 4.3.: *(a) Microscopic images of EBT-XD film partially irradiated using Densimet as absorber. (b) Line spread function as derivative of the summed edge profile with Gaussian fit to the left tail. The full width at half maximum (FWHM) of the fit accounts to 17.3 µm, corresponding to a resolution of 10.75 µm at 10% MTF.*

Scattering contributions from photoelectric and Compton effect (see chapter 2.1.3.a)

can affect the film resolution, which is thus energy-dependent. Considering microbeam dosimetry, the irradiated edge can be regarded as a simplified picture of the transition from peak to valley in MRT. Close to the edge, dose is mainly deposited by secondary electrons arising from Compton scattering, whereas secondary electrons resulting from the photoelectric effect have a longer mean free path, and thus enhance the dose far from the edge. With a wide-ranging dose distribution, the application of fine microbeam structures for MRT might imply a low PVDR. Yet, when irradiating with a single microbeam or well-spaced beamlets instead of an open field, the dose contributions from (the smaller) peak area to the valley area can be reduced. Before studying the microbeam dose profile in more detail in simulations, the performance of EBT2 and EBT3 films will be investigated.
EBT3 film resolution was tested with the tungsten slit array. The resolution of the film using the flatbed scanner accounts to 22.2 µm, which equals the previously measured scanner resolution. Hence, microscopic imaging was performed. In Fig. 4.4, a detailed view from the microscopic image of an EBT3 film shows three vertically aligned microbeams.

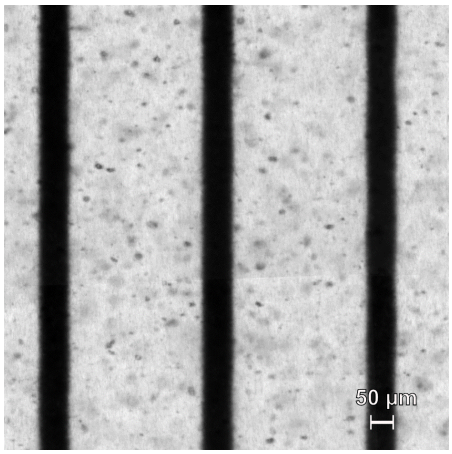

Figure 4.4.: *Microscopic image of a region of interest on an EBT3 film. The film was irradiated through a tungsten slit array of 50 µm slit width separated by 300 µm.*

The edge spread functions were taken from two regions of interest (ROIs) featuring each a peak-to-valley transition. The ROIs were chosen carefully to avoid blurring caused by grating imperfections. For 10% MTF, features in the range of 8.3 µm and 8.9 µm can still be resolved. The slightly deviating values might be influenced by inhomogeneities in the film or imperfections of the tungsten grid, which were minimized where possible. Hence, a slightly higher resolution compared to the EBT-XD film is obtained for the EBT3 film. While the active layer of the EBT-XD film is thinner, which should improve resolution, the granularity of this film type might have an adverse effect on its final performance. The resolution of the EBT films does not reach the 5 µm measured by Bartzsch *et al.* for the film types, HD-810 and HD-V2. This might be due to the alignment of the hair-like

elements in EBT films with more than 10 µm in length compared to the 2 µm crystal structures in the HD-810 and HD-V2 films.

As features on the order of 10 µm are resolvable with the EBT film type, EBT-XD and EBT2 films were irradiated with grating 20 and grating 10 (20.29 µm and 10 µm period, respectively). This allows to investigate the detectability of microbeam features at the resolution limit and, moreover, the microbeam dose distribution in a water-equivalent material.
Fig. 4.5 (a) shows a scanned image of the EBT-XD film irradiated with grating 20. Brightness and contrast were modified in Fig. 4.5 (b) to enhance visibility of the microbeams.

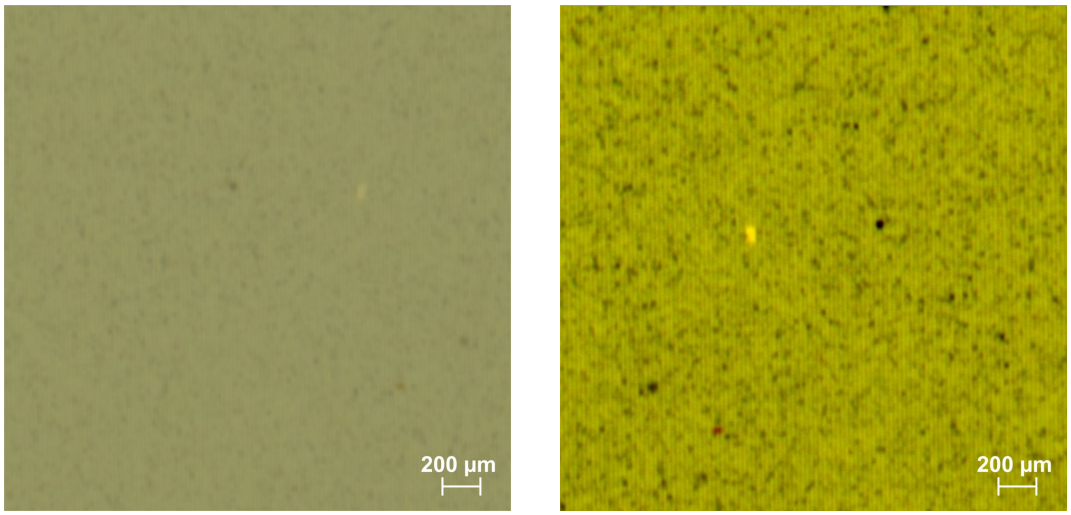

(a) **(b)**

Figure 4.5.: *EBT-XD film irradiated through a Au grating with 7 µm microbeam size. (a) Film as scanned. (b) Optimized brightness, and contrast subsequent to film scanning. Scanning was performed with 6400 dpi using a flatbed scanner.*

Albeit with very low contrast, a periodic pattern from grating features of 7 µm size can be recognized. As already stated for the edge irradiated film in Fig. 4.2 (b), the film granularity hinders full visibility of the periodic structure and impairs absolute dosimetry of fine microbeam structures. While a low PVDR of the microbeam profile could also result from X-ray absorption of the grating substrate or X-ray scattering, for example, the limited resolution of the flatbed scanner further deteriorated image quality.
To overcome this limitation, microscopic readout with 0.16 µm effective pixel size of the films was conducted in addition. In Fig. 4.6 (a), the microbeam dose profile created by grating 20 shows a high contrast between peak and valley dose. Small distortions in the image probably originate from impurities on the objective and on the glass slide used for microscopy even though background correction was applied. As already visible from the images obtained with the flatbed scanner, the film

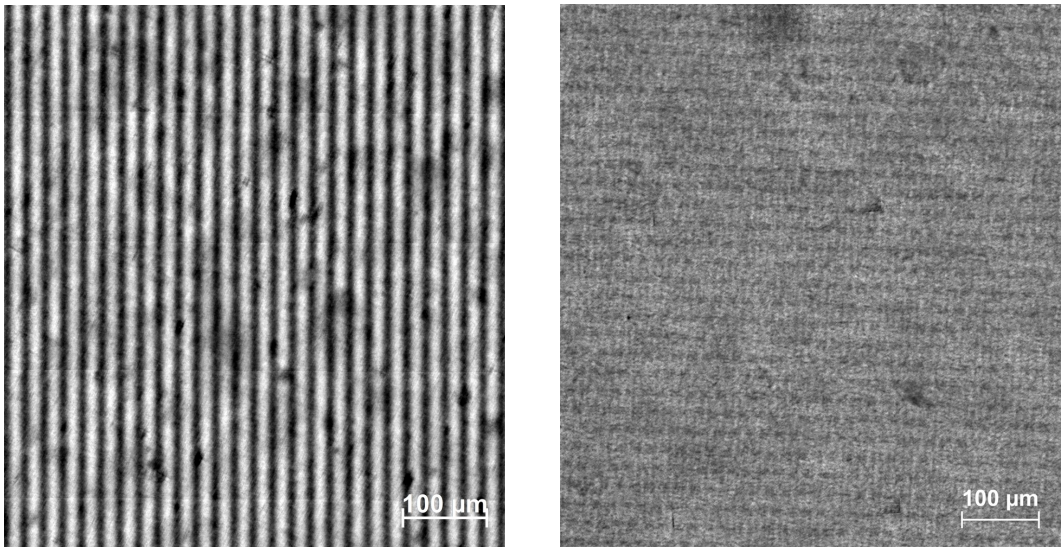

Figure 4.6.: *Microscopic images of radiochromic films irradiated with microbeam patterns produced by absorption gratings. (a) EBT-XD film irradiated with grating 20. (b) EBT2 film irradiated with grating 10. Contrast settings were optimized for structure visibility.*

granularity of EBT-XD films deteriorates the signal-to-noise ratio considerably. An even finer microbeam pattern was created by grating 10 irradiating an EBT2 film, which resulted in the dose profile in Fig. 4.6 (b). Compared to the dose profile from grating 20, the contrast between peak and valley is reduced. Especially, the bridge layout of the grating seems to disturb the creation of a profile with well separated microbeams. With microbeam widths of 5 µm only spaced by 5 µm, the previously determined film resolution of 10 µm is reached such that the microbeam dose profile might still exhibit a higher PVDR but cannot be resolved with the film. Moreover, the additional horizontal gaps in this grating design possibly enhance scattering into valley areas. To analyze if a higher PVDR can be expected with such fine microbeam structures, simulations were conducted additionally.

4.1.3.d. Simulations – methods and results

The resolution values were measured for mean energies of about 20 to 30 keV. Importantly, the penetration depth of secondary electrons – mainly responsible for dose deposition – reaches up to 20 µm in this energy range (see section 2.1.1). To verify if the peak-to-valley dose ratio at low grating periods is high enough to yield sufficient image contrast, the dose distribution in the center of an EBT3 film (water layer of 280 µm) was simulated (Adjoint Monte-Carlo simulation in Geant4 following [61]). A point-like X-ray source and an ideal microbeam pattern were assumed. As the integration of contributions from the 28 µm thick active layer did not show a significant difference compared to a full integration of the 280 µm thick

film, the latter was used to benefit from improved statistics. Fig. 4.7 shows the dependence of the PVDR with the grating period assuming a duty cycle of 0.5 and a $10 \times 10\,\mathrm{mm}^2$ field size for four different energy spectra: the ESRF spectrum with a mean energy of 100 keV (blue curve), the 25 keV MuCLS spectrum (green curve), a hypothetical MuCLS spectrum at 50 keV (red curve), and a 40 kVp molybdenum spectrum (cyan curve).

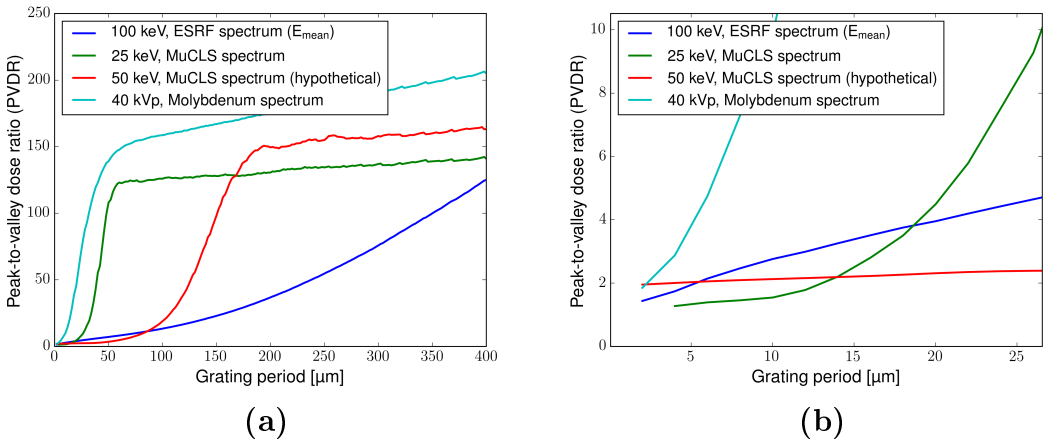

Figure 4.7.: *Simulated peak-to-valley dose ratio (PVDR) for different grating periods in water in a depth of 100 to 128 µm to approximate the active layer of an EBT3 film. Four spectra were used: in blue, the ESRF spectrum with a mean energy of 100 keV, in green, the 25 keV MuCLS spectrum, in red a hypothetical MuCLS spectrum at 50 keV, and in cyan, a 40 kVp molybdenum spectrum. A grating with equal microbeam width to spacing, i.e. a duty cycle of 0.5 was assumed. In (a) periods up to 400 µm are shown. (b) A focus on grating periods below 25 µm is given, as used in this chapter.*

The graph in Fig. 4.7 (a) shows grating periods up to 400 µm complemented with a ROI for grating periods below 25 µm in Fig 4.7 (b). In this range, using the ESRF spectrum results in lower PVDR values at grating periods from 100 to 400 µm than with X-rays of lower energies, but yields similar or even superior PVDR values at very low grating periods. Interestingly, with the 50 keV MuCLS spectrum, grating periods above about 170 µm result in comparably high PVDR values with a rapid falloff when reducing the period. With smaller grating periods, the PVDR approaches 1, which becomes obvious for periods below 5 µm. Even if a film resolution at this scale could be achieved, the contrast of peak and valley would be at the detection limit. More accurately, the microbeam dose profile from irradiation with grating periods below 5 µm corresponds rather to a homogeneous dose profile as the scattering contributions from the peaks into the valleys are too high to maintain the initial rectangular microbeam pattern (cf. the simulations in chapter 2). Considering, moreover, scattering at the grating surfaces, grating imperfections, penumbral blurring, and film inhomogeneities, such small grating periods cannot yield a microbeam dose profile with a peak and valley pattern. Thus, a preferential effect of MRT in contrast to homogeneous irradiation cannot

be expected.

A higher duty cycle of the grating might be beneficial to increase the PVDR. However, simulations would be required to investigate at which peak-to-peak spacing the valley dose is sufficiently low to achieve the desired PVDR. In the case of the 20 µm period grating with 13 µm spacing, for example, the microbeam dose profile was observed with high contrast of peak and valley dose.

Concluding the simulation results, there is a lower limit of a useful microbeam width and spacing for X-ray MRT, which increases with energy. Moreover, the minimum microbeam width and spacing depends on the desired peak dose as the resulting valley dose should not exceed the tolerance dose of the normal tissue.

4.1.4. Summary of film resolution for MRT

Finally, the results on performance and resolution of the different film types, XRQA2, EBT2, EBT3, and EBT-XD using flatbed scanner or microscope are summarized in Table 4.1.

Using a flatbed scanner for absolute dosimetry, only features larger than 20 µm are resolvable. This is not enough to correctly determine the dose in a 50 µm wide beam with a sharp lateral dose falloff, for example, as the edge cannot be sufficiently resolved. The microscopic evaluation yields high resolution but reproducibility has to be studied in detail to evaluate the resulting error in dose. The EBT3 film showed high resolution, reduced granularity, absence of Newton rings, and low energy-dependence, which are important parameters for absolute dosimetry. For a larger dose range, EBT-XD films provide a similar resolution with 10.75 µm at 10% MTF. The granularity of EBT-XD films strongly affects the dose values, especially in small regions of interest. If only verification of the irradiation pattern is desired with a very low dose, e.g. at a microfocus X-ray tube, XRQA2 films provide a resolution better than 20 µm. Absolute high-resolution dosimetry is impaired by the large range of inconsistent results observed with this film type. Consequently, due to film quality, EBT3 films are preferred for standard dosimetry. Absolute high-resolution dosimetry with EBT3 films seems yet to be limited to microbeam sizes above 9 µm when read out with a microscope, or to homogeneous fields with sizes in the mm-range in case of standard film scanning. As simulations suggest that microbeam widths in the range of 5 µm with equivalent spacing will not produce a microbeam dose pattern with high PVDR in water, a preferential MRT effect cannot be expected. Hence, the resolution of EBT films with about 10 µm seems to be sufficient at the current stage. Yet, if higher duty cycles are used with small microbeams, or if online dosimetry is required, different methods in addition to film dosimetry need to be considered. In particular with regard to absolute dosimetry, the error in dose resulting from the dosimetric measurement should be low. Therefore, an estimate of the uncertainty in dose introduced by film dosimetry is given in the following paragraph, finalizing this section.

Table 4.1.: Summary of the resolution measurements using radiochromic films.

	Flatbed scanner	**Microscope**	**XRQA2**	**EBT2**	**EBT3**	**EBT-XD**
Material	Standard	Glass slide supporting film	Semi-opaque, 10 µm LiPCDA layer	Transparent, asymmetrically embedded 30 µm LiPCDA layer	Transparent, symmetrically embedded 28 µm LiPCDA layer	Transparent, symmetrically embedded 25 µm LiPCDA layer
Dynamic dose range	-	-	1-200 mGy	0.1-10 Gy (-40 Gy using green channel)	0.1-20 Gy	0.1-60 Gy
Resolution measure	XRQA2 & EBT-XD film (10% MTF)	- (Manufacturer's specifications)	Resolution pattern (by eye)	Grating 10* (by eye)	Tungsten slit array (10% MTF)	Densimet edge (10% MTF)
Resolution limit	1200 dpi → 21 µm	Below 1 µm (depending on objective)	15-20 µm (microsc.)	- (see EBT3 film)	• 30 µm (scanner) • 9 µm (microsc.)	• 10.75 µm (microsc.) • 22 µm (scanner)
Features	Dependence on • scanning direction • positioning • dpi setting Good reproducibility	• High resolution • Reproducibility unknown	• Strong energy dependence† • Large calibration uncertainty [135] • Dominant fiber structures • Scan in reflection mode → Lower scan resolution • Low-dose limited • High resolution	• Newton rings • Energy-dependence • Dpi-dependence	• dpi-dependence • limited resolution • Good homogeneity	• High granularity • Good resolution
Absolute dosimetry for MRT	No – insufficient resolution of microbeams	Yes – reproducibility to be checked	No – large uncertainties and limited dose range	Yes – but EBT3 superior	Yes – above 9 µm	• Yes – for average along planar microbeams • No – for small areas because of inhomogeneities

*grating parameters are given in Table 5.1 in chapter 5.
†due to additional high Z materials that enhance the film response for low-dose measurements.

4.1.5. Errors in absolute film dosimetry

When discussing absolute film dosimetry, it should be noted that due to calibration, additional errors are introduced that stem from the different conditions for ionization chamber calibration, film calibration, and actual experiment, as well as the film readout. The former includes e.g. temperature and pressure measurements, the error on the given correction factors for the ionization chamber, and most importantly, the difference in energy spectrum and dose rate between calibration and experiment. Following the specifications given by Ashland [121], the dose rate response influences the dose by less than 5%, film uniformity by less than 3%, and the energy-dependence from 100 keV to 18 MeV by less than 5%. To study the energy-dependence of EBT3 films, calibration curves were acquired with X-ray tube voltages of 30, 50, and 70 kVp. Only a very low energy-dependence was observed for 50 compared to 70 kVp. The calibration curve at 30 kVp showed a slight deviation of about 3% to the other two curves [120]. Consequently, the energy-dependence can be neglected for experiments using the 25 keV configuration at the MuCLS and the 50 kVp spectrum of the rotating anode X-ray tube. Applying Eq. (3.4) in chapter 3.2 for dose determination, the errors in dose rate response and film uniformity are propagated to a maximum of ∼6% error in dose. Scanning reproducibility can be achieved with a standard deviation of 0.6% using the flatbed scanner V700 [137]. Moreover, photon noise might introduce additional dose uncertainty. This can be avoided by averaging the optical density over several cm^2 of homogeneously irradiated film. Errors from fitting a rational function to the calibration data (see chapter 3.2.3) are minimized by the acquisition of a large number of dose points. Statistic errors due to different handling of calibration or experimental films are avoided if possible. In total, a dose uncertainty below 10% can be expected for film dosimetry in our experiments.

4.2. CR-39 nuclear track detection for X-ray MRT

Another approach to achieve higher resolution in microbeam dosimetry is to investigate existing methods that detect ionizing radiation. As mentioned above, such detectors exhibit high spatial resolution to retrace the incidence of individual particles. Dedicated to alpha particles, and nowadays also used for neutrons and charged ions, the response of a CR-39 solid-state nuclear track detector to X-rays was investigated. In a previous study, these detectors were successfully used for soft X-ray imaging with atomic force microscopy (AFM) readout at an expected resolution of 100 nm or less [132]. However, this study used a laser plasma source delivering doses in the kGy range to obtain a large etching rate. Energetic particles can break chemical bonds of the plastic polymer CR-39 (allyl diglyol carbonate). If brought in contact with alkali solution, the hydroxide ions react with the polymer structure, break it, and etch the bulk of the plastic. This process is accelerated

at sites of radiation damage such that the ion tracks can be visualized. Confocal white light microscopy allows for non-contact three-dimensional topologic analysis of such detectors with a maximum lateral resolution of 1-2 µm. While these one-way detectors require chemical etching post irradiation in contrast to fluorescent nuclear track detectors based on aluminum oxide crystals, they provide superior spatial resolution [97, 138].

4.2.1. Materials and methods

CR-39 detectors (*short:* CR-39) of $5 \times 5\,\mathrm{cm}^2$ (TASTRAK CR-39[9]) were irradiated with 50 kVp X-rays from a rotating anode X-ray tube at 70 mA (specifications in chapter 5). The impact of X-rays is comparably low to ion damage such that CR-39 are generally stated to be insensitive to X-rays. Therefore, absorbers with known structure were used for testing purposes. First, a rectangular piece of tungsten alloy (Densimet, see section 4.1) was placed in front of the lower part of the detector yielding a non-irradiated reference area and producing a simple edge. Additionally, a tungsten wire of 200 µm diameter was positioned in the upper part of the same CR-39, cf. Fig. 4.8. Markers carved into the back of the detector

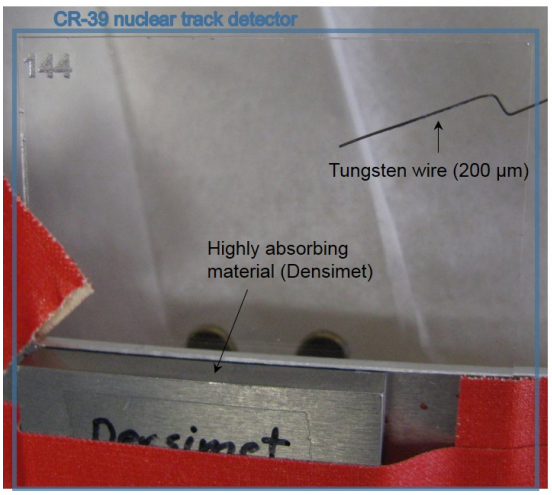

Figure 4.8.: *CR-39 detector (outline marked in blue, numbered with '144') irradiated at 50 kVp and 70 mA at a rotating anode X-ray tube for over 10 h. Two absorbers, a piece of tungsten alloy in the lower part and a 200 µm thick tungsten wire were placed in front of the CR-39 to generate transitions from irradiated to non-irradiated regions.*

glass with a scalpel facilitated the location of the absorbers. Following more than 10 hours of irradiation, the CR-39 detector was etched for 2 min in 6 to 7 mM/l sodium hydroxide (NaOH) solution and carefully rinsed with pure water, adapting a protocol from [132]. Read-out was performed with high-resolution white light microscopy (for details on the microscope setup, see [139]).

[9] TASL, Bristol, UK

4.2.2. Results

While the location of the tungsten wire could not be easily identified, an edge was measured at the marked outline of the Densimet edge on the CR-39 (cf. 4.9). Fig. 4.9 (a) shows an extract of the observed edge with the corresponding mean of the vertical line profiles in Fig. 4.9 (b). The image was corrected for inhomogeneous illumination by plane subtraction fitted through three points. In Fig. 4.9 (c), the topography of the microscopic image is presented, excluding outliers for visualization purposes.
A clear step could be observed in all acquired images. However, the difference in height of the two planes is only on the order of a few hundred nanometer, which makes definite evaluation of the X-ray impact difficult. In a next step, a 7 µm slit Au grating with 0.66 duty cycle (fabricated at PSI[10]) was positioned in front of the detector, covering 2/3 of the field of view. To reach more realistic exposure times, X-rays were applied for about 1½ hours. In this case, no clear irradiation effect could be detected on the microscopic images of the etched CR-39 – only an oscillating pattern was observed with a very low signal-to-noise ratio.

4.2.3. Possibilities and limitations

Considering the long irradiation time that seems to be required for sufficient contrast, further investigation of the detector response necessitates X-ray sources with higher photon flux. With accurate calibration, CR-39 detectors might be useful to map the peak-valley dose distribution of MRT with high resolution. In addition to the pattern detection, X-ray imaging could be applied for in-vitro experiments, as described in [132]. To track cell motion occurring in the incubation time after irradiation when performing γ-H2AX assays, for example, images of cellular distribution acquired with CR-39 during irradiation could be compared to DAPI and γ-H2AX fluorescence images taken after irradiation and incubation (cf. chapter 3). Higher resolution than with white light microscopy can be achieved with atomic force microscopy, which, however, requires a relatively long acquisition time. Currently, detector sensitivity and/or photon flux is the limiting factor to achieve quantitative X-ray dosimetry with CR-39 detectors.

4.3. High-resolution camera system

In a further attempt to increase the resolution in the analysis of MRT patterns, high-resolution camera systems were analyzed in theory and experiment. In this section, the benefits and challenges of such systems are discussed to enable the implementation of a high-resolution setup. To detect X-rays with a standard CCD or CMOS camera, a scintillating screen (scintillator) is placed in the focal plane that converts X-rays to visible light (CCD: charged-coupled device; CMOS: complementary metal oxide semiconductor). Naturally, its emission spectrum should be

[10]Paul Scherrer Institute (PSI), Villigen, Switzerland

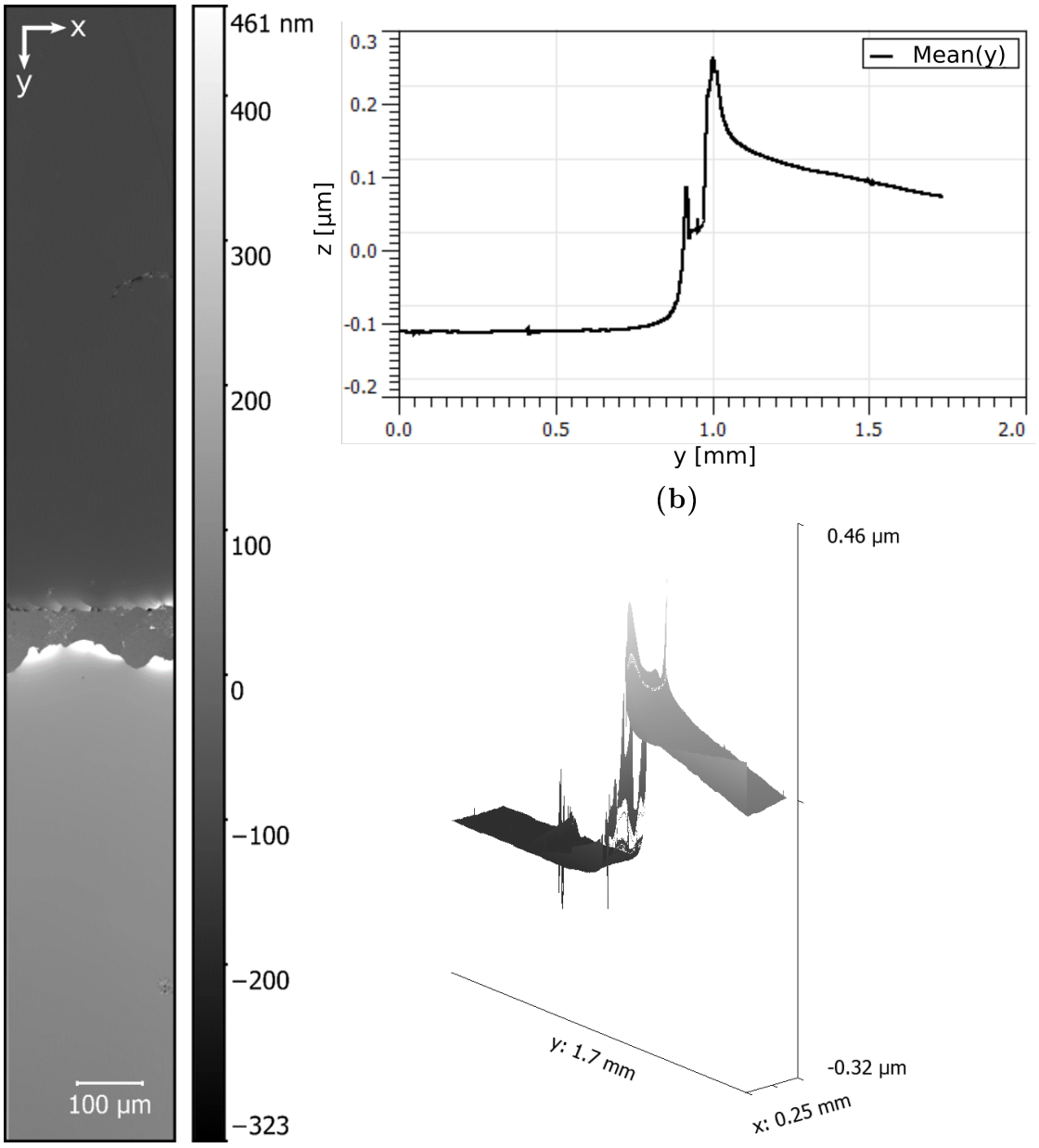

Figure 4.9.: *CR-39 detector scanned with white light microscopy. (a) Selected region of interest at expected edge. Plane subtraction was performed to correct for inhomogeneous illumination. (b) Mean of the line profiles along vertical axis (y) of (a) to visualize the step and determine its height (z) quantitatively. (c) A topographic view of the detector, masking out the outliers at the edge for better visualization. The grayscale setting in (a) and (c) is identical.*

appropriate to the wavelength sensitivity range of the camera chip. The scintillator efficiency is material- and energy-dependent. Appropriate scintillating materials are single crystals of YAG or LuAg:Ce, for example. Single crystals allow to reduce light scattering. To perform high-resolution X-ray imaging, several important factors have to be taken into account (cf. e.g. [140]):

- The diffraction limit for visible light is the system's ultimate resolution limit depending on the emission wavelength of the scintillator and the numerical aperture of the optical components.
- Optical magnification can be achieved with additional (microscope) objectives behind the scintillator. However, the numerical aperture increases with the magnification factor such that scattered light deteriorates the signal-to-noise ratio, and thus resolution. Therefore, a more than 20-fold optical magnification might not lead to any improvement in resolution.
- As X-ray sources have a finite spot size, so-called *penumbral blurring* [141] has to be below the desired resolution. Hence, the camera system might have to be close to the object under investigation. Thus, geometrical magnification is limited. If the point-spread function of the source is well-known, the blurring might be compensated using deconvolution algorithms, which might however affect quantitativeness.
- Polychromatic sources worsen contrast as, depending on the energy, photon absorption can occur at different depths in the scintillator, creating a varying intensity of visible light.
- The thinner the scintillator, the higher the resolution due to reduced scattering but the lower the efficiency and thus the signal-to-noise ratio. The relationship of scintillator thickness to resolution is almost constant. For YAG or LuAG:Ce scintillators with 5 µm thickness, an efficiency of less than 10% can be expected for the 25 keV MuCLS spectrum.
- The sampling frequency of the detector given by its effective pixel size determines the Nyquist limit [142]. Hence, the camera should provide sufficiently small pixels in the range of a few micrometers. Up to now, photon-counting detectors, which would simplify quantification, cannot fulfill this requirement.

4.3.1. Materials and methods

The potential of a CCD camera with 12 or 24 µm pixel size (PL09000 or PL1001E[11]) for imaging in the context of MRT was investigated using a rotating anode X-ray tube. CCD sensors provide high linearity with photon flux, which is important for quantitative imaging. Due to its high sensitivity to scattered X-rays, full lead

[11] Finger Lakes Instrumentation, Lima, NY, USA

shielding of the camera system was required. A black-colored polyimide film assured optical light absorption in front of the scintillator. Flat-field correction was applied to account for inhomogeneities of the scintillator or the CCD sensor. In order to improve resolution step by step, first a 100 µm thick cesium-iodine (CsI) scintillator was inserted in the focal plane of the camera. Following setup optimization with respect to shielding, distances, and focusing, a thinner scintillator of about 50 µm was used subsequently. In order to place the scintillator in the focal plane of the camera, either camera or scintillator have to be moved. However, it is technically advantageous to adjust the scintillator. A motorized focusing option is recommended when working with X-rays. In the here-described case, only the fine focus could be tuned with the FLI Focuser[11]. As the optimal focal plane can be very narrow, a programming script was developed to calculate the MTF from an edge profile while varying the focus distance. Therefore, a piece of copper was inserted, which covered half of the field of view. The focal plane was then determined to the position with the maximum 10% MTF. This method is applicable for a sufficiently high signal-to-noise ratio, which may require long exposure times. Increasing the focal aperture of the lens not only enhanced efficiency but also reduced electronic noise, which outweighed the consequent loss in resolution.

4.3.2. Results

Fig. 4.10 shows images acquired with the improved setup, i.e. the 50 µm thick scintillator and the PL09000 camera with 12 µm pixel size. An objective lens with 35 mm focal length was mounted reversely to the camera to achieve an effective pixel size of about 1.9 µm. Applying 50 kVp X-rays with a tube current of 70 mA, an exposure time of 120 s was chosen. System resolution was studied with two Au gratings, placed close to the scintillator: the first, depicted in Fig. 4.10 (a), grating 20, with 7 µm slit size and a duty cycle of 0.66, the second, grating 10, in Fig. 4.10 (b), with 5 µm slit size and a duty cycle of 0.5 (details on grating manufacturing can be found in chapter 2.1.4, a table of all gratings in chapter 5.1).

While the 7 µm microbeams of the continuous grating structure in Fig. 4.10 (a) can be well distinguished, the bridge layout of the 10 µm period grating is blurred and structure visibility is impaired by noise. Compared to the EBT film analyzed by microscopy in the previous section (cf. Fig. 4.6), the contrast for grating 10 is significantly improved with the camera setup. From MTF analysis of measured edge profiles, the resolution of the camera system was estimated to below 5 µm at 10% MTF, which confirms superior resolution compared to film dosimetry. As the film is water-equivalent and thus yields a dose profile instead of an image of the microbeam pattern, the dose deposition might still be better represented by radiochromic films. To analyze dosimetry with the camera system, a simulation of the dose distribution in the tissue of interest would be necessary, given the intensity pattern measured with the camera system.

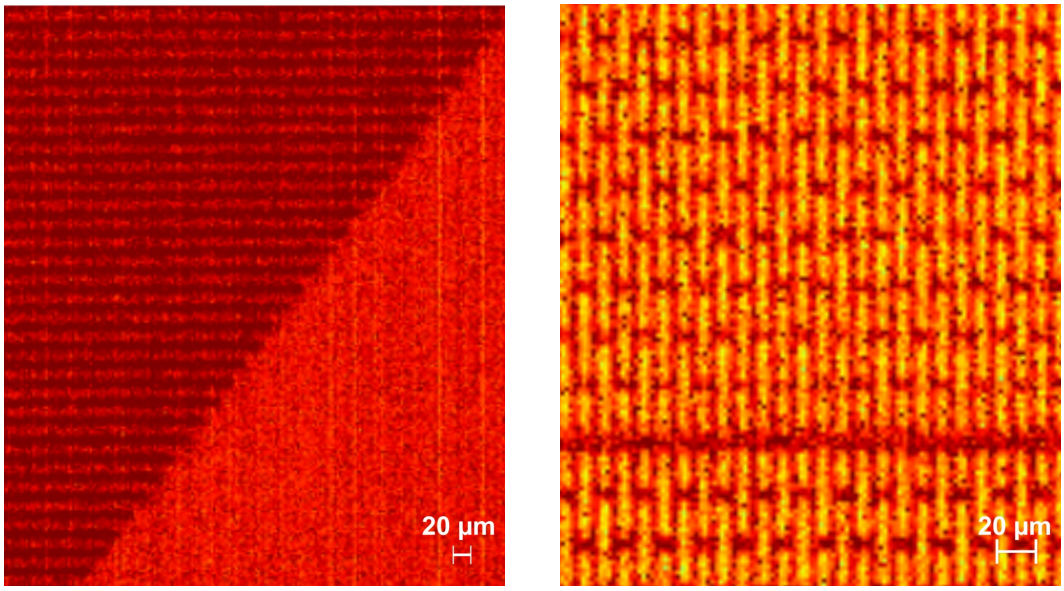

Figure 4.10.: *Resolution of microbeam structures from Au gratings with a CCD camera system. (a) 7 µm microbeams with 13 µm center-to-center distance were created with a horizontal Au grating. A copper plate was inserted additionally in front of the scintillator for focus optimization. (b) An Au grating of 10 µm period (duty cycle = 0.5) with bridge layout [73] is visualized. Contrast settings were adjusted to improve structure detectability.*

4.3.3. Possibilities and limitations

In conclusion, using this camera system with a 50 µm thick scintillator already allows to resolve microbeams of a few micrometer. Considering that the center-to-center spacing in MRT is often more than twice the beam width, good distinction as seen with the duty cycle of 0.66 can be expected. Unfortunately, the blurring of the pattern by scattered light due to the finite thickness of the scintillator and the polychromaticity of the source, as well as scintillator inhomogeneities might not allow for quantitative imaging so far. As mentioned above, a scintillator thickness of down to 5 µm will further increase resolution at the cost of illumination time. Additionally, microscopic objectives with different magnification factors could be used. Changing the objectives behind the scintillating screen needs high reproducibility to maintain the focus position, which is challenging to optimize at high magnification. High linearity of the image sensor is required for quantitative imaging. With the advancement of CMOS sensors, a linear response comparable to CCD sensors can be expected, combined with a wide dynamic dose range and low readout noise, which might further improve image quality (e.g. [143]). Moreover, the point spread function (PSF) of the detector system is an important characteristic. Depending on the quality of camera and scintillator and their mutual alignment, the detector system's PSF might be large. Hence, deconvolution is required, which might introduce additional artifacts and loss of quantitativeness.

While magnifying optics can improve resolution up to a certain numerical aperture, a camera sensor offering a small pixel size of a few micrometers might be beneficial. If the requirements above can be fulfilled, resolution below 1 µm for microbeam detection is achievable with current techniques. At X-ray sources appropriate for MRT, however, resolving features below 1 µm will remain very challenging or even impossible in reasonable measurement time and with the typical setup accuracy available.

4.4. X-ray fluorescence

To verify the creation of very fine microbeam structures before performing dosimetry, we should avoid detector systems which depend on the penetration depth of secondary electrons like radiochromic films and we need to overcome the limitation of detector pixel size, numerical aperture of optics, and finite scintillator thickness, described above. For this purpose, an X-ray fluorescence (XRF) setup was developed, which allows to acquire a raster scan of the microbeam pattern (basic information on XRF can be found in chapter 2.1.3.a). The MuCLS with its almost monochromatic energy spectrum is well suited for excitation of the material of the scanned probe while avoiding spectral contributions in the range of fluorescent emission.

4.4.1. Materials and methods

4.4.1.a. Setup

The XRF setup was built in hutch 1 at the MuCLS (cf. chapter 5.2) close to the source to benefit from high flux as a field of view below 1 mm in diameter is sufficient. A silver (Ag) dot of 150 nm height and 150 µm diameter was placed parallel to the grating lines of an absorption grid on a motorized high precision stage moving perpendicular to beam and grating line direction. Close to the dot, an energy-dispersive detector (KETEK AXAS-D[12]) was positioned at 90° to the beam path to avoid the direct beam and scattering contributions, but record X-ray fluorescence from the Ag dot (operation of spectrum analyzers is described in chapter 3.2.1). Figs. 4.11 (a) and 4.11 (b) show the setup as schematic drawing and photograph, respectively. The MuCLS was operated at 31 keV to excite Ag with its K-edge at 25.5 keV while reducing contributions from the MuCLS spectrum due to scattering at the support of the Ag dot.

4.4.1.b. Silver dot manufacturing

The Ag dot was manufactured by vapor deposition and photolithography at the Center for Nanotechnology and Nanomaterials (ZNN[13]).

[12]KETEK, Munich, Germany
[13]TUM, Garching, Germany

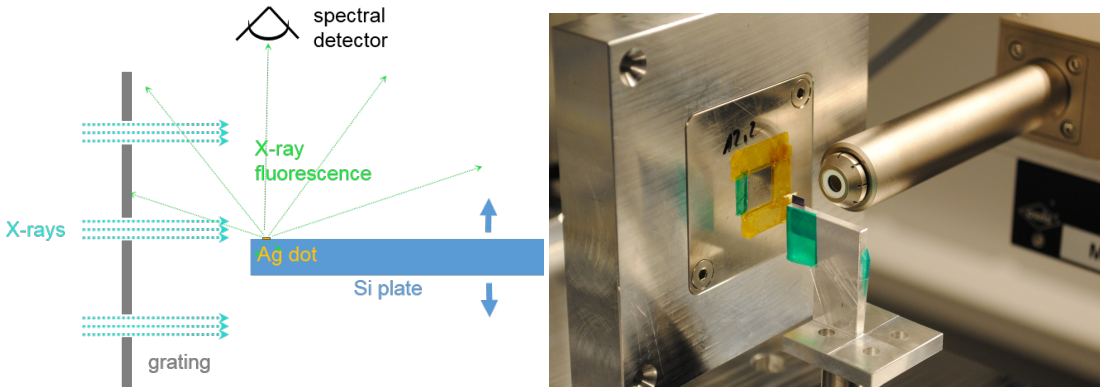

Figure 4.11.: *(a) Schematic drawing and (b) photograph of the X-ray fluorescence setup for high resolution of a microbeam pattern. The pattern is produced by a grating in the X-ray beam. An Ag dot is stepped transversally to the beam, emitting fluorescent X-rays recorded by a spectral detector at 90° to the beam path.*

The steps are shown in a simplified schematic drawing in Fig. 4.12. First, a lithographic mask with different circular and rectangular sizes for the silver dot was created. A silicon (Si) plate of $4 \times 6 \times 0.75\,\mathrm{mm}^3$ with a top layer of 300 nm silicon oxide (SiO_2) served as support for the Ag dot. Its surface roughness was about 1.5 nm rms (root mean square). To optimize X-ray interaction with the Ag atoms along the beam axis, a circular field of 150 µm diameter was chosen for the Ag deposition. The Si plate was cleaned in an ultrasonic bath for 5 min in acetone and isopropanole. Subsequent to blow drying with nitrogen, remaining particles were removed by soft plasma baking. A droplet of negative tone resist (AZ-5214[14]) was spin-coated on the Si plate to achieve a homogeneous, thin layer, which was then baked supported by a glass slide on a heating plate at 100 °C for about 5 min. Bulges from the resist at the edges of the plate were carefully reduced with a toothpick to avoid absorbing material in front of the Ag dot. With a mask aligner, the region with the desired field on the mask was aligned on the Si plate in contact mode, positioning the circular aperture at a corner. This allows to place the dot later on close to the grating and to avoid a large fluorescence signal from the Si plate itself. The sample was exposed to ultraviolet (UV) light for 70 s at 200 W. Reverse-baking was performed at 115 °C followed by UV exposure for 70 s, as before. On top of the resist, a silver layer of 150 nm was grown by vapor deposition (for details on the instrumentation, cf. [144]). Lastly, the Si plate was panned in a loop in appropriate developer (e.g. 351b[15]) solved 1:4 in H_2O for 16 s and subsequently, in purified water. To avoid dust formation, the Si plate, when not used, was covered with a glass container at all times.

[14] MicroChemicals GmbH, Ulm, Germany
[15] MicroChemicals GmbH, Ulm, Germany

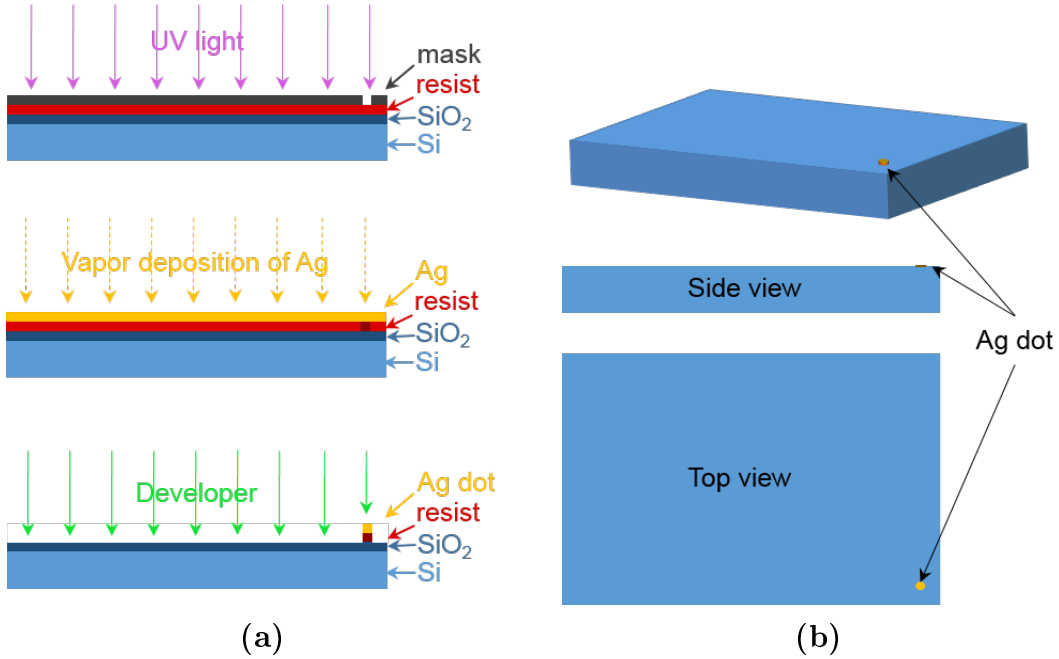

Figure 4.12.: *Ag dot fabrication by vapor deposition and photolithographic preparation of Si plate. (a) From top to bottom, the processing steps are depicted schematically (not to scale). Negative tone resist is spin-coated on the Si plate followed by UV light exposure masking the area where no Ag should be deposited. Reverse-baking and a second UV light exposure without mask turns the resist removable in the before-masked area. Vapor deposition of Ag on the resist in the desired height is performed homogeneously over the Si plate. Panning the plate in developer removes the resist with Ag layer while sparing the unmasked area. (b) A schematic drawing shows the Ag dot on the Si plate in 3D at the top, as side view in the center, and as top view at the bottom.*

4.4.1.c. Alignment

For a proof-of-principle experiment, a tungsten slit array with 50 µm slit width and 350 µm period (cf. chapter 2.1.2.b) was positioned on a motorized rotation table perpendicular to the beam path with the grating lines in vertical direction. The grating was fixed on a support with a 3.4 mm round aperture, which minimized scattering from surrounding material and allowed the central part of the beam to pass. By imaging with an Andor Zyla 5.5 sCMOS camera[16] with a fiber-coupled (1:1) scintillator (gadolinium oxysulfide[17]), or a photon-counting detector (Pilatus 200K[18]), the central position in the beam was determined between two extremal points, given by the half shadow of the aperture in front of the grating. Subsequently, the Si plate with the Ag dot was placed directly behind the grating on a motorized translation stage with high precision such that the grating pattern could be rasterscanned with the 150 nm height of the Ag dot. Therefore, the Ag

[16] Andor Technology Ltd., Belfast, UK
[17] Crytur, spol. s r.o., Turnov, Czech Republic
[18] Dectris, Baden-Dättwill, Switzerland

dot had to be placed precisely parallel to the grating, i.e. perpendicular to the beam path using a rotation stage. The alignment was verified with the above-mentioned imaging systems.

4.4.2. Results

The fluorescent signal shown in the following was acquired using the Ketek spectral detector with 100 s exposure time per step (further specifications are given in chapter 3.2.1). A high-resolution scan over one tungsten slit edge was acquired in addition to an overview scan over several grating periods (350 µm) with lower resolution, i.e. larger step size. In Fig. 4.13 (a), three spectra are shown: exemplarily for the transition area between microbeam peak and valley (spectrum 1 in blue), for the peak region (spectrum 2 in green), and for the valley region (spectrum 3 in red). The characteristic $K_{\alpha 1}$ lines are marked for Ag (∼22.16 keV) and also for tin (Sn) (∼25.27 keV), and Si (∼1.74 keV) [145]. Further characteristic lines possibly originate from the tungsten grid and the its support, made of stainless steel. Sn is potentially part of the support of the Si plate with the Ag dot (aluminum holder) and might also be contained in the stainless steel holder of the tungsten grid. Si is the substrate onto which the Ag dot is grown. Thus, Sn can be considered as *background fluorescence* signal, which should be relatively constant over the grating period as it depends rather on the amount of the full beam passing through the aperture in front of the grating than on the position of the Ag dot with respect to a slit. Fluorescence from Si can, however, largely influence the Ag signal, as photons scattered by the Si substrate and penetrating into the Ag dot, can trigger Ag fluorescence. Due to the Si thickness of 750 µm, Si fluorescence might not only reflect a single slit width but can result from two different slits simultaneously and reaches minimum intensity, when the front of the Si wafer – moving parallel to the grating – has not yet entered the next microbeam. The intensity of these fluorescent peaks was integrated subsequent to Gaussian smoothing of the fluorescence signal for all spectra acquired along the slit. The corresponding intensity value of Ag is presented in blue, for Sn in green, and for Si in red in Fig. 4.13 (b). The Ag signal was corrected for both Si and Sn fluorescence individually to better understand the behavior of Ag fluorescence (cyan and magenta line, respectively). Vertical black lines mark the positions along the slit at which the spectra shown in Fig. 4.13 (a) were taken.
From the characteristic $K_{\alpha 1}$ lines in the spectra and the integrated and normalized peak intensity, it is evident that the background fluorescence, represented by Sn, changes only slowly with respect to the Ag dot position. The intensity drop of Sn after about 300 µm might be due to a reduced fluorescence contribution from the support of the Si plate, which contains Sn, as it moved out of the irradiation field. In contrast to the quite constant Sn signal, a clear intensity change can be observed for Ag, which is already visible in the characteristic $K_{\alpha 1}$ line (see detailed view inserted in Fig. 4.13 (a)) and becomes apparent in the representation of the integrated peak intensity in Fig. 4.13 (b). While within 300 µm almost a full period

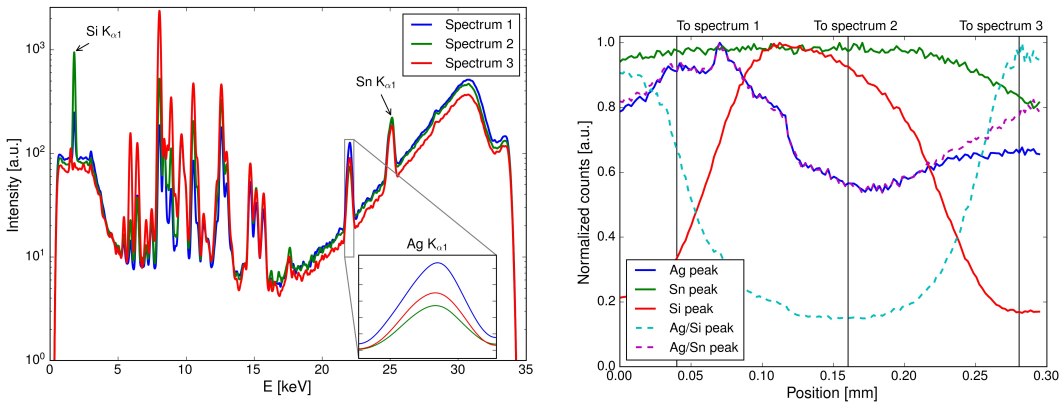

Figure 4.13.: *Normalized fluorescence intensity obtained from fine sampling along the edge of a tungsten slit with the Ag dot. (a) Spectra on logarithmic scale corresponding to three different positions: spectrum 1 (blue) to the transition from peak to valley, spectrum 2 (green) to the valley, and spectrum 3 (red) to the peak region. (b) Line profiles of the integrated fluorescence of Ag, Si, and Sn, acquired by stepping the Ag dot along the x-axis. Corrections to the Ag profile were applied for Sn as a background fluorescence material and for Si to eliminate distortions caused in the Ag signal. The positions corresponding to the spectra in (a) are marked with vertical black lines.*

of the grating should be covered (mainly the valley region is visualized here), the edges of the microbeam are not well observable in the blue Ag curve. Normalization with the background fluorescence given by the Sn signal allows to slightly recover the ascending signal intensity towards the next slit. As the Si signal should already include background fluorescence seen in the Sn signal, in a second step, the Ag fluorescence was normalized solely to the Si signal (cyan line). Thereby, a clear peak and valley pattern can be retrieved. However, both transition zones from peak to valley and valley to peak are broadened significantly in a range of about 50 to 100 µm. This might be due to scattering contributions from surrounding materials – including the tungsten of the tungsten slit array – to the Ag fluorescence even if the Ag dot is not directly illuminated by the X-ray beam.

To verify if the observed pattern in Fig. 4.13 (b) corresponds to the actual grating period, a longer distance parallel to the tungsten grid was rastered in a second scan with a larger step size. The corresponding spectra and profiles of integrated fluorescence are depicted in Fig. 4.14 (a) and 4.14 (b), respectively. In the former, three spectra represent the peak region (cyan lines) in contrast to three spectra from the valley region (magenta lines). The position of the spectra with respect to the microbeam profiles are highlighted with accordingly colored vertical lines in Fig. 4.14 (b).

For visualization purposes, the Sn fluorescence is not shown. Its intensity is constantly decreasing with a slight modulation following the Si fluorescence. This intensity drop is observed in all three integrated fluorescence signals (Ag and Si

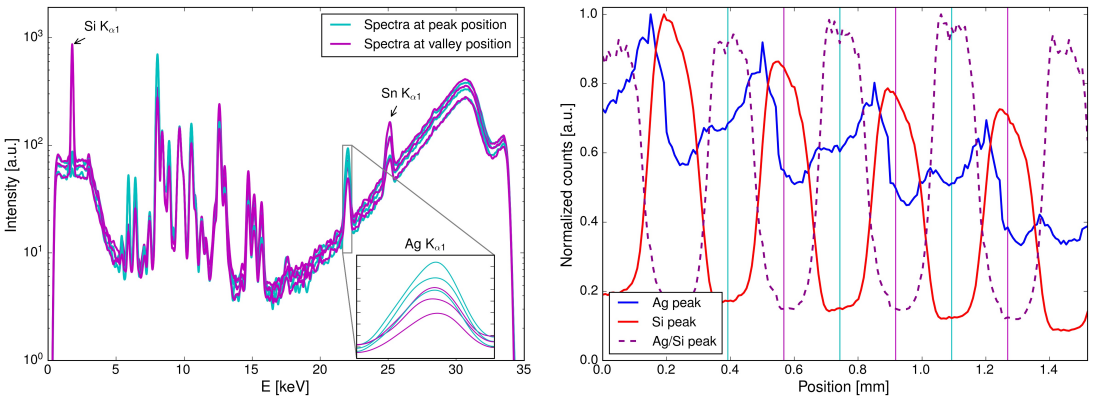

(a) (b)

Figure 4.14.: *Normalized fluorescence intensity obtained from coarse sampling over several periods of the tungsten slit array with the Ag dot. (a) Spectra on logarithmic scale corresponding to a position of the Ag dot in either peak (cyan) or valley (magenta) region. (b) Line profiles of the integrated Ag (blue), and Si (red) fluorescence from stepping the Ag dot along the x-axis. Moreover, the correction of the Ag profile with the Si fluorescence is shown (violet dashed line). The peak and valley positions along the periods corresponding to the spectra in (a) are highlighted by cyan and magenta colored vertical lines.*

signal in Fig. 4.14 (b)). As above, the intensity reduction might reflect the decreasing X-ray flux over time but it could also result from approaching the border of the aperture in front of the tungsten grid. The correction of the integrated Ag peak with the integrated Si peak allows to recover the signal (violet dashed line). The period of the pattern corresponds well to the 350 µm period of the tungsten slit array such that the working principle of the Ag dot fluorescence method can be confirmed. Yet, the extension of the peak with up to 100 µm is considerably larger than the expected 50 µm. Additionally, the beam penumbra is blurred. Both observations might be caused by scattered photons, which increase the Ag fluorescence. Moreover, the correction of the Ag fluorescence with the Si fluorescence introduces further signal distortions. In the ideal case, considering self-absorption, stepping of the Si plate along the microbeam pattern should yield a triangular Si fluorescence signal, whereas the Ag dot should only yield a fluorescent signal when it is directly illuminated. In the peak region of the measured profile, a maximum fluorescence is visible as a periodic spike before the Si signal becomes maximal. This high Ag signal could be related to the Ag dot being fully illuminated by a microbeam right before entering in the valley region behind the tungsten, which would correspond to the following steep signal decrease. Correcting the Ag signal with the Si signal eliminates this information as the resulting signal is dominated by the Si fluorescence. Therefore, this correction might not be the appropriate method to retrace the microbeam profile. While the influence of the Si signal on the Ag signal is unquestionable, its exact contribution requires further investigation. In a future study, the Si signal from the 750 µm thick substrate could be simulated

considering the distance of the Si plate to the tungsten grid and to the spectral detector. Moreover, in the experimental setup shown here, the distances were minimized to reduce scattering contributions from surrounding material and to avoid the mainly forward-directed Compton scatter. However, a dedicated shielding of the beam path to the Ag dot and subsequently, to the detector might be useful. Because of the large influence of the Si on the Ag signal, a different substrate would allow to better extract the Ag fluorescence from direct illumination.

4.4.3. Possibilities and limitations

In principle, X-ray fluorescence with a 150 nm Ag dot is well-suited to verify the irradiation pattern with high resolution. However, very precise alignment of the Ag dot is crucial to benefit from its small height. Any vibrational motion must be excluded. Similarly as for the high-resolution camera systems, the efficiency of this method is dependent on the available flux such that long measurements times might be needed for a sufficient signal-to-noise ratio. It has to be questioned if resolution of such a fine microbeam structure is actually required for microbeam irradiation from a practical point of view, as the dose distribution in the tissue depends mainly on the penetration depth of the electrons. The latter is in the micrometer range for energies above 10 keV. Else, the height of the Au dot could be increased to enhance efficiency.
The first experimental results with such a setup have demonstrated that the periodicity of the microbeam pattern produced by the tungsten slit array can be well retrieved. However, to avoid scattering from surrounding materials, in particular from the substrate of the Ag dot, the setup has to be optimized. Simulations to account for remaining signal distortions are proposed to reconstruct the Ag fluorescence and thus the microbeam profile. Additionally, accuracy in signal evaluation could be improved by fitting the fluorescence peaks. In conclusion, resolving features in the range of a few micrometers with X-ray fluorescence will be challenging due to the highly complex process of data acquisition.

4.5. Summary and outlook

Different approaches towards high-resolution dosimetry for microbeams with small widths were presented in this chapter.
Conventional radiochromic films were found to resolve features of about 10 µm yielding directly dose values due to their water-equivalence with an accuracy better than 10%. Simulations showed that the penetration depth of secondary electrons in the film material strongly reduces the PVDR for small grating periods, such that a typical microbeam dose distribution cannot be achieved. However, if the spacing between the grating lines would be increased, smaller microbeams than resolvable with films could be used for MRT. To measure the creation and dose distribution of such patterns, higher resolving methods were demonstrated using

a nuclear track detector, a camera system, and X-ray fluorescence:

- Applying a CR-39 detector for X-ray detection requires extremely high exposure times for conventional X-ray tubes. The readout with white light microscopy or even AFM is additionally time-consuming but yields resolutions in the range of a few hundred nanometers. Therefore, the performance of nuclear track detectors could be further investigated at X-ray sources with higher flux, like the MuCLS.

- The installation of a high-resolution camera system allows to distinguish features of a few micrometer. Thinner scintillators to increase resolution would lead to an increase in noise and significant reduction of efficiency. With a dedicated camera system, a resolution as high as 0.7 µm could be reached in the future.

- Lastly, the basic principle of X-ray fluorescence imaging for high resolution characterization of a microbeam pattern was introduced. Relative intensity measurements with a resolution on the order of a few hundred nanometers might be achievable (e.g. [146]). However, precise setup alignment and long integration times of the spectral detector are required.

Hence, these three methods suffer from low efficiency but can potentially resolve microbeam features with higher resolution than radiochromic films. Additional simulations can then yield the dose distribution in the object under investigation. Therewith, the difference between the created microbeam pattern and the dose profile becomes observable. Highest resolution might be achieved with the CR-39 detector if sufficient X-ray intensity is applied, followed by the XRF analysis, and subsequently, the camera system – but inversely with regard to the exposure time. All in all, the three listed methods are promising to achieve high resolution but need further investigation on reproducibility as well as development towards dosimetry. Therefore, in the present work, radiochromic film dosimetry was preferred if resolution up to 10 µm was required.

5. Experimental studies on Microbeam Radiation Therapy

As the radiobiological response to microbeam irradiation differs in many aspects from homogeneous irradiation, further research is needed to understand the underlying mechanisms. This includes but is not limited to gene expression, DNA damage and repair, apoptosis and proliferation, and intra and extracellular signaling. Using large-scale synchrotron facilities for MRT is cost-intensive and limited by the available beam time. Here, two approaches are presented that allow to overcome these challenges. First, X-rays from a standard rotating anode X-ray tube are used for MRT experiments. The production of a variety of microbeam geometries is shown, verified by γ-H2AX phosphorylation or 53BP1 staining of HeLa cells (subchapter 5.1). In a further step, the Munich Compact Light Source (MuCLS), the first commercially available compact synchrotron based on inverse Compton scattering, serves as X-ray source. Bridging the gap between conventional X-ray tubes and large-scale synchrotron facilities, such a source might allow to make MRT available to a larger number of patients in the future. While further development is required for human patient treatment at such a compact synchrotron in terms of energy and flux, the implementation and application of MRT at the MuCLS allows to contribute to an improved understanding of its radiobiological effects, and to investigate the benefits and challenges working at such a compact device. Therefore, in the second part of this chapter, 5.2, an overview of the required setup components for MRT experiments is given. Subsequently, in subchapter 5.3, radiation-induced biological effects are analyzed quantitatively in-vitro with respect to cell survival and chromosome aberrations. For comparison to standard conditions, homogeneous, and sham irradiations are performed additionally to microbeam treatment. Subsequently, the design of an in-vivo study treating a xenograft grown in the mouse ear is presented in subchapter 5.4. Here, the radiation response in tumorous tissue is investigated with focus on tumor growth delay and a variety of histological endpoints. First results on tumor growth delay are discussed. Conventional 2D histology is complemented by 3D imaging of resected tumor volumes to improve future tumor analysis. Subchapter 5.5 concludes the work on MRT studies in-vitro and in-vivo at compact X-ray sources with an outlook on future experiments.

5.1. In-vitro irradiations at a rotating anode X-ray tube

Studying MRT at a conventional X-ray tube opens the possibility to investigate the radiobiological effects of MRT at readily available machines at considerably reduced costs. Therefore, microbeam irradiations in-vitro were established at a rotating anode X-ray tube at the Chair of Biomedical Physics[1]. In particular the lower limit of fine microbeam structures resulting in an alternating dose pattern, i.e. a significant peak-to-valley dose ratio (PVDR), is explored by studying radiation-induced DNA double-strand breaks (DSBs) in cells.

5.1.1. Setup

5.1.1.a. Irradiation parameters and dosimetry

An Enraf-Nonius FR 591[2] rotating anode X-ray tube with a molybdenum target was operated at 40 or 50 kVp and 60 to 70 mA offering a source size of about $0.3 \times 0.3\,\mathrm{mm}^2$. Depending on the alignment of the molybdenum filament, the source size can vary slightly. Due to the large opening angle of the source, beam defining slits were used to avoid X-ray scattering at objects not included in the dose calibration (see below). At a distance of 50 to 120 cm to the source, different highly absorbing gratings, edges, or wires were positioned. In a minimal distance of about 3 mm from the absorbers, the cells were placed, seeded in a dedicated holder (cf. Fig. 5.1; for details on the cell holder, see chapter 3.1.1).
Following irradiation, the cells were incubated between 10 to 30 min to optimize foci fluorescence versus movement of the cell nucleus. Staining of DNA DSBs was performed with γ-H2AX and/or 53BP1 following the protocol in section 3.1.2.
With an ionization chamber (TM23342-002053, calibrated by PTW[3]), the dose was calibrated to the number of photons measured by a photon-counting detector (Pilatus 200K[4]) at the same distance to the source. Radiation quality, temperature, and pressure were considered in dose determination (cf. chapter 3.2.2). As the radiation quality of the calibration condition differs with respect to the spectrum (aluminum filter not used, molybdenum instead of tungsten anode), a maximum error of 0.5% is introduced into the dose calculation.
Additionally, the dose measured with the ionization chamber was compared to a dose calculation based on the measured photon flux, taking energy spectrum and detector efficiency into account. The measured molybdenum spectrum at 50 kVp is shown in Fig. 5.2 (obtained with Amptek X-123 energy-dispersive detector[5], following 3.2.1).

[1] TUM, Garching, Germany
[2] *former* Enraf-Nonius, *now* Bruker AXS B.V., Delft, The Netherlands
[3] PTW, Freiburg, Germany
[4] Dectris, Baden-Dättwill, Switzerland
[5] AMPTEK, Inc., Bedford, MA, USA

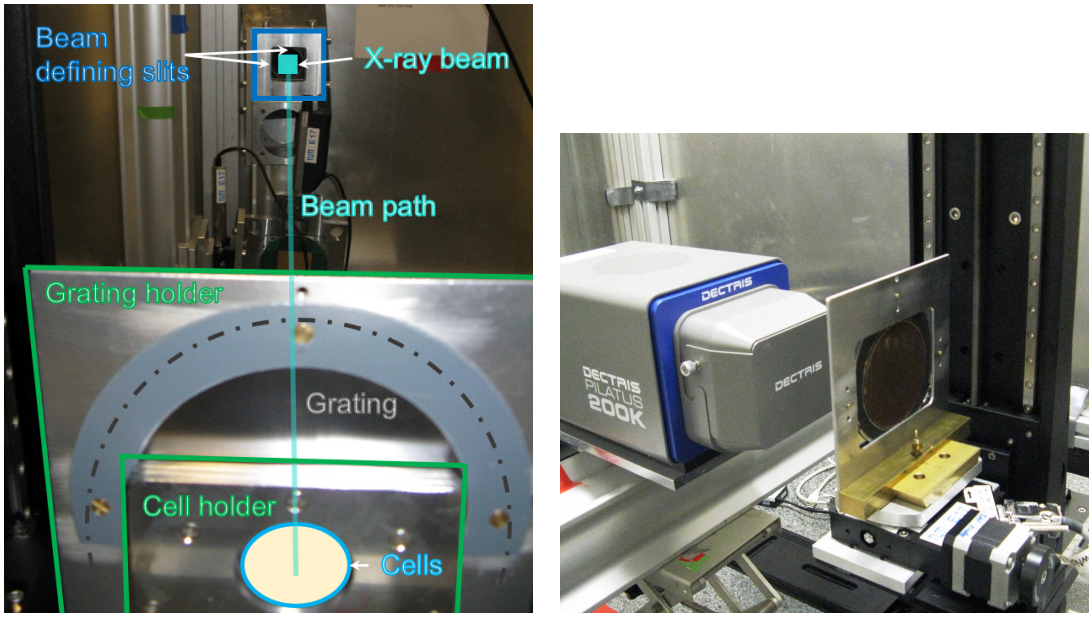

Figure 5.1.: *Setup in experimental hutch at the rotating anode X-ray tube. (a) Overview of beam path and cell holder with grating. (b) Grating holder on rotation stage and in front of the photon-counting detector (Pilatus 200K) as used for grating alignment (Si sensor of detector uncovered for experiments). Cell holder to be installed between grating and detector.*

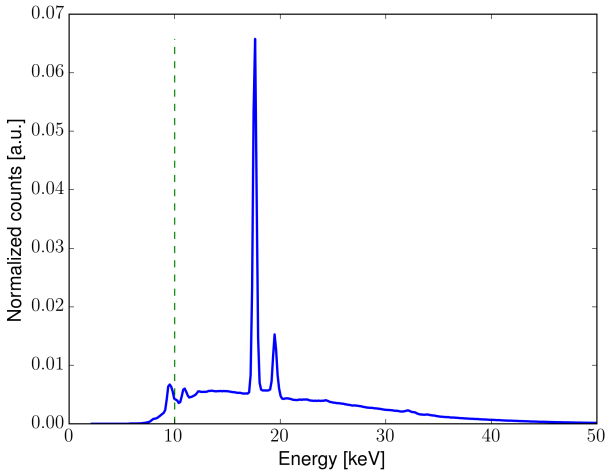

Figure 5.2.: *Molybdenum spectrum of the rotating anode X-ray tube at 50 kVp. The dashed line shows the cutoff energy of 10 keV used for dosimetric calculations.*

As the X-rays exit through a beryllium (Be) window into the experimental hutch, the transmission of X-ray energies below 10 keV (marked with a dashed line) is negligible. Therefore, only the energy spectrum above 10 keV was used for dose

calculation. The characteristic lines appearing at low energies are possibly related X-ray fluorescence from the lead collimator of the energy-dispersive detector used. With this data, the delivered dose was deduced from the measured photon flux following Eq. (2.5) in chapter 2. The dose rate from the photon flux measurement was significantly lower than from the ionization chamber measurement, which might be related to the uncertainties of absorption coefficients used for the calculation (further discussed in 5.3.2.b. As, here, the dose determination with the ionization chamber was assumed to be less error-prone, the corresponding conversion factor from photon flux to dose was used to determine the dose for all subsequent experiments. Prior to each irradiation, the flux was recorded with the photon-counting detector for several time intervals to verify a constant dose delivery. The dose rate at 50 kVp and 60 mA for homogeneous irradiation was on the order of 700 mGy/min with a good stability throughout the experiment.

5.1.1.b. Microbeam creation with absorption gratings

Regarding the optimization of microbeam geometry, previous simulations have shown a decrease in valley dose when reducing the microbeam width due to the lower amount of scattered photons from the peak area [147]. As the fabrication of a slit array based on laser drilling, used for the tungsten grid (chapter 2.1.2.b), becomes challenging below 30 µm due to the laser focusing abilities and heat dissipation, absorption gratings made by the LIGA process were chosen for this study, see section 2.1.2.b. In Table 5.1, the parameters of the employed grating structures are presented. All gratings are fabricated on 500 µm thick silicon (Si) wafers. gold (Au) is used as absorber material. The grating area varies between $1 \times 1\,\mathrm{cm}^2$ and 70 mm round, mainly depending on aspect-ratio of height to slit width and layout. As proof-of-principle experiment, simple absorbers like a copper plate and a tungsten wire of 200 µm diameter were placed in front of the cells. After optimization of source-to-sample distance and grating orientation, absorption gratings as given in Table 5.1 were used to create a microbeam pattern. Grating orientation was determined by maximization of the photon flux with the rotation angle (around the vertical axis). Following these preparations, cell irradiations were performed.

5.1.2. Cell irradiation analyzed by γ-H2AX and 53BP1 staining

In this section, the results from microbeam irradiations of cells with respect to radiation-induced DNA double-strand breaks are shown. A selection of the fluorescence images from the correspondingly performed γ-H2AX and 53BP1 assays are presented in the following to illustrate the observations. Additional images can be found in Appendix A.3.

Table 5.1.: Absorption gratings. *Parameters of grating structures used for MRT experiments at the rotating anode setup.*

Grating name	Slit width [µm]	Grating period [µm]	Duty cycle	Au height [µm]	Layout[1]
24	11.98	23.95	0.5	150	Continuous
20	6.9	20.29	0.66	130	Continuous
15-0.5	7.35	15	0.49	51	Continuous
15-0.6	5.85	15	0.61	51	Continuous
15-0.7	4.35	15	0.71	51	Continuous
10	5	10	0.5	150	Bridge
5	2.5	5	0.5	120-130	Bridge
4.8cont	2.4	4.8	0.5	100	Continuous
4.8sun	2.4	2.4	0.5	100	Sunray
2.4cont	1.2	2.4	0.5	90	Continuous
2.4brid	1.2	2.4	0.5	130	Bridge

[1] *Continuous*: continuous grating lines without stabilizing structures.

Bridge: grating lines interrupted every 2 µm due to stabilizing structures, so-called *bridges*, in the resist design.

Sunray: grating lines partially interrupted due to 30 ° tilted stabilizing structures, so-called *sunrays*, in the resist design.

For details on grating fabrication, see section 2.1.2.b or refer to [73], for example.

5.1.2.a. Fluorescence signals

First of all, exemplary fluorescence images from a sham and a homogeneously irradiated sample are shown to explain the fluorescence signals. As the images are not evaluated quantitatively, the contrast settings were chosen for optimal visibility of each fluorescence channel. Fig. 5.3 shows microscopic images of sham irradiated cells (left) and homogeneously irradiated cells (right) with three fluorescent signals: (a) and (b) DAPI in blue, staining the cell nuclei; (c) and (d) 53BP1 in green, (e) and (f) γ-H2AX in red, both staining DNA DSBs. In (g) and (h), the three signals are combined.

Note that the protein 53BP1 clusters at specific sites in the cell nucleus in standard, non-irradiated condition, visible in (c), but is distributed at the sites of DNA DSBs caused by irradiation, as shown in (d). In (f), the given dose results in such a high concentration of foci that individual foci become indistinguishable. Hereby, the overall signal strength is considerably increased compared to the sham irradiation in (e). Combining the stained DNA damages with the DAPI signal in (g) and (h) highlights the foci location in the cell nucleus. Fluorescent labeling in sham irradiated images (left) can occur at spontaneous DNA DSBs, or in cells that

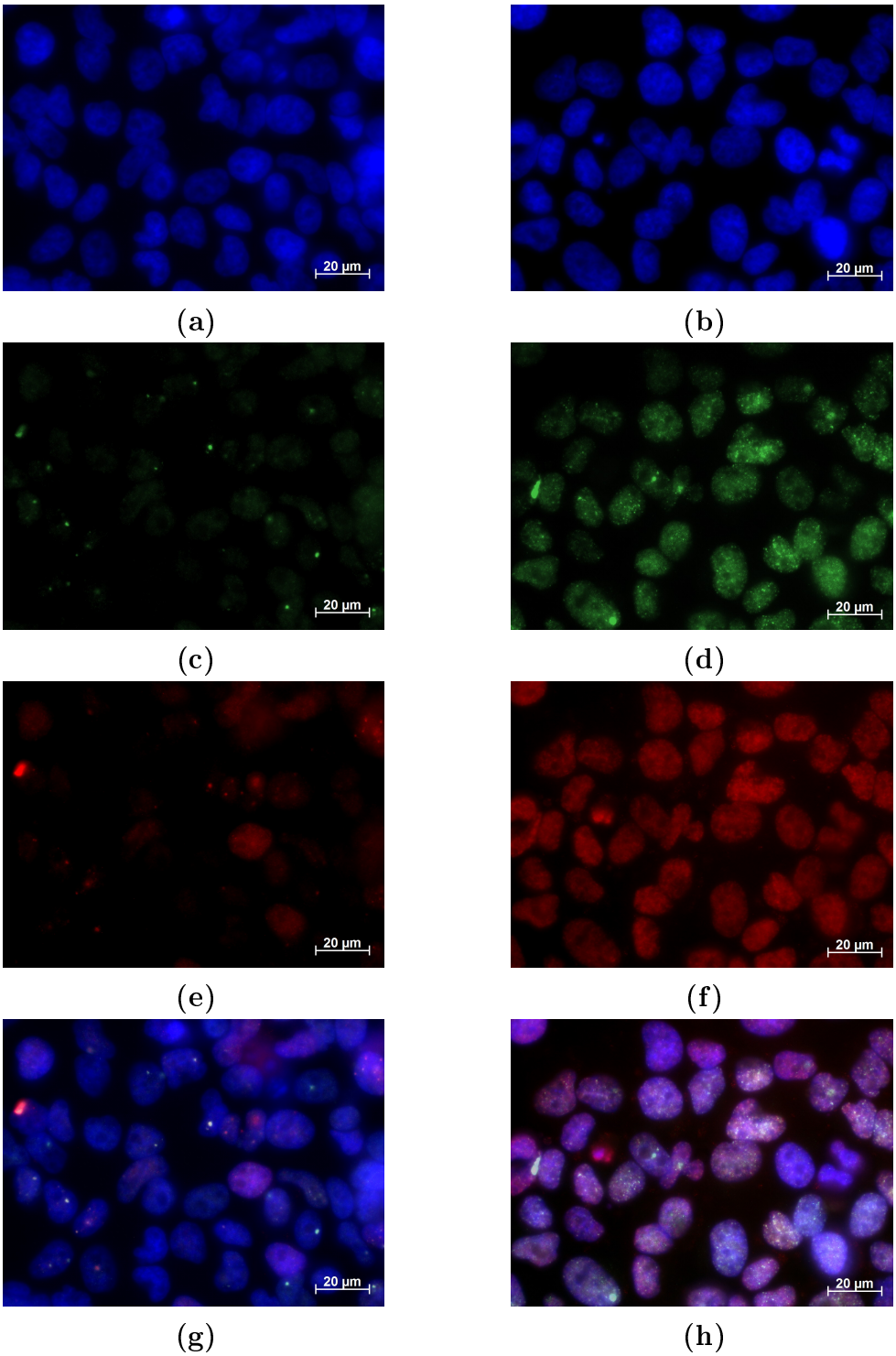

Figure 5.3.: *Microscopic images of sham (left) and homogeneously (right) irradiated cells acquired quasi-simultaneously with 63-fold magnification optics. (a) and (b) Blue fluorescent DAPI, staining the cell nuclei. (c) and (d) Green fluorescent 53BP1. (e) and (f) Red fluorescent γ-H2AX staining. (g) and (h) Combined fluorescence signals of (a), (c), and (e), as well as (b), (d) and (f), respectively.*

are not in G1 phase of the cell cycle, or due to unspecific binding. In most of the following microscope images, γ-H2AX staining was performed with fluorescent labeling in red and 53BP1 staining in green. In case of interchanged coloring, the secondary antibody was exchanged (see protocol in section 3.1.2). Generally, HeLa cells were chosen to qualitatively visualize the radiation-induced damage, unless stated otherwise.

5.1.2.b. Proof-of-principle study with tungsten wire

To verify the setup performance, a tungsten wire of 200 µm diameter was placed directly in front of the cells. For this experiment, the cell holder was positioned at 70 cm to the source. The X-ray tube was operated at 50 kVp and 70 mA.
Fig. 5.4 shows the microscope image acquired following irradiation and staining procedure. Cells in the lower right corner of the image were protected by the tungsten wire in contrast to irradiated cells in the upper left corner.

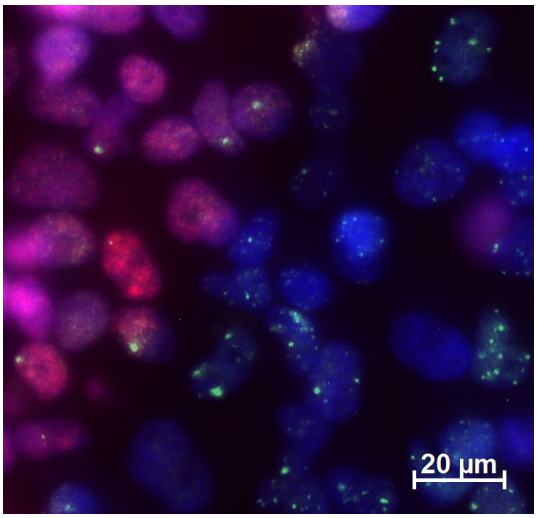

Figure 5.4.: *Microscope image of cells at the edge of a 200 µm thick tungsten wire. Cells were irradiated in the upper left corner of the image, irradiation was obstructed by the tungsten wire in the lower right corner. Blue fluorescent DAPI marks the cell nucleus, γ-H2AX staining highlights DNA double-strand breaks in red, while the protein 53BP1 – visible as a foci accumulation in green in non-irradiated areas – is distributed to radiation-induced DNA double-strand breaks.*

The other side of the tungsten wire is shown in Fig. 5.5, with microscope images containing all three fluorescence signals in Fig. 5.5 (a), and removed 53BP1 staining in 5.5 (b). Segmentation of the DAPI image allowed to extract the γ-H2AX signal at the location of cell nuclei only, using the image analysis software *CellProfiler* [128]. A rotated region of interest of the processed γ-H2AX image is given in Fig. 5.5 (c) together with the corresponding normalized projection along the vertical axis.

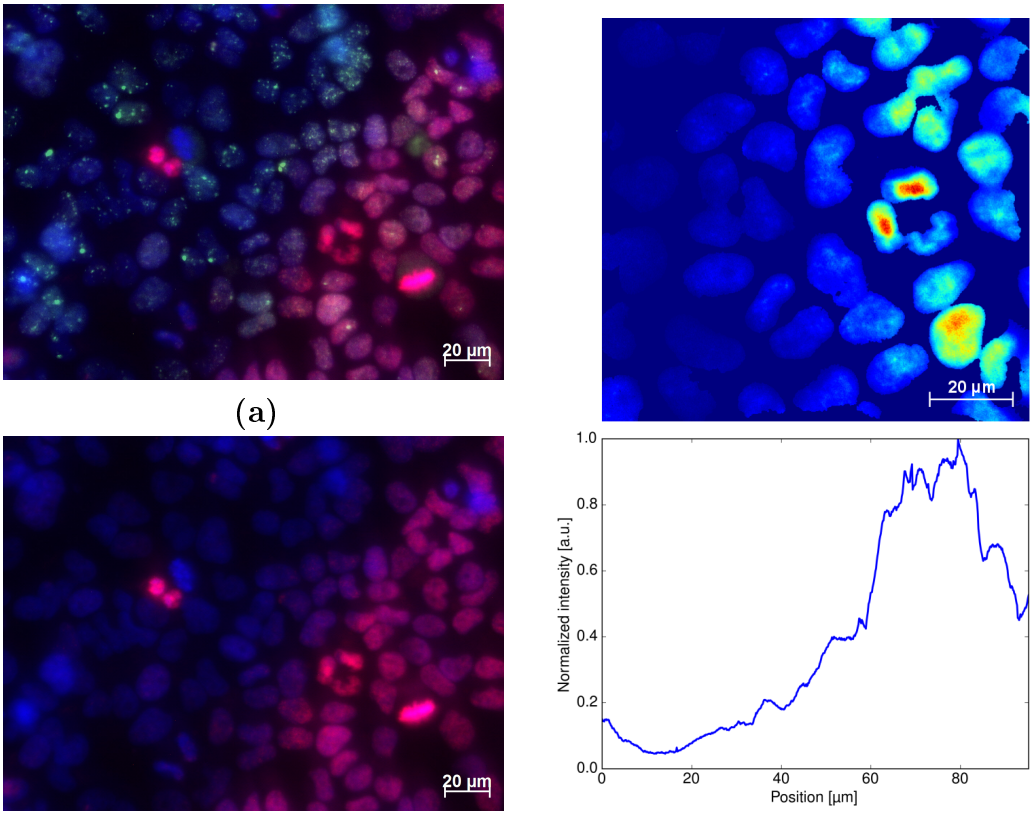

Figure 5.5.: *Microscope image of cells at the edge of a 200 µm thick tungsten wire. Cells were irradiated in the lower right corner of the image, irradiation was obstructed by the tungsten wire in the upper left corner. (a) Blue fluorescent DAPI marks the cell nucleus, γ-H2AX staining highlights DNA double-strand breaks in red, while the protein 53BP1 – visible as a foci accumulation in green in non-irradiated areas – is distributed to radiation-induced DNA double-strand breaks. (b) Only DAPI and γ-H2AX staining are shown, used for edge analysis. (c) A rotated region of interest of the γ-H2AX channel. Cell nuclei were segmented using the DAPI channel and the resulting binary image was multiplied with the γ-H2AX signal. Horizontal line profiles of this image were summed up and normalized to acquire the graph below.*

Despite the low statistics of this exemplary image, which adds noise to the signal, and despite the reduced absorption at the side of the wire, a clear step in intensity is apparent. However, quantitative readout would require – additionally to a larger number of cells – the removal of signal from unspecific binding as visible in the dividing cell right to the center of the image. Hence, sparing of cells by an absorbing tungsten wire yields a dose distribution (given by DNA DSBs) with a quite steep dose falloff from irradiated to non-irradiated area using a conventional X-ray tube. Several cells show only partial irradiation which highlights the feasibility of dose application with intracellular variations. This means that microbeams created a width of a few micrometer might only cause a partial irradiation of the cells even

though scattering, diffusion of the DNA during incubation time, and bystander effects can blur the microbeam pattern.

5.1.2.c. Microbeam widths below 20 µm

In a next step, microbeam widths below 20 µm were created with the gratings described in Table 5.1 to analyze if these fine structures still yield an alternating dose pattern of peaks and valleys in the cells, given by DNA DSBs.
Fig. 5.6 shows a microscopic image taken with 63-fold magnification of cells irradiated with 8.4 Gy mean dose at 70 cm source-to-cell distance using grating 24, i.e. 24 µm period creating 12 µm wide microbeams, and respectively, Fig. 5.7 using grating 20, i.e. a period of 20.29 µm creating 6.9 µm wide microbeams. Additionally, Fig. 5.8 shows a microscopic image acquired with 40-fold magnification of cells irradiated with 4.2 Gy using grating 20.

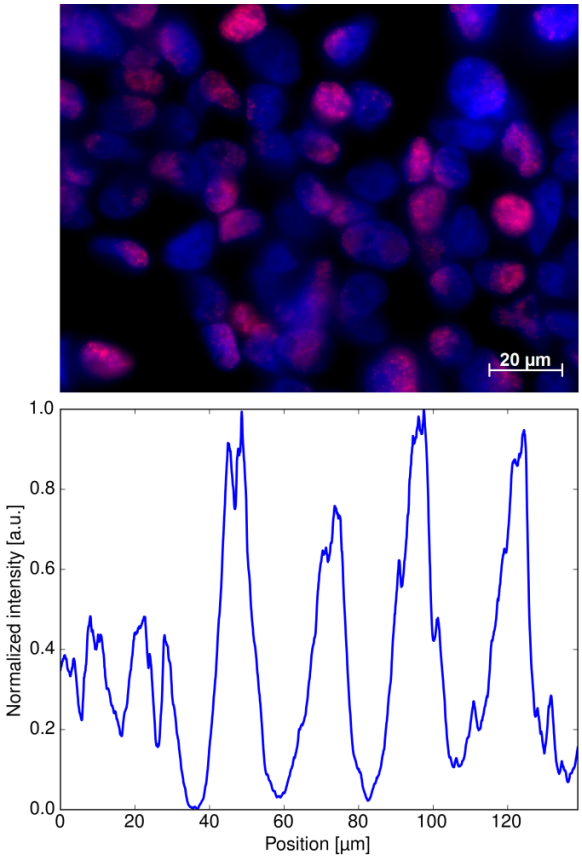

Figure 5.6.: *Microscopic image of HeLa cells using grating 24, creating 12 µm wide microbeams with a mean dose of 8.4 Gy. Image taken with a 63-fold immersion objective.*

To optimize the grating alignment in the setup, its orientation can differ between individual gratings and was re-oriented for visualization purposes. All three figures present additionally a line profile of the cell images. These profiles were acquired by segmentation of the DAPI image to obtain the cell distribution. Subsequently,

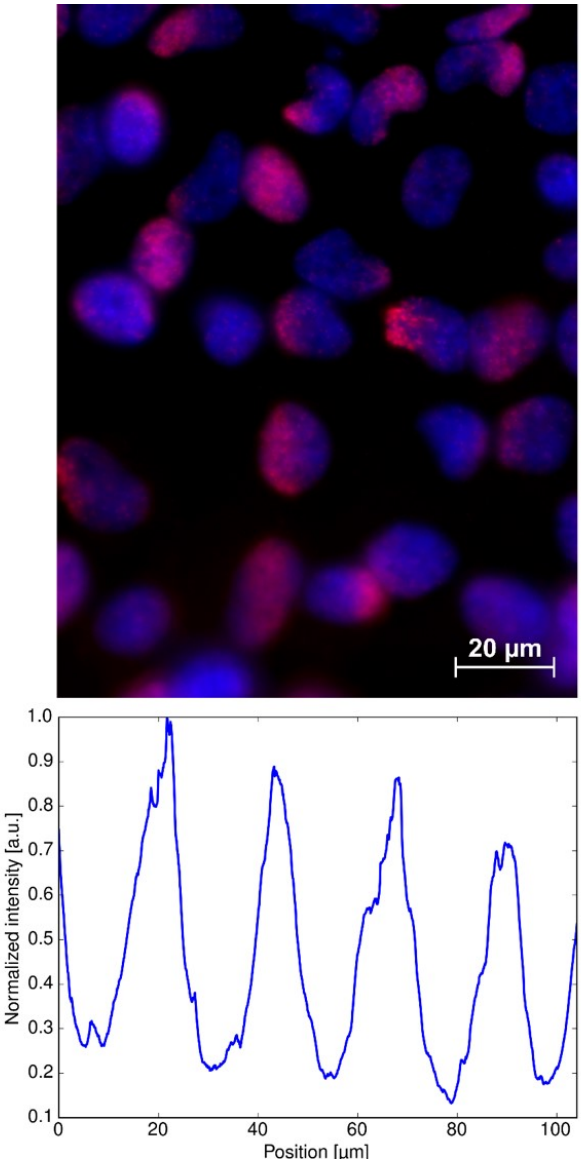

Figure 5.7.: *Microscopic image of HeLa cells using grating 20, yielding 6.9µm wide microbeams with a mean dose of 8.4 Gy. Image taken with a 63-fold immersion objective.*

the γ-H2AX image was segmented and weighted with the binary DAPI image to account for the local cell density, followed by projection along the microbeam lines (for the segmented images, see Appendix A.3). Fluctuations seen in the line profiles additionally to the expected periodic pattern are mainly due to the low number of cells in these exemplary images, which are thus not considered for quantitative analysis. The reproduction of the grating period in the DNA DSBs can be well observed in the line profiles. However, in Fig. 5.6 it becomes clear that unspecific binding of the γ-H2AX antibody – here at a cell to the lower left of the image – can strongly alter the line profile and destroy the periodicity of the pattern.

In general, for DNA DSB localization in immunofluorescence microscopy, it is

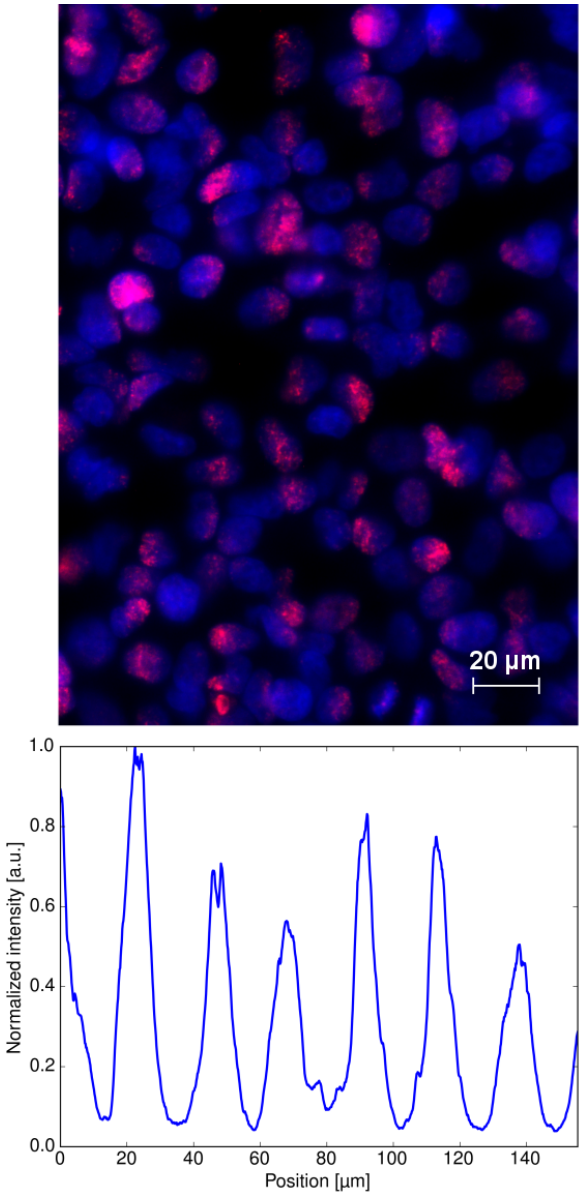

Figure 5.8.: *Microscopic image of HeLa cells using grating 20, yielding 6.9 µm wide microbeams with a mean dose of 4.2 Gy. Image taken with a 40-fold objective.*

important to avoid overlaying cells such that the foci in the individual cell nuclei can be well distinguished. However, as the microbeams might only hit part of a cell, the cell density should not be too low either to optimally trace the dose deposition. As a consequence, the signal-to-noise ratio might suffer from this trade-off. In particular the detection of even smaller microbeams might be difficult and requires evaluation of individual cells over larger areas.

To avoid movement of the radiation-induced DNA DSBs, i.e. the stained foci, during the incubation period and thus a blurring of the microbeam pattern, shorter incubation times of as low as 10 min were investigated in contrast to the standard

30 min incubation time, where the γ-H2AX fluorescence in HeLa cells reaches its highest intensity [148]. However, no contrast improvement could be detected with respect to the microbeam dose pattern produced with several gratings from Table 5.1 (data not shown here). The lower foci intensity after 10 min incubation time resulted in a reduced signal-to-noise ratio, which might have additionally worsened the contrast between peak and valley. Therefore, further cell irradiations were performed with 30 min incubation time.

Exemplarily, microscopic images of microbeam patterns produced by grating 15-0.7, grating 10, and grating 2.4brid are shown in Figs. 5.9 to 5.12. In these images, no clear line pattern is visible. Different algorithms were implemented to determine the preferential direction of the microbeams in addition to markers on the cell carrier foil. While the analysis of line profiles obtained from segmented cell images in image space can be useful, the analysis in Fourier space with the knowledge of grating period and duty cycle allows to obtain the orientation of the microbeam pattern in the most stable fashion. However, poor peak-to-valley dose ratios as apparent in Fig. 5.12 do not yield meaningful results. Consequently, no line profiles are shown for these images. In Fig. 5.9, foci appear in locally confined areas within individual cell nuclei. The foci distribution seems to follow the applied microbeam pattern of 4.35 µm wide planar beams spaced by 11.65 µm. While the cell density is too low to verify this assumption quantitatively, corresponding foci accumulation was also observed in other ROIs of the same sample (see Appendix A.3). Grating 10 resulted in Figs. 5.10 and 5.11, where the cells seem not to be homogeneously irradiated as the foci are not evenly distributed within single cells. As this grating has a bridge layout, i.e. gaps in the absorbing line structures, the view of the line pattern might be distorted.

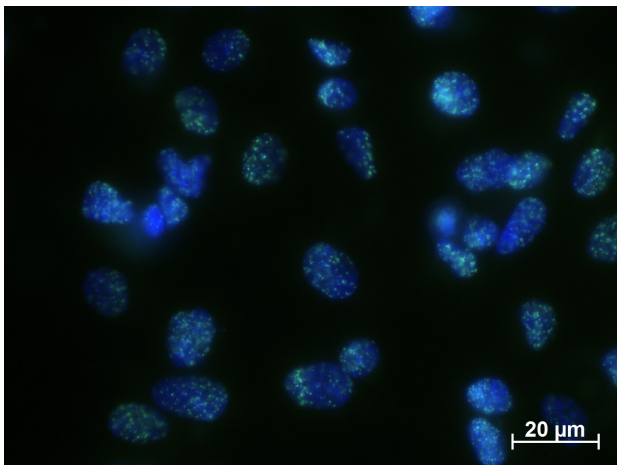

Figure 5.9.: *Microscopic image of CHO cells using grating 15-0.7, yielding 4.35 µm wide microbeams with a mean dose of 5 Gy. Image taken with a 63-fold immersion objective. Note that γ-H2AX is stained in green.*

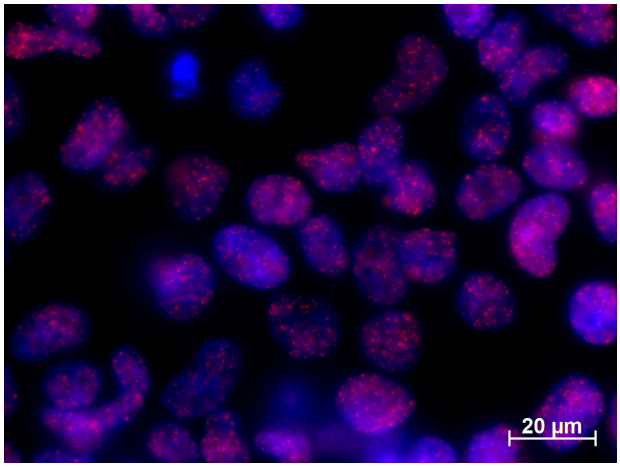

Figure 5.10.: *Microscopic image of HeLa cells using grating 10, yielding 5 µm wide microbeams with a mean dose of 4.2 Gy. Image taken with a 63-fold immersion objective.*

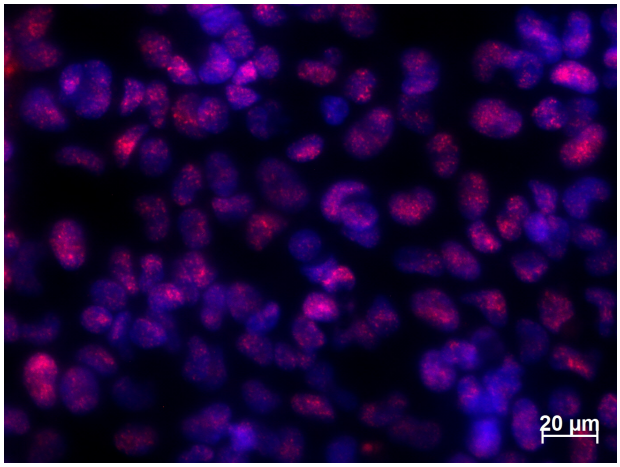

Figure 5.11.: *Microscopic image of HeLa cells using grating 10, yielding 5 µm wide microbeams with a mean dose of 4.2 Gy. Image taken with a 40-fold objective.*

5.1.3. Discussion and conclusion

The results shown in this subchapter demonstrate that the radiobiological effect of MRT can be well studied at a conventional X-ray tube. The dose rate is sufficient to perform experiments in-vitro. Adjusting the source-to-sample distance, penumbral blurring can be reduced below 1 µm if the cells are placed directly behind the absorber or collimator. Fine microbeam structures with microbeam width down to 7 µm distant by 13 µm allow to create a dose pattern with considerable peak-to-valley dose ratio using X-ray energies from a 50 kVp molybdenum spectrum. With the gratings used here, the dose rate is reduced due to their fabrication by LIGA on 500 µm Si substrate. Nowadays, thinner Si substrates of 200 µm thickness are available to reduce the absorbing material. Moreover, lifting the Au structure off the Si substrate onto a polyimide film is feasible. For MRT, gratings with a

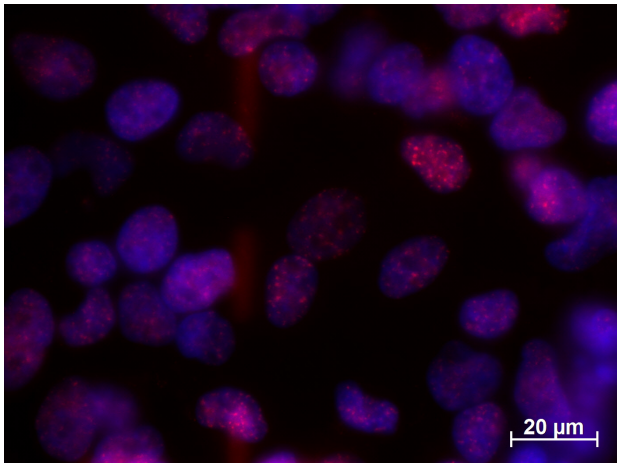

Figure 5.12.: *Microscopic image of HeLa cells using grating 2.4cont, yielding 1.2 µm wide microbeams with a mean dose of 4.2 Gy. Image taken with a 63-fold immersion objective. For orientation purposes, the cell carrier foil was structured with a grid of dashed lines, slightly visible in the γ-H2AX channel to the center left. Microbeams should thus appear in almost vertical direction. Note that γ-H2AX histones are stained in red.*

continuous layout are preferential, which are more difficult to produce with high aspect-ratios. Consequently, the line pattern could be well observed using grating 24 and 20 with 150 and 130 µm Au height, i.e. at least 80% absorption at the maximum energy of 50 keV, while with a Au height of 90 µm in case of grating 2.4cont, absorption is reduced by more than 10%. With the development of higher aspect-ratio gratings of grating manufacturers as the KIT[6], the microbeam creation can be significantly improved in the future. Using such high aspect-ratio gratings, precise alignment of the grating lines perpendicular to the beam path is highly important to avoid shadowing. Even if the technical requirements are fulfilled, it should be considered that the dose distribution visualized by the DNA double-strand breaks does not reflect the microbeam pattern created by the absorbing structure but the radiation-effect in the cells. This means that even if the creation of small microbeams with such gratings is feasible, the DNA DSBs do not stay locally concentrated as in the case of high LET (linear energy transfer) radiation, e.g. heavy ions. In particular secondary electrons from Compton scattering and photoelectric effect (cf. results in chapter 4.1), or bystander effects can cause DNA DSBs next to the microbeam path. However, it could be interesting to investigate cell survival and relative biological effectiveness with such a slight re-distribution of the dose as observed in single cells irradiated with grating 15-0.7 or 10 compared to standard homogeneous irradiation. Several studies, especially with protons and heavy ions, have demonstrated that a locally high concentration of DSBs within a cell nucleus can lead to an enhanced RBE compared to homogeneously distributed DSBs (e.g. [49]). Possibly, also the intracellular redistribution of DNA DSBs could be beneficial for tumor cell killing while sparing normal cells.

[6]Karlsruhe Institute of Technology, Karlsruhe, Germany

5.2. Creation and characterization of microbeams at the Munich Compact Light Source

Experimental results presented in the subsequent subchapter have been published in Burger et al., PLoS ONE, 2017 [149].

In the course of this thesis, in-vitro and in-vivo microbeam experiments were established at the MuCLS from 2015 to 2017. As this first commercially available compact synchrotron is a prototype machine that is subject to continuous improvement, the experiments have been performed at different conditions. Therefore, specific setup components and evaluation methods are introduced in the respective subsections individually. In the following, an overview of the entire experimental setup at the MuCLS is given (section 5.2.1) including the most important equipment for both the in-vitro and the in-vivo study. In section 5.2.2, acquisition and processing of the MuCLS spectrum for dosimetric considerations are explained for the 25 keV configuration. The microbeam experiments shown in this chapter are performed with a tungsten slit collimator. Its characterization is presented in section 5.2.3. As discussed in chapter 2.1.4, precise dosimetry is highly important to compare results from different MRT studies. Thus, different techniques for dosimetry at the MuCLS were established, described in section 5.2.4.

5.2.1. Setup and operation

In Fig. 5.13, a sketch of the experimental setup at the MuCLS is shown (not to scale). In the cave, the compact synchrotron is located, which is represented by the

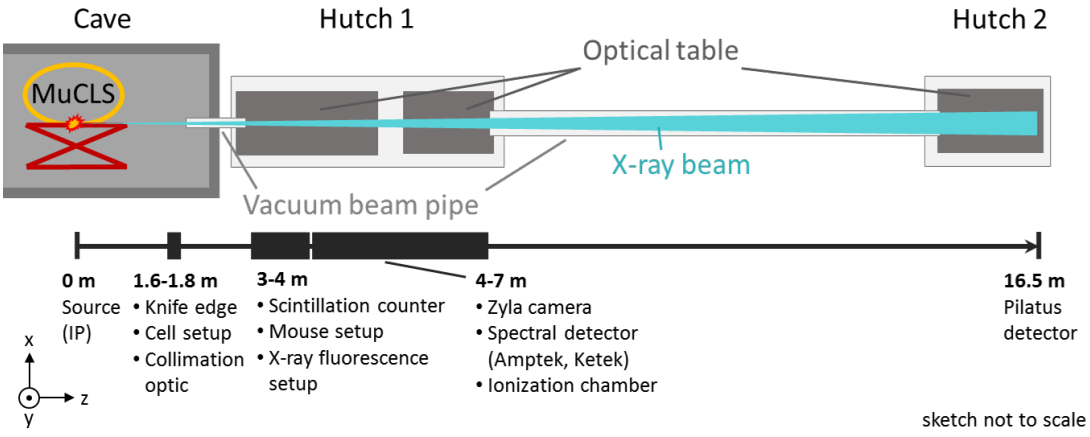

Figure 5.13.: *Sketch of the cave for the MuCLS and of the two subsequent experimental hutches. The location of different components important for the present thesis is marked on the length axis with respect to the source position (not to scale).*

electron storage ring (yellow) and the laser enhancement cavity (red). The term *interaction point (IP)* is used synonymously with *(X-ray) source*. For experiments,

two lead hutches are available: experimental hutch 1, close to the cave at about 3 m to the IP with a length of 5 m and experimental hutch 2 at about 15 m to the source with a length of 2 m. Due to the ongoing installation and commissioning of these two endstations (mid 2015 until mid 2016), the cell irradiation setup for in-vitro irradiations was positioned within the cave at 1.7 m, while in-vivo irradiations (end 2016-2017) could be performed in hutch 1 at about 3.7 m from the source. In the latter case, the X-ray beam was shaped by a collimation optic placed in the cave to increase the flux for small irradiation fields (further described in section 5.4.3). Motorized stages and corresponding motor controllers are available at all endstations. Communication with the devices is mostly performed via the software *spec* [123]. Alternatively, a Python interface [124] is used to pause the X-ray beam creation at the MuCLS for irradiations with online dose calculation.
Characterization of the X-ray beam is performed using various components: the knife edge at 1.6 m allows to measure source size and position by edge profile analysis prior to the experiment. The necessary images are taken with the photon-counting Pilatus 200K detector[7] at 16 to 16.5 m from the source. Moreover, the flux is determined as mean value from a central region of interest on the Pilatus image (for more details, see [150]). With this information, spatial and temporal overlap of electron bunch and laser pulse can be optimized. To monitor the X-ray flux 'online' during experiments in front of the object under investigation (for dosimetric reasons), a different detector is required. For this purpose, a 15 µm thin polyester film was placed in the beam at the beginning of hutch 1, which scatters a small fraction of the X-ray beam onto a scintillation counter (see section 5.2.4). The herewith acquired relative counts have to be calibrated to the photon counts measured by the Pilatus detector to obtain absolute flux values. In order to analyze the X-ray beam shape in hutch 1, a Zyla sCMOS camera[8] with a 1:1 fiber-coupled scintillator was used, which is mounted on motorized linear stages. Intensity measurement with this camera can be limited due to saturation at its minimum exposure time, which is already reached at typical photon flux values using the collimation optic. The X-ray energy spectrum is recorded with an energy-dispersive analyzer, namely the Amptek[9] or the Ketek[10] detector. The spectral detectors were placed in hutch 1 close to the respective experimental setup to reduce uncertainties introduced by the correction factors for air absorption but with the drawback of overexposure in the direct beam. Due to the latter, additional attenuation by a well-known material is required.
Knowing X-ray flux and spectrum as well as absorbing material along the beam path, the dose given to a known material can be deduced. This dose value was compared to direct, absolute dosimetry, using an ionization chamber, operated as described in 3.2.2. To minimize measurement errors, the chamber was positioned at the MuCLS at the end of hutch 1. Here, a comparable field size of 3 cm in diameter

[7] Dectris, Baden-Dättwill, Switzerland
[8] Andor Technology Ltd., Belfast, UK
[9] Amptek X-123, AMPTEK, Inc., Bedford, MA, USA
[10] KETEK AXAS-D, KETEK GmbH, Munich, Germany

as used for initial calibration is available and the requirement of a minimum dose rate of 50 mGy/min given by the electrometer can be fulfilled.

5.2.2. X-ray spectrum – measurement and simulation

With an energy bandwidth (FWHM) of 3 to 4% (varying because of machine development), the 25 keV spectrum is almost monochromatic. The absorption coefficient of water (cf. chapter 2.1.3.a, Fig. 2.10), which is the main component of cells and soft tissue, changes rapidly in this energy range. Hence, accurate dosimetry using the photon-counting detector (see Eq. (2.5)) requires a well-known spectrum. Thus, spectra were recorded before each experimental study in case the MuCLS configuration was changed in between (e.g. in form of re-adjustment of the electron beam path in the storage ring via magnet settings).

Measurement. An energy-dispersive X-ray detector (Amptek or Ketek detector) was placed in the direct beam behind attenuating PMMA slabs, which prevent saturation of the detector (for operational details of the detectors, see chapter 3.2.1). Calibration of the detector was performed via the characteristic K_α and K_β lines of lead (Pb) and/or copper (Cu). The measured spectrum was corrected for all absorbing elements along the beam path (air, PMMA, polyester windows, Si mirror of cavity), and for the detector efficiency to obtain the source spectrum.

Simulation. Because of the large correction factor for the PMMA attenuator at energies below 20 keV, noise in this energy range is upscaled significantly. To overcome this problem, a Monte Carlo simulation of the inverse Compton scattering process was used to achieve more realistic values. With the specifications of the laser undulator of the MuCLS and the 4 mrad output aperture, the spectral power density of an undulator is calculated following [151]. Taking the X-ray peak energy determined in the measured spectrum into account and adjusting the electron's energy spread and emittance (cf. section 2.2.1), allows to simulate the X-ray spectrum (Monte Carlo model implemented in LabView by Rod Loewen [152]).

Results and Discussion. The resulting measured and simulated spectra are shown in Fig. 5.14. The measured spectrum (blue curve) has a peak energy of ~24.95 keV, which is used as input parameter for the corresponding electron energy in the simulation. The green curve depicts the simulated spectrum averaged over the full aperture, the red curve contains only the spectral information from the beam center.
The shape of the spectra is dictated by the electron energy spread for the high energy tail above 25 keV. For the low energy tail, additional contributions from the non-zero electron beam emittance lead to a larger spectral broadening with exponential decay [40]. In accordance with the centered positioning of the spectral detector in the beam, the measurement agrees very well with the simulation of the spectrum from the beam center. A slightly higher contribution of lower energies is

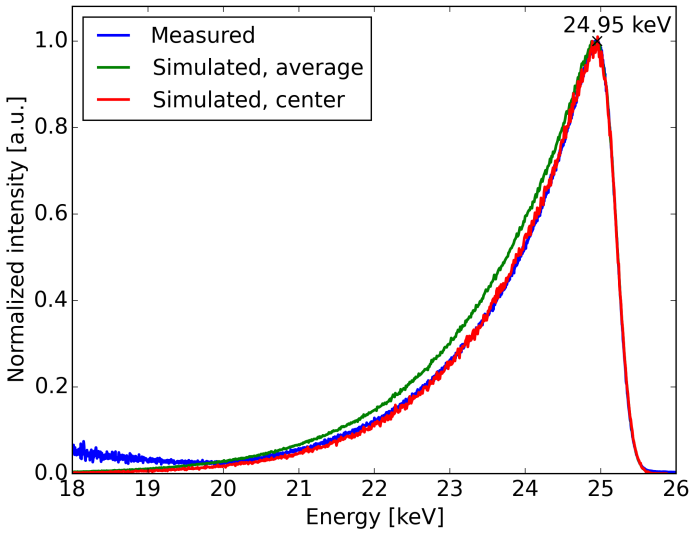

Figure 5.14.: *Measured and simulated spectra for the 25 keV configuration of the MuCLS. The measurement (blue) shows a higher intensity at lower energies compared to the exponentially decaying simulations. The green curve contains the spectral components averaged over the full beam, whereas the red curve shows the contribution of the central beam only. Simulations were performed by Rod Loewen [152].*

seen for the spectrum averaged across the entire aperture, which is related to the angular energy spread from inverse Compton scattering. With larger scattering angle, the X-ray energy decreases (cf. chapter 2.2.3, Fig. 2.13 (a)).
In contrast to theoretical expectations, the measured spectrum shows an increase in intensity at lower X-ray energies. As several cm thick PMMA slabs were used for beam attenuation, the correspondingly large correction factor upscales not only signal but also noise present in this energy range. Hence, this contribution is considered to be artificial. Moreover, the measurement can be error-prone because of the uncertainties of theoretical absorption coefficients needed for spectrum correction (for more details, see 5.2.4). Consequently, simulated spectra are used for further analysis. For most irradiations, the full X-ray beam is employed such that simulations averaged across the entire aperture are preferred. If, in the future, the electron beam emittance would be measured in the linear accelerator instead of estimated from the spectrum measurements, even higher accuracy of the simulation could be achieved. Further upgrades of the machine might include such a diagnostics.

5.2.3. Microbeam creation with a tungsten slit array

A tungsten slit array was manufactured by laser micromachining to create microbeam widths of 50 µm with a period of 350 µm. The design is presented in chapter 2.1.2.b.

5.2.3.a. Characterization

To characterize the tungsten array, projections were taken with a visible light microscope (Zeiss Axio Imager M2[11]) and an X-ray microtomography system (Zeiss Xradia 500 Versa[12]). Thereby, the size of the taper and resulting X-ray absorption at the slit edges were investigated.
Quantitative analysis of the taper at the tungsten edges was performed with visible light microscopy as shown for an exemplary slit in Fig. 5.15. The tungsten plate was positioned with the wide slit opening to the top towards the imaging system such that by changing the focal plane, both sides of the plate could be measured without plate movement. The upper image was achieved by focusing at the bottom side of tungsten plate. Subsequently, the focal depth was reduced by about 200 µm (the thickness of the tungsten plate) to image the top of the plate – seen in the central image. The graph to the bottom shows averaged horizontal line profiles – from the upper image and the lower image in blue and green, respectively.
The extension of the slit width reaches from about 90 µm at the upper extreme to the desired 50 µm at the lower extreme, which indicates a 20 µm wide taper at each edge instead of the expected 10 µm (cf. chapter 2.1.2.b). In visible light microscopy, different effects like blurring due to the finite source size (so-called *penumbral blurring* [141]), and scattering from the tungsten plate and from other setup components might have additionally broadened the signal. Moreover, the taper might not behave linearly, which was not investigated quantitatively. Yet, observations from microscopic imaging indicate a steeper edge, i.e. a less pronounced taper, towards the narrower side of the slit. Furthermore, the appearance of burrs at the tungsten edge can influence the shape of the taper (additional images in Appendix A.4).

To analyze the effect of the observed taper on X-ray transmission, the tungsten plate was measured in projection in a high-resolution microtomography system. The measurement was performed at 30 kVp applied at a tungsten anode (to resemble the spectrum to the 25 keV configuration at the MuCLS), choosing a source-sample distance of 100 mm and a sample-detector distance of 40 mm. The source size of about 2 µm [153] causes a penumbral blurring on the order of 0.7 µm. Positioning errors of the grating were minimized as rotation of the tungsten grid on a tomographic axis allowed for perpendicular alignment with respect to the beam path. To give an overview, an exemplary radiograph is shown in Fig. 5.16 (a), supplemented by a region of interest measured with higher magnification in Fig. 5.16 (b). Inhomogeneous illumination could be partially corrected by a reference image. Possible source fluctuations might have caused the remaining difference to the reference image, seen as intensity increase towards the center.
While a few slits could not be fabricated with the desired slit width (e.g. top left of Fig. 5.16 (a)), larger areas of the grating show quite good homogeneity which

[11] Carl Zeiss Microscopy GmbH, Jena, Germany
[12] Carl Zeiss Microscopy, Pleasanton, CA, USA

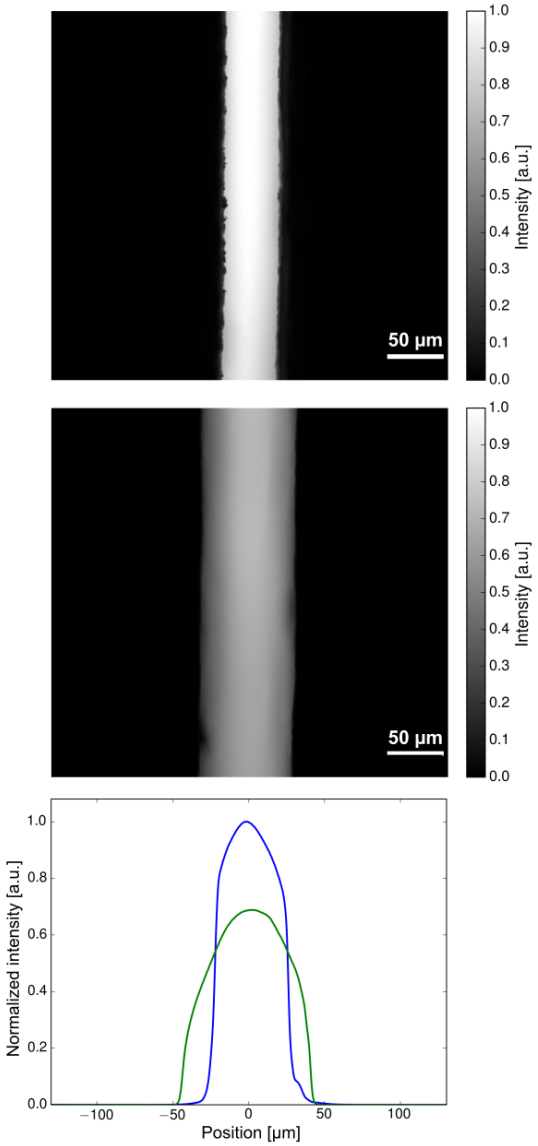

Figure 5.15: *Exemplary slit in tungsten plate for microbeam creation imaged with visible light microscopy. In the upper image, the focal plane is set to the bottom of the plate. At the top side of the plate, about 200 µm higher, the larger opening of the tungsten grid was observed (center image). The graph below shows line profiles of normalized intensity obtained from averaging along the vertical axis of both images. The line profile from the upper image is represented in blue, from the lower image in green.*

allows to create a regular microbeam pattern for the cell and small animal experiments presented later on. However, it is necessary to measure the actual X-ray transmission through the grating for correct dose calculation instead of assuming a transmission of 1/7 – the ratio of slit width to grating period – of the homogeneous beam (see section 5.2.4 below).

In Fig. 5.17, the measured edge sharpness (blue line profile) is compared to a simulation (green line profile) of the X-ray transmission through a 200 µm thick tungsten plate assuming a taper of 20 µm at the slit edges. Line profiles from a region of interest along the central slit of Fig. 5.16 (b) were averaged, followed by base line subtraction and normalization with respect to the intensity at the peak center.
Firstly, it is evident that the measured microbeam with a width of about 40 µm in

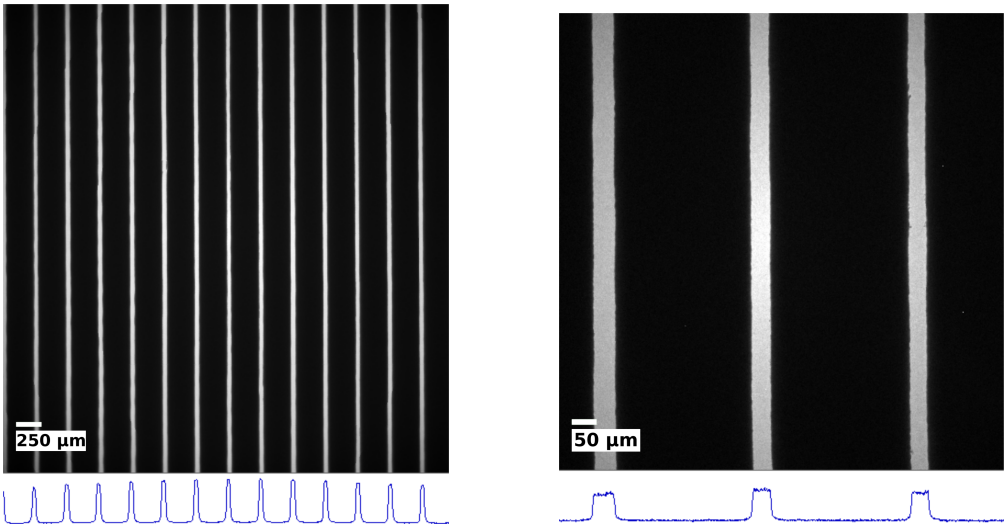

Figure 5.16.: *(a) Radiographic image taken with an X-ray microtomography system with 4-fold magnification optics applying 2-fold binning. The measurement was performed at 30 kVp, with a source-sample distance of 100 mm, and a sample-detector distance of 40 mm yielding an effective pixel size of 4.8 µm. (b) Zoom into (a) using a 20-fold magnification objective and 2-fold binning achieving 1 µm effective pixel size. A projection of the line profiles is added below to estimate the influence of the taper at the tungsten edges on X-ray absorption.*

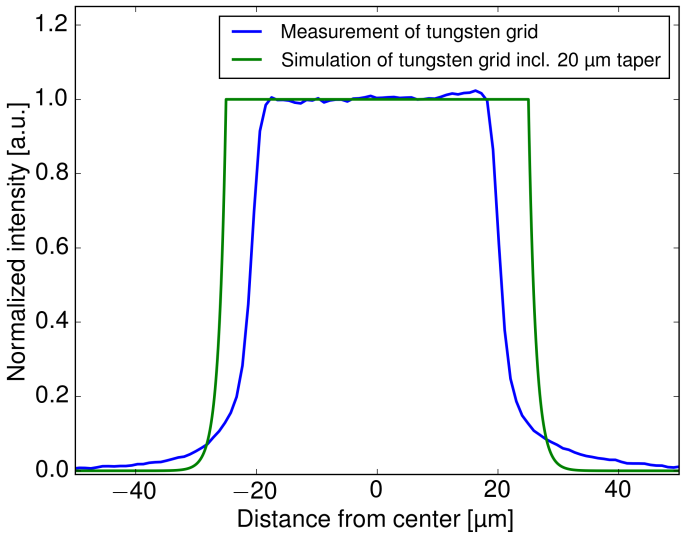

Figure 5.17.: *Line profile of a simulated (green) and a measured (blue) microbeam profile using the tungsten slit array with 50 µm slit size. The simulation of X-ray transmission assumes a 200 µm thick tungsten plate and at each edge a taper of 20 µm. Line profiles were averaged over a region of interest along the central slit in Fig. 5.16 (b).*

the peak stays well below the desired width of 50 µm. In contrast, for visible light microscopy, slit widths of ∼50 µm were measured. This difference indicates that the precision of slit fabrication by laser micromachining is subject to fluctuations, which can also result from the previously mentioned burrs at the tungsten edges. Secondly, the edge profile from the radiographic image shows a larger blurring of the edges than expected from the simulation of a 20 µm taper. X-ray transmission approaches zero at ±40 µm, which is consistent with the taper measured by visible light microscopy of up to 20 µm. The edge profile is steep close to the peak followed by a quite long tail, which could result from a non-linear taper, as discussed above. Also X-ray scattering at the tungsten plate, for example, can contribute to the measured intensity in the valley, such that the actual taper might be smaller. This is similar to the observations from visible light microscopy, where reflectance and scattering of light at the tungsten borders possibly led to additionally broadening of the microbeam profile.

Consequently, while a clear assignment of the edge blurring to the taper of the tungsten slit array is not possible, a taper below 20 µm can be assumed. Qualitatively, the intensity falloff at the edge is shown to be quite steep, which will allow for a high peak-to-valley dose ratio in MRT experiments at the MuCLS using the 25 keV configuration. Irregularities of the slit widths due to grating fabrication require specific dosimetric considerations. From the analysis of the acquired radiographic images, the most homogeneous area of the tungsten slit array was chosen for irradiation purposes.

5.2.3.b. Conclusion and outlook

In conclusion, the tungsten grid fabricated by laser micromachining allows to achieve quite high peak-to-valley dose ratios with a slightly higher valley contribution at a distance of up to 20 µm from the microbeam. The homogeneity of the slit width and the degree of taper is sufficient to create a microbeam pattern with approximately 50 µm wide beamlets. At this scale, the deviation from the ideal pattern might only play a role if crossfiring or interlacing schemes are desired (cf. chapter 2.1.1).
Further analysis would be useful to improve the dose distribution in order to facilitate interpretation and comparison of the results. In the future, especially irregular slits need to be avoided and smoothness of the slit borders could be improved to achieve higher accuracy in dose delivery. With a reduced taper, an even higher PVDR would become achievable. This might require modifications in the laser micromachining process, e.g. towards water-jet guided laser cutting [154]. If higher X-ray energies should be applied, the tungsten plate has to be thicker for full absorption. Hence, the taper caused by laser micromachining might even increase. In this case, the more cost-intensive fabrication of a slit array by, for example, wire cutting could be advantageous (cf. chapter 2.1.2.b).

5.2.4. Dosimetry

As concluded in chapter 2.1.4, highly accurate dosimetry is required to relate the applied dose to the observed radiobiological effect in MRT and to compare the experimental results with other studies using different setups. To investigate the PVDR, the microbeam dose profile must be measured with sufficiently high resolution and the dosimetric method must provide a large sensitivity range. Moreover, at the MuCLS, especially due to thermal drifts, fluctuations of the photon flux can occur which thus has to be monitored permanently. As high-resolution dosimetry yielding absolute dose values is challenging and often does not fulfill the requirement of online dosimetry (see chapter 4), the following experiments are only considering mean dose values. To compare the radiobiological effect of homogeneous and microbeam irradiation, the same mean dose is given – averaged over an adequate region of interest. Thus, the only difference in dose from homogeneous to microbeam treatment is the spatial redistribution of the dose from the evenly irradiated full field into high-dose beamlets spaced by low-dose areas.
Consequently, instead of high-resolution dosimetry, standard dosimeters or intensity detectors can be employed. In the following, the dosimetric methods applied at the MuCLS are presented: on the one hand, radiochromic film dosimetry, on the other hand, dose calculation from photon flux measured with a photon-counting detector or from relative intensity-values using a calibrated scintillation counter. In the case of transparent or low-absorbing samples like cell monolayers, a photon-counting detector allows for online dosimetry. As a control mechanism, film dosimetry can be applied additionally with readout post irradiation. In cases where the material composition of the irradiated object is unknown, a transparent dosimeter in front of the object, e.g. a transmission chamber, is useful. However, the transmission chamber has to fit the beam size at the desired position of the MuCLS setup and should support inhomogeneous irradiation. Calibration of such a chamber for absolute dosimetry is required. Hence, an in-house built scintillation counter was used for this purpose.

5.2.4.a. Radiochromic films (ionization chamber)

To either analyze the absolute dose value, or to measure the intensity distribution, or to verify the irradiation position, radiochromic films were placed directly behind the irradiation target in the experiments described later on. Films were read out at least 24 hours after irradiation. Absolute dose values can be obtained from comparison of the optical density of the irradiated area to a calibration curve. As such a calibration curve could not be obtained directly at the MuCLS, films were calibrated with an ionization chamber at a conventional X-ray tube with a spectrum similar to the spectrum of the 25 keV configuration of the MuCLS. The detailed protocol for radiochromic film readout is described in chapter 3.2.3.
Less than 10% uncertainty is expected for dose values measured with film dosimetry at the MuCLS (cf. chapter 3.2.3). Systematic errors include, for example, inhomogeneity and energy-dependency of the film. Statistical errors might arise

from differences in film handling, which were minimized where possible.
To simultaneously perform film dosimetry and online dosimetry with the photon-counting detector positioned behind the film, the transmission of the film was measured using the 25 keV configuration at the MuCLS. Therefore, a Gafchromic EBT3 film[13] was placed in the beam path covering the full irradiation field. The photon flux was monitored by the photon-counting detector iteratively with and without the film in the X-ray beam. This resulted in 1.85%±2.7% (SD) absorption of the total photon flux by the film. Thus, the photon flux in the experiments with film dosimetry was multiplied by a factor of 1.02.

5.2.4.b. Photon-counting detector

For online dosimetry and calibration of the scintillation counter, the photon flux recorded by a photon-counting detector allows to determine the mean absorbed dose if the material of the target is known. Additionally, the X-ray spectrum is required and all absorbing elements along the beam path have to be taken into account. As a reminder, the calculation of the dose D from Eq. (2.5) introduced in chapter 2.1.3.a is repeated here:

$$D = \frac{N}{A} \int_{E_{\min}}^{E_{\max}} \omega(E) \frac{\mu_{en}}{\rho}(E) E dE, \tag{5.1}$$

requiring the knowledge of the number of photons per area N/A, i.e. the photon fluence, the contributing X-ray energy E and its contribution to the spectrum, given by the differential energy spectrum $\omega(E)$, as well as the mass energy absorption coefficient $\mu_{\text{en}}(E)$. As the mean dose computation for the in-vitro study differs from the in-vivo experiment, detailed information on dose calculation is given in the respective sections. Here, the opportunities and limits using a photon-counting detector for dosimetry are briefly discussed.
With a pixel-size of $172 \times 172\,\mu\text{m}^2$ and its position at ∼16 m from the interaction point, the photon-counting Pilatus detector does not allow for high-resolution microbeam dosimetry. However, due to the geometrical magnification of about 8.5 (cell experiment) or 3.5 (mouse-ear study), the microbeam pattern generated with the above described tungsten slit array is recognizable on the detector image. An exemplary radiograph in Fig. 5.18 shows the microbeam pattern created at 1.7 m from the source (for cell irradiation). A circular aperture was inserted to limit the beam only to the area in which the cells were seeded (using the cell chambers described in chapter 3.1.1). In Fig. 5.18 (a), the radiographic image is shown without further processing, while in Fig. 5.18 (b), a non-linear iterative deconvolution algorithm (Richardson-Lucy deconvolution based on [155]) was applied to account for penumbral blurring. Thus, the actual microbeam pattern is retrieved. As the Richardson-Lucy algorithm does mostly not converge to a stable global minimum, the amount of actually performed iterations can greatly influence the results. For

[13] Ashland, Bridgewater, NJ, USA

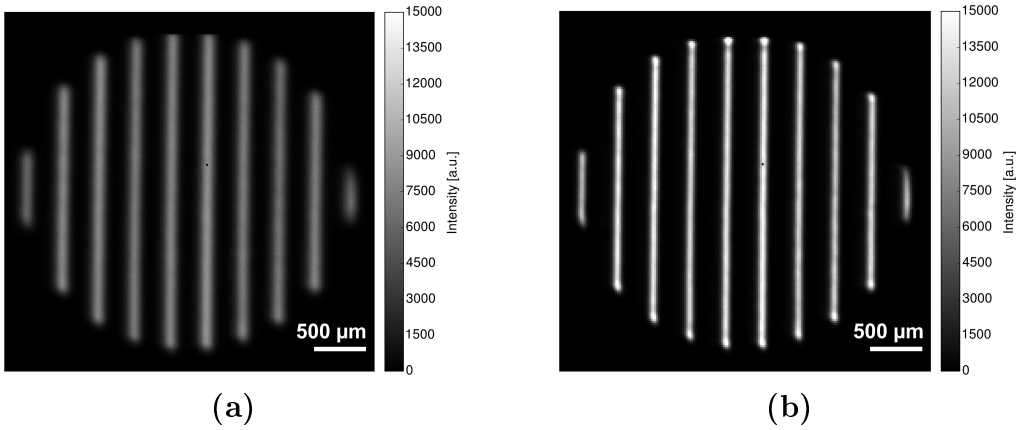

Figure 5.18.: *Radiographic image of the cell irradiation field (approx. 4 mm diameter) with tungsten slit array inserted obtained with a photon-counting detector. High intensity at the edges is an artifact of the deconvolution algorithm used to correct for penumbral blurring.*

example at steep edges, non-quantitative high intensity values occur, visible in Fig. 5.18 (b). Hence, such a deconvolved image cannot be used for quantitative analysis of the PVDR. To improve quantitativeness, advanced implementations of the Richardson-Lucy model with regularization (e.g. [156]) or even a different deconvolution method might be useful.
Following the concept of an equivalent mean dose value for homogeneous and microbeam geometry, a photon-counting detector is well-suited to measure the necessary photon flux – integrated over the desired region of interest. If the irradiation target is not transparent, relative intensity detectors can be calibrated with the photon-counting detector before the experiment. In this case, the absorption of the tungsten slit array has to be determined additionally such that the same number of photons is delivered during microbeam and homogeneous irradiation.

5.2.4.c. Relative transmission counter

Relative intensity values are recorded with a scintillation counter at the front side of the experimental hutch 1 if the investigated target (placed behind the scintillation counter) has an unknown material composition or is too thick to measure in transmission. A calibration to the Pilatus detector permits to determine photon flux. To minimize intensity loss, the X-ray beam is passed through an inclined polyester film (15 µm thick) that scatters only a small fraction of the incoming X-rays. A scintillator (sodium iodide (NaI) crystal) absorbs the scattered radiation and converts the X-ray photons to visible light, which is subsequently enhanced by a photomultiplier (for more information, please refer to [150]). Because of control system overheads, an acquisition with the scintillation counter takes about 1.7 s per 1 s exposure time. Thus, the measured intensity value has to be upscaled to the full exposure period assuming an unchanged intensity during readout time. For

calibration measurements, the scintillation counter has to be synchronized with the Pilatus detector.

5.3. In-vitro experiments at the MuCLS

As the source parameters at the MuCLS differ significantly from previous microbeam irradiations at large-scale synchrotron facilities, the radiobiological effect of microbeam compared to homogeneous beam geometry needs investigation. In particular the lower X-ray energy of about 25 keV in contrast to a mean energy of 100 keV at the ESRF, for example, can lead to an enhanced PVDR because of a steeper beam penumbra, as shown in chapter 2.1.1. Due to the lower dose rate at the MuCLS, the mechanisms for DNA repair initiated or effected in the cell nuclei before the end of the irradiation time might additionally influence the biological reaction.
To analyze the radiobiological effect of MRT at the MuCLS on cellular level, three different endpoints are studied following microbeam, homogeneous, and sham irradiation of normal-tissue cells seeded in a monolayer.

- Firstly, using the γ-H2AX assay, DNA damage following radiation exposure can be localized and visualized by fluorescence microscopy. Thus, the microbeam dose distribution which results from the pattern created by the tungsten slit array is verified qualitatively.

- To determine the radiation damage in a quantitative manner, clonogenic cell survival of CHO-K1 cells is studied in a second experiment. The survival fraction of the cells following microbeam irradiation is an indicator for normal tissue sparing achieved by the geometrical redistribution of the dose compared to homogeneous irradiation.

- Thirdly, a chromosome aberrations test in A_L cells permits to indirectly access the radiation-induced cytogenetic damage for each irradiation geometry. The study focuses on dicentric chromosomes (dicentrics) and centric rings as these chromosome aberration types are generally used for biological dosimetry after radiation exposure of humans.

For both the clonogenic cell assay and the chromosome aberration test, values of the relative biological effectiveness (RBE) were calculated at the MRT mean doses (averaged over irradiated area, cf. section 5.2.4). As a reminder, the RBE is defined in this thesis as the ratio of the mean dose delivered homogeneously to the MRT mean dose yielding the same biological effect (here, corresponding to survival fraction, dicentrics per cell, or centric rings per cell):

$$\mathrm{RBE} = \left.\frac{\text{Homogeneous dose}}{\text{Microbeam dose}}\right|_{\text{same effect}}.$$

The results will provide new insights into the radiobiological mechanisms of MRT as up to date only few publications have reported on clonogenic cell survival after X-ray MRT (e.g. [28, 88]) and no data on chromosome aberrations like dicentrics and centric rings following X-ray microbeam irradiation are available in the literature (to the best of the author's knowledge).

5.3.1. Irradiation setup and concept

First cell irradiations were performed within the cave of the MuCLS at 1.7 m to the interaction point, which is about 40 cm downstream of the beryllium exit window. At this location, the beam offers a homogeneous intensity distribution of about 7 mm diameter. As the spectrum differs only slightly between the beam center and the outer region (see Fig. 5.14), also considering the dose, a homogeneous distribution can be expected.
To measure the dose distribution over the irradiation field, an EBT3 film was irradiated at the cell holder position (1.7 m source distance). The normalized dose distribution is shown in Fig. 5.19 with the full field in Fig. 5.19 (a) and the horizontal (blue) and vertical (red) line profiles from the center of the field in Fig. 5.19 (b). Noise mainly stems from film inhomogeneities and scanning performance. The el-

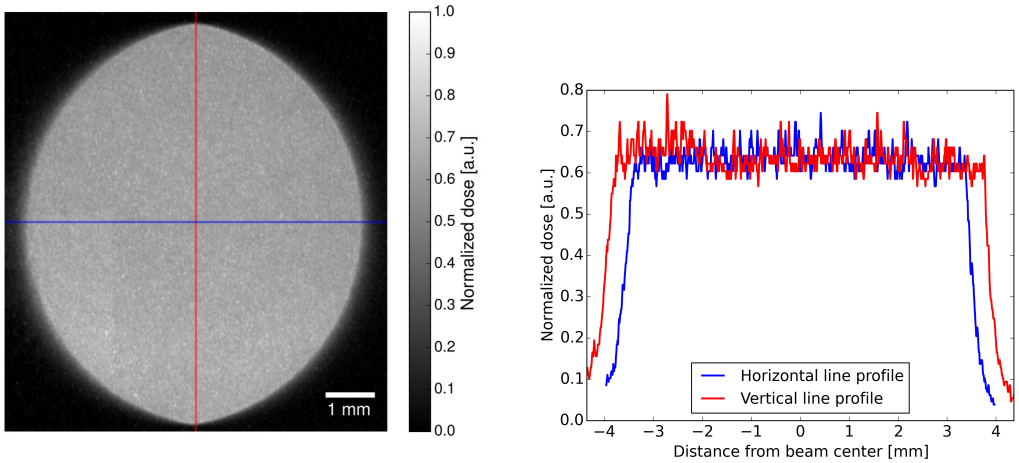

Figure 5.19.: *Dose distribution measured with an EBT3 film at 1.7 m from the source as used for cell irradiations. (a) Two-dimensional dose distribution with highlighted horizontal (blue) and vertical (red) center lines. (b) Corresponding line profiles to (a).*

lipsoidal shape of the beam is related to the geometry of the X-ray exit window resulting in a sharp edge at the upper and lower border and a smoother transition at the left and right border. The irradiation area accounts to $6.8 \times 8.2 \times \pi\,\mathrm{mm}^2$ with a quite homogeneous dose distribution.

For irradiation, cells were seeded onto a 6 µm thick Mylar foil mounted in a dedicated cell holder (cf. 3.1.1), which was placed vertically in the beam during irradiation. For the γ-H2AX assay, the available seeding area with a diameter of about 3 cm was covered with a monolayer of cells, which were only partially irradiated due to the smaller beam size. As the cells are kept on the Mylar foil for immunofluorescence imaging, the irradiation field can easily be retraced. In case of the quantitative evaluation of cell survival and chromosome aberrations, the cells are detached from the Mylar foil after irradiation. Hence, all seeded cells have to

be covered by the irradiation field. Therefore, the seeding area was restricted to a circle of about 4 mm diameter.
Spatially separated planar microbeams were created with the tungsten slit array, characterized in section 5.2.3, with 50 µm beam width and a peak-to-peak spacing of 350 µm. For homogeneous irradiation, the tungsten slit array was removed. A schematic drawing of the cell irradiation setup is shown in Fig. 5.20.

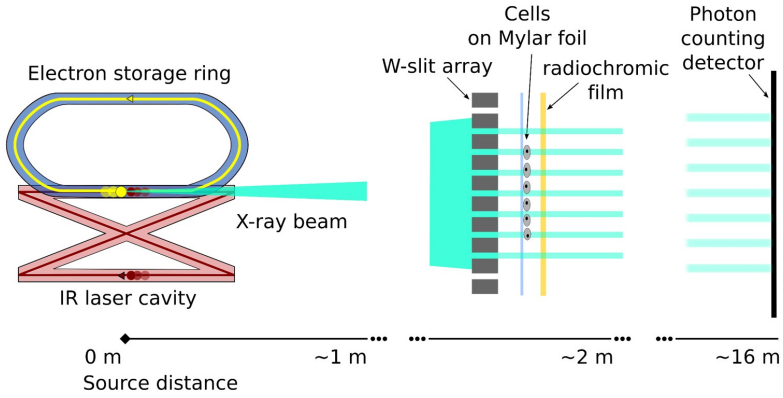

Figure 5.20.: *Schematic drawing of the cell irradiation setup. The MuCLS is drawn by means of the electron storage ring (electrons as yellow circles) and the laser enhancement cavity (two laser pulses as red circles) producing an X-ray beam (cyan) of about 25 keV. At a source distance of 1.7 m, the tungsten slit array is inserted in the X-ray beam to create a microplanar radiation field. Directly behind the array, cells are situated in a dedicated cell holder. For verification of irradiation field and dosimetry, a radiochromic film is placed behind the cell holder. Live dose monitoring is performed with a photon-counting detector at 16 m distance to the source.*

Sham irradiation was performed in the cave of the MuCLS in a lead-shielded environment. The cell holder was placed upright to ensure the same treatment conditions for all cells except for irradiation. As irradiation times varied depending on dose and irradiation geometry from a few minutes up to one hour, the duration of sham irradiation was adjusted accordingly to reflect the range of possible irradiation times. During irradiation, cells were not covered with medium but the humidity from the medium which is contained in the sealed cell holder creates a saturated atmosphere to avoid dehydration. The viability of the cells and their adhesion to the Mylar foil was controlled after irradiation. Abnormalities with respect to these criteria led to exclusion of the sample from further analysis.

5.3.2. Online dosimetry for cell irradiations

5.3.2.a. Method

To calculate the mean absorbed dose via the photon flux, three pieces of information are required: the mean photon flux at the sample position, the X-ray spectrum, and the material composition of the irradiation target for absorption

coefficient and penetration depth. From the number of photons per pixel measured by the Pilatus detector, the mean photon flux is deduced from a region of interest (ROI). The Pilatus detector 200K has two modules separated by a central horizontal gap, which can image almost the full beam at 16 m from the interaction point. As the irradiation target is centered in the beam, the detector is positioned off-center to avoid the gap covering the relevant part of the beam. An exemplary image is shown in Fig. 5.21, where two orange ROIs highlight the area contributing to the mean photon flux value in case of homogeneous irradiation. For microbeam irradiation, the ROI has to cover an integer number of periods of the peak-and-valley pattern. Therefore, automatic extraction of the peak positions within the ROI was implemented, followed by a reduction of the ROI to fulfill the peak-to-peak criterion (green area). Thus, the mean photon flux measured by the Pilatus detec-

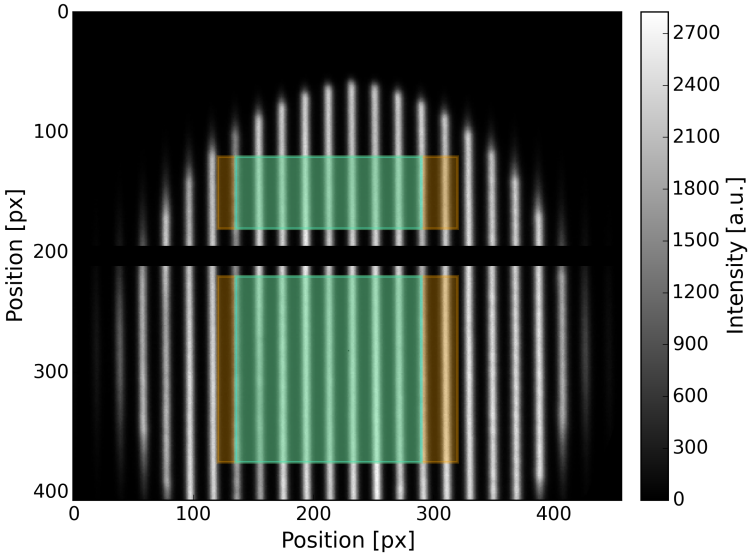

Figure 5.21.: *Radiographic image taken with the Pilatus detector. The two modules of the detector are separated by a gap, visible as black horizontal line in the center. The detector is positioned to take the central part of the full beam. The orange rectangle marks the region of interest (ROI) chosen to compute the mean photon flux. As an integer number of periods is required for the ROI, the peak positions are automatically extracted and the ROI is adjusted accordingly (green rectangle).*

tor is computed from the respective ROI. In a next step, the mean photon flux at the sample position is retrieved. Correction of the photon flux for all absorbing elements along the beam path includes:

- four 125 µm thick polyester films covering the beampipes
  → absorption coefficient of polyethylene terephthalate ('Mylar') taken from [76],
- air gaps between the evacuated beampipes (vacuum-pumped to a pressure below 0.3 mbar before each experiment)

→ X-ray transmission values for air from [157] based on [158],

- 1 mm thick Si sensor of Pilatus detector to determine its quantum efficiency
  → photoelectric absorption coefficient for Si taken from [76].

The second component to obtain the mean dose absorbed by the irradiation target is the X-ray spectrum at the sample position. As described above, the Monte Carlo simulation yields a spectrum at the source position. The spectrum at the sample is changed by the following elements along the beam path:

- a Si mirror, thinned to 200 µm for X-ray beam exit from laser cavity
  → absorption coefficient for Si from [76],
- a 127 µm thick beryllium (Be) window at beam exit from the source
  → neglected because of low absorption in relevant energy range,
- an air gap from the Be exit window to the cell holder
  → X-ray transmission values for air from [157] based on [158].

Values of absorption coefficients were acquired with a high sampling frequency from the online databases cited above and subsequently linearly interpolated for the required energy range.

Finally, the absorption coefficient of the irradiation target is needed. To account for the energy that is transferred to kinetic energy of charged particles upon X-ray interaction with matter, and the possible loss of this energy in the target material, the mass energy absorption coefficient is retrieved from [76]. The cell monolayer is approximated with water – its mass energy absorption coefficient is shown in Fig. 2.10 in chapter 2.1.3.a.
Including mean photon flux at the sample position, energy spectrum, and absorption coefficient, the absorbed mean dose can be obtained via Eq. (5.1).
For online dosimetry, the Pilatus detector records the photon flux every second. Hence, the mean photon flux value is updated in the same interval. Integrating the mean dose per second over the irradiated time yields the applied mean dose and allows to determine the remaining time needed to achieve the desired mean dose value. Thus, the beam creation can be interrupted at the end of the countdown (directly at the electron beam of the MuCLS).

5.3.2.b. Accuracy

To compare the results from the photon-counting method to film dosimetry, films were evaluated on a random basis with a flatbed scanner (cf. 3.2.3). Film dosimetry resulted in about 20% higher absolute dose values. An error in film dosimetry of up to 10% could possibly result from differences between calibration (with an ionization chamber) and measurement settings as well as film composition as discussed in chapter 4.1.5.

To further analyze the error in film dosimetry, the ionization chamber was positioned directly in the beam in parallel to the Pilatus detector at the end of hutch 1 as a trade-off between beam size and X-ray fluence rate (cf. 5.13). Thus, the sensitive area of the ionization chamber was fully illuminated in the lower center of the beam while for imaging with the Pilatus detector a region of interest in the upper center of the beam could be evaluated. Yet, with dose rates on the order of 60 mGy/min, the ionization chamber had to be operated at its lower limit. As a result, 15 to 20% higher absolute dose was measured by the ionization chamber than using the photon-counting method. Hence, film dosimetry and ionization chamber dosimetry agree well with each other. Consequently, the dose difference of about 20% seen in film dosimetry might not be based solely on the film quality or its calibration but can mainly be traced back to the ionization chamber measurement. The parameters used for initial calibration of the chamber might differ from the measurement with respect to radiation quality. Here, the calibration factor for TW50 with an uncertainty of 3.3% was used. However, this factor affects the absolute dose value only slightly in the investigated energy range. The largest uncertainty in ionization chamber dosimetry at the MuCLS is introduced by operating the chamber at its lower limit of the required dose rate. To verify functionality of the system, further experiments at higher dose rates have to be performed in the future. This will be feasible due to recent upgrades of the MuCLS yielding a significantly higher X-ray flux. As error sources from film and ionization chamber dosimetry are unlikely to cause a 20% difference in dose compared to the photon-counting method, the latter needs to be studied in more detail.

Statistic and stochastic errors occur when the dose is determined via the photon-counting method. Especially, the use of theoretical absorption coefficients introduces uncertainties, which can lead to several percent of dose deviation, also discussed in literature.

For example, the absorption coefficient for silicon – necessary to calculate the efficiency of the spectral and the photon-counting detector, as well as the transmission of the X-ray exit mirror of the enhancement cavity – has been investigated in [159–161]. Differences of theoretical to experimental values in [160] range between 1.1 to 1.7% for energies close to 25 keV. Measurement precision is stated to 1% or better for almost all experimental studies mentioned here. In [161], a summary of various studies is given with respect to the discrepancies in the total mass attenuation cross section of Si. Up to about 19 keV, most theoretical and experimental values agree within ∼1%, whereas at higher energies, larger differences of approximately 3% become observable. Hence, the 'theoretical' absorption coefficient of Si is subject to an estimated uncertainty of about 1 to 2% for the 25 keV configuration of the MuCLS.
Moreover, the assumption that only photoelectric absorption yields a measurable signal in the silicon photodiode of the detectors is a simplification because photons undergoing Thomson and Compton scattering before being absorbed are neglected.

This might lead to a slight underestimation of the detector efficiency, which would result in an even higher dose difference compared to ionization chamber dosimetry.

Additionally, the air gaps have to be considered along the beam path, which requires the calculation of X-ray transmission through air. Therefore, the beam path, as well as temperature and pressure are recorded.

- The accuracy of measuring the total beam path of several meters with a laser distance meter is sufficiently high such that this measurement error has a very small effect on the calculated X-ray transmission.
- As the temperature is quite stable during the measurement and can be determined easily within about 1 °C, the influence of its deviation is small. However, it can change from a calibration measurement to the actual experiment, which could introduce an additional error if no correction is applied. However, for typical values of pressure, air gap, and X-ray energy, the X-ray transmission changes only by 0.7% for a relatively large temperature difference of 10 °C from 290 to 300 K.
- While the temperature measurement only slightly affects the X-ray transmission, the pressure needs to be determined with good accuracy as the laboratory is ventilated and thus subject to changes of the air conditioning system instead of the natural environment. During the period of experiments, instabilities in the air conditioning system were observed. Hence, as an example, a pressure reduction of 80 mbar leads to an increase in X-ray transmission of 1.7%, using typical parameters.

If temperature and pressure are determined with standard thermometer and barometer, respectively, the measurement error can be minimized. Yet, the calculation of X-ray transmission is error-prone due to the use of absorption coefficients from respective data bases (compared e.g. in [162]). The absorption coefficient of air as a compound of different elements – nitrogen, oxygen, carbon, and argon – includes the errors of the corresponding absorption coefficients, which can be estimated from the above named studies to about 1 to 2% each. Taken the above mentioned error sources into account, the calculation of X-ray transmission through air is assumed to be within 3% uncertainty.

Similarly as for the absorbing elements above, the correction of the photon flux for the Mylar windows is based on the respective absorption coefficient. As the X-ray transmission through such a window is higher than 99%, the influence of the corresponding error on the dose error can be neglected.

To calculate the absorption of water, the mass energy absorption coefficient is used. However, the data bases rarely include accurate uncertainty values but only estimates, which range from 1% to above 5% below 100 keV [162]. Boone *et al.* [163] studied the difference of two data sets for a variety of atomic numbers

Z, which was 3.9% for $Z = 10$, i.e. approximately for water. As this information is not contained in the data bases themselves, uncertainties on the mass energy absorption coefficient for water were discussed in [162]. For the more recent data bases, deviations of 2 to 3% were found. Measurements in the energy range from 8 to 60 keV confirm theoretical values which are used for the NIST [76] and the XCOM [164] data base within 1 to 4%. All in all, the uncertainty of the mass energy absorption coefficient for water at about 25 keV can be estimated to about 3%.

The simulation of the spectrum based on the information of the measured spectrum entails a dose error which is difficult to quantify. Inaccuracies in calibration of the spectral detector influence the measured X-ray spectrum as well as the absorption coefficient required for the PMMA absorber, air transmission, and the silicon of the cavity mirror and of the photodiode. Furthermore, the lower energy tail is fixed by the simulation to avoid the large amount of noise present in the measurement (see section 5.2.2). Thereby, real scattering contributions might be neglected. While the accurate uncertainty value cannot be deduced without dedicated measurements, an estimated error in dose of about 3% is considered realistic, which corresponds to 60 mGy for a dose of 2 Gy.

An additional contribution to the dose error results from the choice of a ROI on the Pilatus image used to calculate the mean dose. This region does not correspond perfectly to the irradiation area, which would represent a lower number of pixels on the detector (about $100 \times 100\,\mathrm{px}^2$), and thus the accuracy of the mean number of photons might be affected – especially in the case of microbeam irradiations, where the evaluated ROI is further reduced to peak-to-peak area. While the photon-counting detector benefits from the absence of readout noise and dark current, Poisson noise can influence the photon counts. To minimize further errors, the module gap, pixels at the borders of the readout chips, as well as hot or dead pixels were excluded from the ROIs where possible. Small changes of the ROI showed a dose variation on the order of a few mGy for homogeneous irradiation. Due to the imperfect grating structure of the tungsten slit array, a change in position of the ROI for mean dose calculation can yield a difference in dose of tens to hundreds of mGy. Hence, the region must be well placed in the beam center including the microbeams used for irradiation.

In conclusion, the dose calculation from photon flux is subject to systematic uncertainties, which are mainly introduced by the absorption coefficients of a large variety of materials. Stochastic errors like inaccuracies of distance measurements were minimized where possible. From the above mentioned sources of errors, weighted according to their influence on the dose calculation, a dose uncertainty of about 10% can be assumed. Due to the large amount of influencing factors and their often undetermined uncertainty, an accurate error on the absolute dose value is difficult to achieve. Moreover, this error is not sufficient to explain the discrepancy between film dosimetry and the photon-counting method such that absolute

dosimetry at the MuCLS requires further investigation. To exclude errors introduced by scattering material, for example, a systematic dosimetric analysis using ionization chamber and Pilatus detector at a well-known X-ray tube could be conducted in a future study. Additionally, the effect of the threshold energy set for the Pilatus detector for signal detection could be analyzed. However, for comparison of homogeneous to microbeam irradiation applying the same mean dose, a relative dose value is sufficient. Thus, the error in dose given in the experimental results stems from the dose differences between the replicates and does not refer to the absolute dose value.

5.3.3. Results and discussion of cell irradiations

5.3.3.a. γ-H2AX assay

The γ-H2AX assay is a common tool to investigate radiation-induced DNA damage in a qualitative or quantitative manner (for MRT, see e.g. [25, 165–167]). As the tungsten slit array does not provide an ideal microbeam pattern and scattering as well as bystander effects can lead to an increase of the valley dose, the microbeam dose profile in tissue might exhibit a low PVDR. Localization of DNA damage by staining γ-H2AX histones allows to qualitatively analyze this dose distribution. For this purpose, HeLa cells from a cervical cancer cell line were prepared following the protocol given in chapter 3.1.2. After microbeam or homogeneous irradiation with 2 Gy mean dose or sham irradiation, cells were incubated for 30 min to allow for DNA repair before staining procedures were applied. The sites of DNA DSBs were labeled in green (Alexa 488) and the nuclear DNA in blue (DAPI). Fig. 5.22 shows exemplary images obtained quasi-simultaneously via immunofluorescence microscopy. Fig. 5.22 (a) shows the DNA DSBs by green fluorescent foci, Fig. 5.22 (b) highlights the nuclear DNA, and Fig. 5.22 (c) presents an overlay of both images. To the left, a microbeam irradiated cell layer can be seen with a maximum peak dose of 14 Gy (assuming an ideal microbeam pattern with 100% dose in the peak and 0% dose in the valley). In the center, homogeneously irradiated cells are shown, and to the right, sham irradiated cells. The image sets of each staining procedure were acquired with equal acquisition, contrast, and scaling settings.

Considering Fig. 5.22 (a), the microbeam pattern with 50 µm wide beamlets distant by 300 µm is well reflected via the DNA double-strand breaks. With the peak dose of up to 14 Gy in each microbeam, the density of fluorescent foci is too high to distinguish them individually with 20-fold magnification optics. Therefore, quantitative analysis of the DNA damage by foci counting might be difficult, even if a deconvolution would be applied to account for intensity contributions from neighboring sections. An increase of the overall brightness with respect to the sham irradiated cells can be observed in the homogeneous case. Due to spontaneous or cell cycle dependent foci accumulation, background fluorescence is visible, in particular in the non-irradiated sample. Fig. 5.22 (b) allows to compare the cell

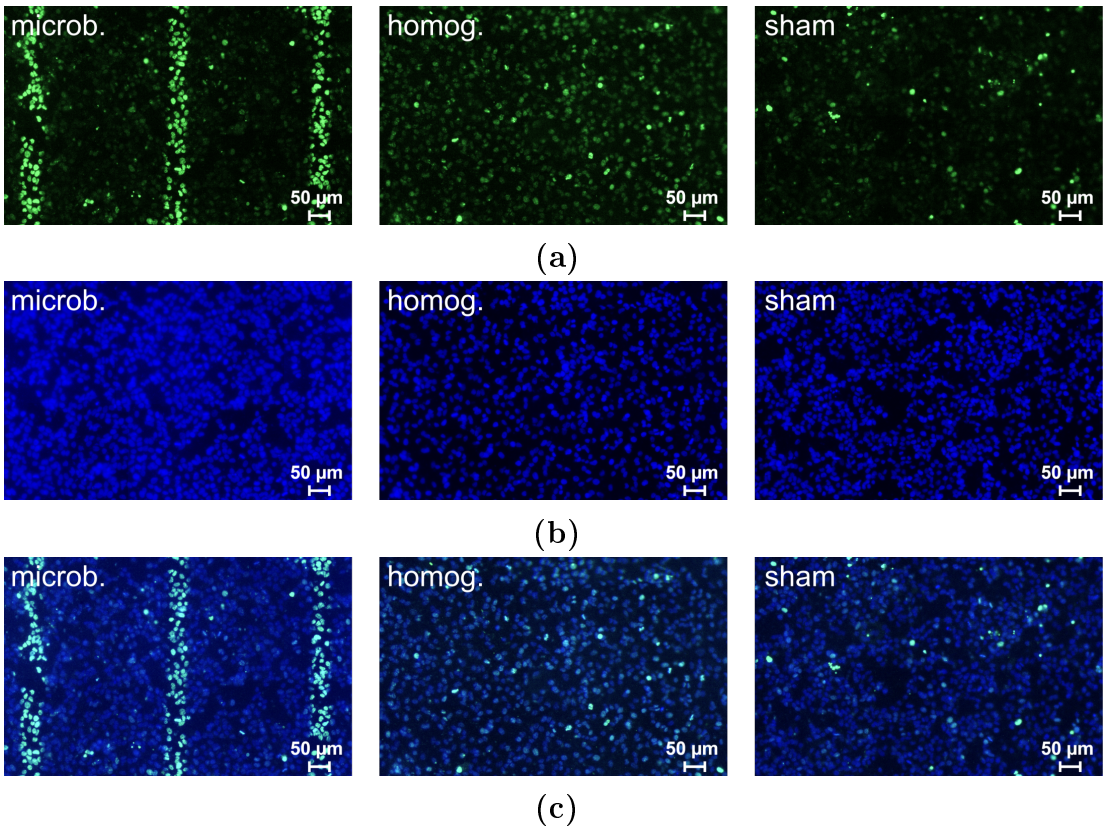

Figure 5.22.: *Fluorescence microscopy images applying the γ-H2AX assay to HeLa cells following microbeam (microb.), homogeneous (homog.) or sham irradiation with a mean dose of 2 Gy. (a) DNA double-strand breaks were stained using green fluorescent dye. (b) Blue fluorescent DAPI stains cell nuclei. (c) Combined fluorescence images from γ-H2AX and DAPI staining to verify the position of the γ-H2AX marker with respect to the cell nuclei. Equal acquisition, contrast, and scaling settings were applied for γ-H2AX and DAPI images, respectively.*

nuclei distribution between the different samples. Slight differences in sharpness can be due to the mounting process of the Mylar foil with the cover slide. The microbeam irradiated sample shows a dense cell distribution that enables easier visualization of the grating structure. Even though the distribution of the cells is more even in the homogeneous case compared to the sham, the increased brightness seen in the γ-H2AX channel for homogeneous irradiation is not related to a denser cell distribution. The combined image in Fig. 5.22(c) supports this observation. In conclusion, the visualization of DNA double-strand breaks via the γ-H2AX assay demonstrates that the applied microbeam pattern is well reflected by the distribution of cellular damage. Hence, a quite steep dose falloff at the microbeam edges can be expected. Consequently, with this setup at the MuCLS, a sparing effect of tissue by dose redistribution from homogeneous to microbeam irradiation might be possible.

5.3.3.b. Colony forming assay

Methods. Cell survival was determined in CHO-K1 cells, i.e. normal tissue cells, following microbeam and homogeneous beam irradiation with mean doses ranging from 1.4 to 3.7 Gy. The CHO-K1 cell line has shown high robustness in previous experiments, which is important because transportation and environmental changes might cause stress and could lead to reduced adhesion or even cell death. A colony-forming assay was conducted following the protocol described in chapter 3.1.3 in three independent experiments. To relate the number of colonies grown from irradiated cells to the plating efficiency (PE) of non-irradiated samples, sham irradiations were performed additionally. Thus, the survival fraction and the relative biological effectiveness (RBE) with respect to the microbeam dose (cf. Eq. (2.11)) can be calculated. For each of the three experiments (I, II, and III), a low dose ($< 2\,\mathrm{Gy}$), and a high dose ($> 2\,\mathrm{Gy}$) were delivered, which resulted in six data points composed of 3 to 5 replicates each to assess reproducibility and inter-test variability.

Results. Fig. 5.23 shows the survival fraction for both geometries (microbeam: cyan diamonds, homogeneous: blue circles), as well as sham irradiated controls (magenta triangles) for different mean absorbed doses. A linear-quadratic model

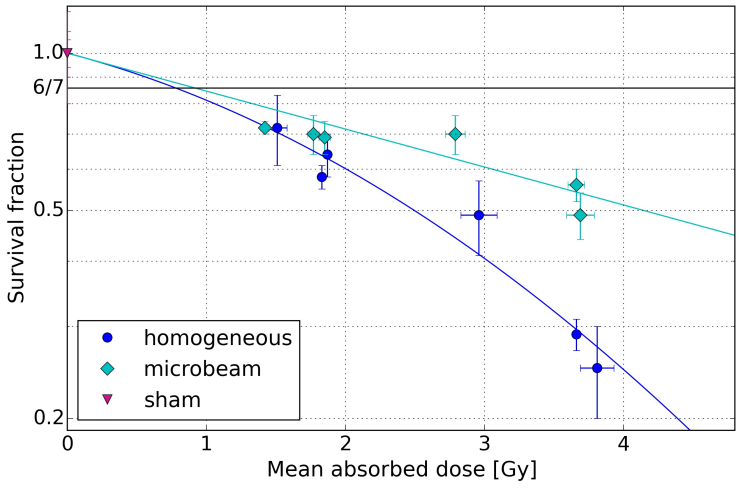

Figure 5.23.: *Dose-dependent survival fraction of CHO-K1 cells. Survival fraction (± SEM) of CHO-K1 cells plotted logarithmically with respect to the mean absorbed dose (± SD) determined by three independent clonogenic cell assays including three different doses each (0 Gy, < 2 Gy, > 2 Gy). Sham irradiated cells are marked with magenta triangles, homogeneously irradiated cells with blue circles and microbeam treated cells by cyan diamonds. A linear-quadratic model was fitted to the survival data (blue and cyan solid lines) to estimate the relative biological effectiveness. The potential saturation of the survival fraction for microbeam irradiation was estimated by the geometry of the tungsten slit array with* 6/7 *(solid black line).*

(LQM) was fitted to the survival data (blue and cyan solid lines). Moreover, a

black solid line marks the survival fraction of 6/7, which would be reached under the assumption of an idealized microbeam application that results in 0% survival in the peak (1/7 of grating period) and 100% survival in the valley (6/7 of grating period). The uncertainty on the survival data is given as standard error of the mean (SEM). Dose values in Fig. 5.23 include statistical errors, represented as standard deviation (SD) (details on error calculation are given in chapter 3.2.4). Fitting the data from homogeneous irradiations to the LQM results in the following sensitivity coefficients: $\alpha = 0.160 \pm 0.044$ Gy^{-1} and $\beta = 0.047 \pm 0.015$ Gy^{-2}. As the survival of microbeam data does not show a quadratic dependence on the dose, only a linear coefficient $\alpha = 0.167 \pm 0.066$ Gy^{-1} was determined in this case.
While the survival fractions at lower mean absorbed doses are quite similar for both microbeam and homogeneously irradiated cells, the curves diverge towards higher mean doses. From 72% survival at 1.4 Gy for both irradiation geometries, the survival fraction following MRT decreases to about 50% at 3.7 Gy in contrast to the corresponding survival rate of homogeneous cells of below 30%. From this study, the difference in cell survival between the two irradiation geometries becomes significant for mean doses above 1.9 Gy with a p-value < 0.05, determined by a two-tailed t-test for two independent means (p-value ranging from 0.01598 to 0.00007, based on [122]). Fitting an LQM to the survival fractions suggests an even earlier divergence of the resulting dose effect curves at ∼0.5 Gy. The RBE reflects this behavior as it decreases with increasing dose (cf. Table 5.2).

Table 5.2.: Clonogenic cell survival – RBE values. *Relative biological effectiveness (RBE) for equivalent cell survival of microbeam to homogeneous irradiations based on fitted data.*

Exp. no.	Microb. dose [Gy]	$\mathrm{RBE}_{\mathrm{survival}}$ (± SEM)
I	1.4	0.79 ± 0.17
I	2.8	0.67 ± 0.11
II	1.8	0.75 ± 0.14
II	3.7	0.62 ± 0.10
III	1.9	0.74 ± 0.14
III	3.7	0.62 ± 0.10

Discussion. The survival fractions measured with CHO-K1 cells prove that at least above a certain mean dose, less cells are lethally damaged after MRT irradiation than following homogeneous irradiation. This difference becomes significant above ∼2 Gy. Assuming a lethal peak dose and no valley dose in the ideal geometry of the tungsten slit array, the non-irradiated area of $6/7 \approx 85.7\%$ should determine the minimum survival of the microbeam irradiated cells. However, the highest mean dose of 3.7 Gy given in this experiment led to a survival fraction lower than 60%. This discrepancy has several reasons: generally, the limit of 6/7 represents only a rough estimate of the survival fraction and disregards a variety

of effects on the dose distribution. Geometrical effects such as penumbral blurring (<100 nm) and tungsten-slit-array imperfections deteriorate the sharpness of the microbeam edges. The taper at the tungsten edges can reach up to 20 µm, which causes an increase of the number of irradiated cells. Especially close to the slit, the X-ray absorption by the remaining tungsten layer is small such that cells at this position might receive a lethal dose. Furthermore, radiation damage in the valley zone is introduced by X-ray interactions with matter occurring primarily in the peak area. These interactions include, for example, scattering at tungsten edges. At 25 keV, the range of secondary electrons reaches 13 µm in water (water used here as approximation for the cell composition), which possibly increases the valley dose close to the peak. Due to the dominance of the photoelectric effect in this energy range, which comes along with isotropic scattering, a higher dose is contributed to the valley at a larger distance to the microbeam than in the case of forward-directed Compton scattering relevant at higher energies of about 100 keV, for example (cf. [168]). Additionally, bystander effects play a role, in particular in the transition zone from peak to valley [26–28]. While these arguments hold true in close vicinity to the microbeam, it is important to emphasize that the microbeam pattern could be observed with a clear distinction of peak and valley using the γ-H2AX assay. Unfortunately, a measurement of the PVDR was not possible in this configuration due to setup-related limitations. However, estimations allow to conclude on a PVDR value above 200. Compared to MRT experiments at large synchrotron facilities like the ESRF, where the PVDR is reduced due to the large energy spectrum with considerably higher energies and consequently, a longer penetration depth of secondary electrons (cf. Fig. 2.7 (b), chapter 2.1.2), the PVDR at the MuCLS is quite high.

Despite the blurring effects mentioned above, the survival fraction of cells irradiated with microbeams is significantly higher above 2 Gy mean dose than if the dose is distributed homogeneously. Therefore, a sparing effect following MRT at the MuCLS can be confirmed. In other words, using the same mean dose as in conventional radiotherapy, less damage in normal tissue, e.g. skin tissue, might be caused.

As mentioned in the introduction, only few publications report on clonogenic cell survival after MRT such that it is difficult to compare the observed sparing effect to existing literature. Ibahim *et al.* [88] performed clonogenic cell assays after microbeam irradiation with ∼100 keV X-rays using several cell lines and calculated the biologically equivalent dose for the homogeneous case. Microbeams are created by a collimator of 7/8 of absorbing structure. With a PVDR of 75, the given MRT peak dose of 50 Gy corresponds to 6.8 Gy mean absorbed dose. The authors state that this 6.8 Gy mean MRT dose leads to the same survival fraction as homogeneously delivered mean doses of 2.9, 3.1, or 3.2 Gy for three different cell lines. The fitted RBE of the here-presented data in this dose range (cf. Table 5.2), yields an equivalent mean MRT dose of 5.2 to 5.9 Gy instead of the reported 6.8 Gy. In view of the different energy settings, MRT pattern, and inter-cell-line variations, this comparison is not straightforward. Despite these differences, the deviation of

the here-shown measurement to the previously reported value can be considered quite small. Thus, it allows to conclude that using the MuCLS, a similar sparing effect can be achieved as with higher energies at large-scale synchrotron facilities (∼100 keV). For low-energy irradiation of superficial tumors, exploiting the sparing effect of MRT for faster skin repair could be of high interest. In order to verify the benefits of this increased cell survival observed in-vitro, further in-vivo studies are necessary.

5.3.3.c. Chromosome aberration test

Methods. To analyze radiation-induced chromosome aberrations, dicentrics and centric rings were studied in A_L cells following homogeneous, microbeam, and sham irradiation in three individual experiments (I, II, and III). Three replicates were analyzed at each irradiation condition. A mean dose of 1 and 2 Gy was applied in the first experiment, 1 Gy in the second experiment and 1.8 Gy in the third experiment. Thus, reproducibility of the results can be verified and, with the additional sham irradiations, statistical quality for the background aberrations is improved. On average, 390 metaphase cells were scored per exposure condition for every experiment, limited by the irradiation field. Among these cells, about 570 cells were scored for sham irradiation in each experiment, while a lower number of approximately 320 X-ray irradiated cells were evaluated, which is associated with the reduced cell survival after X-ray irradiation.
Additionally, the intercellular distribution of dicentrics and centric rings for each experiment and irradiation setting was recorded. To evaluate if the dicentric or centric ring yields follow a Poisson distribution, the dispersion ratio σ^2/μ was evaluated, with the standard error σ and the mean number of chromosome aberrations per cell μ (see Table 5.3) [114]. Its significance is stated by the u-value that is, for a null-hypothesis, standard normal distributed. For a 95% confidence interval, the standard deviation of the unit u-value is ± 1.96.

Results. Considering Table 5.3, the dispersion ratio for dicentrics is close to 1 in most cases. Exceptionally, in the case of 1 Gy microbeam irradiation in experiment I, only two dicentrics were found in two of all scored cells (294), which causes an outlier with a dispersion ratio of 2 and an u-value of 13.79. Otherwise, the u-value of microbeam data ranges from -0.44 to -0.26, which suggests a trend towards underdispersion. In contrast, the u-value of the homogeneous data from -1.0 to 3.0 covers a larger interval slightly shifted towards overdispersion. Similarly, for the induction of centric rings, the data follows a Poisson distribution with a slight underdispersion represented by a u-value of the microbeam data between -0.12 and -0.32. In contrast, the u-value of the homogeneous data ranges from -0.48 to 2.27 with a trend towards overdispersion.
The amount of dicentrics (dic) and centric rings (cr) per cell in dependence of the mean absorbed dose is shown in Fig. 5.24, together with the respective least-square fits using a linear-quadratic regression model. As above, microbeam data are

Table 5.3.: Detailed data on chromosome aberrations. *Frequency of dicentrics or centric rings per analyzed cell and their intercellular distribution in A_L cells after homogeneous and microbeam irradiation with 25 keV. X-rays in three experiments (Exp. I, II, III). Three replicates were performed with each irradiation condition.*

Exp.	X-ray dose [Gy]	Radiation	Cells scored	Dicentrics per cell ± SEM	Intercellular distribution of dicentrics						Centric rings per cell ± SEM	Intercellular distribution of centric rings				
					0	1	2	3	σ^2/μ	u-value		0	1	2	σ^2/μ	u-value
Ext. data*	0.0	backgr. freq.	3000	0.0007	2998	2	-	-	1.0	-0.02	0	-	-	-	-	-
I	0.0	sham	540	0	540	-	-	-	-	-	0	-	-	-	-	-
	1.0	homog.	337	0.059 ± 0.014	318	18	1	-	1.25	0.54	0.047 ± 0.012	322	14	1	1.08	1.04
		microb.	294	0.014 ± 0.010	292	-	2	-	1.99	13.79	0.007 ± 0.005	292	2	-	0.99	-0.12
	2.0	homog.	340	0.124 ± 0.018	299	40	1	-	0.92	-1	0.097 ± 0.017	308	31	1	0.96	-0.48
		microb.	281	0.021 ± 0.009	275	6	-	-	0.98	-0.28	0.011 ± 0.006	278	3	-	0.99	-0.15
II	0.0	sham	603	0	603	-	-	-	-	-	0	-	-	-	-	-
	1.0	homog.	332	0.093 ± 0.019	305	24	2	1	1.23	3	0.054 ± 0.014	316	14	2	1.17	2.22
		microb.	428	0.016 ± 0.006	421	7	-	-	0.98	-0.26	0.007 ± 0.004	425	3	-	0.99	-0.13
III	0.0	sham	559	0	559	-	-	-	-	-	0	-	-	-	-	-
	1.8	homog.	278	0.144 ± 0.024	242	33	2	1	1.11	1.26	0.086 ± 0.018	255	22	1	1	-0.04
		microb.	284	0.035 ± 0.011	274	10	-	-	0.96	-0.44	0.025 ± 0.009	277	7	-	0.98	-0.32

*External data on background frequency (non-irradiated A_L cells) from [118].
Note: σ^2/μ, dispersion ratio; u-value, test quantity (cf. [114]).
Abbreviations: backgr. freq.: background frequency, homog.: homogeneous, microb.: microbeam.

shown with cyan diamonds, homogeneous data with blue circles and non-irradiated data with red triangles. Solid symbols correspond to dicentrics, whereas open symbols represent centric rings. The uncertainty on the frequency of chromosome aberrations is given as standard error of the mean (SEM).
From Fig. 5.24, it becomes evident that the percentage of dicentrics and centric rings per cell increases similarly with the dose. For sham irradiation data, despite the different treatment times, no dicentrics were observed, yielding an SEM of zero. The background frequency of dicentrics reported in the literature [118] is with 2 individual dicentrics in 3000 cells also similarly low (cf. Table 5.3).
Higher cytogenetic damage is observed following homogeneous irradiation than after microbeam irradiation applying the same mean dose. From fitting an LQM to the data, the amount of chromosome aberrations along the studied dose range can be estimated. Following [111], chromosome aberration tests consider typically doses, which range from 0.25 to 5 Gy with a maximum energy of several hundred keV. Here, due to the application of rather high doses ranging from 1 to 2 Gy at low keV energies, the quadratic relation of the fit model described by β becomes negligible. The respective fit of homogeneous irradiation data yielded a linear coefficient α_{dic} in the dicentrics case of $0.072 \pm 0.008\,\mathrm{Gy}^{-1}$ and for centric rings, α_{cr} approximated $0.049 \pm 0.002\,\mathrm{Gy}^{-1}$. Microbeam data were fitted with $\alpha_{\mathrm{dic}} = 0.015 \pm 0.003\,\mathrm{Gy}^{-1}$ and $\alpha_{\mathrm{cr}} = 0.008 \pm 0.002\,\mathrm{Gy}^{-1}$. For both aberration types, dicentrics and centric rings per cell, the RBE was determined based on the fitted data. Already

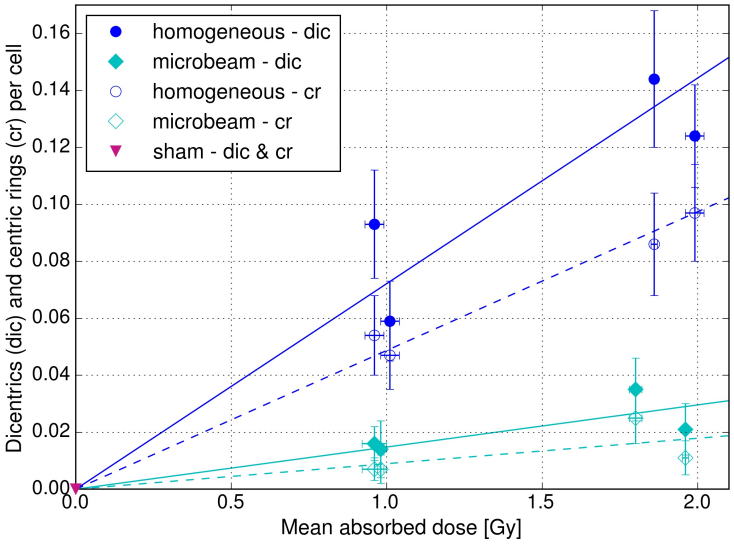

Figure 5.24.: *Dose-dependent chromosome aberrations in A_L cells. Dicentrics (dic) and centric rings (cr) per cell (± SEM) from three individual experiments for mean doses of 0, 1, 1.8, and 2 Gy. Homogeneous irradiation results are shown with blue circles, microbeam irradiation data with cyan diamonds and non-irradiated sham data with magenta triangles. A linear-quadratic model was fitted to the data (blue and cyan, solid and dashed lines). Solid symbols refer to dicentrics, open symbols to centric rings.*

at 1 Gy mean dose, microbeam irradiation leads to a distinctly lower amount of dicentrics and centric rings per cell compared to homogeneous irradiation. For both, 1 and 2 Gy, the difference in cytogenetic damage is significant according to a two-tailed t-test for two independent means. For dicentrics, the same mean $\mathrm{RBE}_{\mathrm{dic}}$ of 0.18 was estimated at 1 and ∼2 Gy absorbed dose (cf. Table 5.4). Equally, the mean $\mathrm{RBE}_{\mathrm{cr}}$ from centric ring data accounts to 0.18 at 1 Gy and ∼2 Gy. The RBE values are given ± SEM, determined by the errors of the fit parameters.

Table 5.4.: Chromosome aberrations – RBE values. *Relative biological effectiveness (RBE) for equivalent dose effect (number of dicentrics (dic) or centric rings (cr) per cell) of microbeam to homogeneous irradiations based on fitted data.*

Exp.no.	Microb. dose [Gy]	$\mathrm{RBE}_{\mathrm{dic}}$ (± SEM)	$\mathrm{RBE}_{\mathrm{cr}}$ (± SEM)
I	1.0	0.18 ± 0.01	0.18 ± 0.02
I	2.0	0.18 ± 0.01	0.18 ± 0.03
II	1.0	0.18 ± 0.01	0.18 ± 0.02
III	1.8	0.18 ± 0.01	0.18 ± 0.01

To place the results on dicentrics in context with commonly acquired data, the dicentric yield of a 200 kVp X-ray reference curve (homogeneous irradiation) is added in Fig. 5.25, obtained from [169], and from private communication [170]. An LQM was fitted to the reference data acquired at mean doses of 0, 0.5, 1, 2, 4,

and 8 Gy. The orange filled background corresponds to the SEM of the reference curve. The data from MuCLS experiments are given as above. The linear fit of these data points is not based on measured data at doses above 2 Gy and does not allow for data extrapolation. Especially after homogeneous 25 keV irradiation, cell death might occur in this dose range. Yet, for comparison, the higher dose range of the reference curve is of interest such that the fitted data is shown for both cases, 25 keV and 200 kVp irradiation.

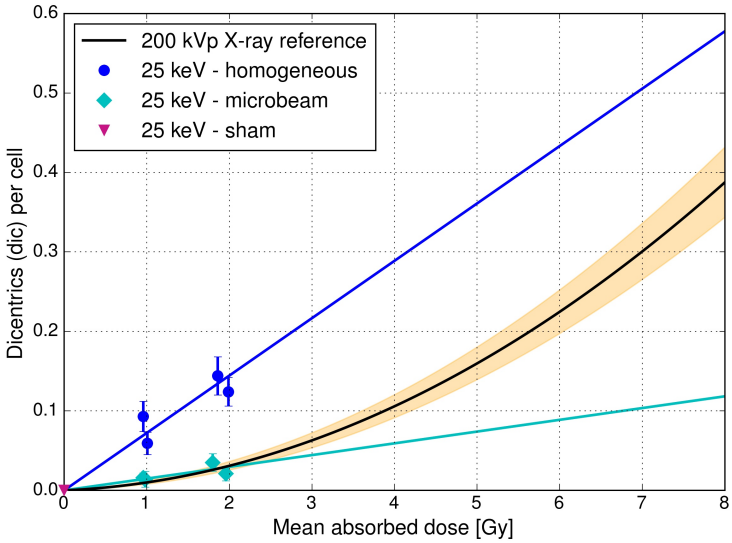

Figure 5.25.: *Dicentric yields (± SEM) in dependence of the dose in A_L cells. Reference data from a 200 kVp irradiation with doses between 0 and 8 Gy are shown together with the data on dicentrics already presented in Fig. 5.24. A linear-quadratic model is fitted to the reference data, which results in the black curve surrounded by an orange filled area for the SEM. Colors and markers for the MuCLS irradiation are used as above (homogeneous: blue circles, microbeam: cyan diamonds, sham: magenta triangles). A linear-quadratic model was fitted to the data (blue and cyan lines). The extrapolation of the MuCLS data towards 8 Gy is not based on measured data in contrast to the reference data.*

The reference curve applying 200 kVp X-rays shows a lower amount of dicentrics per cell than the data from homogeneous irradiation with 25 keV as the linear energy transfer is higher at lower energies (shown, for example, in [171]). At doses above 5 Gy, the reference curve rises almost linearly. With 200 kVp compared to 25 keV, higher doses are necessary to achieve the same cytogenetic damage. Hence, the dicentric yield measured between 1 and 2 Gy at 25 keV seems to follow the linear behavior of the high dose range of the reference curve.

Additionally to the commonly analyzed dicentrics per cell, acentric fragments were investigated. However, less emphasis has been placed on the dose effect relationship for acentric fragments as, e.g. in human cells, these chromosome aberrations are more frequent in background materials due to non-radiological insults such

as mutagenic chemicals. Consequently, their relation to radiation dosimetry is limited. Similarly to dicentrics and centric rings, a lower amount of acentric fragments was observed in MRT irradiated cells. Their number also increases with the absorbed dose but significantly less than after homogeneous irradiation.

Including all three aberration types (dicentrics, centric rings and acentric fragments) as well as excess fragments, the percentage of cells which showed any structural damage was recorded. Only 0.2% of sham irradiated cells in each of the experiments I and III, as well as 0% in experiment II presented such damages. Homogeneous irradiation with 1 Gy led to 24.1% of structurally damaged cells in experiment I and 26.2% in II, in contrast to 6.6% and 6.1% for microbeam irradiated cells. Following 2 Gy and 1.8 Gy irradiation (exp. II and III, respectively), homogeneous treatment caused 39.7% and 39.9% structural damage in the cells while due to the microbeam geometry the damage is reduced to 6.7% and 15.5%, respectively.

Discussion. 5-fold higher cytogenetic damage was observed using a conventional homogeneous beam geometry compared to MRT. The data from all three experiments demonstrate good reproducibility within the standard errors. With chromosome aberrations like dicentrics or centric rings, lethal damages were determined. In parallel, non-lethal aberrations, like translocations, occur that are more difficult to measure directly. The here-presented approach allows to conclude indirectly on the relative amount of non-lethal radiation-induced cytogenetic damage that might cause second cancer development. Moreover, it has been demonstrated that inactivated dicentrics can lead to DNA damage and genomic instability [117]. Already at the lower dose of 1 Gy, MRT irradiated cells rarely showed dicentrics or centric rings compared to an 8-fold higher number after homogeneous irradiation. These two different chromosome aberrations led to almost equivalent RBE values, which highlights their correlation. The yield of acentric fragments agrees well with the observations for dicentrics and centric rings, which is further confirmed by the number of cells with structural damage. From 1 to 2 Gy, the amount of cytogenetic damage in MRT irradiated cells stayed at a very low level in contrast to the much higher number of aberrations after homogeneous irradiation. Despite the high dose in the microbeam, the intercellular distribution of dicentrics or centric rings per cell did not change remarkably in contrast to observations made with other radiation qualities [49]. Moreover, the overall dispersion rate is even reduced, which indicates less severe cytogenetic damage compared to homogeneous data. Hence, these results suggest a lower second cancer risk following MRT irradiation than after homogeneous treatment. In conclusion, this study showed that cytogenetic damage is reduced significantly using microbeams. This might be due to the lethal peak dose such that only at the microbeam edge, cells damaged by X-ray irradiation can survive, which leads to a lower overall risk of chromosome aberrations.

5.3.4. Conclusion of the in-vitro study at the MuCLS

Microbeam irradiations of normal tissue cells could be successfully performed at the MuCLS. The source could be operated with relatively high stability in terms of photon flux yielding reproducible results. To apply the desired dose, online dosimetry was established using a photon-counting detector yielding an error in absolute dose of about 10%. Due to larger discrepancies to film and ionization chamber dosimetry, absolute dosimetry requires further investigation. Deviations of the relative dose could be minimized to a few percent to guarantee the same mean dose for each replicate.
The in-vitro results shown for microbeam and homogeneous irradiations strongly suggest that their radiobiological effect differs also using the low energy of about 25 keV produced by a compact synchrotron X-ray source. For MRT irradiations, a slower decrease of cell survival for doses from 1 to 4 Gy, which results in a decreasing RBE value with dose, suggests a tissue sparing effect. Hence, even if the peak doses are low compared to several hundreds of Gray delivered in MRT studies at large synchrotron facilities, the sparing effect of MRT seems to hold true. Moreover, the chromosome aberration test demonstrates that, at the same mean absorbed dose, cytogenetic damage after microbeam irradiation is significantly reduced compared to conventional, homogeneous irradiation. This beneficial effect, confirmed by a low RBE value, possibly correlates with a lower risk of second cancer development. Following these promising results in-vitro, studies in-vivo are necessary including tumorous tissue with vascular structures to prove if higher tumor control can be achieved while sparing normal tissue after MRT at the MuCLS. Accordingly, first experiments are presented in the next subchapter.

5.4. In-vivo study of tumor-bearing mice at the MuCLS

This subchapter contains first results from in-vivo microbeam experiments at the MuCLS. For this purpose, a dedicated microbeam irradiation setup was developed and characterized to treat tumor-bearing mice in-vivo at this prototype machine. Subsequently, the first experimental results of a tumor growth delay study and the establishment of protocols for histological analysis are shown. First, the study design is described and a commented protocol of the mouse treatment is given in sections 5.4.1 and 5.4.2, respectively. In the next two sections, the individual setup components are explained, including the performance analysis of an X-ray focusing device, a polycapillary optic, serving to increase the dose rate at the MuCLS (section 5.4.3) and the mouse irradiation setup in the experimental hutch (cf. section 5.4.4). Thereafter, in section 5.4.5, the realization of online dosimetry is presented with respect to changes to the previously described online dosimetry for cell irradiations (subchapter 5.3.2). In section 5.4.6, experimental results on tumor growth delay are investigated. Lastly, methods for analysis of the irradiated tumors in 2D by microscopy of histological slices and in 3D by X-ray imaging of stained tumor volumes are introduced in sections 5.4.7 and 5.4.8, respectively.

5.4.1. Study design

To macroscopically study the radiation effect in-vivo, tumor growth of irradiated and non-irradiated xenografts in the mouse ear was measured with about 30 days follow-up. Growth delay of irradiated tumors is analyzed with respect to sham irradiated or control tumors. In line with the in-vitro study at the MuCLS described in the previous section, the 25 keV configuration of the MuCLS was chosen.
An in-vivo model offers the advantage that the previously highlighted effect of MRT on the vascular system becomes observable. The choice of tumor growth in a mouse ear has several key advantages:

- tumors can be detected at an early stage to match the desired size for irradiation,
- due to the transparency of the mouse ear, the tumor can be accurately positioned in the X-ray beam,
- the extremal location of the ear allows to spare other body parts from radiation,
- the tumor volume can be easily measured in three dimensions with a caliper.

In Fig. 5.26, a schematic drawing shows an overview of the study design, which represents the broad outline of this subchapter. Thickness of the connection lines refers to the approximate percentage of mice contributing to each part of the study. Following tumor cell injection, xenografts develop in the mouse ear (marked in orange, cf. 5.4.2), which are exposed to sham, homogeneous, or microbeam irradiation (marked in green, cf. 5.4.4 & 5.4.5). Subsequently, three scenarios are

possible. To analyze tumor growth delay induced by radiation, tumors are measured with a follow-up of about 30 days after irradiation (marked in dark blue, cf. 5.4.6). Subsequently, the tumor is resected. Transferring tumor cells of the irradiated entity into culture allows to measure clonogenic cell survival, and to visualize complex interchromosomal rearrangements via fluorescence in-situ hybridization (FISH), for example [172] (carried out in related projects, and thus not part of this thesis). Moreover, histological analysis of the tumors shall be performed (cf. 5.4.7). Marking apoptosis, proliferation, hypoxia, and angiogenesis can help to understand differences in tumor growth delay. To analyze proliferation and apoptosis, tumors are harvested 24 hours after irradiation (marked in mid-blue). An additional γ-H2AX assay yields visualization of the radiation-induced DNA double-strand breaks to verify position and effect of the damage. For this purpose, the tumor has to be resected 1 hour after irradiation (marked in light blue). Additional to conventional staining, computed tomography (CT) of X-ray stained tumors was applied to analyze the vascular system in three dimensions (cf. 5.4.8). To realize the analysis of resected tumor volumes, existing staining protocols were adapted to our study.

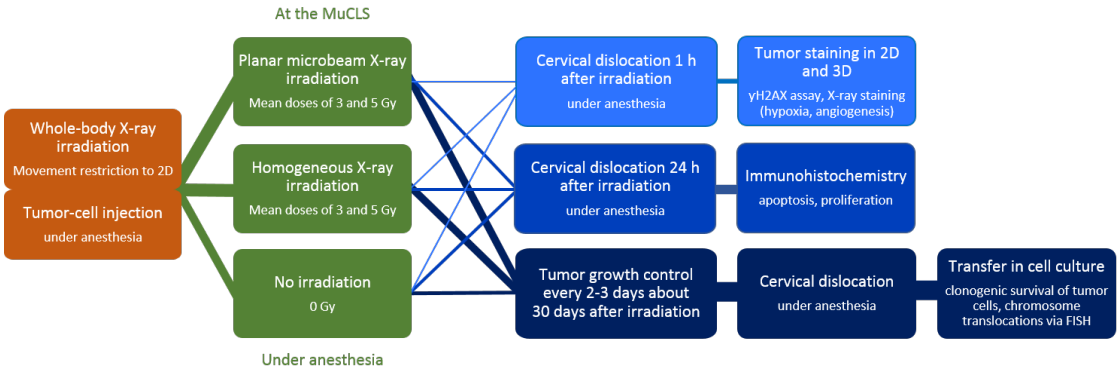

Figure 5.26.: *Schematic drawing of the MRT study designed for tumor irradiation in the mouse ear at the MuCLS. The thickness of the connecting lines represents the approximated percentage of mice required for each experimental section.*

The in-vivo experiments reported in this thesis are complying with ethical regulations and are based on the application entitled "Untersuchung des Tumorwachstums nach Mikrokanalbestrahlung im Vergleich zu konventioneller homogener Bestrahlung mit brillanter Röntgenstrahlung am weltweit ersten kompakten Synchrotron für den Einsatz in der Radioonkologie" approved by the ethics committee of the government of Upper Bavaria (reference number 55.2.1.54-2532-62-2016, non-technical summary NTP-ID: 00009166-1-7). This project is an interdisciplinary work between physics, biology, and medicine involving, amongst others, the work of Annique C. Hunger (Ph.D. student in radiation biology), and Ann-Kristin Porth (Ph.D. student in medicine) supervised by PD Dr. Thomas E. Schmid. The project was carried out in the group Advanced Technologies in Ra-

diation Therapy[14] and at the Chair of Biomedical Physics[15]. Therefore, e.g. the protocols for re-culturing of tumor cells, and the staining procedure on histological slices are not contained in this thesis. Note that this project is on-going such that not all experiments mentioned in the study design have been performed yet.

5.4.2. Commented protocol

In this section, details on the execution of the study with focus on animal preparation and handling are given, which was developed in cooperation with Annique C. Hunger. Technical realization with respect to setup and dosimetry is further described in sections 5.4.4, and 5.4.5.
Tumors were grown as xenografts in mouse ears from the undifferentiated human squamous cell carcinoma FaDu cell line [173] in immunodeficient NMRI (nu/nu) mice (Charles River Laboratories[16]), adapting a protocol described in [174, 175]. The 8 to 10 week old mice accustomed for about one week prior to the experiment to the animal keeping facility at the Klinikum rechts der Isar. The mice were held according to the EU guideline 2010/63 (for further specifications, please refer to the ethics application referenced above).
First, suppression of the immune system was achieved by whole-body irradiation of the mice. Thus, a rejection of the tumor cells can be minimized. The mice were confined in a specifically designed cage to restrict movement to two dimensions for dosimetric reasons and irradiated with 4 Gy in 4 min 12 s at 200 kVp and 15 mA at a table-to-source distance of 500 mm (Irradiator: RS225[17]). Absolute dosimetry was performed previously by Prof. Jan J. Wilkens[14] with a calibrated ionization chamber[18].
As a next step, possible inflammations, e.g. due to needle injection, were prevented by subcutaneous (s.c.) injection of antibiotics (Convenia[19] in a concentration of 20 µl per 20 g body weight) diluted 27:73 in 0.9% sodium chloride (NaCl) solution into the nuchal fold. To follow the expected weight loss after whole-body irradiation, the mice had to be marked and weighed at this stage. Distinction of the mice was achieved by ear perforation at the left ear ridge. The same perforation pattern was used for the individually numbered cages. If perforation could be postponed to the day of tumor cell injection for pain minimization, the tails were colored with one to five rings using permanent markers. Due to preening, these marks needed up to daily refreshing.
Two to four days following irradiation, tumor cells were injected into the right mouse ear. Therefore, a solution of 100 000 FaDu cells (determined with a Neubauer counting chamber) per 50 µl Matrigel (#356237, Corning Matrigel Base-

[14]Department of Radiation Oncology, Klinikum rechts der Isar, TUM, Munich, Germany
[15]Physics Department, TUM, Garching, Germany
[16]Charles River Laboratories, Sulzfeld, Germany
[17]*former* Gulmay Medical, *now* xstrahl, Surrey, UK
[18]PTW, Freiburg, Germany
[19]Zoetis Schweiz GmbH, Zürich, Switzerland

ment Membrane Matrix[20]) was prepared and stored on ice until injection. Matrigel improves binding of the tumor cells to the injection position at the outer ear in contrast to a phosphate buffered saline solution as proposed in [175] (resulting from private communication with Dr. Elke Beyreuther [176]). This is important as a locally confined tumor growth is required by the setup at the MuCLS. In a pilot study, the tissue reaction to and degradation of Matrigel was tested by additional injection of pure Matrigel into the left ear.
Before tumor cell injection, mice were anesthetized with MMF[21] i.p. (Medetomidin (0.50 mg/kg) + Midazolam (5.0 mg/kg) + Fentanyl (0.05 mg/kg), intraperitoneal). Eyes were covered with Bepanthen ointment[22] to avoid dehydration. The Matrigel-FaDu cell solution was re-mixed with a vortex mixer and about 5 µl were drawn into a microneedle. The ear was folded lengthwise with flat tweezers such that the solution could be injected parallel to the ear arteries with a small incidence angle below 30°(cf. Fig. 5.27). Due to the 200-300 µm thin ear [177], the injection be-

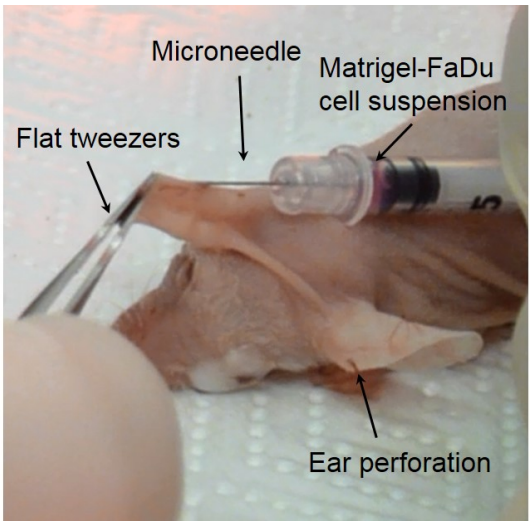

Figure 5.27.: *Tumor cell injection. A suspension of FaDu cells in Matrigel is injected into the right ear of an anesthetized NMRI (nu/nu) mouse with a microneedle.*

tween epidermal layer and the cartilage is challenging. If the injection volume did not reach 1-2 µl, or was not visible as a whitish, flat bubble below the skin, re-injection at a neighboring spot was performed. In general, 3 to 5 µl cell solution were injected in the right ear of each mouse. To avoid interpersonal variations, Marlon Stein (Technical Assistant[14]) performed the injections while a second person stretched the ear with the tweezers. As antagonist, AFN[21] (composed of atipamezole (2.5 mg/kg), flumazenil (0.5 mg/kg), and naloxone (1.2 mg/kg)) was injected s.c. in the nuchal fold according to the body weight.
To avoid clustering of irradiations at the MuCLS to a few days, the tumor cell

[20] Corning Inc., Tewksbury, MA, USA
[21] Zentrum für präklinische Forschung, Klinikum rechts der Isar, Munich, Germany
[22] Bayer Vital GmbH, Leverkusen, Germany

injection was phased by two days for each of the three groups of mice. The date of whole-body irradiation was adjusted accordingly.
Tumor growth was measured in three dimensions every two days starting from at least 0.5 mm in length. The tumor area is defined here as the plane parallel to the mouse ear with 'length' in the direction of the ear arteries and 'width' perpendicular to the arteries. The day of radiation therapy is determined by the tumor area. With the setup at the MuCLS, round-shaped or elongated tumors can be treated with the following beam sizes: a single circular field of 2.3 mm diameter or two fields stitched together to cover an ellipse of $1.5 \times 2.8 \times \pi\,\mathrm{mm}^2$. It is important to irradiate tumors with similar sizes but as well sufficient blood supply, i.e. vascularization. Therefore, only tumors that had turned reddish were irradiated.
The irradiation doses were chosen from a pilot study performed at the Klinikum rechts der Isar, where several tumors were irradiated with 3 or 6 Gy homogeneously (following [175]) with a 4 mm circular field using a Small Animal Radiation Research Platform (SARRP[23]) operated at 70 kVp, and 30 mA at a dose rate of 2.4 Gy/min. Two 6 Gy irradiated mice showed tumor control, but three 3 Gy irradiated mice had tumor growth behavior similar to a control group. Thus, two doses of 3 and 5 Gy seemed appropriate to remain in the window of visible effect and tumor control with sufficient distance between the two data points.
On the day of irradiation, mice bearing appropriate tumors were transported from the Klinikum rechts der Isar, TUM, Munich, Germany to the Munich School of BioEngineering, TUM, Garching, Germany. For X-ray irradiation, geometry (microbeam or homogeneous) and dose were selected randomly. The transported mice were randomly allocated to the determined irradiation setting. Before irradiation, the respective mouse was anesthetized on a sterile bench, and positioned in a pre-heated mouse holder made of aluminum. Eyes were covered with Bepanthen ointment as above. The tumor-bearing right ear was slightly stretched to center the tumor on an aperture below the mouse bed. The mouse bed itself is protected from radiation by an additional stainless steel plate. The ear was fixed with removable tape at the ridges sparing the tumor.
To avoid scattered radiation, a beam aperture of 3.4 mm diameter was placed on a motorized translation stage in front of the tumor and well-centered in the X-ray beam using a photon-counting Pilatus 200K detector[24]. To allow for microbeam production, the aperture, made of stainless steel has an inset for the tungsten slit array (characterized in section 5.2.3). As the tungsten plate is fragile, the entire aperture with tungsten grid is exchanged to an aperture without inset to switch between microbeam and homogeneous irradiation. The tumor was positioned accurately in the X-ray beam by three motorized linear stages with the help of visible light imaging using a CCD camera (for details, see section 5.4.4.d). Subsequently, a Gafchromic EBT3 film was placed behind the ear aperture to verify the irradiation position and the pattern geometry post-irradiation. Successful production

[23] xstrahl, Surrey, UK
[24] Dectris, Baden-Dättwill, Switzerland

of X-rays was verified beforehand such that the irradiation was started by simply opening a fast shutter. Simultaneously, the recording of X-ray intensity was triggered. As a next step, the computation of the irradiation time necessary to achieve the desired dose was activated, which was updated every second. During irradiation, the mouse was monitored via a webcam installed at the ceiling of the experimental hutch. The electron beam of the MuCLS was shut off automatically by the script as soon as the required dose was reached. Subsequently, the irradiated film was labelled and stored together with a reference film before readout. The mouse was removed from the holder, and woken up with a weight-dependent fraction of AFN.
After recovery, the mouse was transported back to a quarantine area at the Klinikum rechts der Isar, where tumor growth was measured with a caliper up to 30 days after irradiation. Well-being and behavior of the mice were controlled according to the scoring guidelines of the ethics application. The end tumor volume for data comparison was previously determined to be 15 times the volume measured on the day of irradiation (further details on volume determination are given in section 5.4.6.a). Considering this information and the stop criteria (reaching a tumor diameter of 8 mm or suffering of the mouse), mice might not be observed as long as 30 days post irradiation.
At the end of the tumor growth measurement, tumors were harvested and transferred into cell culture to investigate cytogenetic damage via chromosome aberrations and radioresistance by clonogenic cell survival following additional radiation exposure.

For γ-H2AX staining, the mouse was sacrificed about one hour after irradiation and the tumor was resected including the surrounding epidermal and cartilage structure. Subsequently, it was fixated in formalin before a standardized paraffin-embedding and staining procedure was applied by the pathology of the Klinikum rechts der Isar followed by histological sectioning and microscopic imaging.

To develop 3D X-ray imaging of stained vascular structure in resected tumors, different tumor sizes were acquired from mice used in the pilot-study to establish the correct tumor cell injection or from mice which had to be excluded from further analysis due to e.g. insufficient tumor growth or poor health. The staining protocol and detailed acquisition parameters for X-ray imaging can be found in the respective section below.

5.4.3. Increasing the X-ray fluence via polycapillary optics

The mouse irradiation setup is positioned in the experimental hutch 1 (cf. Fig. 5.13 in section 5.3) at about 3.7 m from the source. At this position, the beam reaches an extension of almost 16 mm diameter in contrast to the 7 mm circular beam profile used for cell irradiation in the cave. Therefore, the dose rate is significantly lower. As the xenograft model in the mouse ear allows to treat tumor sizes of

a few mm in diameter, only a small beam area is required. Hence, an X-ray focusing system is useful to enhance the X-ray fluence and hereby the dose rate. Its characterization is presented in the following.

5.4.3.a. Prerequisites

Optimization of beam size and dose rate is required to ensure fast treatment with full tumor coverage. Therefore, the available beam size of 16 mm needs to be confined to the tumor size of a few mm with relatively low losses. Different optic devices allow to focus or collimate an X-ray beam. Yet, to account for the small but present energy bandwidth of the MuCLS spectra, and moreover, to make use of a single system for different energy configurations, purely monoenergetic optics are not applicable. Additionally, the device must accept the divergence angle of the cone of 4 mrad and offer an entrance diameter of 7 mm with a focus distance of 2 m and device length below 20 cm for installation in the cave, or an entrance diameter of 16 mm with a focus distance in the centimeter range. For tumor coverage, the focal spot should reach a diameter of about 2 to 3 mm. While bent mirrors like so-called *Kirkpatrick-Baez optics* or *Wolter optics* would fulfill most of these requirements, the infrastructure at the MuCLS does not allow the installation of such cost-intensive, large, and heavy devices.

Alternatively, *polycapillary optics* provide suitable characteristics despite of a possibly lower efficiency. They consist of up to millions of bundled glass capillaries divided into subunits of about 10 000 hollow fibers (each a few micrometer in diameter) with a bending radius that allows for multiple total external reflection of the transmitted X-rays [178]. Reflection at the boundary of the gas atmosphere in the capillary channel and glass wall occurs due to change (decrease) in refractive index. If the incident angle of X-rays is equal or smaller than the so-called *critical angle*, total external reflection is achieved. Following the approximations for borosilicate glass in [178], the critical angle accounts to 0.07° for 25 keV. The capillary channels need to be considerably smaller than their bending radius to maximize the number of X-rays that fulfills the criterion for total external reflection. With an output focal distance f_{out} of about 2 m, we can expect a focal spot size of about 5 mm. To image the beam at its source size of ∼50 µm, a focusing optic would require a focal distance of 16 mm. Hence, a collimation optic can be installed far from the experimental setup whereas a focusing optic has to be placed directly at the object under investigation.

The critical angle is inversely proportional to the X-ray energy. Therefore, at larger distances from the center, especially X-rays with higher energies yield lower transmission values than close to the polycapillary center. As a result, the efficiency of polycapillary optics increases towards lower energies. In the case of polychromatic X-rays, the initial spectrum might be altered by the optic.

5.4.3.b. Design

According to the above-mentioned requirements, polycapillary optics for beam collimation and focusing were developed by the Institute for Scientific Instruments GmbH[25]. In the following, beam collimation with slight focusing is considered as the resulting focal spot size is relevant for the irradiation study presented here. A schematic drawing of a collimation optic with the X-ray beam path is shown in Fig. 5.28. As optics with a relatively large entrance diameter of about 16 mm

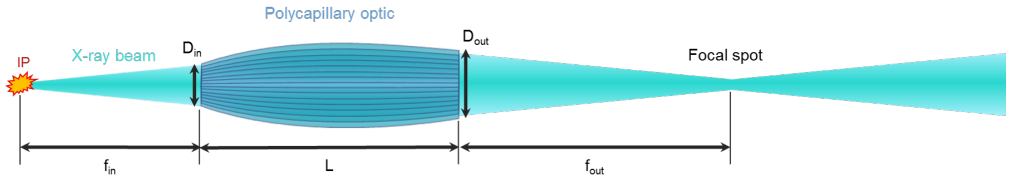

Figure 5.28.: *Schematic drawing of the polycapillary optic used for beam collimation (not to scale). f_{in} designates the source distance, D_{in} and D_{out}, the entrance and exit opening of the optic, and f_{out} the focus distance from the optic. X-rays travel through the capillaries by total external reflection and are deflected from their original path depending on the curvature at the exit. The central beam passes directly.*

are challenging to manufacture with necessary precision for high efficiency, the installation option in the cave of the MuCLS setup was preferred, requiring a smaller entrance diameter of about 7 mm to capture the full beam. The parameters of the collimating polycapillary optic are summarized in Table 5.5. The optic was

Table 5.5.: Parameters of the polycapillary optic used for the in-vivo experiments.

Parameter	Length [mm]
Estimated f_{in}	~1800
Estimated f_{out}	~2100
D_{in}	11.85
D_{out}	11.95
L	62.3
IP-focal spot=f_{in}+L+f_{out}	~4000

inserted at an input focal distance of f_{in}=1.8 m from the source in the cave of the MuCLS (cf. 5.13). The entrance diameter D_{in} with 11.85 mm allows to use the full X-ray beam of 7 mm diameter. The deflected X-rays exit through an opening of D_{out}=11.95 mm and are collimated to a focal spot size of a few millimeters at an output focal distance of approximately 2 m.

[25]IfG GmbH, Berlin, Germany

5.4.3.c. Characterization

The performance of this polycapillary optic was characterized with respect to focal spot, final energy spectrum, and efficiency. For alignment purposes, the optic was mounted on motorized linear stages for horizontal and vertical movement perpendicular to the beam axis. Moreover, motorized tilts in the same directions allowed to fine-tune the position of the optics in the beam. The focal spot was optimized by raster scanning with the four motors with decreasing step sizes.

First, the focal spot quality was determined regarding intensity and shape by direct imaging at the output focal distance using an Andor Zyla 5.5 sCMOS camera with a fiber-optically coupled scintillator ($6.5 \times 6.5\,\mu m^2$ pixel size) and by indirect imaging of the diffraction-like pattern at about 12.5 m distance to the focal spot with the Pilatus 200K photon-counting detector. To stay below the saturation limit of the sCMOS camera, the X-ray beam flux was reduced by a slight misalignment of electron bunch and laser collision. Images from both detectors for an optimized focal spot are shown in Figs. 5.29 (a) and (b). From the direct measurement, horizontal and vertical line profiles crossing the center of the focal spot (marked with blue and red lines, respectively, in Fig. 5.29 (a)) were processed (median filter with a kernel size of 15) and a Gaussian was fitted to the curves to estimate the FWHM of the focal spot (for fitting, the SciPy package was used [126]).

A quite homogeneous spot size is obtained using the polycapillary optic. Structures visible in the background in Fig. 5.29 (a) originate from inhomogeneities of the scintillator of the camera system. On a plane out of focus, in Fig. 5.29 (b), a ring-like structure is built when the optic is well aligned. The star-like pattern on the outer side is possibly caused by structures within the optic to stabilize the bundled capillaries. A slight deviation of the focal spot center compared to the original beam center was noticed, which might be due to the composition of the optical device. This allows to avoid the central beam that passes the optic without being deflected, which could otherwise deteriorate the homogeneity of the focal spot. While often, a central beam block needs to be installed, in the case of a deviated focal spot, a simple aperture in front of the experimental setup allows to remove this undesired contribution. The horizontal (blue) and vertical (red) line profiles in Fig. 5.29 (c) demonstrate a Gaussian-like intensity distribution in the focal spot, which was fitted accordingly. The FWHM in horizontal direction accounts to 2.5 mm, and is slightly enlarged in vertical direction to 2.7 mm. This ellipsoid shape is consistent with the raw beam profile of the MuCLS (cf. Fig. 5.19 in section 5.3.1). The slight blurring due to the median filter does not change the FWHM values significantly, but allows to suppress noise from the camera system. However, the point-spread function of the Zyla camera ($\sim$11.5 px, i.e. 75 µm, see [150]) can cause blurring of the pattern such that the actual FWHM of the focal spot is smaller. Therefore, a Richardson-Lucy deconvolution algorithm was applied to the data, resulting in a horizontal FWHM value of 2 mm and a vertical FWHM value of 2.3 mm. The irradiation field size was chosen accordingly to the

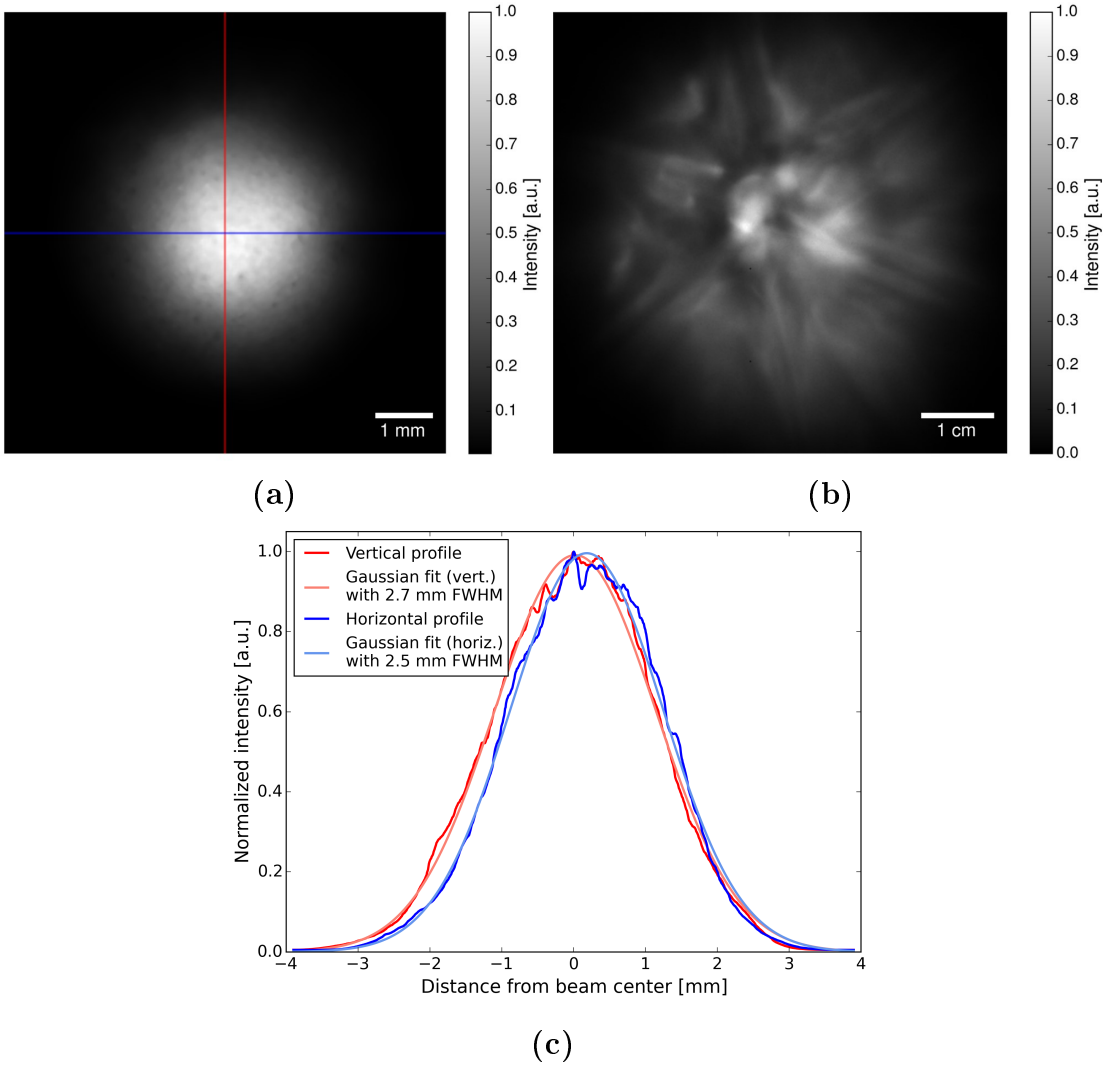

Figure 5.29.: *Focal spot imaged with (a) an sCMOS camera at f_{out}, and (b) a photon-counting detector at 12.5 m behind focal spot. (c) Line profiles taken from the center of the focal spot in (a) in horizontal (blue) and vertical (red) direction smoothed with a median filter of kernel size 15. A Gaussian fit was applied to both curves to estimate the full width at half maximum (FWHM) of the focal spot in each direction.*

FWHM, described in more detail in section 5.4.5.

Secondly, the efficiency of the polycapillary optic was measured. Following the estimated specifications of the optic, a collimation of the beam to 3 mm FWHM, and thus an irradiation area of $1.5^2\pi\,\mathrm{mm}^2$ should be possible. Due to the actually smaller FWHM values (stated above), an elliptic beam size of $2.3 \times 2 \times \pi\,\mathrm{mm}^2$ was chosen for the experiments. To analyze the optic's efficiency for the beam intensity within the FWHM compared to the total photon flux, efficiency values were computed for both irradiation geometries.
For this purpose, relative intensity values were recorded by the scintillation counter

with and without collimation optic in the beam. To be able to derive absolute flux values, the scintillation counter was calibrated to the photon-counting Pilatus detector for both geometries prior to the actual measurement.
To measure the photon flux with and without polycapillary optic, the device was moved in and out of the beam on a motorized stage. A series of 10 images with 1 s exposure time was taken at each position repeatedly. Only values with a low standard error of the mean within one series were processed. Moreover, if a decrease in X-ray flux was observed, the according series of intensity values was excluded from further analysis.
From this measurement, a transmission of 44% of the polycapillary optic was deduced. Using the collimation optics and considering a 3 mm round focal spot, 11-fold flux enhancement can be expected. Assuming the photons to be confined within an ellipse of $2.3 \times 2 \times \pi\,\mathrm{mm}^2$, the flux is enhanced by a factor of 22. The efficiency of the polycapillary optic could be raised by reducing the X-ray energy at the MuCLS. However, a lower energy for MRT would result in even shallower penetration of the X-rays, which is not desired. Moreover, the X-ray flux produced by inverse Compton scattering is reduced at lower energies, such that the current energy setting of 25 keV seems to be reasonable. In the long term, improvements of the polycapillary optic or a change of the focusing/collimating system might allow to further increase transmission and efficiency.

As the polycapillary optic might cause an energy shift of the spectrum due to its absorbance and energy-dependent efficiency, X-ray spectra were recorded following section 5.2.2 with and without polycapillary optic inserted in the beam. A 14 mm thick aluminum absorber was used instead of PMMA to avoid saturation of the energy-dispersive detector. Fig. 5.30 shows both spectra taken at the position of the mouse irradiation setup, corrected for aluminum absorption (Al absorption coefficient from [74]): in blue, the non-modified spectrum, in green the spectrum with collimation optic. The spectra are almost equivalent. At the lower energy tail, a slight energy shift towards lower energies is discernible for the spectrum with collimation optic in the beam. The polycapillary optic possibly influences the X-ray spectrum due to its energy-dependent efficiency, which is higher at 15 keV than at 25 keV. All in all, the marginal difference of the X-ray spectrum using the polycapillary optic leads only to minor changes of the calculated dose and is thus neglected for further processing.

5.4.3.d. Conclusion and outlook

In conclusion, successful beam collimation of 25 keV X-rays at the MuCLS could be demonstrated for the investigated polycapillary optic. While the focal spot can be found via mesh scanning, optimization of the focal spot size and shape requires further automation for fast and reproducible alignment. The beam shape of the focal spot is Gaussian-like as expected. When a perfectly flat beam is desired, different X-ray beam collimation systems might be of interest. Alternatively, if the

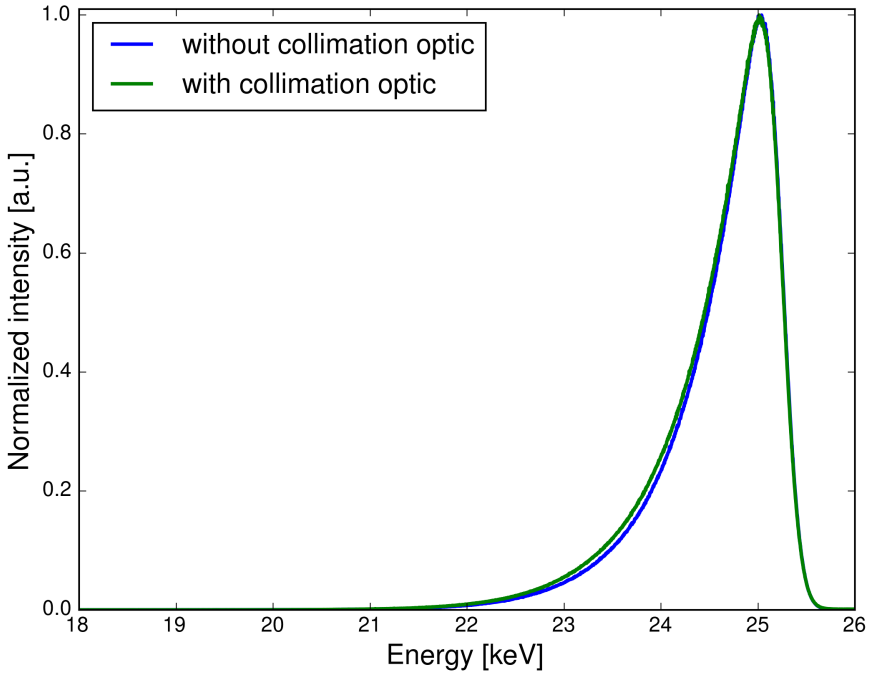

Figure 5.30.: *Spectrum of the 25 keV configuration of the MuCLS with (green) and without (blue) collimation optic inserted in the beam path.*

X-ray flux is high enough, an appropriately formed absorber could equilibrate the intensity drop towards the FWHM, for example. The FWHM is reached for beam extensions of 2.3 mm in vertical and 2 mm in horizontal direction, which are smaller than predicted by the manufacturer. The collimation optic yields an enhancement of the X-ray flux by a factor of 10 to 20 for output focal spot diameters of 2 to 3 mm at 25 keV. Concerning the X-ray spectrum, the optic only slightly influences the lower energy tail towards 18 keV, which does not significantly affect dosimetry. Consequently, in-vivo irradiations at the MuCLS can be performed at 25 keV using this polycapillary optic.

To optimize the beam parameters for larger tumor sizes in the future, a second polycapillary was manufactured that offers a focus diameter of roughly 4 mm (FWHM). Therefore, the length of the polycapillary optic was reduced to offer a smaller bending radius at the beam exit than with the previous option. A slight reduction in dose rate because of the larger beam size is expected. The X-ray spectrum behind the polycapillary optics was compared to the non-modified spectrum as above and yielded similar results. Further characterizations of this second optic regarding focal spot optimization and efficiency are to be performed.

5.4.4. Mouse irradiation setup

The experimental setup installed in hutch 1 at the MuCLS for beam shaping and positioning of the mouse is presented in the following. This includes monitoring of X-ray intensity by a scintillation counter, a beam defining aperture, a removable tungsten slit array, and a mouse holder. Irradiations in-vivo require a dedicated setup design from accurate positioning systems to heating and temperature control for the mouse holder.
The photograph in Fig. 5.31 shows an overview of the mentioned devices.

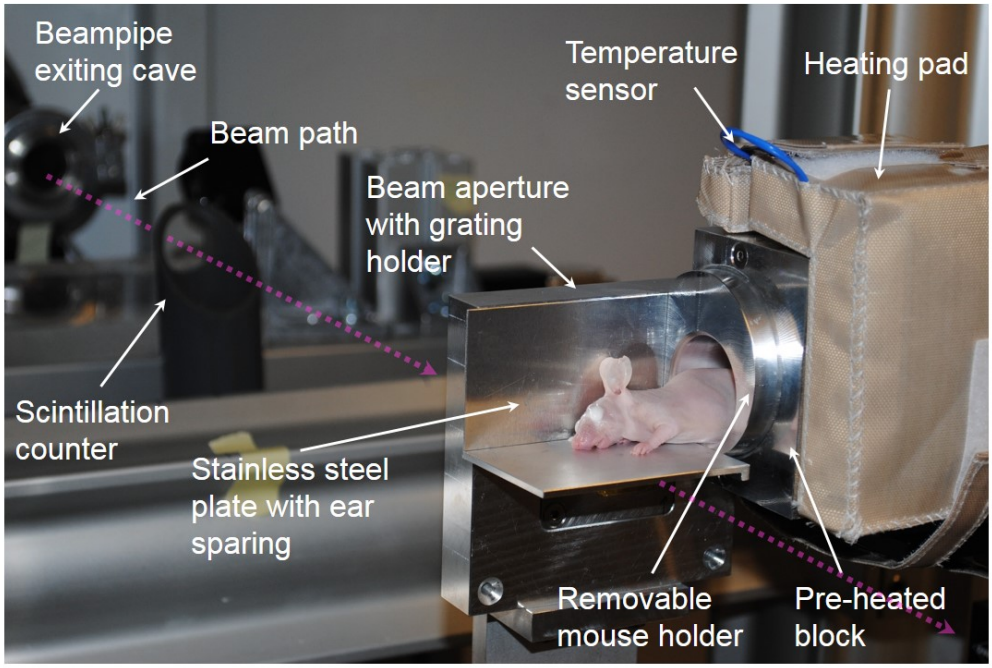

Figure 5.31.: *Setup in the experimental hutch. The photograph shows along the beam path (magenta arrow): the beampipe through which the X-rays exit the cave, the scintillation counter with transparent polyester film, the beam aperture with removable grating holder, the removable mouse holder with head support, additional beam protection by a stainless steel plate, and a cylindrical body holder, inserted into an aluminum block covered with the heating pad including a temperature sensor insertable into the mouse holder.*

The X-ray beam exits the transport line from the cave into the hutch at about 3 m from the source through a polyester window. Downstream of the window, the scintillation counter was placed to measure the relative beam intensity during irradiation, which is necessary for online dosimetry (for more details, see next section). As next component, the beam defining aperture was positioned – here realized as plate with a hole in its center – including an inset for the tungsten grating. Behind the aperture, the mouse ear was fixed on the ear support of the mouse holder (not visible in the photograph). The mouse holder itself was placed in an aluminum block, which was heated by a specifically designed pad. The temperature was controlled by a sensor inserted through the aluminum block into the mouse holder.

In the following, the individual components are introduced.

5.4.4.a. Mouse holder

In Figs. 5.32 (a) and 5.32 (b), front and back side of the mouse holder are shown (additional technical drawings can be found in Appendix A.5).

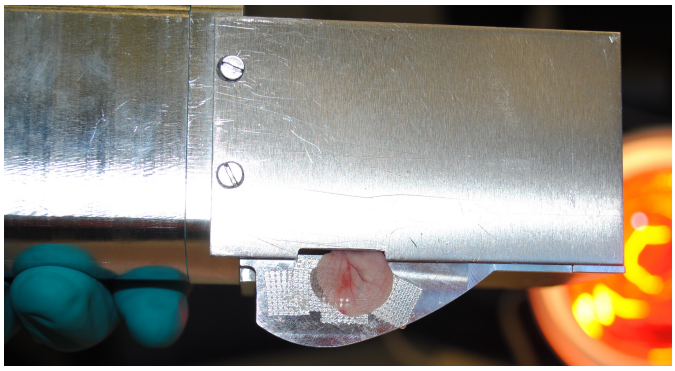

(a)

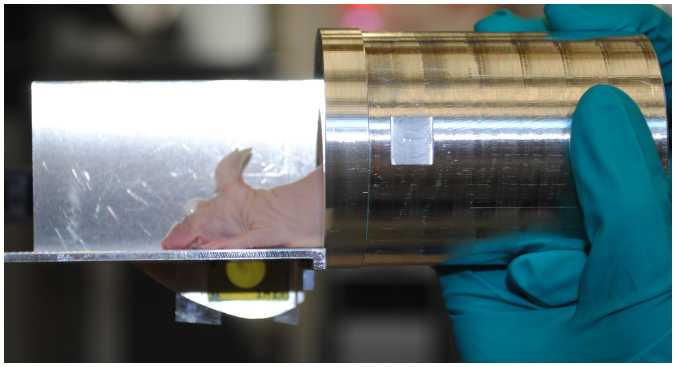

(b)

Figure 5.32.: *(a) and (b) show the front and back side of the mouse holder, respectively. (a) The ear can be drawn through an opening in the head protecting stainless steel plate and fixed with tape onto the ear plate. The tumor, here a reddish vertically elongated ellipse, is stretched over the ear aperture.*
(b) A Gafchromic film was attached behind the ear plate visible as yellow square. The mouse body is placed inside an aluminum block to improve the heating. Only the head and neck are placed on a supporting plate above the beam path.

On the front side, the ear support can be seen. Here, the mouse ear was stretched over the ear aperture and fixed at the ridges with removable tape. The tumor was well supplied with blood and is visible as reddish ellipse, elongated from the junction of the arteries along the dorsal (left) side of the central artery. Before irradiation, a stainless steel plate can be screwed in front of the mouse head to protect it from scattered radiation. An opening on the bottom side allows to pass the mouse ear. The main part of the mouse holder is quasi cylindrical and made of at least 0.5 cm thick aluminum. To minimize the distance between tungsten grating and tumor, the side of the cylinder facing the beam is flattened. When inserted in the aluminum block, it can be fixed additionally to avoid undesired motion of the holder during irradiation. The photograph of the back side of the holder shows that the head and neck of the mouse are positioned on a head support made of aluminum, while the rest of the body is placed within the cylinder to improve the heating of the mouse during anesthesia. Below the head support, a

Gafchromic EBT3 film can be taped to the back side of the ear aperture to verify beam positioning and geometry post-irradiation.

5.4.4.b. Heating

The anesthetized mouse was warmed by a red light lamp distant by about 30 cm during preparation and positioning in the pre-heated aluminum mouse holder. In the experimental hutch, the mouse holder was inserted into an aluminum block heated by a specifically designed heating cuff[26] including temperature sensor and microprocessor based heating regulation. The cuff consists of a heating cable to which a voltage is applied and which is surrounded by a grounded wire mesh of copper. The wire mesh is insulated with synthetic rubber and covered with PTFE fabric foil. The system provides a heating power of 50 W and a maximum temperature of 50 °C. To prevent accidental overheating of the mouse, a temperature limit is installed in the regulator, which mechanically shuts off the voltage supply. The sensor can be positioned close to the inner wall of the mouse holder and regulated by a controller from outside the hutch. As the normal mouse body temperature varies between 36 and 39°C, which is significantly reduced during anesthesia, the holder was heated to a supportive temperature of 32°C. The intrinsic, self-optimizing temperature regulation based on the PID algorithm [179] yields a smooth warm up with low overshoot. Depending on the ambient temperature, the heating temperature stabilizes within about 30 min reaching an accuracy of ±1 °C.

5.4.4.c. Beam aperture with inset for tungsten grating

In Fig. 5.33 (a), the quadratic aperture plate (made of stainless steel) is shown, placed in a milled-out portion of its support. In a dedicated depression in the aperture plate, the tungsten slit array is set and taped at the borders with adhesive polyimide film to avoid any damage to the grid. The resulting microbeam pattern is shown on the irradiated Gafchromic EBT3 film in the photograph. The zoomed picture in 5.33 (b) depicts the grating in more detail and allows to recognize the circular aperture of 3.4 mm diameter behind the upper left corner of the grid. By radiographic imaging, this area of the grid has shown highest quality in terms of the desired microbeam pattern of 50 µm wide slits spaced by 300 µm of tungsten (cf. section 5.2.3).

5.4.4.d. Positioning

First, the beam aperture was aligned perpendicular to the beam axis on a motorized rotation stage with three-dimensional translation. For this purpose, the Pilatus detector at ∼16 m from the source was used to optimize the beam profile, shaped by the 3.4 mm round aperture, for maximal extension in x and y direction. Subsequently, the mouse holder was placed on the translation stages behind the

[26] Horst GmbH, Lorsch, Germany

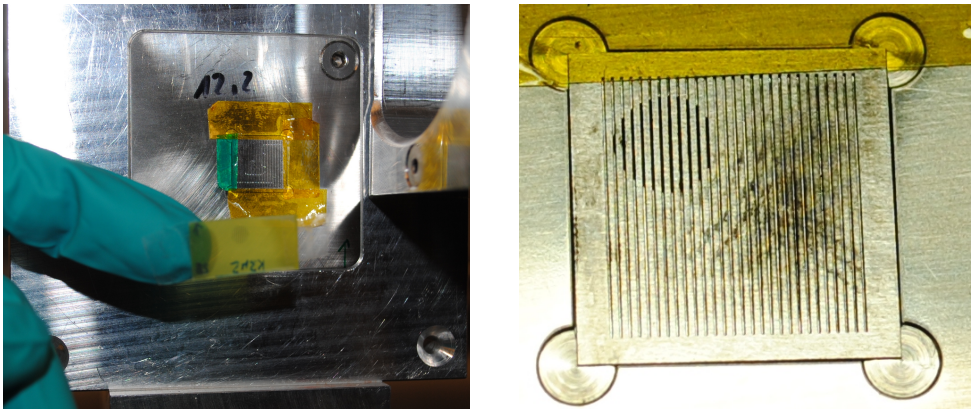

(a) (b)

Figure 5.33.: *The aperture with the grating inset is depicted. (a) The aperture holder includes a removable stainless steel plate, here with tungsten grating. A Gafchromic film was irradiated with the thus created microbeams. (b) Zoomed image of the tungsten grating. The 3.4 mm round beam aperture can be seen through the grating at the top left.*

aperture on the rotation table and the ear aperture of the mouse holder was positioned in line with the beam aperture on the beam axis. To realize the stitching procedure (2-field irradiation, see also section 5.4.5), the relative positions of the upper and lower field were predetermined and verified with Gafchromic films. For irradiation, the mouse was positioned in the preheated mouse holder, slid into the aluminum block, and the temperature sensor was placed in the designated hole reaching the inner wall of the mouse holder. The fixed mouse ear was moved as close as possible without contact behind the beam aperture (with or without grating). A torch lamp was placed in front of the beam aperture as a placeholder for the X-ray beam, shining light through the stretched tumor-bearing mouse ear. Then, the mouse ear was imaged by a pre-aligned, manually focused CCD camera (Flea[27]). The position of the three-dimensionally motorized mouse holder was adjusted to perfectly match the tumor with the center of the aperture. Exemplary images of thus centered tumors taken with the CCD camera are depicted in Fig. 5.34.

Fig. 5.34 (a) shows an ROI of a mouse ear illuminated through the 3.4 mm wide aperture. Two arteries can be seen as dark lines crossing the circular field of view. The skin of the ear in between the vascular system is quite transparent with tiny speckles, possibly originating from pores and hair follicles. In the center, a darker gray area, i.e. with reduced transmission, indicates a protrusion, which corresponds to the tumor. As the flattening of the tumor at the edges might not be perfectly visible and the homogeneity of the illumination might vary, the tumor extension has to be well studied before it is positioned in the center of the aperture. Directly below, in Fig. 5.34 (c), the same setting is shown for a different tumor, but with inserted tungsten grid. Here, while the source size is large, vertical stripes

[27] FLIR Integrated Imaging Solutions, Inc., Richmond, BC, Canada

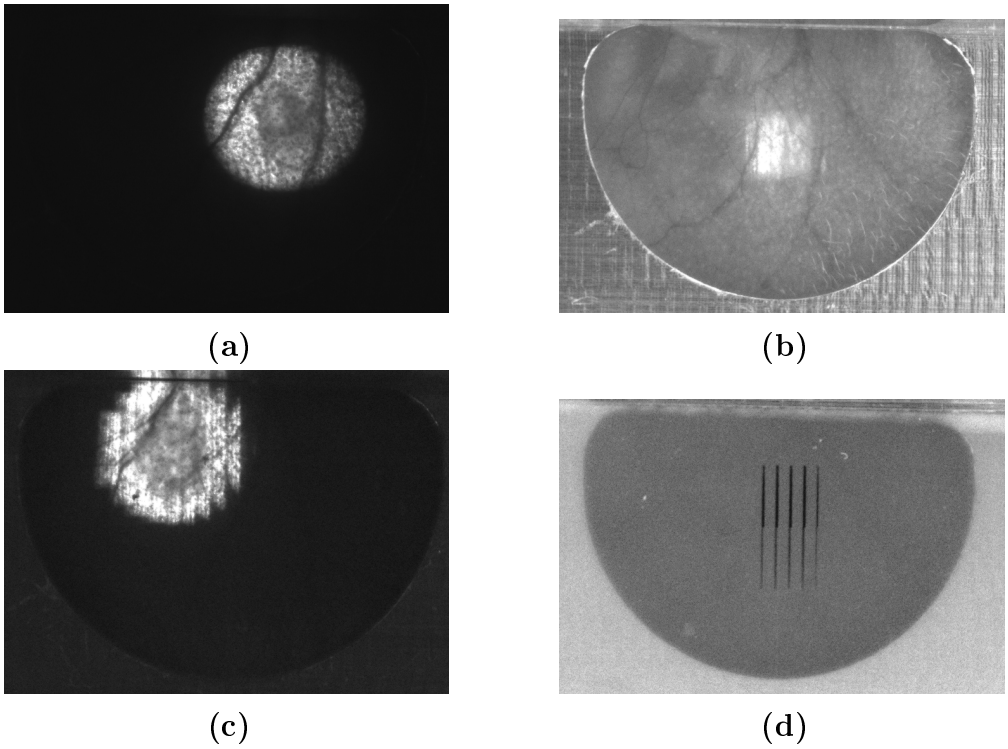

Figure 5.34.: *Tumor positioning with CCD camera and visible light. In all pictures, the aluminum aperture on which the mouse ear is fixed is seen from the back side. The tumor position is adjusted to a fixed beam aperture, seen through the mouse ear as bright field in (a) to (c). (a) A tumor is centered to the 3.4 mm beam aperture in front of the ear. Below, in (c), the positioning with the inserted tungsten grating is demonstrated. (b) The quadratic field of 1.5×1.5 mm^2 is used with grating to irradiate the tumor. Here, positioning needs to be performed before insertion of the tungsten array. (d) Image captured during microbeam irradiation using 2-field stitching with a radiochromic film attached onto the aluminum aperture behind the ear. The top field irradiation was already completed while the irradiation of the bottom field is in progress.*

from the grating remain visible. However, the tumor can be well distinguished from the surrounding ear skin, arteries, and cartilage. The larger extension of the tumor in vertical direction does not pose a problem as it fits to the ellipsoidal focal spot size produced with the polycapillary optic. In Fig. 5.34 (b), the image is taken with a different illumination within the experimental hutch as here the light is only transmitted through a $1.5 \times 1.5\,\mathrm{mm}^2$ aperture. Knowing the approximate tumor position allows to center the tumor also with this small opening. In cases where the tumor extension could not be recognized, it was centered first with the 3.4 mm wide aperture before the smaller aperture for 2-field stitching was inserted. The image below (Fig. 5.34 (d)) is from the treatment of the same mouse with the Gafchromic film placed on the back of the ear aperture upon irradiation. The image was captured during irradiation of the bottom field after completing the top field. On the right side, the last microbeam is smaller because it is cut off by

the aperture (not because of a defect of the tungsten grid). The microbeams from the two fields overlap well with each other, which confirms accurate positioning.

5.4.5. Online dosimetry for mouse-ear irradiations

If the target is not transparent to X-rays like in the case of a cell monolayer, and its absorption is unknown, the Pilatus detector cannot be used for online dosimetry. Therefore, intensity variations are recorded with a minimal-invasive scintillation counter. Its relative intensity values have to be calibrated to the Pilatus detector before irradiation as it is currently the only system at the MuCLS that delivers absolute values for the photon flux, namely photons per second. From the photon flux, the applied mean dose can be calculated as explained in section 5.3.2 taking all absorbing elements along the beam path into account. Compared to the in-vitro experiment, additional flux reduction and spectral changes have to be considered due to a longer air path from the source to the mouse ear and the polyester windows of the beampipe. As in the in-vitro study, the same mean dose is applied for homogeneous and microbeam geometry. With respect to skin damage, this dosimetric concept has been reported to yield a similar response in-vivo for both irradiation geometries [87]. Under this approximation, one can assume the same normal tissue damage while studying the tumor response.

5.4.5.a. Grating absorption

To achieve the same mean dose for homogeneous and microbeam irradiation without a Pilatus image, the absorption of the grating behind each aperture was determined beforehand without collimation optic in the beam. The mean photon flux was recorded for both settings with the Pilatus detector. To account for flux variations over time, the intensity values of the Pilatus detector were normalized to the relative intensity values acquired with the transmission counter. The ratio of the integrated photon flux with grating to the photon flux of the homogeneous beam yields the grating transmission. During in-vivo irradiation, the X-ray intensity recorded with the scintillation counter placed in front of the grating could thus be corrected with the grating transmission value for the respective aperture.

5.4.5.b. Dose distribution in target area

Using a beam aperture of 3.4 mm diameter allows to avoid scattered radiation and simultaneously permits to irradiate the tumor with a security margin of a few hundred micrometer. Yet, the FWHM of the focal spot produced by the polycapillary optic with 2 mm in horizontal and 2.3 mm in vertical direction was considered the border of quasi-homogeneous irradiation. Therefore, the mean dose was calculated for this inner ellipse. In case of the 2-field stitching with a field size of $1.5 \times 1.5\,\mathrm{mm}^2$ each, a total ellipse of $1.5 \times 2.8 \times \pi\,\mathrm{mm}^2$ was chosen to achieve a quasi-homogeneous irradiation area. For stitching, only tumors with well-defined vertical borders were used. The preferred elongation of the tumors

in vertical direction possibly results from the injection of the tumor cells with the needle inclined and retraced parallel to the arteries as described in section 5.4.2. To minimize the induction of artifacts due to a different dose distribution, the one-field irradiation with the circular field size was prioritized over 2-field stitching.
With the choice of these ellipsoids for dose calculation, the inhomogeneous dose distribution resulting from the insertion of the collimation optic had to be taken into account. The dose distribution of both irradiation fields was recorded via film dosimetry with Gafchromic EBT3 films placed directly behind the ear aperture of the mouse holder using the same beam parameters as for the actual in-vivo irradiation. The films were scanned (cf. chapter 3.2.3) and evaluated as visualized in Fig. 5.35. The normalized dose distribution is shown for the 3.4 mm wide aperture in Fig. 5.35 (a) and for the irradiation area of $1.5 \times 3\,\mathrm{mm}^2$ from 2-field stitching in Fig. 5.35 (b). The mean dose of the inner ellipsoids with $2{\times}2.3{\times}\pi\,\mathrm{mm}^2$, and $1.5 \times 2.8 \times \pi\,\mathrm{mm}^2$ (depicted in Figs. 5.35 (c) and 5.35 (d)) was computed and compared to the corresponding full irradiation area. Thus, the photon flux at the mouse ear was weighted accordingly.

5.4.5.c. Dose computation during irradiation

With the correction factors for grating absorption, target area, and dose inhomogeneity, the applied mean dose can be calculated during irradiation. The relative transmission counter recorded intensity values every second and its readout time was taken into account. The intensity value that had to be achieved for the desired dose was computed at the beginning of the irradiation (programming code implementation in Python). The value of the already applied dose was updated every second. The electron beam of the MuCLS was automatically shut off as soon as the desired mean dose was reached. Depending on the X-ray flux and the irradiation geometry, slight overshoots are possibly caused by the finite readout time of the scintillation counter. To prevent overdosage, in extreme cases (low dose, homogeneous irradiation), the X-ray flux was reduced directly at the MuCLS by reducing the electron bunch charge.

In summary, the mean absorbed dose can be obtained during irradiation for two quasi homogeneous irradiation areas of $2 \times 2.3 \times \pi\,\mathrm{mm}^2$, and $1.5 \times 2.8 \times \pi\,\mathrm{mm}^2$ taking absorption of the tungsten grid and inhomogeneous intensity distribution from beam collimation into account. Different irradiation areas are important to achieve a good target volume coverage. The main aspect for fair comparison of the experimental results is the tumor size itself, which should be as similar as possible. In contrast, the small differences in dose distribution are expected to make little impact on the behavior of the tumor.

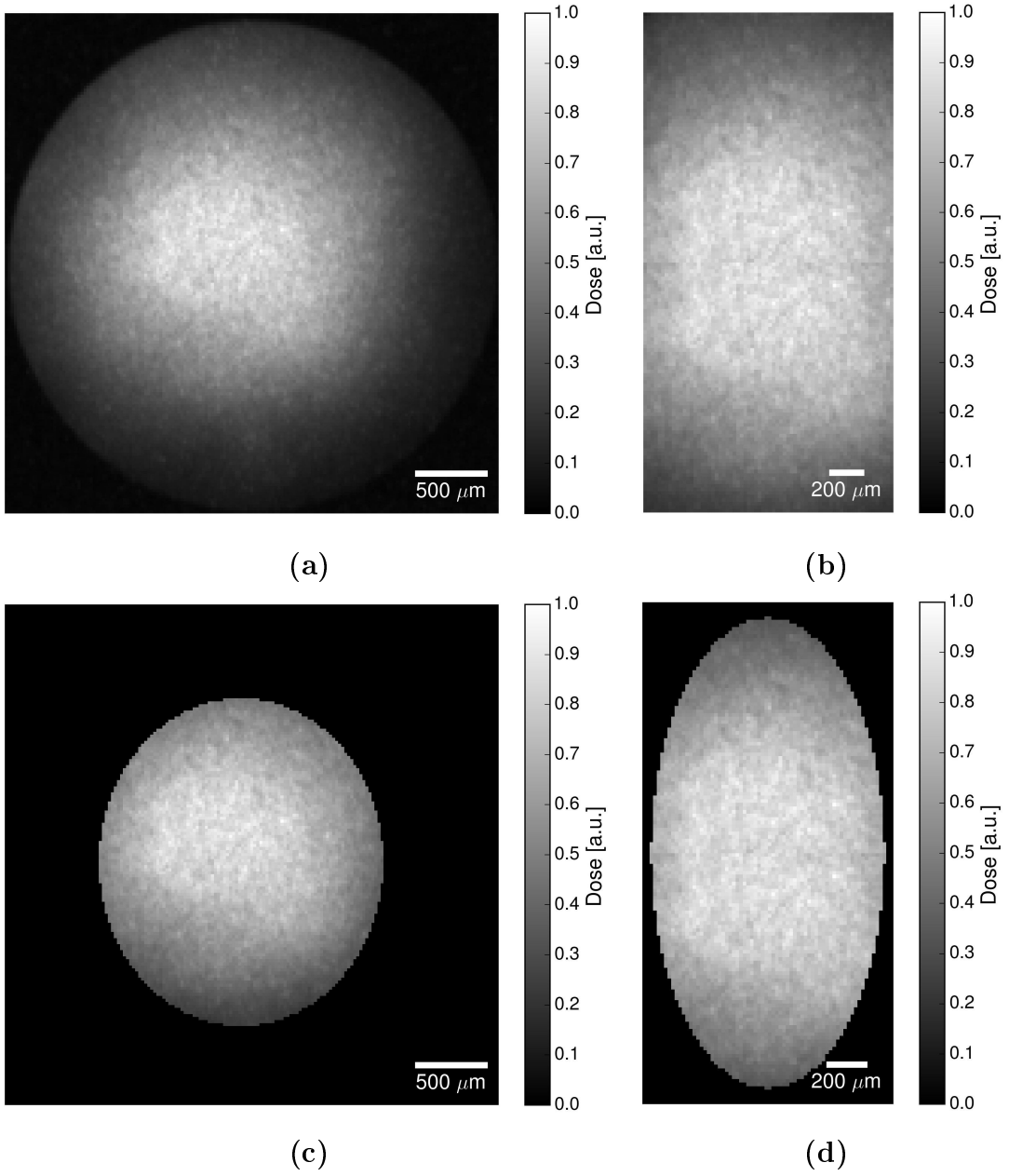

Figure 5.35.: *Dose distribution measured with Gafchromic EBT3 films at the mouse holder position with inserted collimation optic. Two different fields were irradiated: (a) a single field shaped by a 3.4 mm wide aperture and (b) two vertically stitched fields shaped by a 1.5×1.5 mm² sized aperture. The dose was calculated for a tumor area of a 2×2.3×π mm² ellipse as shown in (c) or a 1.5×2.8×π mm² ellipse as depicted in (d), yielding quite homogeneous dose distributions.*

5.4.6. Tumor growth study

In this section, the experimental results of the tumor growth delay study are presented – shown as dark blue route in the schematic overview in Fig. 5.26. Therefore, measurement and evaluation of the tumor volume are explained. Subsequently, the accordingly processed tumor growth values are discussed. An outlook gives insight into further investigations of the re-cultured tumor cells, followed by a summary of the achievements.

5.4.6.a. Tumor volume evaluation

Microbeam, homogeneously, or sham irradiated mice were followed up for about 30 days. To determine the tumor volume V with high accuracy, we chose the standard volume formula considering [180, 181]:

$$V = \frac{\pi}{6} \times \text{length} \times \text{width} \times \text{height}. \tag{5.2}$$

While 'length' and 'width' form the irradiated tumor area, the 'height' of the tumor extends in the direction of the thickness of the mouse ear. The maximum tumor elongation was measured every two days in three dimensions with a digital caliper of 0.01 mm accuracy (DigiMax 29422[28]) almost exclusively by a predetermined person (Ann-Kristin Porth, PhD student) to minimize statistical errors. Before the experiment, a 15-fold relative tumor growth with respect to the day of irradiation was fixed as comparative figure. Mice were sacrificed under anesthesia by cervical dislocation if the stop criteria were met, i.e. a tumor diameter >8 mm, or lack of well-being (as defined in the ethics approval), or, if no further development could be expected. The latter was only the case for abnormal, insufficient tumor growth.

The relative tumor volume $V_{rel,i}$ was calculated as the ratio of the volume at day i with respective to the volume on the day of irradiation (i=0): $V_{rel,i} = V_i/V_0$. Standard cell division allows the assumption of exponential tumor growth. Thus, an exponential model, $a \cdot e^{bx}$, was fitted by a non-linear least-square approximation (SciPy, Python Package [126]) to each growth curve from sham irradiated and control mice. The mean of the resulting fit parameters a and b was computed to $\bar{a} \pm$SEM and $\bar{b} \pm$SEM to obtain the control curve with $\bar{V}_{rel,i}^{control}$. Due to radiation-induced deviations of the tumor growth from exponential behavior, this fitting model cannot be applied to irradiated tumors. To determine $\bar{V}_{rel,i}$ as a mean for all replicates, we calculated the relative tumor volume for i=1,2...,15 with $i \in \mathbb{N}$ by linear interpolation between the measured data points of each mouse. The uncertainty of the day d to achieve the designated 15-fold volume $\bar{V}_{rel,15}$ is given as SEM resulting from the replicates broadened by the Student's t factor for normal distribution (see section 3.2.4). Finally, the tumor growth delay TD of irradiated

[28] Wiha, Buchs, Switzerland

tumors with respect to the controls can be calculated for $\bar{V}_{rel,15}$ as follows:

$$TD_{15} = \bar{d}_{15}^{control} - \bar{d}_{15}^{irr}. \tag{5.3}$$

Growth curves that did not achieve 15-fold relative volume, $V_{rel,15}$, were excluded from further evaluation.

5.4.6.b. Experimental results

In this section, the tumor growth measurements are presented and discussed. Mouse handling and data acquisition (tumor growth measurement) were conducted together with Annique C. Hunger and Ann-Kristin Porth. The MuCLS was mainly operated by Martin Dierolf and Benedikt Günther.

Treatment and evaluability of results. In Table 5.6, the number of treated mice and the number of evaluable data sets (reaching $V_{rel,15}$) are shown. 5 mice were foreseen for each irradiation type. Additional reserve mice were treated equivalently to guarantee the statistical relevance of this explorative study. The number of treated mice differs for each irradiation setting as not all mice developed tumors after tumor cell injection and allocation to groups was randomized. Even though a pilot study showed tumor growth to about 2 mm in diameter within 9 to 14 days after cell injection, a prediction of this time frame highly depends on the amount of injected cells [182] and the performance of cell injection. As only tumors from two sham irradiated mice showed sufficient tumor growth, an additional group of control mice was treated and held at the animal facility of the Klinikum rechts der Isar. Possibly due to a lower amount of injected tumor cells in the control group, the tumor take rate was very low, resulting in only two control tumors which reached $V_{rel,15}$. Because of the different handling, sham irradiated and control mice are differentiated in the table. Moreover, the number of tumors irradiated with 2-field stitching is assigned to each irradiation type. Unless specified otherwise, all results presented in the following are based on evaluable data only.

Table 5.6.: Statistical data. *Overview of the tumor growth delay study with respect to the number of mice.*

Irradiation setting	No. of treated mice	Data in evaluable range	2-field stitching
Sham	5	2	-
Control	9	2	-
Homog. 3 Gy	6	5	1
Homog. 5 Gy	6	5	0
Microb. 3 Gy	7	7	2
Microb. 5 Gy	7	6	2

Mean doses of 3 and 5 Gy were applied according to results from the pilot study (mentioned in section 5.4.2), where homogeneous irradiation of 3 Gy did not show significant tumor growth delay, whereas 6 Gy already caused tumor control. The latter is to be avoided in a tumor growth delay study such that a lower dose of 5 Gy was preferred for the experiments at the MuCLS. As microbeam treatment with 3 Gy mean dose could potentially be more effective than homogeneous treatment, the application of 3 Gy with varying dose distribution might already show different effects.
In the homogeneous case, the '3 Gy' irradiation corresponds to 3.15 ± 0.03 Gy ($\pm$SD), for microbeam treatment 3.16 ± 0.00 Gy were applied. '5 Gy' corresponds effectively to 5.13 ± 0.05 Gy for homogeneous, and 5.13 ± 0.06 Gy for microbeam geometry. For each field, a mean dose rate of 4.24 Gy/min was reached in homogeneous irradiations, and a mean dose rate of 0.57 Gy/min for microbeam irradiations. Due to grating imperfections and variations of the flux over time, the ratio of $4.24/0.57 = 7.44$ approaches but does reach the ideal factor of 7, which would reflect a microbeam width of 1/7 of the grating period. Exemplary dose distributions from microscopic read-out of radiochromic films are shown for different irradiation settings in Appendix A.6.

Tumor growth. Due to the slow tumor growth in a large number of mice – attributed to the small tumor size upon irradiation – the follow-up was extended up to a maximum of 48 days if the well-being of the mouse was not affected. In some cases, the animal was sacrificed before the end of the follow-up because of fast growing secondary tumors and metastases in the head and neck area. In general, a quite high rate of secondary tumors was noticed with this tumor model. Similar observations were reported recently in [182].
First of all, the relative tumor volumes over time of sham and control irradiated mice are given in Fig. 5.36. Day 0 represents the day of 'irradiation' , which requires a tumor of relevant treatment size and sufficient blood supply. M1 (blue) and M2 (green) correspond to the sham irradiated mice, M3 (red) and M4 (cyan) to the control mice. The relative tumor volumes result from interpolation of the measurements acquired in an interval of 2-3 days, as explained in section 5.4.6.a above. Thus, data points are given for every integer relative volume (the underlying measured data for all sham irradiated and control mice is given in Appendix A.6). As tumor growth shows an exponential behavior resulting from cell division, the data were fitted accordingly (orange line).
From this measurement, it becomes clear that the xenografts grow at different rates without obvious influence of sham irradiation or control treatment. On average, a tumor volume doubling time ($\pm$SD) of about 5.7 ± 0.4 days was determined from the four data sets assuming that the tumor at day 0 has already started to grow exponentially. The mean values of the exponential fit parameters account to $\bar{a} = 0.940$ and $\bar{b} = 0.128\,\text{days}^{-1}$. This curve is given as a reference in the subsequent results for homogeneous and microbeam treated tumors.
Fig. 5.37 shows the tumor growth for every irradiation setting and dose over time

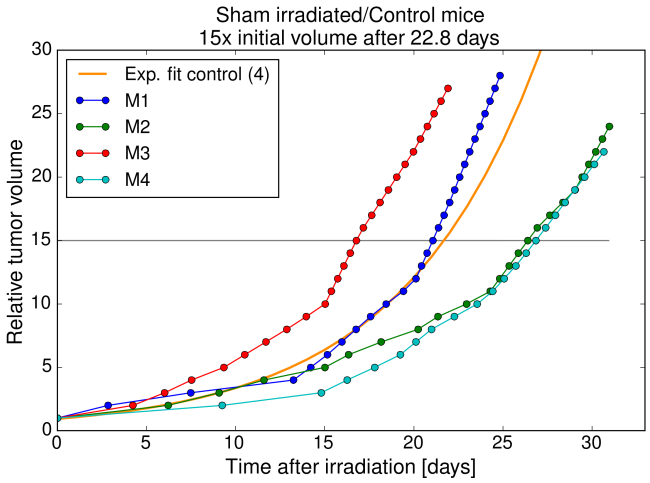

Figure 5.36.: *Tumor growth over time in days for sham irradiation and control data. The relative tumor volume with respect to the volume on the day of irradiation is given. For every integer, relative tumor volumes were computed by linear interpolation of the neighboring measured values. Measurements were acquired in an interval of 2-3 days. An exponential model (orange line) was fitted to the data. Hereby, the time point for reaching the 15-fold relative tumor volume was estimated to 22.8 days.*

in days. The relative tumor volumes are obtained as described above. The underlying measured data for all irradiated mice are shown in Appendix A.6. Note the difference in observation time for the different curves. Serving as comparative figure, the 15-fold relative tumor volume is marked with a gray line. The deduced tumor growth delay is given in the title of the respective figure and will be discussed later on. As mentioned before, the initial tumor growth after cell injection can vary strongly until a treatable tumor size is reached. Therefore, three more aspects were investigated: the time between tumor cell injection and irradiation, the day of tumor cell injection (injection was performed in three groups in an interval of 2 days), and the irradiation field size (single field or 2-field stitching).

The tumor growth curves after 3 Gy microbeam irradiation (Fig. 5.37 (a)) do not show a clear trend, but rather seem to fluctuate around the tumor growth curve of sham irradiated/control tumors. While M5 and M6 have been treated 9 days after M2 and M7, no obvious delay in tumor growth can be attributed to the different irradiation dates. Considering as well the day of tumor cell injection, there are the following three groups: M1, M6, and M7, followed by M4 and M5, and lastly M2 and M3. Interestingly, the first group shows a rather slow tumor growth after irradiation compared to the other two groups, which exhibit a quite similar behavior. Moreover, the fast growing tumors of M2 and M4 have been irradiated with 2-field stitching. Hence, in this case, the time between tumor cell injection and irradiation did not influence tumor growth remarkably, while the day of tumor cell injection and 2-field stitching could have played a role.

In Fig. 5.37 (b), the data from relative tumor volumes after 3 Gy homogeneous

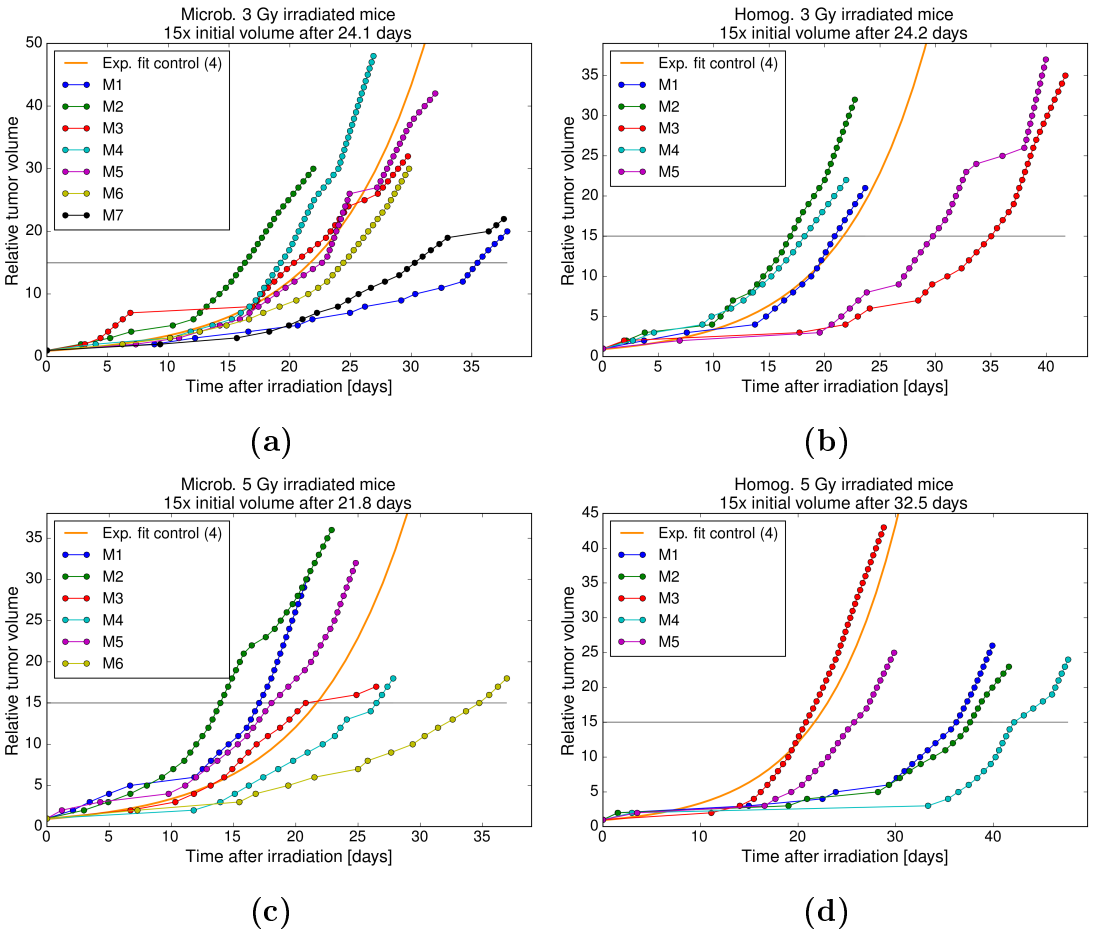

Figure 5.37.: *Tumor growth over time in days. The relative tumor volume with respect to the volume on the day of irradiation is given. For every integer, relative tumor volumes were computed by linear interpolation of the neighboring measured values. Measurements were acquired in an interval of 2-3 days. All plots contain the exponential fit to the sham irradiation data from 4 replicates as reference (orange line). Tumor growth is shown in (a) after 3 Gy microbeam irradiation, in (b) after 3 Gy homogeneous irradiation, in (c) following 5 Gy microbeam irradiation, and in (d) following 5 Gy homogeneous irradiation. On average, 15-fold relative tumor volume was achieved after 24.1 (3 Gy microb.), 24.2 (3 Gy homog.), 21.9 (5 Gy microb.), and 32.5 days (5 Gy homog.), respectively.*

irradiation are shown, which present a comparable tumor growth with respect to microbeam treatment at the same mean dose. Due to the random allocation of irradiation setting and mice, these tumors were treated within 4 days. Although M3 was treated the latest and shows the slowest tumor growth, no clear influence of the irradiation date on tumor growth can be stated. M5 belongs to the first group of tumor cell injection, followed by M2, M3, and M4 in group 2 and M1 in group 3. Here as well, the tumor from group 1 grows rather slow. Due to the large spread of tumor growth behavior in group 2, no clear trend can be stated. 2-field stitching was applied for M1, which shows an average tumor growth within

the irradiation group.
Fig. 5.37 (c) contains the data from 5 Gy microbeam irradiated tumors. On average, a faster tumor growth with respect to the sham/control data can be observed. In this case, M3, M4, and M6 were treated the latest with up to 8 days after the first one (M2). The corresponding three curves show all considerably slower tumor growth than the tumors treated several days earlier, in particular with respect to M2 that grows the fastest. In contrast to previous observations (cf. Figs. 5.37 (a) and 5.37 (b)), the fast growing tumor of M2 belongs to the cell injection group 1, together with the moderately growing tumor of M5, and a relatively slow growing tumor of M6. M3, and M4 received tumor cell injection two days later, followed by M1. M3, and M4 yielded slightly slower growing curves than M1. M1 and M4 were irradiated with 2-field stitching and show rather slow tumor growth. No correlation of their tumor growth behavior is apparent nor an obvious difference to the other growth curves from this irradiation group.
Lastly, in Fig. 5.37 (d), the tumor growth after homogeneous irradiation with 5 Gy is shown. Unlike the three other data sets, a clear tumor growth delay after irradiation is visible with a wide range of growth behaviors. The mice were irradiated within 4 days beginning with M4 and ending with M1, and M2. Tumor cell injection varied from M1, and M2 in group 1 over M4, and M5 in group 2 to M3 in group 3. The mouse in the third group shows a faster tumor growth than mice from the other groups. Yet, no clear trend is observable. One data set had to be excluded from evaluation because the tumor was controlled – probably by irradiation – before $V_{rel,15}$ was reached. The standard, single dose field was applied to all mice.

Furthermore, the injection volumes, which amounted to about 2-4 µl, were investigated on a random basis and related to tumor growth. No significant difference could be detected between smaller and larger injection volumes. However, the take rate might be higher if larger volumes are injected. This observation was confirmed by Beyreuther *et al.* in [182].

Additionally, measurement errors due to handling of the caliper and difficulties in detectability of the tumor outline at small sizes can affect the measured tumor size. Hereby, irregularities within individual curves can be explained.

In summary, tumors within the same irradiation group present quite large differences in growing behavior. Possible reasons were investigated:

- Tumors that needed more time to reach the desired irradiation volume showed on average a slightly slower growing behavior. Maybe, not all tumors have arrived at the stage of exponential growth behavior on the day of irradiation due to the technically required small tumor size.

- If the tumor cell injection was performed within group 1, most of the tumors grew slower than if the injection was performed in group 2 or 3. While tumor cell injection was always performed by the same person, it could be that cell

injection efficiency was improved from the first day of injection to the second and third day.

- As expected from dosimetric considerations (cf. 5.4.5), the application of different irradiation fields did not visibly influence tumor growth behavior.

Another explanation for different growth behavior could stem from varying initial tumor volumes V_0 (on the day of irradiation). Tumors were irradiated, when a tumor reached about 2 mm in length and 1.5 mm in width, and also sufficient blood supply as a marker for vascularization could be detected by the reddish appearance of the tumor. Because of the latter requirement and even though daily control of relevant tumors was performed, the tumor size on the day of irradiation can vary. In Table 5.7, the average tumor volumes are given within the respective population's standard deviation for each irradiation geometry (sham and control summarized to 'Control'). While for the control group, homogeneous 3 Gy and microbeam 5 Gy irradiation, the average tumor volumes are quite similar with about 1.7 mm^3, tumors receiving homogeneous 5 Gy and microbeam 3 Gy irradiation were on average about 15% smaller with slightly higher standard deviations. Tumors that could not be evaluated due to insufficient tumor growth after irradiation had an initial tumor volume V_0 in the same range as the evaluable data sets. Hence, one cannot conclude from the initial volume to the growth rate after irradiation.

Table 5.7.: Average initial tumor volumes per irradiation setting. *Tumor volumes on the day of irradiation including the population's standard deviation for each group.*

Irradiation setting	V_0 [mm^3]
Control	1.71 ± 0.11
Homog. 3 Gy	1.70 ± 0.25
Homog. 5 Gy	1.45 ± 0.27
Microb. 3 Gy	1.44 ± 0.32
Microb. 5 Gy	1.71 ± 0.26

The results on tumor growth presented above are summarized in Fig. 5.38 for the five irradiation settings (combining the data from sham and control mice). The average of the relative tumor volumes was computed including the standard error of the mean (SEM) with respect to the time after irradiation. Sham/Control data are shown in orange, homogeneous irradiation data with 3 Gy in blue, with 5 Gy in green, data from microbeam irradiation with 3 Gy in red, and with 5 Gy in cyan. The 15-fold relative tumor volume, $V_{rel,15}$, is marked with a gray line.
Obviously, most of the tumor growth curves overlap within their error bars. As an exception, the 5 Gy homogeneous irradiated tumors show a considerable tumor growth delay with respect to the control group. Almost no difference can be observed between control, homogeneous 3 Gy, and microbeam 3 Gy data. While 25 keV X-rays might have a slightly higher linear energy transfer than the 70 kVp

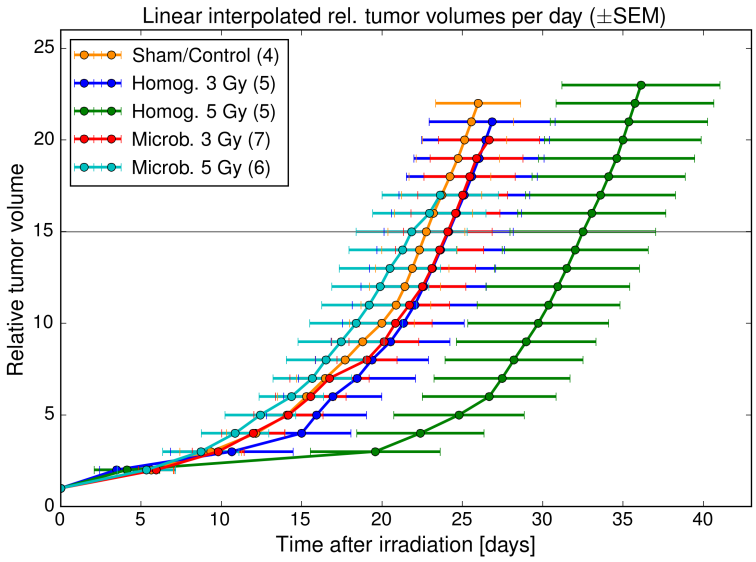

Figure 5.38.: *Mean of the relative tumor volumes over the time after irradiation. The error bar was computed from the accuracy in days for every integer relative volume as standard error of the mean (SEM). Sham/Control irradiation data are plotted in orange, data from homogeneously irradiated tumors applying 3 Gy in blue, 5 Gy in green, from tumors after microbeam irradiation with 3 Gy in red, and with 5 Gy in cyan. The horizontal gray line corresponds to 15-fold relative tumor volume.*

X-rays at the SARRP used for the pilot study, the energy change did not cause a visible difference in tumor growth delay. After 3 Gy homogeneous irradiation, tumor growth seems to be slightly retarded for days 10 to 20 before approaching the growth behavior of the control and the microbeam 3 Gy data. Unexpectedly, microbeam irradiation with 5 Gy did not yield tumor growth delay, but rather shows a trend towards enhanced growth up to day 22 after irradiation.

Tumor growth delay. As the tumor growth curves do not differ considerably between the investigated irradiation settings, values of tumor growth delay have to be interpreted with caution. Moreover, the statistics of this explorative study only allow to indicate a trend of growth behavior. However, to enable careful comparison with results from other studies, tumor growth delay at $V_{rel,15}$ for each irradiation setting with respect to the control data ($\bar{d}_{15}^{irr}$=22.8 ± 2.4 days) is given in table 5.8. The significance of the tumor growth delay is stated by the p-value of a two-tailed Student's t test for two independent means. For a standard significance of $p < 0.05$, no significant tumor growth delay was measured. Yet, tumors irradiated homogeneously with 5 Gy approach considerable tumor growth delay of almost 10 days with a p-value of 0.09, which confirms the observations from the tumor growth curves.

Table 5.8.: Tumor growth delay for each irradiation setting. *The table shows the time after irradiation to reach 15-fold initial tumor volume and the resulting tumor growth delay with respect to control data including the standard error of the mean (SEM). The level of significance for the tumor growth delay is given by the p-value of a two-tailed Student's t test.*

Irradiation setting	$\bar{d}_{15}^{irr}$ [days]	*TD*	p-value
Homog. 3 Gy	24.2 ± 4.0	1.4 ± 4.7	0.77
Homog. 5 Gy	32.5 ± 4.5	9.7 ± 5.1	0.09
Microb. 3 Gy	24.1 ± 2.8	1.3 ± 3.7	0.74
Microb. 5 Gy	21.9 ± 3.5	-0.9 ± 4.2	0.84

5.4.6.c. Discussion

Even though **no significant tumor growth delay** after microbeam irradiation with respect to control irradiation could be stated and also only slight differences of tumor growth became visibly between microbeam and homogeneous irradiations, the experiment revealed other interesting aspects.

It is of high importance to notice that **MRT mean doses of 3 and 5 Gy are not sufficient to cause a therapeutic effect** visible as tumor growth delay. The peak doses reached up to 21 and 35 Gy, respectively. Compared to MRT studies at large-scale synchrotron facilities, these doses were chosen deliberately low to analyze the dose range below 100 Gy. With these parameters, the dose limit for a therapeutic effect of MRT could not be reached.

One possible explanation is based on the **vessel destruction** by high dose beamlets reported as part of the beneficial MRT effect, e.g. in [19, 183]. While the permeability of the cell membrane is already enhanced at lower doses of a few tens of Gy and significant vascular damage is caused (cf. [78]), it seems that rupture of the vascular structures in the tumorous tissue is required to reduce the repair efficiency by the tumor and hereby affect tumor growth after MRT.

The use of 25 keV X-rays in contrast to a mean energy of about 100 keV at the ESRF, for example, involves a higher linear energy transfer by the secondary electrons. With this argument, a more pronounced radiobiological effect after MRT would be expected. However, simultaneously, a high **peak-to-valley dose ratio (PVDR)** is achieved using 25 keV at the MuCLS (cf. chapter 2.1.1), which was determined for the valley center in simulation to 270 ± 20, and in experiment via film dosimetry with microscopic readout to 210 ± 20 (valley and peak dose determined separately, both results acquired by T. Urban [120]). Briefly, a PVDR above 200 can be assumed for the mouse irradiation setup, which decreases towards 100 at the microbeam edges. This PVDR value is relatively high in comparison to previous MRT studies reporting on simulated PVDR values of 60, or 120 for the same microbeam width of 50 µm and periods of 200 µm or 400 µm, respectively [94]. In many studies, valley doses in the range from 12 to 40 Gy have been applied [184].

Here, the steep dose falloff at the microbeam edges resulting from the high PVDR at the MuCLS and the valley doses well below 1 Gy lead to reduced damage of cells close to the microbeam and in the valley region. Thus, overall tumor cell survival might be higher using the irradiation parameters at the MuCLS in contrast to previous studies.

Moreover, a recent study, which used computational modeling of the microvasculature indicates that with higher PVDR, the conservation of vessel length is increased [185]. The authors did not include repair mechanisms in the model and thus suppose that an even higher tissue tolerance to radiation can be expected in-vivo. Consequently, the high PVDR at the MuCLS might hinder persistent destruction of tumor vasculature.

Furthermore, **bystander effects** can be triggered by X-ray radiation. In a variety of MRT studies at large-scale synchrotron facilities, bystander effects were observed (e.g. [28,80,81,186]), which were suggested to cause an increase of DNA damage in the valley region additionally to direct radiation-induced damages. As an example, peak doses of 350 Gy with an estimated valley dose of 7 to 35 Gy were applied [89]. One might conclude that this higher DNA damage after MRT due to bystander effects could hamper tumor growth. Contradictory observations were made in-vitro at valley doses below 10 Gy suggesting that tumor growth is unlikely to be suppressed because of bystander effects or cellular damage in the valley region [184]. Hence, the contribution of the bystander effect in the present study remains somewhat unclear. Due to the lower peak doses applied here, its influence on tumor growth delay might be small.

Insufficient tumor damage after MRT at the MuCLS could also be explained by the sparing effect (higher **cell survival**) observed in-vitro after microbeam irradiation compared to homogeneous irradiation in normal tissue cells (see previous chapter 5.3). Using the microbeam geometry, also tumor cells might be spared. Yet, tumor cells often show higher radiosensitivity than normal tissue cells and moreover, the macroscopic environment is changed from monolayer to tissue such that the survival rate of tumor cells in-vivo might be different.

Regarding the slight acceleration in tumor growth after **5 Gy microbeam irradiation**, the given valley dose might be of interest. For many cell lines, so-called *low-dose hypersensitivity* becomes relevant at doses below 0.5 Gy followed by a rise of **radioresistance** (discussed in the literature, e.g. in [187–193]), which coincides well with the here-applied valley dose of almost 200 mGy with a transition zone of about 300 mGy towards the peak dose of up to 35 Gy. Maybe, such a low valley dose can also lead to acceleration of tumor growth. In contrast, the tumor growth is slightly suppressed after **3 Gy microbeam irradiation**. Following the argument above, this could result from a **hypersensitization** due to the lower valley dose of 100 to 200 mGy. Yet, to confirm the potential enhancement of tumor growth after 5 Gy microbeam irradiation and the tumor growth delay after 3 Gy MRT, a larger cohort would have to be analyzed. Before investigating this effect in-vivo, clonogenic cell survival after homogeneous irradiation with a staggered valley dose in the range of a few hundred mGy would allow to study in-vitro if

such a low dose changes the pace of cell division in tumor cells.
Tumor growth delay after 5 Gy homogeneous irradiation of almost 10 days was observed with the setting at the MuCLS. While in the pilot study with doses of 6 Gy performed at 70 kVp at the SARRP 2 out of 2 tumors were controlled, the reduced dose of 5 Gy with 25 keV X-rays resulted in only 1 out of 6 tumors being possibly controlled by irradiation (not shown). A study using similar doses (4 to 9 Gy) in the valley of a microbeam pattern stated that neither apoptotic cells nor tissue death were detected in that zone (nor in the peak area with a dose of 130 Gy) [184]. The authors claim that tumor growth suppression observed in their experiments is unlikely to result from the valley dose. The here-measured, quite considerable tumor growth delay after homogeneous irradiation indicates that a valley dose of 5 Gy does actually contribute to growth suppression. Moreover, the authors of the paper suppose that their observation of tumor growth suppression was induced by lower cell proliferation in the peak areas. This might also hold true for the visible delay in tumor growth after 5 Gy homogeneous irradiation, seen in the present study. To analyze a change in **proliferation of the irradiated cells** following tumor growth delay, according protocols were established in a pilot study (cf. study design in 5.4.1) and will be performed in the future.

To discuss the **tumor model** itself, the presented results on tumor cell injection in NMRI (nu/nu) immunodeficient mice are compared to a recent 'external study' study by Beyreuther *et al.* [182]. In the present study, FaDu cells were injected in a suspension with pure Matrigel, which allows to **control the location of tumor growth** in contrast to a suspension with phosphate buffered saline (PBS) observed in a pilot study. To avoid a drift of the tumor cells towards the ear base seen after injection of 50 µl cell suspension (with a concentration of 10^5 cells per 50 µl), the injection volume was reduced stepwise to 2-4 µl, which significantly improved location control. It is of utmost importance to position the tumor correctly in the X-ray beam for irradiation at the MuCLS. While the **take rate** in the main experiment for tumor growth delay with almost 90% was quite high, the subsequent cell injection for an additional control group reached only 30% take rate. These values do not include insufficient tumor growth in several animals, which might also be related to the injection procedure. In the external study, an injection volume of 25 to 30 µl was applied, which led to a high take rate of 90 to 100% for 10^5 cells in (diluted) Matrigel. Concrete localization of the tumors was not reported, however, one might assume a position close to the center of the ear instead of a drop to the ear base. For an injection volume of 50 µl, the authors of the external study confirmed the observation of such an undesired drop. Hence, in a future study, an **injection volume** above 10 µl could be useful, depending on the capacity of the mouse ear. Additionally, a higher **tumor cell concentration** might be beneficial. Moreover, a considerable number of animals developed **secondary tumors**. This can alter tumor volume measurements if they grow too close to the primary tumor or lead to sacrifice of the animal prior to the end of the tumor growth delay study to avoid suffering. Consequently, a tumor model which includes a lower rate of

secondary tumors is required. Beyreuther *et al.* proposed the cell line LN229 instead of FaDu with the trade-off of tumor scabbing. A higher radioresistance was observed, possibly resulting from early developing hypoxic areas in the tumor. This increased radioresistance could be advantageous to mimic the behavior of larger tumor volumes and allows to increase the homogeneous dose such that the concept of the same mean dose for microbeam and homogeneous treatment might still be applicable. Maybe even **other xenograft models** need to be established, providing a typical tumor structure already at small tumor sizes of a few mm with reduced side effects like secondary tumors, and a high take rate.
The different tumor growth behaviors within one irradiation group are likely caused by the setup-limited choice of **tumor volumes** with 1.4 to 1.7 mm^3. In [182], tumor volumes are calculated with an area-based approach by $V = \pi/6 \times \text{length}^2 \times \text{width}$, which would result in a range of 3.3 to 4.7 mm^3, respectively. Yet, Beyreuther *et al.* recommended tumor volumes of $\sim$10 mm^3 to ensure that the tumor has reached the stage of exponential growth and sufficient perfusion. Using a collimation optic with a larger focal spot as discussed in section 5.4.3, will permit to irradiate larger tumor sizes. If – contrary to careful observation – the tumors have not been fully developed on the day of irradiation, a more stable growth behavior could be expected with this change of the irradiation setup.

5.4.6.d. Conclusion of the tumor growth study

No tumor growth delay was observed after microbeam irradiation with 3 and 5 Gy mean dose using 25 keV X-rays at the MuCLS. Possibly, the MRT peak dose and thus the MRT valley dose need to be increased to achieve a visible effect on tumor growth. Maybe, deterioration of the PVDR is important for a tumoricidal effect of MRT. This could be performed by the application of an additional homogeneous irradiation field or by positioning scattering material behind the mouse ear. Moreover, tumors are in most cases embedded in normal tissue, which contributes to scattering, such that a lower PVDR corresponds to a more realistic dose distribution in the tumor. Yet, with the current xenograft model, a further increase of the homogeneously applied dose might result in tumor control which hampers the study of tumor growth delay. Therefore, in a future in-vivo study, different mean doses for microbeam and homogeneous beam geometry have to be considered. It could be interesting to investigate the MRT mean dose required to achieve the same tumor growth delay as with homogeneous irradiation of 5 to 6 Gy. Hereby, the concept of RBE is transferred to tumor growth delay, which has already been developed for the comparison of clonogenic cell survival after homogeneous and microbeam treatment in [88], for example. Following recent upgrades of the MuCLS, an almost 3-fold higher dose rate will allow to reach microbeam peak doses of about 100 Gy within 30 min. However, if larger tumor volumes are to be treated, a larger focal spot produced by a dedicated collimation optic will result in a lower dose rate. Further machine developments are foreseen to increase X-ray flux and flux stability while operating the system at highest flux such that irradiations up

to 100 Gy will be possible within a reasonable time frame.
Additionally to an increase in MRT dose, the tumor model needs to be further improved to enhance take rate, and reproducibility, and to avoid side effects. Tumors should reach a diameter of about 3 mm instead of 2 mm on the day of irradiation to ensure a stable and exponential growth behavior. Moreover, the vascular system and the amount of hypoxic areas might be more pronounced in larger tumor volumes. For these purposes, a different cell line like LN229 could be used. If peak doses on the order of 100 Gy are applied, different radiobiological effects after MRT can be expected due to possible vessel rupture and enhanced radioresistance, for example, which might lead to an advantage of MRT over homogeneous irradiation. Even though the microbeam period of 350 µm is already smaller than often used periods of 400 µm at the same microbeam width, the high PVDR at the MuCLS might require a tighter arrangement of the microbeams to achieve tumor growth delay or – in the treatment case – tumor control. Yet, possible side effects of such a microbeam pattern would have to be studied. Applying this concept at the MuCLS, the dose rate could be increased significantly.
In contrast to the previous propositions, considering the larger beam size of the MuCLS but lower dose rates compared to large-scale synchrotron facilities, the system is as well suited to study the effect of minibeam geometries using several hundred micrometer wide beamlets in the future.

All in all, the setup for in-vivo microbeam irradiations at the MuCLS was successfully established and characterized. Experiments could be realized within a relatively short time frame including accurate positioning and online dosimetry with a high degree of reproducibility despite possible flux variations. Following the observations from the tumor growth delay study, a better understanding of the radiation-induced effects is yet required. In on-going biological experiments of related projects, re-cultured tumor cells from the here-described study are investigated with respect to clonogenic cell survival and chromosome aberrations. Moreover, valuable information can be obtained from tumor analysis in two or three dimensions of the resected volumes following the tumor growth measurement or directly after irradiation. In the next section, insights into the accordingly developed methods are given together with preliminary results.

5.4.7. Tumor analysis in 2D – Histology

The histological analysis seeks to clarify the radiation-induced damage after MRT, homogeneous, or no irradiation. Due to the high PVDR at the MuCLS (above 200), the lower peak doses compared to previous studies, and also the small tumor size, the radiobiological reaction can differ from previous studies. Hence, the tumorous tissue has to be investigated in more detail following microbeam irradiation at the MuCLS.
To perform this analysis, only a single dose in the window between no visible effect and tumor control is necessary, deduced from the tumor growth delay study at the

MuCLS (mid-blue and light blue route in study design, Fig. 5.26). Considering the results presented above, irradiation with 5 Gy mean dose will be useful to analyze the root of tumor growth delay after homogeneous irradiation in contrast to no delay after MRT.

Subsequently, methods are introduced which were chosen for immunohistochemical evaluation in future experiments, following the mid-blue route in the study design. Data presented in this section was acquired in cooperation with Annique C. Hunger.

Apoptosis

With respect to the results from the tumor growth delay study for a mean dose of 5 Gy, a lower amount of apoptotic cells could be expected after MRT compared to homogeneous irradiation. This claim needs to be validated. In principal, the H&E staining also allows to visualize apoptotic cells. As not all lethally damaged cells will actively signal cell death 1 hour post irradiation, apoptosis is rather studied in tumors resected 24 hours after irradiation (cf. study design in Fig. 5.26). Moreover, easier detection of apoptotic cells is enabled by immunohistochemical staining using antibodies against e.g. Caspase 3.

Proliferation

As mentioned in the discussion of the tumor growth delay study, the proliferation of the irradiated cells might influence tumor growth. Potentially, in the 5 Gy microbeam case, the slight acceleration in tumor growth could be correlated with an increase in proliferation. In more detail, differences in peak and valley area of microbeam irradiated tumors could be studied. Antibodies to proliferation proteins like Ki67 are well suited for staining.

According protocols for both, apoptosis and proliferation need to be adapted and established in the future.

In the following, results from stained tumors of a pilot study are shown, referring to the light-blue route in the study design. For this purpose, tumors were resected and stored in 4% paraformaldehyde in PBS. In the pathology department[29], the specimens were dehydrated followed by paraffin-embedding. Subsequently, the tumors were cut in ∼2 µm thick sections perpendicular to the irradiation direction (xy-plane).

H&E staining

To give an overview of the tissue, a histological slice treated with standard hematoxylin-eosin (H&E) staining of a FaDu xenograft resected from a control mouse

[29] Klinikum rechts der Isar, TUM, Munich, Germany

is shown in Fig. 5.39. While hematoxylin allows to stain basophilic structures like cell nuclei in blue/violet, eosin causes red coloring of eosinophilic materials like cytoplasm, extracellular matrix, and collagen. The tumor was harvested with an extension of 5 to 7 mm in length and width, from which a region of interest was imaged via visible light microscopy.

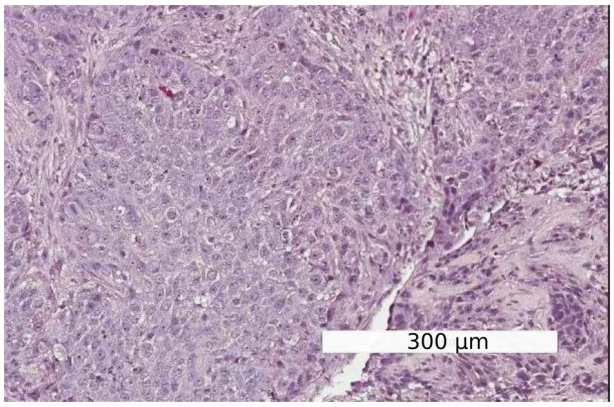

Figure 5.39.: *H&E staining of a histological slice from a resected non-irradiated FaDu xenograft grown in an NMRI (nu/nu) mouse. White spots might stem from remaining Matrigel.*

FaDu cells can be recognized as relatively big, dark-violet cells, especially in the surroundings of the scale bar. Vascular structures become visible due to directional alignment of cells along the vessels. Larger amounts of extracellular matrix might stem from remaining Matrigel, which showed a low degradation rate in this pilot study.

DNA damage

On such slices, radiation-induced DNA DSBs can be highlighted via γ-H2AX staining. Knowing the dose distribution is important to correctly interpret the results from the tumor growth delay study. For this purpose, tumors have to be harvested 1 hour after irradiation (upper, light blue path in study design, Fig. 5.26). Hereby, the dose distribution in the tissue caused by the microbeam (or homogeneous beam) geometry becomes visible. First successful staining of an MRT irradiated tumor is shown in Fig. 5.40.
As the tumor cell distribution is quite inhomogeneous and remaining Matrigel (extracellular matrix) blocks some areas for tumor cells, the microbeams are interrupted at several positions (e.g. left microbeam in Fig. 5.40 (a)). Cutting of the slices might have distorted the location of DNA double-strand breaks. Additionally, some foci in the 'valley zone' might result from spontaneous occurrence of DNA DSBs. Yet, cells in the microbeam path show a clearly increased cellular damage in contrast to cells in the protected 'valley zone'. The microscopic images indicate that parts of the 50 µm wide microbeams are blurred such that a larger area of cells is damaged than expected. This widening of the microbeam has to be

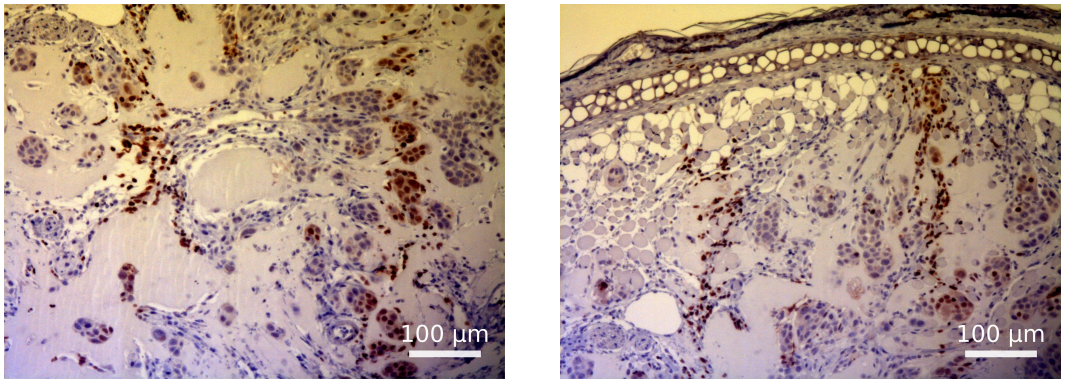

(a) (b)

Figure 5.40.: *Microscopic images of a histological slice from an MRT irradiated tumor grown in NMRI (nu/nu) mice. FaDu cells were stained with γ-H2AX (brown labeling) to visualize the DNA double-strand breaks. In (a) a center region is shown, in (b) the epidermal layer at the top is included.*

proven by a larger number of histological slices to avoid artifacts from the low cell density and cutting. Possible reasons are scattering in the tissue, grating imperfections, and bystander effects. An increase of the γ-H2AX tracks due to scattering from the peak dose into the valley and because of bystander effects is yet unlikely as a previous study reported on peak doses of at least 350 Gy for such effects to take place [89].

Hypoxia

To investigate hypoxia simultaneously to DNA double-strand breaks on neighboring histological sections, pimonidazole (HP2-100Kit[30]) was injected i.p. 1 hour prior to tumor resection. Subsequently, primary and secondary mouse monoclonal antibodies were added for fluorescent labelling. Hypoxia, i.e. oxygen depletion, is caused by insufficient perfusion of the tumor because of its rapid growth. A higher degree of hypoxia is related to an increased radioresistance of tumors. Thus, the results from tumor growth delay can be correlated to the tumor composition. As the histological section only represents a small subregion of the tumor, and because of the small tumor size chosen and additional unspecific binding of the marker, few hypoxic areas could be detected. Hence, further development is required to correctly identify hypoxic areas.

Angiogenesis

Moreover, staining of the vascular system was established with the commonly applied CD31 marker. If vessel ruptures caused by microbeam irradiation become visible, these could be correlated to the γ-H2AX staining on a neighboring histo-

[30]Hypoxyprobe, Burlington, MA, USA

logical section. In a first step, tumors from the pilot study for tumor growth delay were resected after reaching the stop criterion to analyze the vascular system in larger entities of 5 to 8 mm. An exemplary image from fluorescence microscopy is shown in Fig. 5.41 with DAPI stained cell nuclei in blue and CD31 stained vascular structures in red.

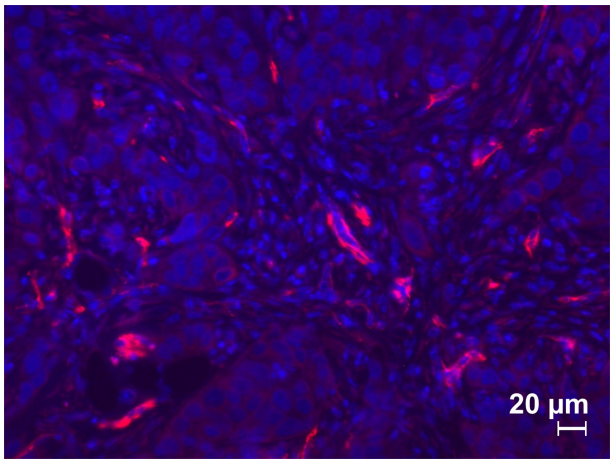

Figure 5.41.: *CD31 staining on histological section of a FaDu tumor. The tumor was resected at a diameter of 5 to 8 mm after studying tumor growth delay in a pilot study.*

A distinct vascular system can be well observed with the chosen staining method. At such a tumor size, some vessels might be large enough in the two-dimensional image to detect radiation-induced ruptures. However, damage to the vascular system needs to be observed directly after therapeutic treatment, where the tumors have reached an extension of 2 to 3 mm along the major axis. First observations indicate that, in this case, the vessels are less pronounced and the entire vascular system seemed to be still quite immature. If the beneficial effect of MRT compared to homogeneous irradiation is partially based on vessel rupture, maybe the small tumors irradiated in the tumor growth delay study might not have been affected as the vascular system had not yet been well-developed.
To validate the histological information based on a two-dimensional extract of a subregion of the tumor, 3D imaging, in particular with regard to the vascular system, is highly advantageous. Therefore, the ex-vivo analysis was extended by X-ray staining for CT imaging as described in the next section.

5.4.8. Tumor analysis in 3D – X-ray computed tomography

The analysis of vascular structures in three dimensions is highly beneficial compared to 2D histological slices. Not only distortions due to the histological cutting procedure can be avoided but moreover, the individual vessels can be imaged as a whole and thus ruptures possibly caused by X-ray microbeams might become observable. Additionally, the tumorous structure can be visualized, analyzed, and compared with the results from tumor growth delay, clonogenic cell survival, and

chromosome aberrations for each irradiation type. If CT staining is followed by standard histological sectioning to stain DNA damages, vascular endothelium, or hypoxia, as described in the previous section, observations from 2D and 3D imaging can be compared and complemented.

5.4.8.a. Protocol

A fast diffusion iodine staining was applied as developed by Martins *et al.* [194]. After resection, tumors were fixed in 4% formaldehyde in PBS. Several days after fixation, tumors were prepared with a graded dehydration series of ethanol (graded ethanol concentration fixation (GECF)) to avoid shrinkage of the sample and subsequently stained with iodine. The GECF was accomplished by a series of ethanolic solutions in concentrations of 50, 70, 80, 90, 96, and 100%, each for 1 h. The dehydrated tumors were then stained in 0.5 wt% I_2 solution in ethanol for 1 h before CT scanning. In some cases, a second staining procedure was applied with the same iodine concentration for another hour to improve penetration of the stain. Subsequent to staining, tumors were washed in ethanol and positioned tightly in 0.5 ml microcentrifuge tubes in air for imaging (described below). Following imaging, ethanol was added to the tumor and the tumor was transported to the pathology department (Klinikum rechts der Isar, TUM) for paraffin embedding.
The CT images were acquired at a commercial micro-CT setup (Zeiss Xradia 500 Versa[31]). The X-ray tube was operated at 40 kVp with at least 1 W power for an exposure time of 1 to 3 s. The source-to-sample and sample-to-detector distances were adjusted to optimize resolution, photon statistics, and sample positioning. Overview scans were taken with 0.39-fold optical magnification, whereas selected regions of interest were measured with 4-fold magnifying optics. A binning factor of 2 was applied. For each CT scan, 1601 projections were taken from 0 to 360°. Tomographic reconstructions were performed with the Xradia volume reconstruction software, or with iterative reconstruction algorithms developed at the Chair of Biomedical Physics (E17)[32].

5.4.8.b. Results and Discussion

A visual impression of the three-dimensional data set is given by a 3D rendering of the tumor in Fig. 5.42. Different perspectives and regions of interest of the tumor were chosen to show an overview of the tumor specimen, which is surrounded by an epidermal layer (Fig. 5.42 (a)), and more detailed vascular structures in Figs. 5.42 (b) to 5.42 (d). These images were acquired interactively within the Xradia software, which did not allow to add a scale bar – the tumor size accounts to several mm (for a quantitative scale, please refer to the next figure). Images shown in this section were taken at a source-to-sample distance of 13 mm and a sample-to-detector distance of 125 mm, yielding an effective pixel size of 6.4 µm. Most

[31] Carl Zeiss Microscopy, Pleasanton, CA, USA
[32] TUM, Munich, Germany

of the bright regions correspond to iodine stained structures. Iodine ($Z = 53$) has a high absorption coefficient compared to tissue consisting mainly of water ($Z \approxeq 7.4$). Only tumors which have been stained twice are shown here as this procedure significantly improved vessel visibility. In the rendered volumes, the transparency was adapted for each image to focus on different aspects. For orientation purposes, several cyan markers indicate the position of epidermal layer, vessels, and hair follicles.

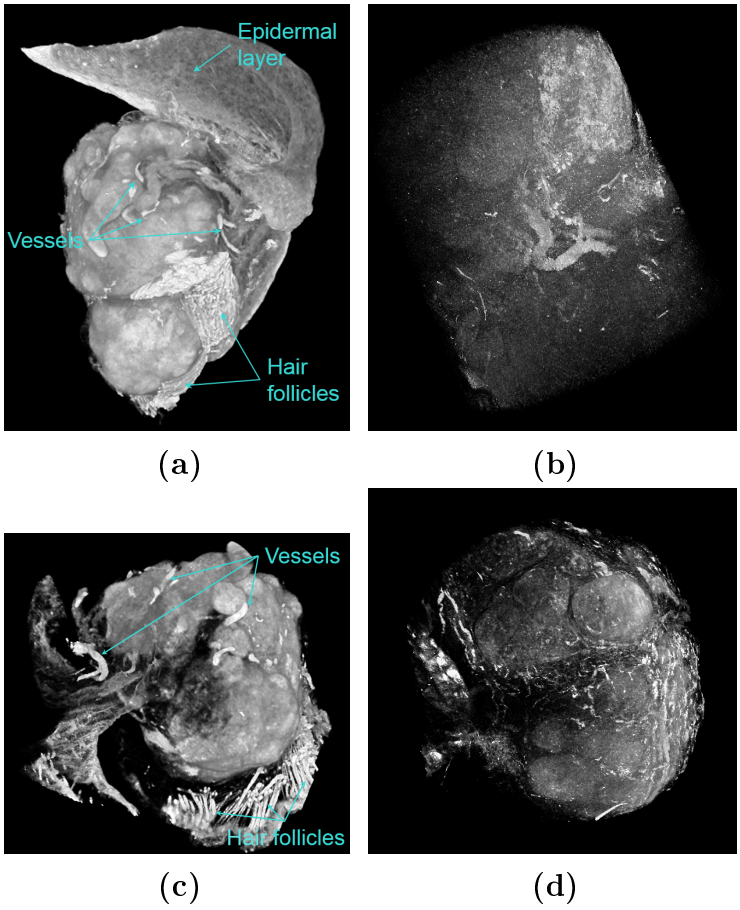

Figure 5.42.: *Three-dimensional rendering from X-ray imaging of an iodine-stained tumor, resected following tumor growth examination. In (a), an overview of the tumor entity is shown, including parts of the epidermal layer of the mouse ear to the top. In (b) to (d), different perspectives and regions of interest of the same tumor entity are presented to visualize the vascular system in 3D. The transparency window and the scale were varied to focus either on vascular structures or tumor composition.*

Fig. 5.42 (a) shows the tumorous tissue partially covered by an epidermal layer, where pores in the skin are distinguishable. When focusing on the tumor itself, a quite large number of short vessels can be discerned surrounded by the cloud-like tissue. At the right side, fibrous structures are visible, which are probably from hair follicles that can be built also in nude mice. Iodine can penetrate through and bind to these channels, such that the follicles appear bright as well. From a different perspective, these follicles are visible at the bottom of the sample in Fig. 5.42 (c). Yet, to analyze the effect of microbeam irradiation on the vascular system, sufficient resolution of vessels is required. A region of interest within the tumor is given in Fig. 5.42 (b), where additionally to the large vascular structures seen in the overview image, many small vessels can be observed. Fig. 5.42 (d) presents the vascular network extending on the adverse side of the epidermal layer

with good resolution.
Fig. 5.43 (a), 5.43 (b), and 5.43 (c) depict axial, coronal, and sagittal slices of the tumor entity, respectively. Post-processing was applied to the reconstructed images to reduce noise using an edge-preserving anisotropic diffusion filter (Perona-Malik filter) as described in [133].

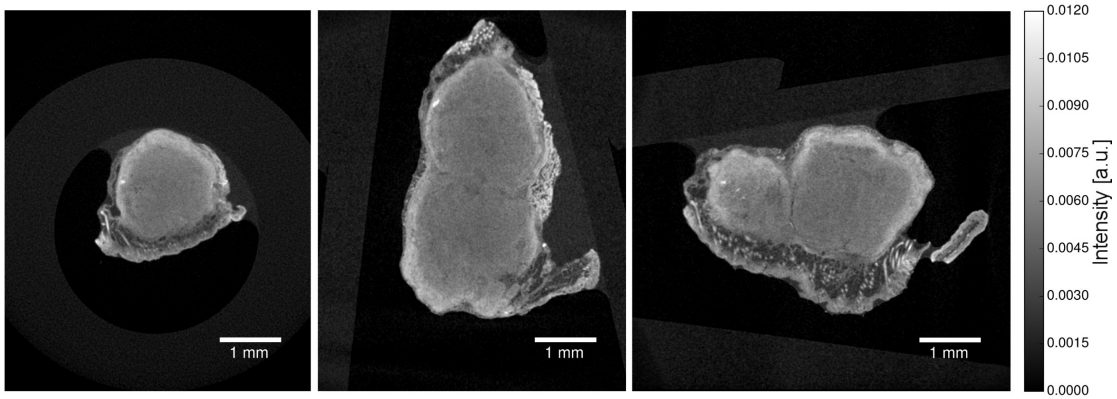

Figure 5.43.: *X-ray microscopy of iodine-stained tumor, resected following tumor growth examination. In (a), the axial slice is shown, complemented by the sagittal slice in (b), and the coronal slice in (c). Post-processing was applied using an edge-preserving anisotropic diffusion filter to reduce noise.*

Several vessels are seen as bright spots in all three sections. The tumor seems to be subdivided in two parts as visible in the coronal and sagittal images. At the center, the density of the tumorous tissue is rather inhomogeneous. In the future, one could investigate if areas with a lower cell density like hypoxic regions can also be detected with X-ray micro-CT. Therefore, a comparison with 2D histological slices of the same region could be performed.
It becomes obvious that in 2D images, the vascular system and the tumor composition cannot be perceived as a whole in contrast to the rendered volumes. In histology, only one of the three sections would be available – or a stack of parallel planes if serial sectioning is applied. Consequently, the three-dimensional information given by micro-CT imaging compared to standard histological sectioning offers clear advantages to correctly analyze the tumor volume. Even if serial sectioning is performed, the subsequent slice can only be acquired at a distance of several µm to the preceding one such that much information is lost. For example, the vessel might already have ended or changed direction with respect to the analyzed plane. If vessel rupture after microbeam irradiation is to be investigated in such small tumor volumes, 3D information is crucial to choose the plane of interest within the tumor volume in a flexible manner.

5.4.8.c. Conclusion of tumor imaging in 3D

In conclusion, micro-CT imaging of iodine stained tumors allows to visualize the tumor vasculature with high resolution and is a promising candidate to study rupture of vessels induced by microbeam irradiation. Extending the staining protocol by a second staining procedure allows to significantly improve contrast in X-ray CT imaging. Further investigations on the compatibility of iodine staining with other staining procedures have to be conducted. Amongst others, hypoxia will be analyzed using pimonidazole. This marker has to be injected one hour before the animal is sacrificed. Subsequently, the tumor is fixed in paraformaldehyde, dehydrated in ethanol, and stained for X-ray CT imaging. Lastly, hypoxia can be analyzed with fluorescence microscopy. If the pimonidazole marker is affected by this procedure or if the iodine staining causes artifacts in fluorescence microscopy has to be analyzed in a future study. Moreover, the combination of CD31 staining and iodine staining has to be tested. In principal, the iodine stain has been reported to be reversible if the specimen is washed with phosphate buffered formal saline (PBFS) until coloration of the PBFS by the stain has ceased [195]. Ideally, the 2D histologically stained slices can then be compared to sections of the 3D volume from CT imaging. Information on the density of tumor tissue, hypoxic areas, and vascular structures could thus be verified and complemented.

5.5. Summary and outlook of experimental studies on MRT

Overview

In conclusion, microbeam irradiations were successfully conducted in-vitro and in-vivo at laboratory-sized X-ray sources. This is an important step to facilitate research on the radiobiological effect of MRT and to prepare a way towards its future clinical application.
In-vitro, the application of microbeam widths smaller than 10 µm using a rotating anode X-ray tube was confirmed via γ-H2AX staining. Further quantitative investigation of the radiobiological effect after MRT can thus be performed with a conventional, cost-efficient, laboratory-sized system. This includes, for example, the optimization of the microbeam geometry. At a compact synchrotron X-ray source, the MuCLS, a beneficial sparing effect of MRT in contrast to homogeneous treatment was observed after irradiation of normal tissue cells with 25 keV X-rays. This included an increased clonogenic cell survival above 2 Gy mean dose with respect to homogeneously irradiated cells and a reduced cytogenetic damage at mean doses of 1 to 2 Gy. With the same settings, a xenograft of FaDu cells grown in the mouse ear was irradiated in-vivo. However, microbeam irradiation with 3 or 5 Gy mean dose did not lead to a measurable tumor growth delay with respect to non-irradiated mice. Only after 5 Gy homogeneous irradiation, a trend for tumor growth delay could be stated. Possibly, the applied doses at a PVDR above 200 (i.e. a low valley dose) were insufficient to achieve a tumoricidal effect after MRT. On the one hand, a peak dose of up to 35 Gy can lead to higher permeability of the vessels but does not lead to vessel rupture, which is assumed to be important for the preferential microbeam effect. On the other hand, the tumor size at the time of irradiation could have been too small such that the vascular system was not developed well enough to observe an effect of vessel damage. To better understand the underlying mechanisms, protocols for immunohistological and X-ray computed tomography staining were adapted to this study. Results regarding the investigation of proliferation, hypoxia, and in particular, vascularity in addition to tumor growth delay after irradiation promise detailed insights into the tumor response in future experiments.

At a rotating anode X-ray tube: optimizing microbeam geometry in-vitro

At a conventional rotating anode X-ray tube, the dose rate is sufficient to investigate the radiobiological effect of MRT in-vitro. The microbeam profile was varied using absorption gratings with different periods and slit widths. Hereby, less than 10 µm wide microbeams could be applied to cell monolayers. The dose profile showed accordingly distributed DNA double-strand breaks with high contrast (PVDR) for microbeams of 7 µm spaced by about 13 µm. Thus, the effect of

smaller microbeams than previously used can be investigated to optimize the microbeam geometry. To this end, quantitative investigation of the radiation-induced damage is necessary, for example, by analyzing clonogenic cell survival for normal tissue and tumor cell lines. With the on-going development of higher aspect-ratio gratings, the PVDR can be significantly improved in the future. Moreover, two gratings with the same structure could be aligned in parallel to vary the microbeam width. Using such high aspect-ratio gratings, precise alignment of the grating lines perpendicular to the beam path will be highly important to avoid shadowing. A recent microbeam study using a conventional X-ray tube reported on the use of a tungsten multislit collimator with tilted slits to avoid penumbral blurring while reducing the distance to the source for higher dose rates [196]. In the last years, methods to bend absorption gratings have been introduced (e.g. [197,198]), which would provide a similar option as the tungsten multislit collimator but for smaller microbeam widths. Even if the PVDR is not as high as in other microbeam studies, it could be worthwhile to investigate cell survival and relative biological effectiveness with a less pronounced re-distribution of the dose compared to standard homogeneous irradiation. Possibly, the locally higher concentration of DNA DSBs at the same mean dose could be beneficial for tumor cell killing while sparing normal cells. Furthermore, as the source size is large, penumbral blurring will lead to a quite homogeneous dose distribution at a relatively short distance to the grating (with the here-described setup). Similar to so-called grid therapy [8] or proton microbeam therapy [51], this effect could be used to irradiate superficial tumors with a homogeneous dose distribution while sparing skin tissue. All in all, using a rotating anode system is a cost-efficient way to investigate the radiobiological effect of microbeams in-vitro.

At the MuCLS: applying MRT to normal tissue cells in-vitro and to tumorous tissue in-vivo

With the first commercial installation of a compact synchrotron X-ray source based on inverse Compton scattering, radiobiological effects after microbeam irradiation were observed in-vitro and in-vivo in contrast to conventional, homogeneous irradiations. 25 keV X-rays were applied with a flux of about 1×10^{10} ph/s yielding a dose rate of up to 5.3 Gy/min (homogeneous beam with collimation optics). Following a recent upgrade of the machine with respect to the laser system, a flux of 3×10^{10} ph/s is achievable such that an accordingly higher dose rate will be available for future experiments.

Setup. For both, the in-vitro and the in-vivo experiment, a dedicated setup was developed, which allowed to control positioning and irradiation remotely. For irradiations of tumors in the mouse ear, an imaging system with a CCD camera was installed to place the tumor in the center of the beam aperture. Appropriate

holder and heating for the anesthetized mouse were designed to protect the animal from unnecessary radiation and guarantee its well-being.

Dosimetry. Methods for dosimetry were evaluated yielding a difference of about 20% between film dosimetry (ionization chamber dosimetry) and dose calculation via photon-counting. In particular, an error of up to 10% in dose can be caused especially by the uncertainties of absorption coefficients and the spectrum used for dose calculation. Small error sources in ionization chamber dosimetry, especially the operation at its lower limit of acceptable dose rate, can further increase the difference in dose. Recent upgrades of the MuCLS, mentioned above, allow to further investigate the difference in absolute dose in a next step. A more accurate simulated spectrum could be achieved in the future if the electron beam emittance is not deduced from the measured spectrum but recorded directly by an appropriate diagnostics. Yet, for comparison of homogeneous to microbeam irradiation applying the same mean dose, a relative dose value was sufficient. Online dose monitoring with the photon-counting method was successfully implemented to take flux variations over time into account and was optimized to deliver the desired dose within a relative standard deviation of $\sim$1% (in-vivo experiment). If the target is oblique to X-rays and its composition is not well-known, a calibrated transparent transmission counter can be used in front of the irradiation target.

Microbeam creation. Microbeams of 50 µm width separated by 300 µm valleys were created with a 200 µm thick tungsten slit array produced by laser micromachining. Comparing homogeneous and microbeam dose rate, a ratio of about 1/7.4 was measured, which approaches the expected ratio of 1/7. The characterization of the tungsten grid allowed to specify a region of interest with a quite regular pattern, well-suited for microbeam experiments in-vitro and in-vivo. In the future, to improve comparability to other studies, a higher degree of homogeneity of the slit width and a reduced taper should be accomplished. Therefore, either optimization of the laser-micromachining technique or different material processing methods could be taken into account. Once higher X-ray energies are available at such a compact synchrotron, the tungsten thickness has to be increased or a different material has to be chosen to guarantee X-ray absorption. In this case, techniques like water-jet guided laser cutting or wire cutting might be preferential.

Beam collimation. A high dose rate is important for microbeam irradiations to avoid any motion artifacts and to minimize repair mechanisms being initiated before the end of irradiation. To increase the dose rate at the MuCLS, a polycapillary optic (custom-made by IfG GmbH) was implemented and tested. Successful beam collimation with slight focusing to a focal spot of $2 \times 2.3 \times \pi\,\mathrm{mm}^2$ was achieved using 25 keV X-rays resulting in a flux enhancement by a factor of 22. As this focal spot size reaches the lower limit for in-vivo experiments, the design of the optic was adapted to create a focal spot of about 4 mm. This recently acquired optic requires further characterization before being used in future experiments. A larger focal

spot implies a lower dose rate as seen in the present studies, which, however, can be more than compensated by the almost 3-fold higher flux meanwhile available at the MuCLS.

Irradiation fields. Additional to single field irradiations, the feasibility to stitch two neighboring fields has been demonstrated, such that different tumor sizes can be treated with good target volume coverage. To further increase accuracy, motorized stages with a finer stepping could be employed. As expected, an impact on tumor growth behavior using differently shaped fields of similar size could not be identified.

In-vitro study. In a first study, radiobiological effects were investigated in-vitro after microbeam irradiation of normal-tissue cells compared to conventional, homogeneous irradiations. The application of higher mean doses – in a dose range from 1 to 4 Gy – resulted in a lower reduction of cell survival using microbeams, i.e. a decreasing RBE value with dose. This suggests a tissue sparing effect for MRT irradiations. Moreover, a very small amount of chromosome aberrations was observed after MRT at 1 and 2 Gy mean dose. The low RBE highlights the significantly reduced cytogenetic damage compared to homogeneous irradiations at the same dose. This can be correlated to a lower risk of second cancer development. Consequently, a beneficial effect of MRT for normal tissue cells could be validated using the MuCLS.

In-vivo study. As a next step, microbeam experiments were established in-vivo to investigate if higher tumor control can be achieved while possibly sparing normal tissue using the MuCLS. For this purpose, xenografts from FaDu cells injected in the mouse ear were irradiated to analyze radiation-induced tumor growth delay. In a first study, no tumor growth delay could be observed after microbeam irradiation with 3 and 5 Gy mean dose using 25 keV X-rays at the MuCLS. After 5 Gy homogeneous irradiation, a trend of tumor growth delay became visible. The MRT peak dose might have been too low to achieve an effect in tumor growth delay as vascular structures might not have been sufficiently damaged. Moreover, the tumor size was quite small which could imply an immature state of the vascular system. Thus, any differences observed between sham or control tumors and irradiated tumors might be less related to vascular damage but rather to radiosensitivity of the cells. For a future study, an increase in MRT dose and in tumor size seem to be required to achieve a preferential MRT effect. Moreover, the xenograft model needs to be improved to avoid development of metastases and to increase take rate and reproducibility, e.g. following [182]. Better understanding of the results will be gained by histological analysis with respect to vascularization, perfusion, and hypoxia, which has been tested in a pilot study. Additionally, 3D X-ray imaging using an iodine staining protocol was successfully applied to the resected tumor tissue, such that the vascular system can now be analyzed as a whole with high resolution. Thus, by CT imaging, vessel rupture could become observable, which

often comes along with reduced perfusion, measurable via histological staining. From the amount of hypoxic areas in these small tumors, one could conclude on the radioresistance of the tumors. The latter is also being analyzed via clonogenic cell survival after tumor growth delay using a dose escalation procedure. Additionally, chromosome aberrations are studied in the re-cultured tumor cells. While not claiming to be exhaustive (e.g. regarding gene expression and other subcellular processes), these diverse approaches shall create an overall picture of the radiation-induced effects of MRT at the MuCLS.
If, in a future experiment, a tumoricidal effect can be achieved by microbeam irradiation, additional investigations with respect to normal tissue sparing would be of interest to validate the promising results observed in-vitro at the MuCLS. Priyadarshika *et al.* [87] report that, using the same mean dose, microbeam and homogeneous irradiation result in the same effect on normal tissue. As this finding somehow contradicts the results of our in-vitro study, further in-vivo studies could clarify this inconsistency, e.g. by targeting the skin of a mouse ear following [52]. Only with the knowledge of radiation-induced effects on both, normal and tumorous tissue, the therapeutic index of MRT compared to conventional treatment can be estimated.

The MuCLS. The first commercial compact synchrotron based on inverse Compton scattering delivers nowadays a homogeneous and stable X-ray beam appropriate for preclinical microbeam irradiations in-vitro and in-vivo. Machine upgrades to the current system have been performed and are foreseen to increase flux and flux stability when operating the MuCLS at high efficiency. Hence, with a higher dose rate, doses on the order of 100 Gy will be available to realize the above proposed studies in-vitro and in-vivo with superficial tumors.
Further development of MRT towards its clinical application will require higher X-ray energies than 25 keV to increase the penetration depth of the X-rays and a higher dose rate. Energies above 100 keV could be achieved by enlarging the linear accelerator and the storage ring to reach a higher electron energy which leads to a quadratic increase of the X-ray energy. The according technical realization seems feasible. Moreover, the laser wavelength could be reduced from infrared to green laser light. Hence, the energy of the laser photons is increased, which scales linearly with the X-ray energy. For this purpose, a corresponding enhancement cavity with sufficient finesse and stability for a CLS has to be developed. Yet, advancement of CLS systems, especially towards higher energies, will depend on the demand of the research community.

Overall summary and outlook

In this thesis, first microbeam irradiations using a compact synchrotron X-ray source were demonstrated in-vitro and in-vivo. The sparing effect of MRT was confirmed in normal tissue cells. In-vivo, tumor growth delay after MRT could not be observed with the current settings. As many aspects contribute to radia-

tion damage of normal tissue and tumor, the analysis of the acquired results is complex. With the established setup at the MuCLS and the biological and imaging protocols developed, experimental studies on MRT at the MuCLS can now provide added value to the understanding of radiation-induced effects. Optimization of technical and biological procedures will allow to improve reproducibility in a future experiment. Moreover, further development of dosimetric methods is required to reduce the error in absolute dose. Additional simulations to the experimental setup are of high interest to analyze dosimetry, for example, with respect to PVDR at the MuCLS.
With experimental and theoretical data at hand, results from microbeam irradiations at the MuCLS can contribute to existing research on MRT and yield new insights by investigating a different parameter space with respect to lower energies and peak doses at a higher PVDR. As a higher therapeutic effect of MRT compared to conventional treatment has been observed in previous studies, MRT will remain a promising candidate for radiation therapy of radioresistant tumors. The feasibility of microbeam irradiations at the MuCLS demonstrates a substantial achievement as only a compact and cost-efficient X-ray source like the MuCLS will allow to realize a routine treatment of human patients with MRT in the future.

6. Summary, conclusions, and outlook

In summary, this work showed the applicability of microbeam radiation therapy (MRT), a preclinical radiotherapeutic approach, for cells and small animals at laboratory-sized X-ray sources. Microbeam radiation therapy has the potential advantage of sparing normal tissue due to the spatially distant microbeams while achieving a high tumor control because of its selective effect on normal and tumorous tissue. Up to now, studies to improve the understanding of the underlying biological mechanisms have been mainly performed at large-scale synchrotron facilities. Here, the possibility to perform further research on MRT at more cost-efficient, laboratory-sized X-ray sources was successfully demonstrated.

Analysis of microbeam geometry towards smaller beam widths

In this context, microbeam geometry was analyzed towards finer structures with regard to typical microbeam widths of about 50 µm and peak-to-peak spacings between 200 and 400 µm. To verify the creation of these microbeam patterns with high resolution, the performance of different detection methods like radiochromic films, nuclear track detectors, camera systems and an X-ray fluorescence setup was investigated. Radiochromic films provide access to the microbeam dose profile via ionization chamber dosimetry whereas for the other methods, conversion of measured intensity values to dose has to be established. For **EBT films** with a dynamic dose range from 0.1 to at maximum 60 Gy, a **resolution on the order of 10 µm** was determined, which is mainly limited by film granularity. Dedicated camera systems can provide resolution below 1 µm at the drawback of low efficiency. While, in principle, nuclear track detectors as well as X-ray fluorescence scanning could allow for even higher resolution in the nanometer range, these techniques are not only limited by efficiency, i.e. require high X-ray flux but also by a high complexity of data analysis. Hence, further development of such high-resolution detection methods is necessary if MRT shall be applied with structures of a few micrometer. Due to the penetration depth of secondary electrons of already 13 µm at 25 keV, the application of very fine structures yields a **microbeam dose profile** which might exhibit a **very low peak-to-valley dose ratio**, contradicting the use of MRT. The contrast between peak and valley could only be enhanced by a large enough spacing of the beamlets considering X-ray energy and target material. By the use of gratings with varying duty cycles, the dependence of PVDR on peak-to-peak spacing was **confirmed via film dosimetry and γ-H2AX staining**

of cells irradiated at a rotating anode X-ray tube. From experiments and simulations, achieving an alternating dose pattern with a reasonable peak-to-valley dose ratio – reasonable in the sense of possible reaching a preferential effect of MRT compared to conventional treatment – requires a **minimum microbeam width and spacing on the order of several micrometers**. This finding implies that the microbeam spacing has an upper limit given by the tumor coverage required to reach tumor control.

Creation of microbeams for low keV X-rays

The creation of microbeams with **fine structures** was achieved with **gold absorption gratings** fabricated by the **LIGA process**. While the fabrication process of such gratings is highly demanding, further developments achieved in the last years with respect to higher aspect-ratios and substrate thinning will allow for an increase of peak-to-valley dose ratio in MRT in the future. For a **typical microbeam pattern**, a **tungsten plate** with 50 µm wide slits was produced by **laser-micromachining** yielding relatively homogeneous structures. This process can be applied for thin plates which fully absorb low X-ray energies but might become challenging with increasing thickness of the absorber. In this case, wire-cutting techniques or, maybe, LIGA for gold absorption gratings might become interesting.

MRT at the MuCLS

At the first commercial compact synchrotron based on inverse Compton scattering, the MuCLS, microbeam irradiation was established in-vitro and in-vivo. During the experiments a **flux of up to 1×10^{10} ph/s** was available at an X-ray energy of 25 keV. To enhance the homogeneously applied **dose rate** to **5 Gy/min**, a dedicated polycapillary optic was successfully implemented. Recent upgrades on the laser system allowed to triple the available X-ray flux such that future MRT experiments can benefit from a correspondingly higher dose rate.
Radiation-induced biological effects were quantified with respect to clonogenic cell survival and chromosome aberrations in normal tissue cells. **Increased cell survival and reduced cytogenetic damage after MRT treatment** compared to homogeneous (conventional) irradiation was observed. This confirms the sparing effect of MRT and indicates a possibly lower risk of secondary tumor development after MRT. To investigate the tumoricidal effect of MRT applied at the MuCLS in-vivo, a tumor growth delay study of xenografts grown in the mouse ear was conducted. With mean doses of 3 and 5 Gy and MRT peak doses of up to 21 and 35 Gy, respectively, tumors of 2-3 mm in diameter were irradiated. For this purpose, an **accurate positioning system** and **online dosimetry methods** were developed. **No tumor growth delay after MRT** compared to a control group was measured. Homogeneous 5 Gy irradiation yielded an almost significant delay. Possibly, a higher MRT mean dose with a peak dose towards 100 Gy is necessary to achieve lasting vascular damage in the tumor, and thus a preferential

effect in tumor control. To visualize the radiation damages, histological analysis of the resected tumors was established and extended to **computed tomography of** accordingly **stained tumors**. Hereby, the vascular system could be imaged with high resolution in three dimensions. If, in upcoming experiments, the staining procedure of resected tumors for computed tomography is shown to be not compatible with further histological staining, **high-resolution phase-contrast imaging** could be applied instead of absorption imaging to achieve a high soft-tissue contrast without staining agents.
In the future, additionally to an increase of the MRT dose, higher stability of the tumor model should be achieved using, for example, a **different tumor cell line** and **treating larger tumor volumes**. The latter can be realized with a polycapillary optic producing a larger focal spot at the disadvantage of a lower dose rate. The latter can be compensated by the higher X-ray flux available nowadays at the MuCLS. To explain the dose difference of 20% measured between film dosimetry and dose calculation using a photon-counting detector, further dose measurements and, maybe, appropriate simulations are required for **absolute dosimetry at the MuCLS**.

Forward-looking ideas

Future investigations of the microbeam effect at the MuCLS could include, for example, the use of **animals with window chambers** and stained vascular systems to track the radiation-induced damages in real time. Another approach would be to combine irradiation and radiographic imaging with X-rays, which would allow for **image-guided application of microbeams** and analysis of radiation-induced effects during irradiation.
The **clinical application** of MRT at a CLS system requires further technical development, in particular with regard to an **increase in X-ray flux** and **higher energies** to achieve a reasonable penetration depth of the X-rays. To realize X-ray energies above 100 keV, an enlargement of the linear accelerator for higher electron energies and a green laser enhancement cavity for higher laser photon energies would be advantageous. As has been shown in this work, the PVDR is highly energy-dependent. Let us assume that a CLS would produce clinically relevant X-ray energies with sufficient penetration depth for MRT. In this case, the almost monoenergetic, tunable X-ray source allows to **tailor the PVDR by the applied X-ray energy** such that an optimal aspect-ratio of peak and valley dose can be achieved. Therefore, among other emerging compact and brilliant X-ray sources, CLS systems might remain an interesting tool for MRT in the future.

Epilog

Coming back to the words of Antoine Béclère, *'La radiothérapie est à la fois le fruit le plus inattendu et le plus précieux de la découverte de Röntgen.'* [1]: yet, radiation therapy will only be a precious fruit as long as we apply the radiotherapeutic treatment in a prudent and conscious manner with respect to radiation

damage caused in the normal tissue. Therefore, it is important to continue research on radiotherapeutic approaches like MRT that allow to widen the therapeutic window. Also if clinical protocols for some cancers are well-developed and show a high success rate, there might be a lower risk of second cancer development with a different therapeutic technique. Particularly with regard to our ageing society, more emphasis has to be placed on the avoidance of second cancer development. With a larger variety of radiotherapeutic methods, personalized treatment can become reality. For example, the irradiation technique could be chosen in dependence on the radiosensitivity of tumor and normal tissue cells of a patient.
While it is of high interest to understand the radiation-induced biological effects of these new techniques to optimize physical and dosimetric parameters, the macroscopic picture of radiation therapy should be kept in view. Up to now, a wide range of studies on MRT have shown its beneficial effect on survival rate and tumor control compared to conventional treatment using small animals up to piglets. Unfortunately, we can only estimate but not predict the future outcome of a therapy on humans unless a large cohort has been tested. Therefore, building a clinically applicable setup for MRT, like a further developed CLS or a so-called line focus X-ray tube as proposed by Bartzsch *et al.* [47], is necessary to progress. Appropriate patient therapy planning systems for MRT are under development [199]. With all these puzzle pieces combined, maybe, we can show one day that microbeam radiation therapy is part of the unexpected and precious fruit of Röntgen's discovery.

A. Appendix

In the following, additional information on experimental and simulated data is given, which offers added value and more detailed insights to the results presented in the main body of this thesis. The section name indicates to which part of the thesis the respective data belongs. The purpose of the figures is directly discussed in the figure caption.

A.1. To chapter 2.1.1

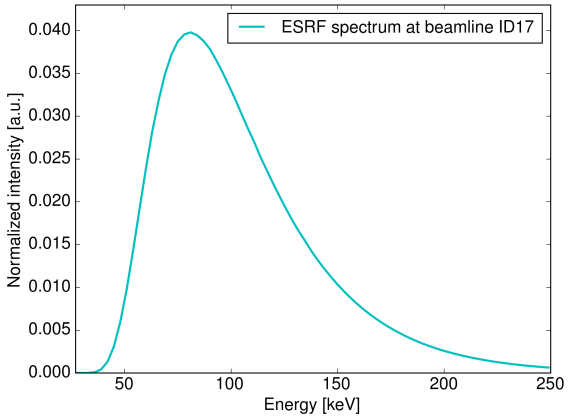

Figure A.1.: *Spectrum used for microbeam radiation therapy (MRT) experiments at the beamline ID17 of the European Synchrotron Radiation Facility (ESRF)*[1] *– labeled as ESRF spectrum throughout this thesis.*

[1] ESRF, Grenoble, France

A.2. To chapter 2.1.2

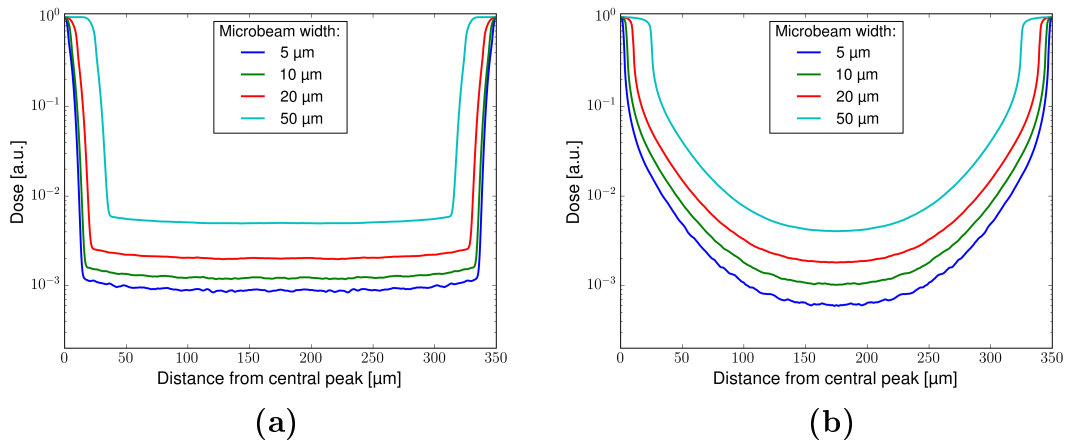

Figure A.2.: *Simulation of dose distribution in water along the distance from the central peak for microbeam widths of 5, 10, 20, and 50 µm with a period of 350 µm using MuCLS spectrum of the 25 keV configuration in (a) and the ESRF spectrum of 100 keV mean energy in (b).*

A.3. To chapter 5.1.2

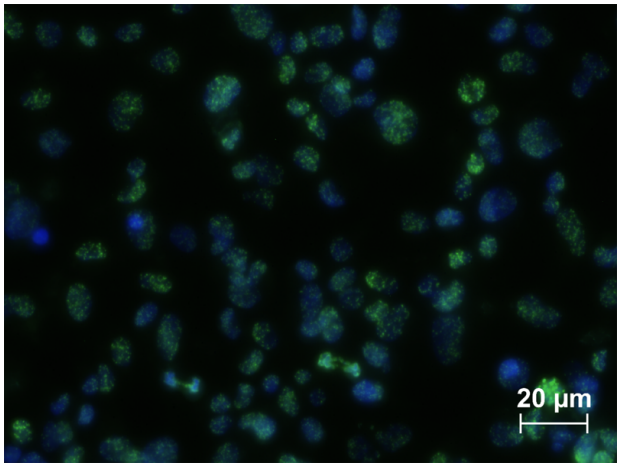

Figure A.3.: *Microscopic image of CHO-K1 cells using grating 15-0.7, yielding 4.35 µm wide microbeams with a mean dose of 5 Gy. Image taken with a 40-fold immersion objective. Note that γ-H2AX is stained in green. Resulting from low cell density, the distinction of valley and peak area is not apparent. Following the foci accumulation, however, a vertical stripe pattern can be recognized.*

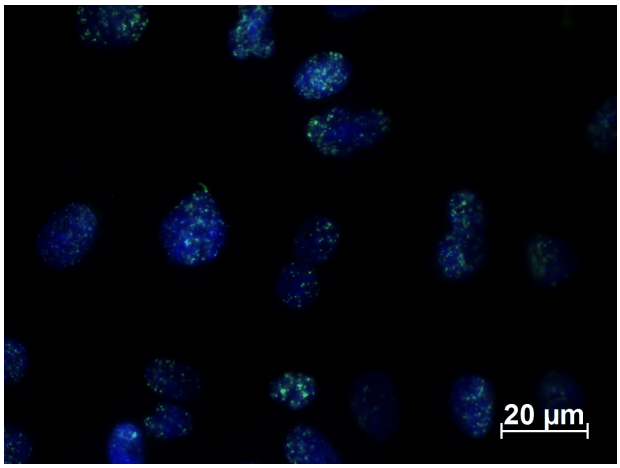

Figure A.4.: *Microscopic image of CHO-K1 cells using grating 15-0.6, yielding 5.85 µm wide microbeams with a mean dose of 5 Gy. Image taken with a 63-fold immersion objective. Note that γ-H2AX is stained in green. Due to the low cell density, the microbeam dose distribution is not clearly recognizable. Yet, the cells seem to be irradiated only partially indicating a successful dose redistribution.*

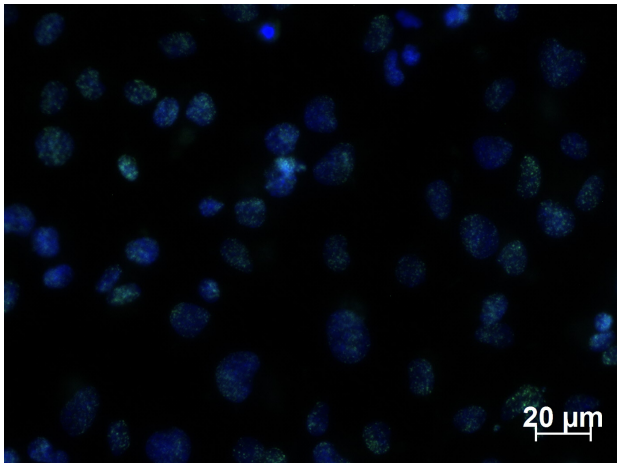

Figure A.5.: *Microscopic image of CHO-K1 cells using grating 15-0.5, yielding 7.35 µm wide microbeams with a mean dose of 5 Gy. Image taken with a 63-fold immersion objective. Note that γ-H2AX is stained in green. The low cell density hampers visualization of the microbeam dose distribution. As in Fig. A.4, the cells seem to be irradiated only partially suggesting that a higher dose is delivered in the peak area compared to the valley region.*

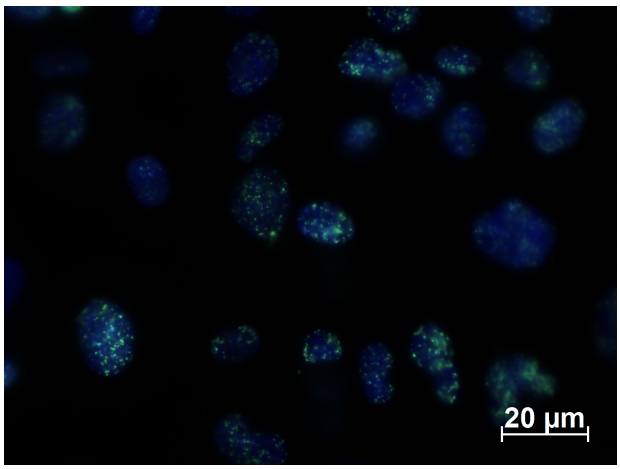

Figure A.6.: *Microscopic image of CHO-K1 cells using grating 5, yielding 2.5 µm wide microbeams with a mean dose of 5 Gy. Image taken with a 63-fold immersion objective. Note that γ-H2AX is stained in green. Preparation for microscopy led to corrugation of the Mylar foil, such that only the foci in the center are in the focal plane. While the foci distribution is not homogeneous, a clear microbeam pattern cannot be observed. This confirms the simulations shown in chapter 4.1 for EBT film dosimetry, where microbeams with a width smaller than 5 µm and a duty cycle of 0.5 showed a dose profile with low PVDR values.*

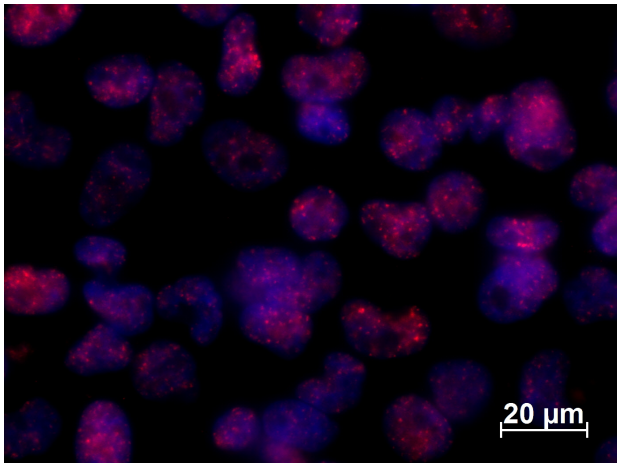

Figure A.7.: *Microscopic image of HeLa cells using grating 10, yielding 5 µm wide microbeams interrupted at periodic distances of a few micrometer because of the bridge design, with a mean dose of 4.2 Gy. Image taken with a 63-fold objective. As shown with 40-fold magnification, a distinction of peak and valley dose areas is not feasible using this grating design.*

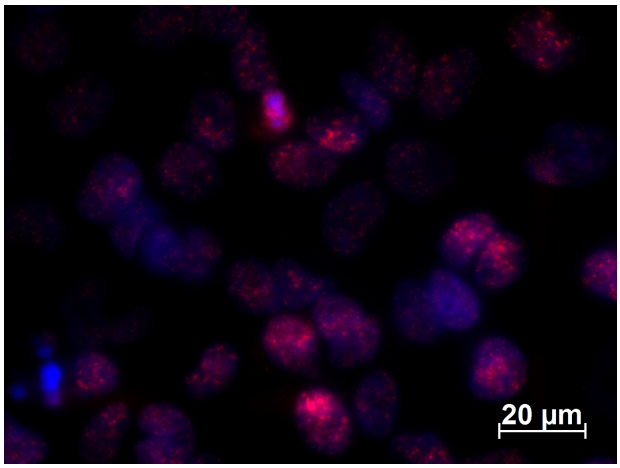

Figure A.8.: *Microscopic image of HeLa cells using grating 2.4cont, yielding 1.2 µm wide microbeams with a mean dose of 4.2 Gy. Image taken with a 63-fold objective. The foci seem to be homogeneously distributed, possibly resulting from a too low PVDR, discussed above for Fig. A.6.*

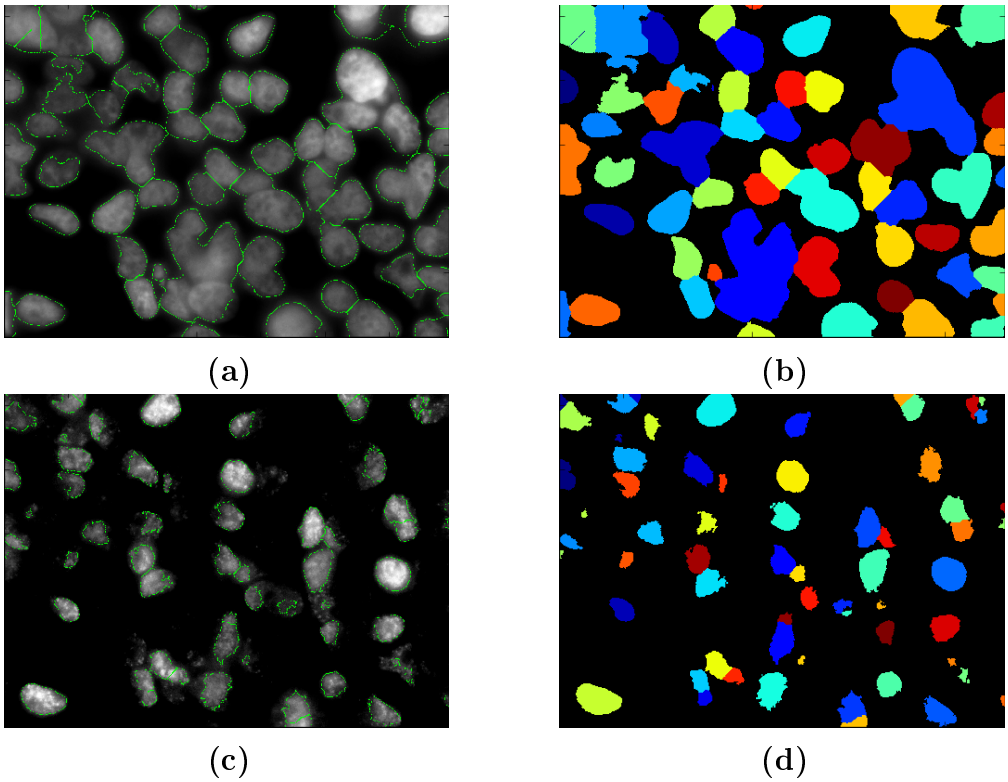

Figure A.9.: *Microscopic image of HeLa cells segmented with the image processing software CellProfiler [128]. Cells were irradiated at the rotating anode setup using grating 24, creating 12 µm wide microbeams with a mean dose of 8.4 Gy. Image taken with a 63-fold immersion objective. (a) DAPI stained cells with the outlines around the cell nuclei for segmentation. (b) Binary image obtained from (a) – the binary image is further processed to extract and weight the γ-H2AX signal from the according microscopic image. (c) Corresponding images visualizing γ-H2AX staining with the outlines around the foci at DNA double-strand breaks, leading to the binary image of the segmented cellular fractions in (d). The γ-H2AX image is presented to highlight the visibility of the microbeam pattern by staining DNA double-strand breaks but is not used for further analysis.*

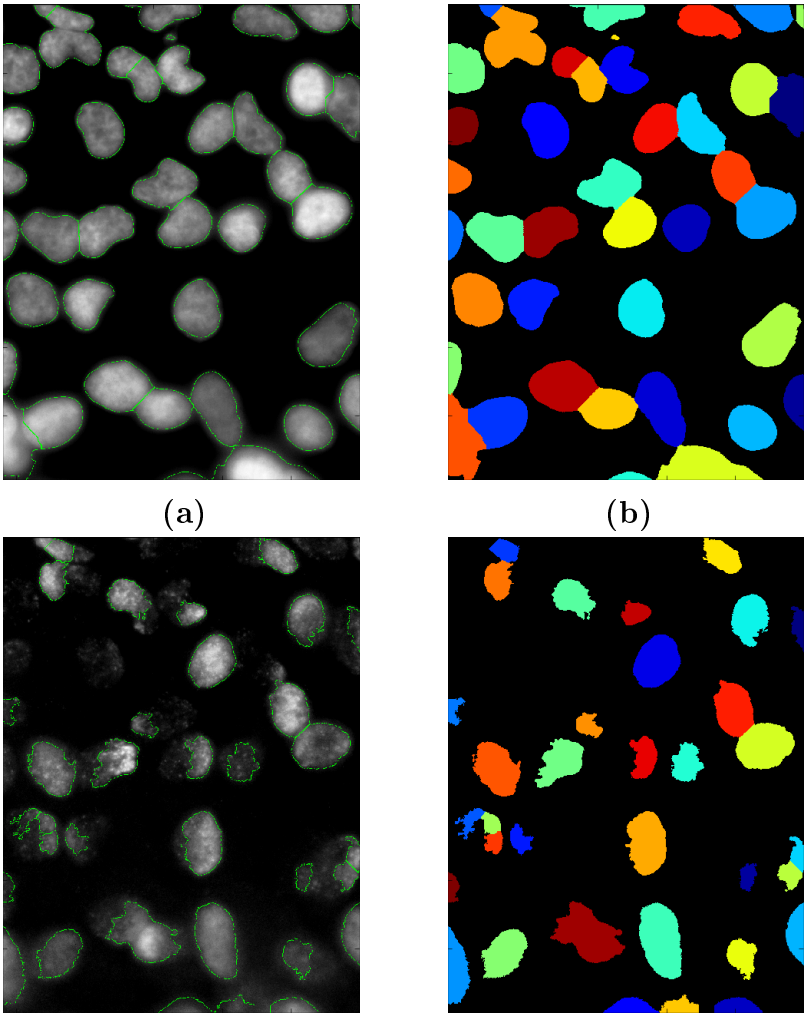

Figure A.10.: *Microscopic image of HeLa cells segmented with the image processing software CellProfiler [128]. Cells were irradiated at the rotating anode setup using grating 20, creating 6.9 µm wide microbeams with a mean dose of 8.4 Gy. Image taken with a 63-fold immersion objective. (a) DAPI stained cells with the outlines around the cell nuclei for segmentation, (b) binary image obtained from (a). (c) Corresponding images visualizing γ-H2AX staining with the outlines around the foci at DNA double-strand breaks, leading to the binary image of the segmented cellular fractions in (d). For comments, see Fig. A.9 above.*

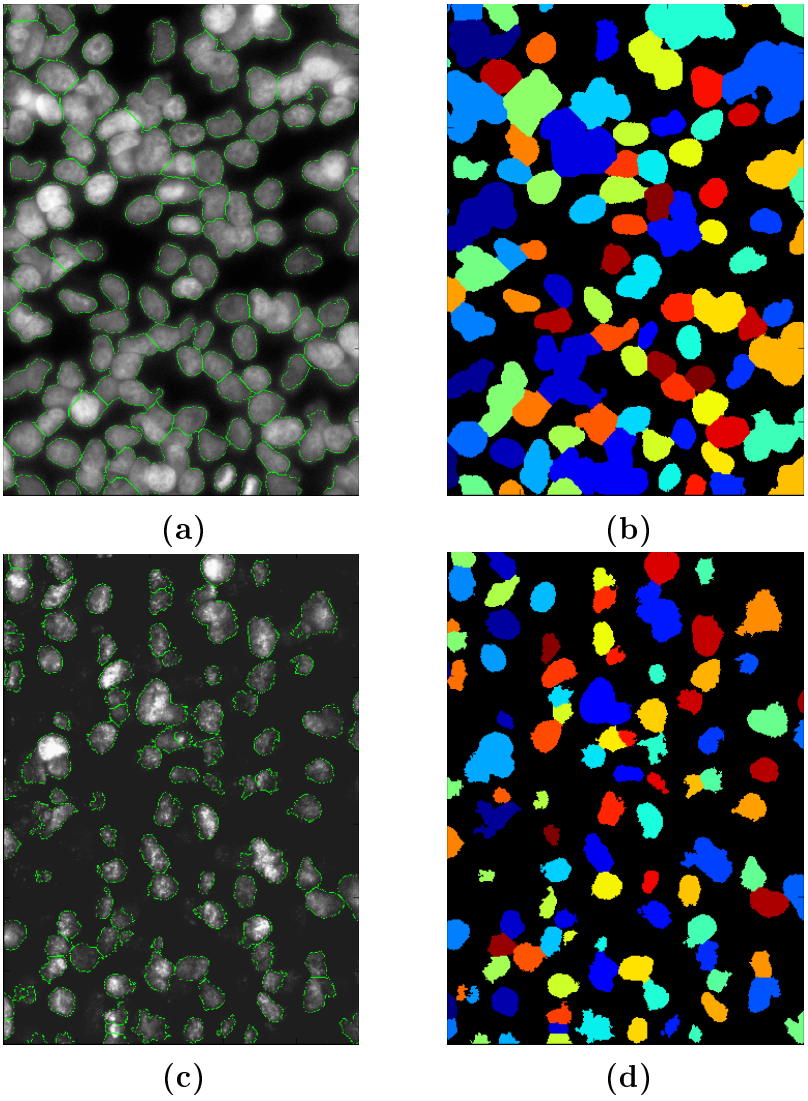

Figure A.11.: *Microscopic image of HeLa cells segmented with the image processing software CellProfiler [128]. Cells were irradiated at the rotating anode setup using grating 20, creating 6.9 µm wide microbeams with a mean dose of 4.2 Gy. Images taken with a 40-fold immersion objective. (a) DAPI stained cells with the outlines around the cell nuclei for segmentation, (b) binary image obtained from (a). (c) Corresponding images visualizing γ-H2AX staining with the outlines around the foci at DNA double-strand breaks, leading to the binary image of the segmented cellular fractions in (d). For comments, see Fig. A.9 above.*

A.4. To chapter 5.2.3

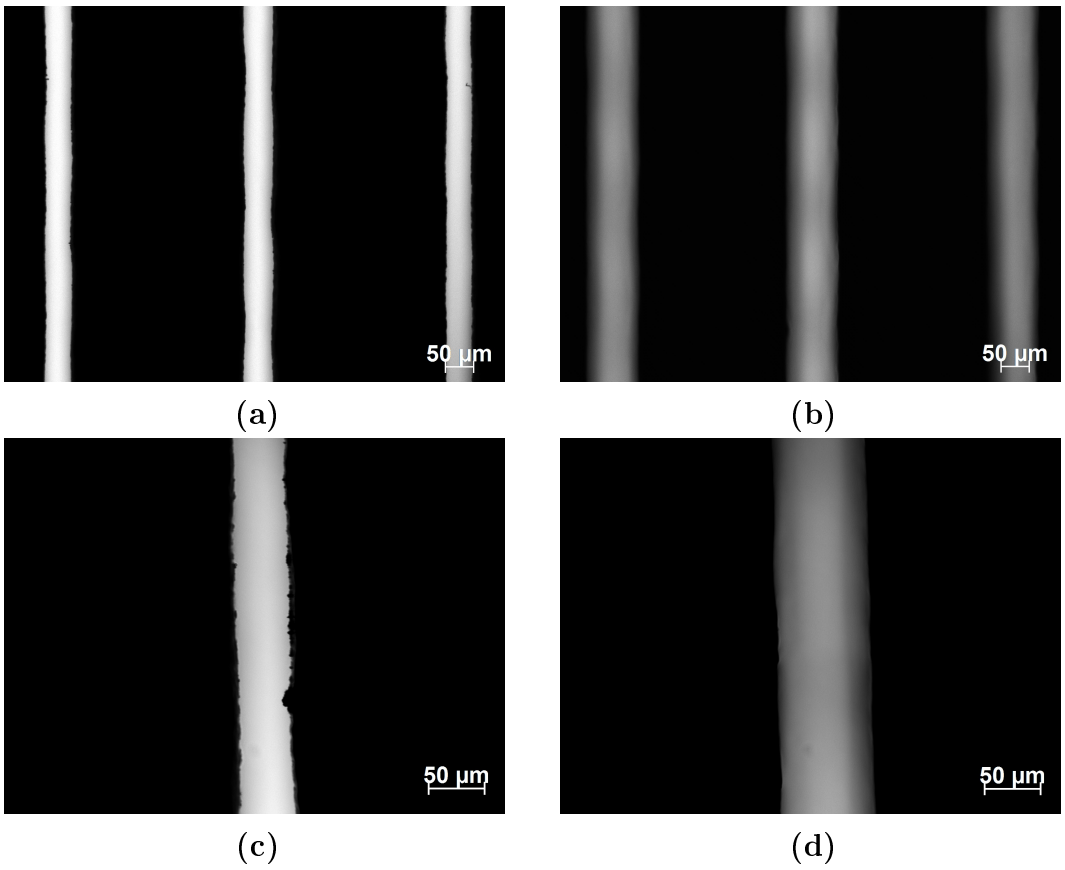

Figure A.12.: *Regions of interest from the tungsten grid acquired with visible light microscopy. In the left images, (a) and (c), the focal plane is chosen at the bottom of the plate. The corresponding images (b) and (d) were taken by focusing at the top side of the plate, about 200 µm higher, to observe the larger opening of the tungsten grid. (a) and (b) show an overview of three slits acquired with a 10-fold magnifying objective. These images visualize the slightly varying slit width resulting from the fabrication process of the grid. The images in (c) and (d) were obtained with 20-fold magnifying objectives to show the burrs at the slit edges in more detail. While in (b), mainly due to burrs, the slit edges are partially blurred such that determination of the slit width is impaired, the borders of the slit at the top side of the plate can be well recognized in (d). In this region of interest, the slit width accounts to approximately 80 µm.*

A.5. To chapter 5.4.4

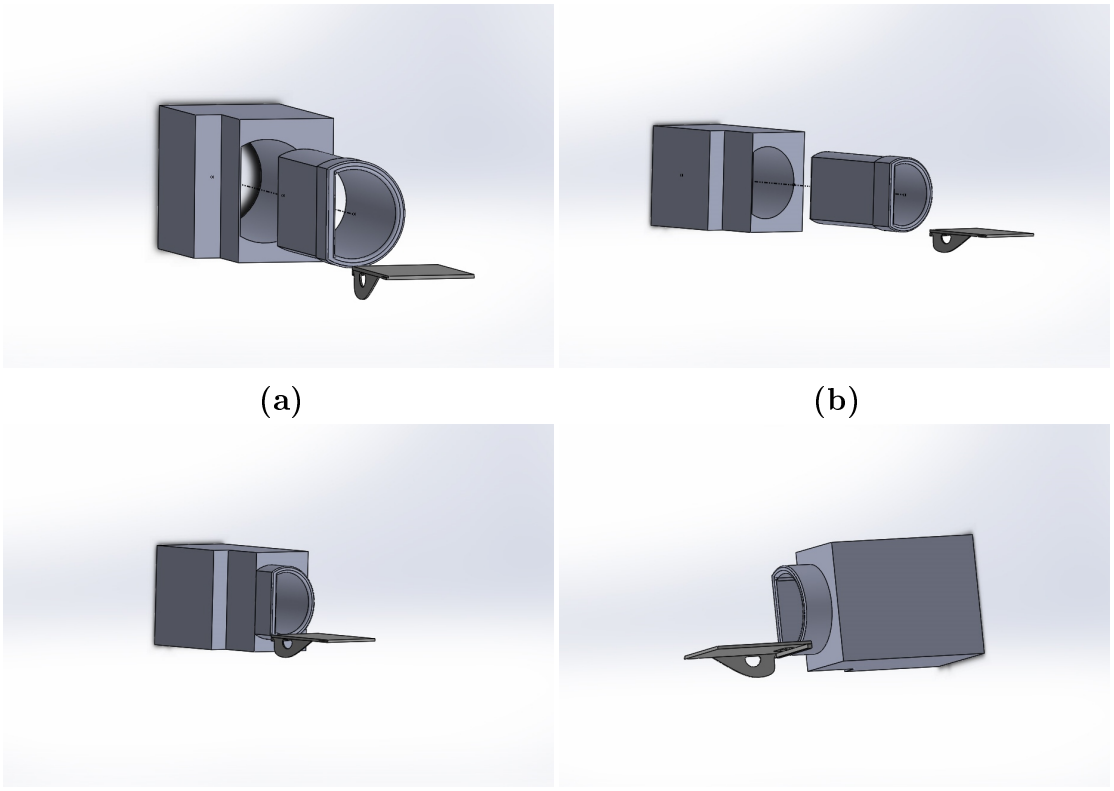

(a) (b)

(c) (d)

Figure A.13.: *3D model of the mouse positioning system. The exploded view in (a) and (b) shows the three main parts of the mouse positioning system (from left to right): the (heatable) aluminum block, and the removable cylindrical body holder including the head support with the ear aperture. For clarity, the additional radiation protection by a stainless steel plate is not shown here. (Model prepared with SolidWorks[2].)*

[2]Dassault Systèmes SolidWorks Corp., Waltham, MA, USA

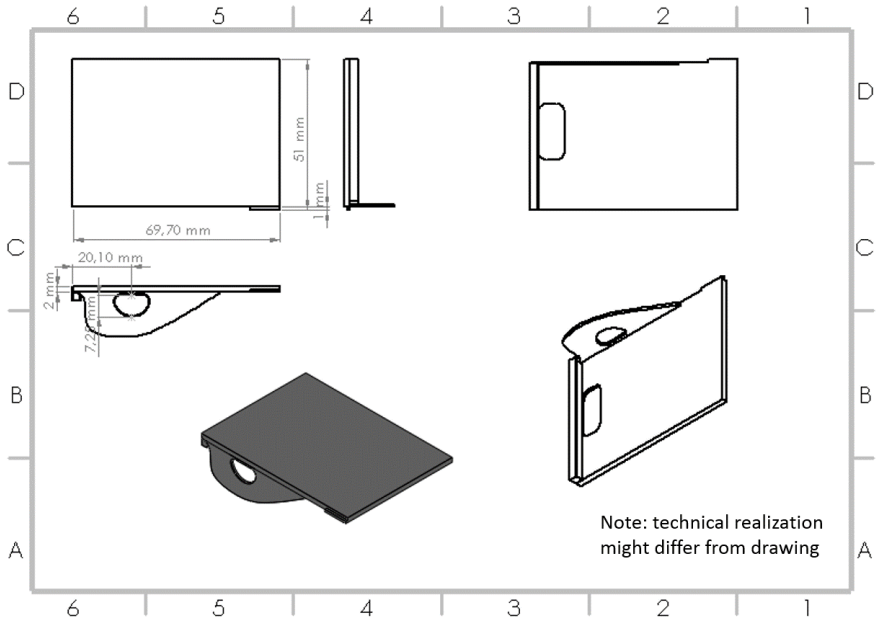

(a)

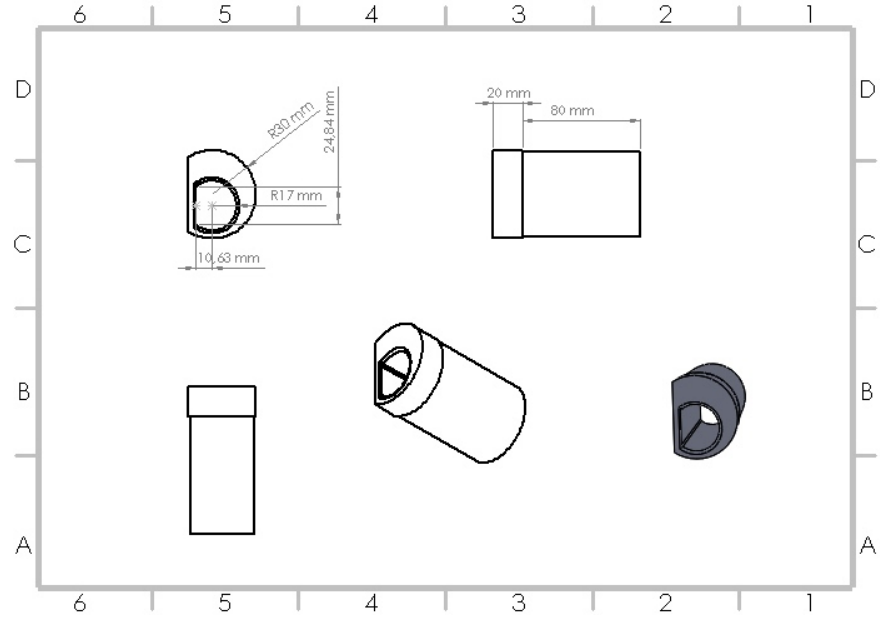

(b)

Figure A.14.: *Technical drawing of (a) the head support with ear aperture and (b) the cylindrical body holder. The technical realization (shown in chapter 5.4.4) might slightly differ from the drawing. In (a) the top view of the head support is given to the upper left with according side views attached. To the upper right, the bottom view is depicted with a dimetric view below. The depression is required to allow screwing the head support to the mouse holder (drill holes not depicted). (Drawing prepared with SolidWorks[2].)*

A.6. To chapter 5.4.6

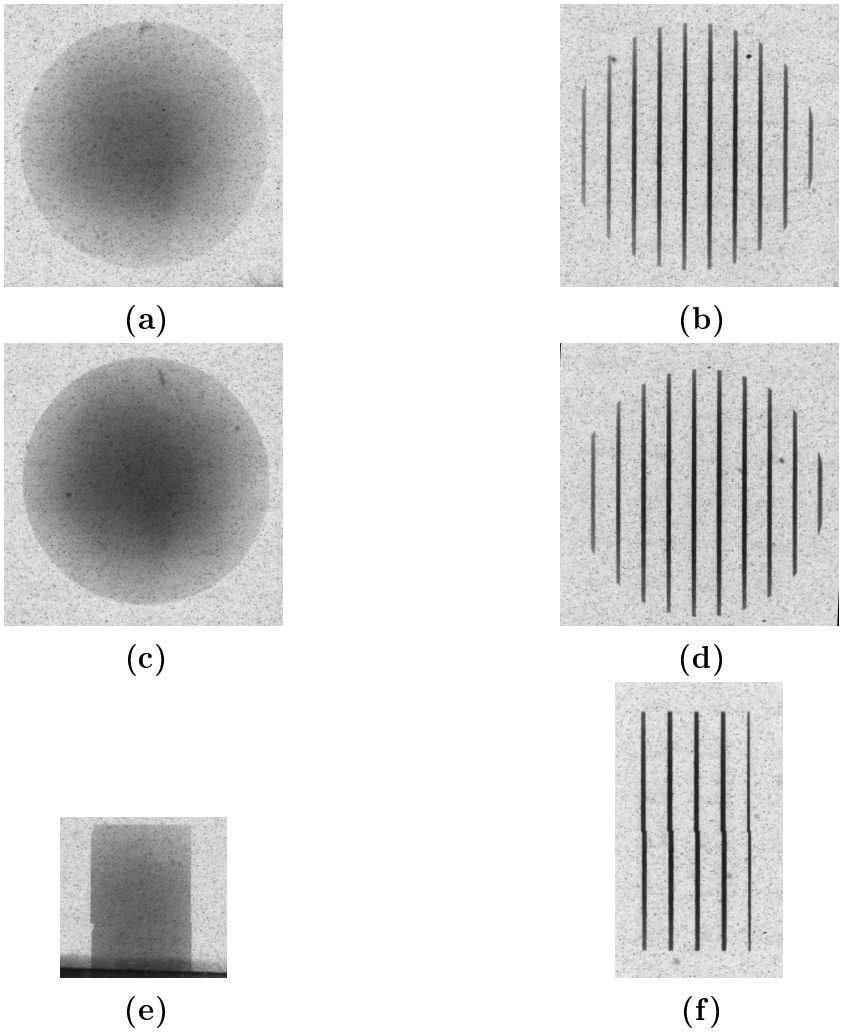

Figure A.15.: *Gafchromic EBT3 films[3] placed behind tumors, which were irradiated for the tumor growth delay study with different fields and mean doses. Microscopic read-out of the films was performed with AxioImager M2. (a) 3 Gy homogeneous irradiation, (b) 3 Gy microbeam irradiation, (c) 5 Gy homogeneous irradiation, (d) 5 Gy microbeam irradiation, (e) 3 Gy homogeneous irradiation using 2-field stitching – the field is only partially represented on the film due to positioning error, (f) 5 Gy microbeam irradiation using 2-field stitching.*

[3]Ashland, Bridgewater, NJ, USA

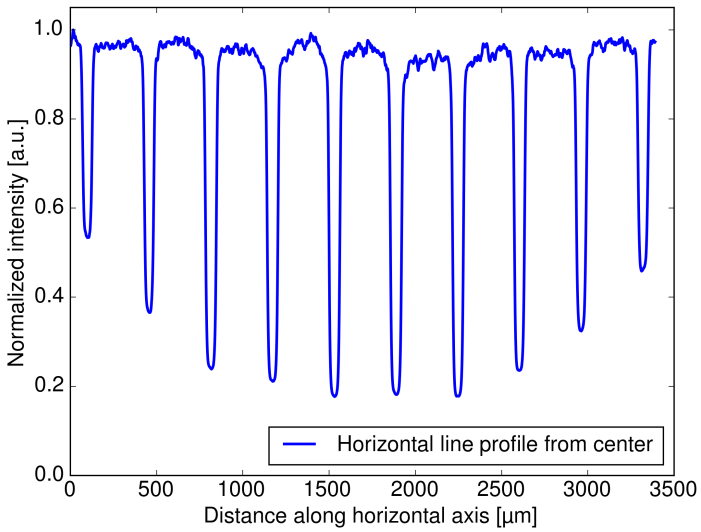

Figure A.16.: *Horizontal intensity profile taken from the center of Fig. A.15 (b). Low intensity in microscopic film read-out corresponds to high absorbed dose. Intensity conversion to absolute dose values is limited by the dose sensitivity of EBT3 films, which ranges from 0.1 to 20 Gy. Yet, microbeam peak doses with up to 21 or 35 Gy and the valley doses of several tens up to hundreds of mGy were applied. This line profile indicates a high PVDR with well separated microbeams and a mean period of 358 µm, i.e. slightly higher than the expected 350 µm. This might be caused by the actual structure of the tungsten grating and by a slight geometrical magnification due to the film positioning behind the ear. Note that the outer beamlets serve as safety margin as the irradiation field for mean dose calculation has a horizontal extension of only 2 mm. Regarding the central microbeam, an even distribution and a quite similar peak intensity is noticeable.*

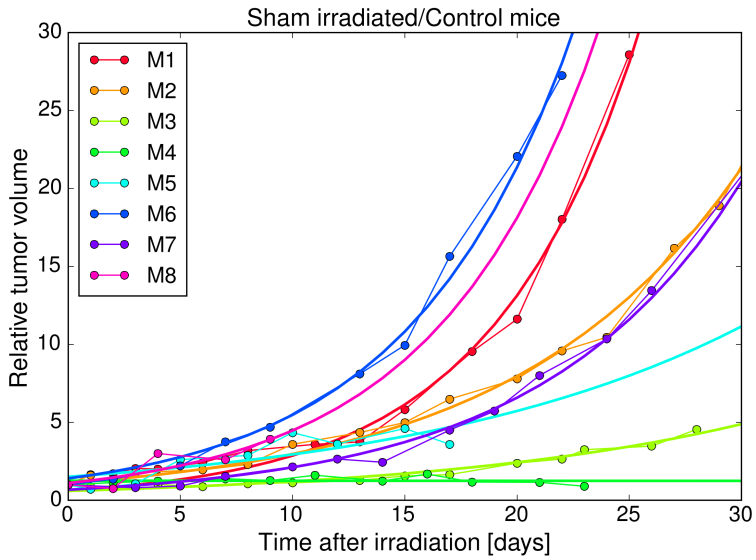

Figure A.17.: *Tumor growth over time in days for sham irradiation and control data. The relative tumor volume with respect to the volume at the day of irradiation is given. Measurements were acquired in an interval of 2-3 days. An exponential model (continuous solid line) was fitted to the data. Only four curves reached 15-fold relative tumor volume and were thus further evaluated (M1, M2, M6, and M7 – renamed to M1-M4 in chapter 5.4.6).*

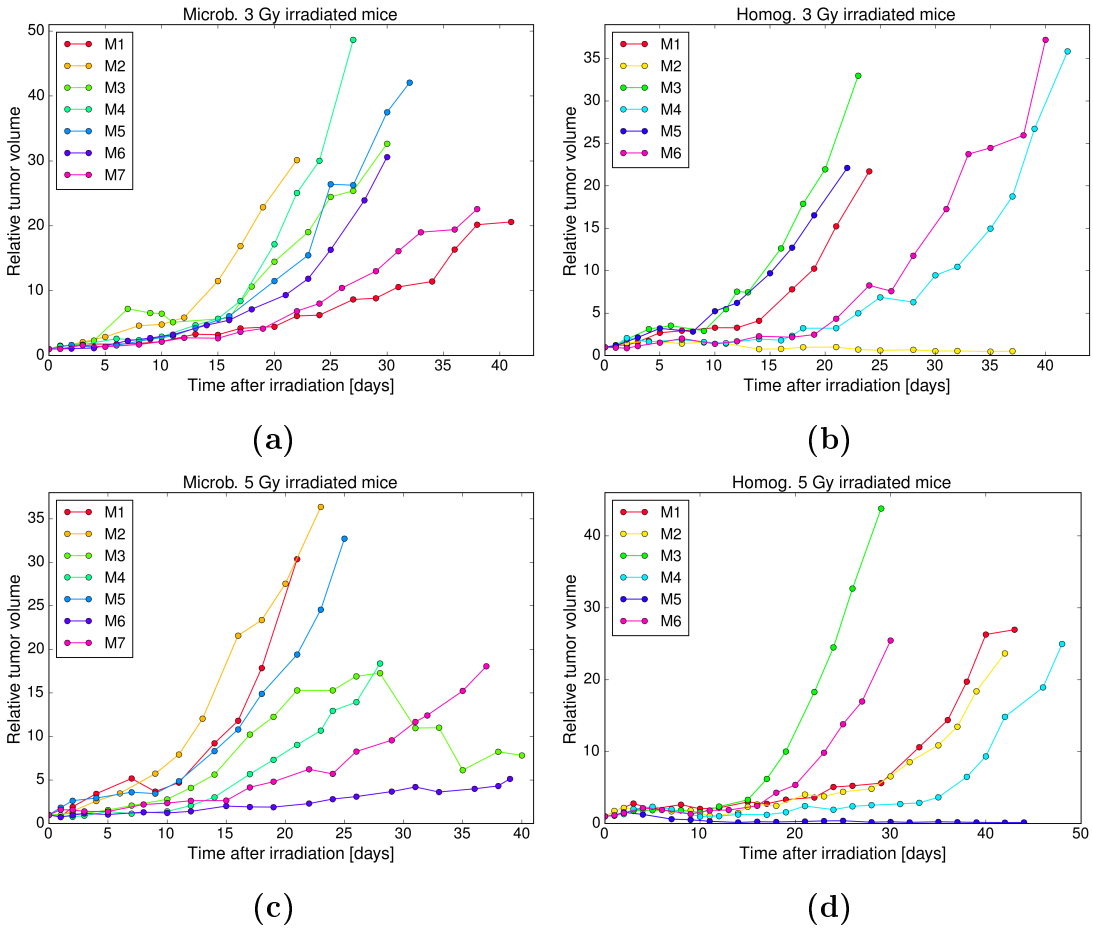

Figure A.18.: *Tumor growth over time in days. The relative tumor volume with respect to the volume at the day of irradiation is given. Tumor growth in all treated mice is shown in (a) after 3 Gy microbeam irradiation, in (b) after 3 Gy homogeneous irradiation, in (c) following 5 Gy microbeam irradiation, and in (d) following 5 Gy homogeneous irradiation. Only tumors reaching the 15-fold relative tumor volume were used for further investigation (note that the numbering using 'Mx' with x=1,2,3,... was restarted in chapter 5.4.6).*

A.7. To chapter 5.4.8

X-ray computed tomography of an iodine-stained tumor, resected following tumor growth examination. The images were acquired using the Xradia software XM3DViewer[4] and show axial (upper left), sagittal (lower left), and coronal (upper right) slices of the tumor volume with a three-dimensional rendering (lower right). Different transparency and contrast settings were chosen to highlight the vascular system and other fine structures within the tumor volume.

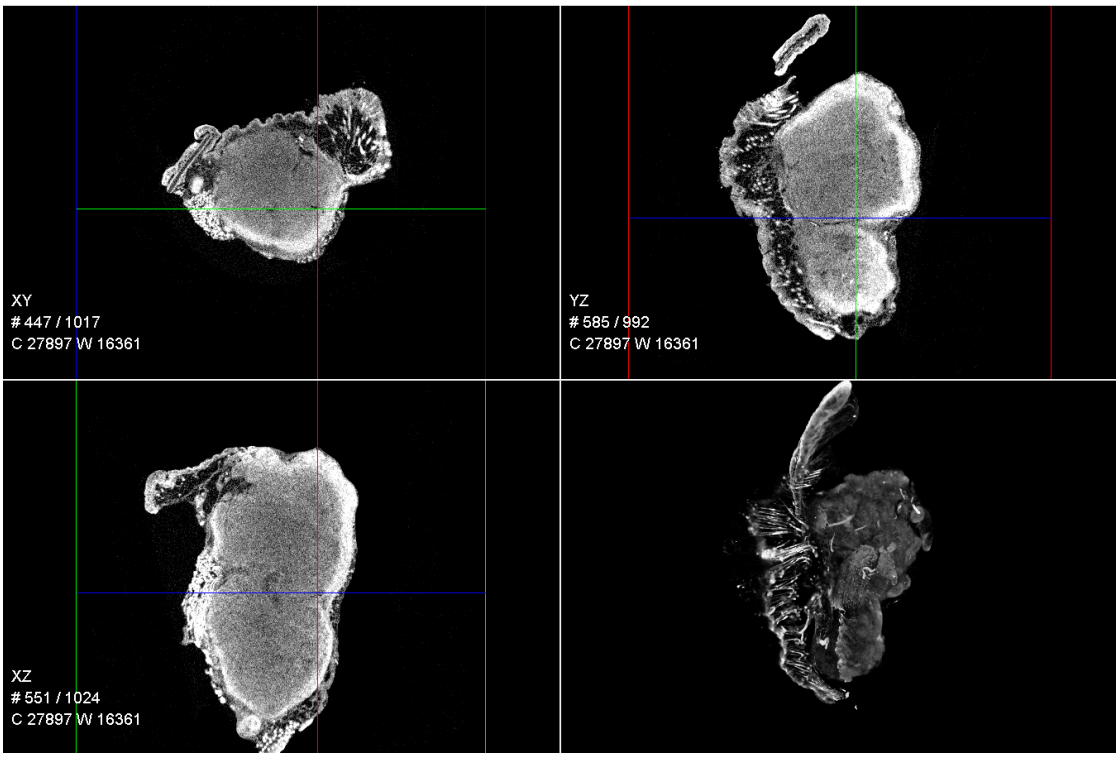

Figure A.19.: *The chosen sections focus on the center of the tumor where several dark regions indicate a low cell density and potential air gaps. Maybe, this finding correlates with hypoxic areas detectable by histological staining. In the three-dimensional rendering, individual vessels can be well observed.*

[4]Carl Zeiss Microscopy, Pleasanton, CA, USA

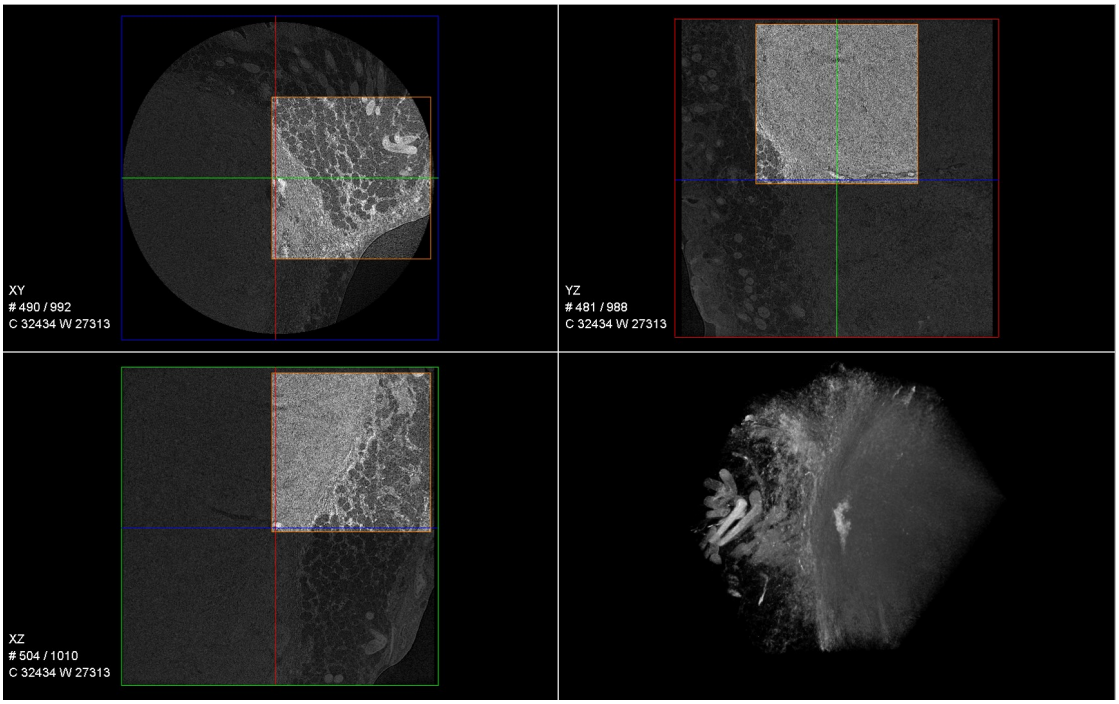

Figure A.20.: *A region of interest was chosen to investigate a single vessel close to the border of the tumor. Its three-dimensional structure is clearly perceptible with high resolution using X-ray staining.*

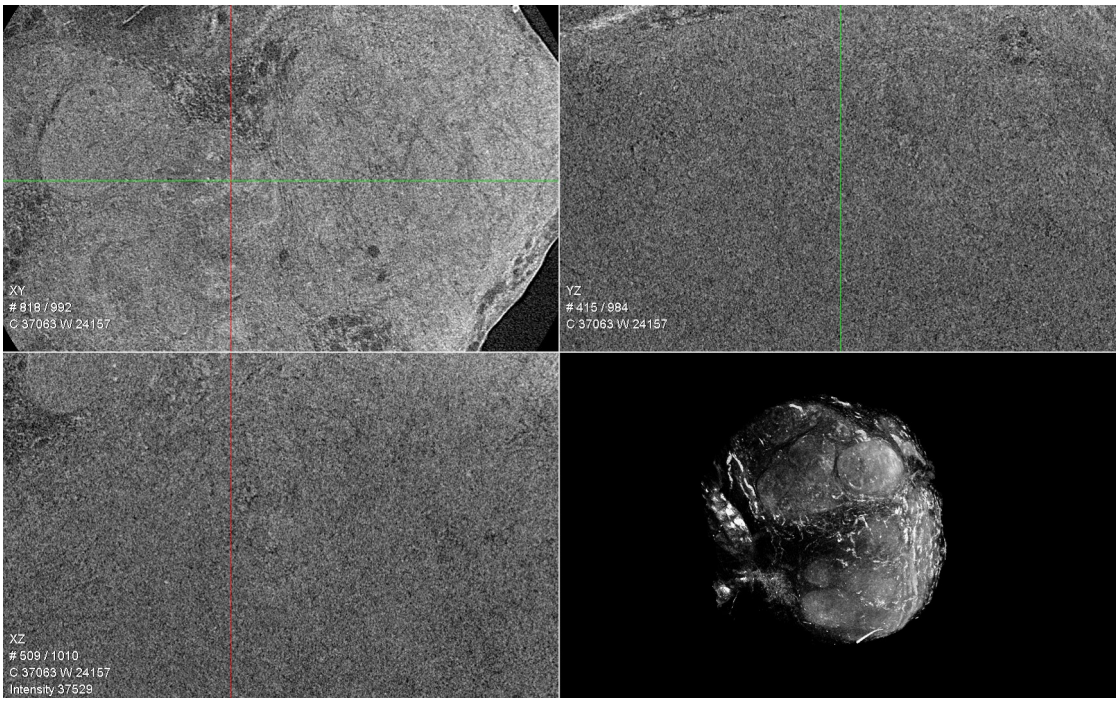

Figure A.21.: *In these sections from the central region of the tumor, the difference in homogeneity of the tumor is demonstrated. While the axial slice (upper left) presents a large variety of features, the sagittal (lower left) and coronal (upper right) section exhibit a quite homogeneous structure. In the three-dimensional rendering (corresponding to Fig. 5.42 (d)), the complexity of the vascular network becomes discernible. Hence, it is challenging to image the tumor entity with individual sections as acquired by histology, which can be overcome by X-ray computed tomography of stained tumors.*

List of abbreviations

AFM	atomic force microscopy
Ag	silver
Al	aluminum
Au	gold
BW	bandwidth
CCD	charged-coupled device
CHO-K1	Chinese hamster ovary cell line
CLS	Compact Light Source
CMOS	complementary metal oxide semiconductor
Cu	copper
DNA	deoxyribonucleic acid
DSB	double-strand break
ESRF	European Synchrotron Radiation Facility
FISH	fluorescence in-situ hybridization
FWHM	full width at half maximum
G1 phase	first gap phase of the cell cycle within the interphase during which the cell grows
GECF	graded ethanol concentration fixation
H&E	hematoxylin-eosin
HeLa	human epithelial cell line from a cervical cancer
IP	interaction point
LIGA	LIGA is a German acronym describing the steps of a fabrication process for microstructures: '**Li**thographie, **G**alvanoformung, **A**bformung', which is lithography, electroplating, and molding

LiPCDA	lithium salt
LMU	Ludwig-Maximilians-Universität München
LQM	linear-quadratic model
MRT	microbeam radiation therapy
MTF	modulation transfer function
MuCLS	Munich Compact Light Source
NaCl	sodium chloride
NaI	sodium iodide
NMRI	Swiss-type mouse transferred to the Naval Medical Research Institute (NMRI), Bethesda, MD, USA at 51st generation.
Pb	lead
PBS	phosphate buffered saline
PMMA	polymethylmethacrylat
PSF	point spread function
PVDR	peak-to-valley dose ratio
RBE	relative biological effectiveness
ROI	region of interest
sCMOS	scientific complementary metal oxide semiconductor
SD	sample standard deviation
SEM	standard error of the mean
Si	silicon
Sn	tin
TUM	Technical University of Munich
UV	ultraviolet
XRF	X-ray fluorescence

Bibliography

[1] Béclère, A. *Antoine Béclère (1856-1939): pionnier en endocrinologie, l'un des fondateurs de la virologie et de l'immunologie, fondateur de la radiologie francaise.* (J.B. Ballière, Paris, 1973).

[2] Siegel, R. L., Miller, K. D. & Jemal, A. Cancer statistics, 2016. *CA Cancer J. Clin.* **66**(1), 7–30 (2016).

[3] Morton, L. M., Onel, K., Curtis, R. E., Hungate, E. A. & Armstrong, G. T. The Rising Incidence of Second Cancers: Patterns of Occurrence and Identification of Risk Factors for Children and Adults. *Am. Soc. Clin. Oncol. Educ. B.* **34**, e57–e67 (2014).

[4] Berrington de Gonzalez, A. *et al.* Proportion of second cancers attributable to radiotherapy treatment in adults: a cohort study in the US SEER cancer registries. *Lancet Oncol.* **12**(4), 353–360 (2011).

[5] Bortfeld, T. IMRT: a review and preview. *Phys. Med. Biol.* **51**(13), R363–R379 (2006).

[6] Slater, J. M. From X-Rays to Ion Beams: A Short History of Radiation Therapy. In Linz, U. (ed.) *Ion beam therapy: fundamentals, technology, clinical applications*, chap. 1, 3–14 (Springer-Verlag Berlin, Heidelberg, 2012).

[7] Wang, D. A critical appraisal of the clinical utility of proton therapy in oncology. *Med. Devices (Auckl.)* **8**, 439–446 (2015).

[8] Laissue, J. A., Blattmann, H. & Slatkin, D. N. Alban Köhler (1874-1947): Inventor of grid therapy. *Z. Med. Phys.* **22**(2), 90–99 (2012).

[9] Zeman, W., Curtis, H. J., Gebhard, E. L. & Haymaker, W. Tolerance of the Mouse-Brain Tissue to High-Energy Deuterons. *Science* **130**(3391), 1760–1761 (1959).

[10] Serduc, R. *et al.* In vivo two-photon microscopy study of short-term effects of microbeam irradiation on normal mouse brain microvasculature. *Int. J. Radiat. Oncol.* **64**(5), 1519–1527 (2006).

[11] Zeman, W., Curtis, H. J. & Baker, C. P. Histopathologic Effect of High-Energy-Particle Microbeams on the Visual Cortex of the Mouse Brain. *Radiat. Res.* **15**, 496–513 (1961).

[12] Laissue, J., Spanne, P., Dilmanian, F. A., Gebbers, J. O. & Slatkin, D. N. Zell- und Gewebeläsionen nach räumlich fraktionierter Mikro-Bestrahlung des ZNS mit Synchrotron Photonen. *Schweiz. Med. Wochenschr.* **122**(43), 16–27 (1992).

[13] Slatkin, D. N., Spanne, P., Dilmanian, F. A. & Sandborg, M. Microbeam radiation therapy. *Med. Phys.* **19**(6), 1395–1400 (1992).

[14] Dilmanian, F. A. *et al.* Interlaced x-ray microplanar beams: a radiosurgery approach with clinical potential. *Proc. Natl. Acad. Sci. U. S. A.* **103**(25), 9709–9714 (2006).

[15] Bräuer-Krisch, E. *et al.* Medical physics aspects of the synchrotron radiation therapies: Microbeam radiation therapy (MRT) and synchrotron stereotactic radiotherapy (SSRT). *Phys. Medica* **31**, 568–583 (2015).

[16] Sette, F. European Synchrotron Radiation Facility (ESRF), URL `http://www.esrf.eu` (Accessed: 2017-03-09).

[17] Bräuer-Krisch, E. *et al.* New technology enables high precision multislit collimators for microbeam radiation therapy. *Rev. Sci. Instrum.* **80**(7), 074301 (2009).

[18] Bouchet, A. *et al.* Preferential effect of synchrotron microbeam radiation therapy on intracerebral 9L gliosarcoma vascular networks. *Int. J. Radiat. Oncol. Biol. Phys.* **78**(5), 1503–1512 (2010).

[19] Sabatasso, S. *et al.* Microbeam radiation-induced tissue damage depends on the stage of vascular maturation. *Int. J. Radiat. Oncol. Biol. Phys.* **80**(5), 1522–1532 (2011).

[20] Bouchet, A. *et al.* Synchrotron microbeam radiation therapy induces hypoxia in intracerebral gliosarcoma but not in the normal brain. *Radiother. Oncol.* **108**(1), 143–148 (2013).

[21] Laissue, J. A., Blattmann, H., Wagner, H. P., Grotzer, M. A. & Slatkin, D. N. Prospects for microbeam radiation therapy of brain tumours in children to reduce neurological sequelae. *Dev. Med. Child Neurol.* **49**(8), 577–581 (2007).

[22] Requardt, H. *et al.* The clinical trials program at the ESRF biomedical beamline ID17: Status and remaining steps. *AIP Conf. Proc.* **1234**, 161–164 (2010).

[23] Renier, M. *et al.* The radiotherapy clinical trials projects at the ESRF: Technical aspects. *Eur. J. Radiol.* **68**(3), S147–S150 (2008).

[24] Bräuer-Krisch, E. *et al.* The preclinical set-up at the ID17 biomedical beamline to achieve high local dose deposition using interlaced microbeams. *J. Phys. Conf. Ser.* **425**(2), 022001 (2013).

[25] Kashino, G. *et al.* Induction of DNA Double-Strand Breaks and Cellular Migration Through Bystander Effects in Cells Irradiated With the Slit-Type Microplanar Beam of the Spring-8 Synchrotron. *Int. J. Radiat. Oncol. Biol. Phys.* **74**(1), 229–236 (2009).

[26] Prise, K. M., Folkard, M. & Michael, B. D. Bystander responses induced by low LET radiation. *Oncogene* **22**, 7043–7049 (2003).

[27] Asur, R. S. *et al.* Spatially fractionated radiation induces cytotoxicity and changes in gene expression in bystander and radiation adjacent murine carcinoma cells. *Radiat. Res.* **177**(6), 751–765 (2012).

[28] Fernandez-Palomo, C. *et al.* Use of synchrotron medical microbeam irradiation to investigate radiation-induced bystander and abscopal effects in vivo. *Phys. Medica* **31**(6), 584–595 (2015).

[29] Dilmanian, F. A. *et al.* Response of rat intracranial 9L gliosarcoma to microbeam radiation therapy. *Neuro. Oncol.* **4**, 26–38 (2002).

[30] Dilmanian, F. A. *et al.* Murine EMT-6 Carcinoma: High Therapeutic Efficacy of Microbeam Radiation Therapy. *Radiat. Res.* **159**(5), 632–641 (2003).

[31] Laissue, J. A. *et al.* Response of the rat spinal cord to X-ray microbeams. *Radiother. Oncol.* **106**(1), 106–111 (2013).

[32] Sedor, J. Neutron Sources and Synchrotrons. In *International Partnerships in Large Science Projects*, chap. 3- U.S. Ex, 86–92 (DIANE Publishing, 1998).

[33] McCarthy, J. ESRF Facility And User Program Overview (2013), URL `aps.anl.gov/Users/3Way/presentations/McCarthy.pdf` (Accessed: 2017-03-09).

[34] Excillum: MetalJet X-Ray Tube Technology, URL `www.excillum.com` (Accessed: 2017-03-09).

[35] Bruker: Sources - METALJET, URL `www.bruker.com` (Accessed: 2017-03-09).

[36] Bordelon, D. E. *et al.* A nanotube based electron microbeam cellular irradiator for radiobiology research. *Rev. Sci. Instrum.* **79**(12), 125102 (2008).

[37] Hadsell, M. *et al.* A first generation compact microbeam radiation therapy system based on carbon nanotube X-ray technology. *Appl. Phys. Lett.* **103**(18), 183505 (2013).

[38] Hadsell, M. *et al.* Pilot study for compact microbeam radiation therapy using a carbon nanotube field emission micro-CT scanner. *Med. Phys.* **41**(6), 061710 (2014).

[39] Huang, Z. & Ruth, R. D. Laser-Electron Storage Ring. *Phys. Rev. Lett.* **80**(5), 976–979 (1998).

[40] Loewen, R. J. *A compact light source: design and technical feasibility study of a laser-electron storage ring X-ray source.* Ph.D. thesis, Stanford University (2003).

[41] Eggl, E. *et al.* The Munich Compact Light Source: initial performance measures. *J. Synchrotron Radiat.* **23**(5), 1137–1142 (2016).

[42] Eggl, E. *Biomedical X-ray Imaging at the Munich Compact Light Source.* Ph.D. thesis, Technical University of Munich (2017).

[43] Sakanaka, S. *et al.* Recent Progress and Operational Status of the Compact ERL at KEK. In *IPAC2015*, TUBC1 (Richmond, VA, USA, 2015).

[44] Jacquet, M. High intensity compact Compton X-ray sources: Challenges and potential of applications. *Nucl. Instruments Methods Phys. Res. Sect. B Beam Interact. with Mater. Atoms* **331**, 1–5 (2014).

[45] Jacquet, M. & Suortti, P. Radiation therapy at compact Compton sources. *Phys. Medica* **31**(6), 596–600 (2015).

[46] Bartzsch, S. & Oelfke, U. X-ray microbeam production and high brilliance x-ray production (2017), Patent no. PCT/GB 2017/051733, UK Intellectual Property Office.

[47] Bartzsch, S. & Oelfke, U. Line focus x-ray tubes – a new concept to produce high brilliance x-rays. *Phys. Med. Biol.* **62**(22), 8600 (2017).

[48] Holthusen, H. Erfahrungen über die Verträglichkeitsgrenze für Röntgenstrah- len und deren Nutzanwendung zur Verhütung von Schäden. *Strahlentherapie* **57**, 254–269 (1936).

[49] Schmid, T. E. *et al.* Low LET protons focused to submicrometer shows enhanced radiobiological effectiveness. *Phys. Med. Biol.* **57**(19), 5889–5907 (2012).

[50] Konishi, T. *et al.* Research and development of focused proton microbeam irradiation system, SPICE for radio-biological studies. *J. Radiat. Res.* **55**(Suppl 1), i104–i105 (2014).

[51] Girst, S. *et al.* The influence of the channel size on the reduction of side effects in microchannel proton therapy. *Radiat. Environ. Biophys.* **54**(3), 335–342 (2015).

[52] Girst, S. *et al.* Proton Minibeam Radiation Therapy Reduces Side Effects in an In Vivo Mouse Ear Model. *Int. J. Radiat. Oncol. Biol. Phys.* **95**(1), 234–241 (2016).

[53] Kłodowska, M., Olko, P. & Waligórski, M. Proton microbeam radiotherapy with scanned pencil-beams - Monte Carlo simulations. *Phys. Medica* **31**(6), 621–626 (2015).

[54] Laissue, J. A. *et al.* Neuropathology of ablation of rat gliosarcomas and contiguous brain tissues using a microplanar beam of synchrotron-wiggler-generated X rays. *Int. J. Cancer* **78**(5), 654–660 (1998).

[55] Stupp, R. *et al.* Radiotherapy plus Concomitant and Adjuvant Temozolomide for Glioblastoma. *N. Engl. J. Med.* **352**(10), 987–996 (2005).

[56] Johnson, D. R. & O'Neill, B. P. Glioblastoma survival in the United States before and during the temozolomide era. *J. Neurooncol.* **107**(2), 359–364 (2012).

[57] Slatkin, D. N., Spanne, P., Dilmanian, F. A., Gebberst, J.-O. & Laissue, J. A. Subacute neuropathological effects of microplanar beams of x-rays from a synchrotron wiggler. *Proc. Natl. Acad. Sci.* **92**, 8783–8787 (1995).

[58] Pouyatos, B. *et al.* Synchrotron X-ray interlaced microbeams suppress paroxysmal oscillations in neuronal networks initiating generalized epilepsy. *Neurobiol. Dis.* **51**, 152–160 (2013).

[59] Siegbahn, E. A. *Dosimetry for synchrotron x-ray microbeam radiation therapy.* Ph.D. thesis, Technical University of Munich (2007).

[60] Perkins, S., Seltzer, S. & Cullen, D. Tables and graphs of electron interaction cross-sections from 10-eV to 100-GeV derived from the LLNL evaluated electron data library (EEDL), Z = 1 - 100. Report UCRL-50400 vol. 31, Lawrence Livermore National Laboratory, Livermore, CA (1991).

[61] Bartzsch, S. *Microbeam Radiation Therapy – physical and biological aspects of a new cancer therapy and development of a treatment planning system.* Ph.D. thesis, Ruprecht-Karls-Universität Heidelberg (2014).

[62] Bräuer-Krisch, E. *et al.* New irradiation geometry for microbeam radiation therapy. *Phys. Med. Biol.* **50**(13), 3103–3111 (2005).

[63] Serduc, R. *et al.* High-Precision Radiosurgical Dose Delivery by Interlaced Microbeam Arrays of High-Flux Low-Energy Synchrotron X-Rays. *PLoS One* **5**(2), e9028 (2010).

[64] Zhang, L. *et al.* Nanotube x-ray for cancer therapy: a compact microbeam radiation therapy system for brain tumor treatment. *Expert Rev. Anticancer Ther.* **14**(12), 1411–1418 (2014).

[65] Skarzynski, T. Collecting data in the home laboratory: evolution of X-ray sources, detectors and working practices. *Acta Crystallogr. D. Biol. Crystallogr.* **69**, 1283–1288 (2013).

[66] Wenz, J. *et al.* Quantitative X-ray phase-contrast microtomography from a compact laser-driven betatron source. *Nat. Commun.* **6**, 7568 (2015).

[67] Cole, J. M. *et al.* Laser-wakefield accelerators as hard x-ray sources for 3D medical imaging of human bone. *Sci. Rep.* **5**, 13244 (2015).

[68] Zhou, O. Z. & Chang, S. X. Compact Microbeam Radiation Therapy systems and methods for cancer treatment and research (2010), Patent no. US 2010/0329413 A1, U.S. Patent and Trademark Office.

[69] Yuan, H. *et al.* Treating Brain Tumor with Microbeam Radiation Generated by a Compact Carbon-Nanotube-Based Irradiator : Initial Radiation Efficacy Study. *Radiat. Res.* **184**, 322–333 (2015).

[70] Zhang, L. *et al.* Image-guided microbeam irradiation to brain tumour bearing mice using a carbon nanotube x-ray source array. *Phys. Med. Biol.* **59**(5), 1283–1303 (2014).

[71] Bräuer-Krisch, E. *et al.* Characterization of a tungsten/gas multislit collimator for microbeam radiation therapy at the European Synchrotron Radiation Facility. *Rev. Sci. Instrum.* **76**(6), 064303 (2005).

[72] Ohno, Y. *et al.* Dose distribution of a 125 keV mean energy microplanar x-ray beam for basic studies on microbeam radiotherapy. *Med. Phys.* **35**(7), 3252–3258 (2008).

[73] Kenntner, J. *Herstellung von Gitterstrukturen mit Aspektverhältnis 100 für die Phasenkontrastbildgebung in einem Talbot-Interferometer.* Ph.D. thesis, Karlsruhe Institute of Technology (2012).

[74] Berger, M. *et al.* XCOM: Photon Cross Section Database (version 1.5). Tech. Rep., National Institute of Standards and Technology, Gaithersburg, MD (2010).

[75] International Commission on Radiation Units and Measurements Inc. Fundamental Quantities and Units for Ionizing Radiation. ICRU Report 60, ICRU, Bethesda, MD, USA (1998).

[76] Hubbell, J. & Seltzer, S. Tables of X-Ray Mass Attenuation Coefficients and Mass Energy-Absorption Coefficients from 1 keV to 20 MeV for Elements Z = 1 to 92 and 48 Additional Substances of Dosimetric Interest. NISTIR 5632. Tech. Rep., National Institute of Standards and Technology (NIST), Gaithersburg (1995).

[77] Hall, E. J. & Giaccia, A. J. *Radiobiology for the radiologist* (Lippincott Williams & Wilkins, Philadelphia, 2006), 6th edn.

[78] Park, H. J., Griffin, R. J., Hui, S., Levitt, S. H. & Song, C. W. Radiation-Induced Vascular Damage in Tumors: Implications of Vascular Damage in Ablative Hypofractionated Radiotherapy (SBRT and SRS). *Radiat. Res.* **177**(3), 311–327 (2012).

[79] Ponnaiya, B. *et al.* Biological Responses in Known Bystander Cells Relative to Known Microbeam-Irradiated Cells. *Radiat. Res.* **162**, 426–432 (2004).

[80] Dilmanian, F. A. *et al.* Tissue-sparing effect of x-ray microplanar beams particularly in the CNS: Is a bystander effect involved? *Exp. Hematol.* **35**(4), 69–77 (2007).

[81] Mothersill, C. *et al.* Transmission of signals from rats receiving high doses of microbeam radiation to cage mates: An inter-mammal bystander effect. *Dose-Response* **12**(1), 72–92 (2014).

[82] Dimitrievich, G. S., Fischer-Dzoga, K. & Griem, M. L. Radiosensitivity of Vascular Tissue: I. Differential Radiosensitivity of Capillaries: A Quantitative in Vivo Study. *Radiat. Res.* **99**(3), 511 (1984).

[83] Blattmann, H. *et al.* Applications of synchrotron X-rays to radiotherapy. *Nucl. Instruments Methods Phys. Res. Sect. A Accel. Spectrometers, Detect. Assoc. Equip.* **548**(1-2), 17–22 (2005).

[84] Brönnimann, D. *et al.* Synchrotron microbeam irradiation induces neutrophil infiltration, thrombocyte attachment and selective vascular damage in vivo. *Sci. Rep.* **6**, 33601 (2016).

[85] Girst, S. *et al.* Improved normal tissue protection by proton and X-ray microchannels compared to homogeneous field irradiation. *Phys. Medica* **31**(6), 615–620 (2015).

[86] IAEA. IAEA Safety Glossary - Terminology used in nuclear safety and radiation protection (2007), URL `http://www-ns.iaea.org/standards/safety-glossary.asp` (Accessed: 2017-01-01).

[87] Priyadarshika, R. C. U., Crosbie, J. C., Kumar, B. & Rogers, P. A. W. Biodosimetric quantification of short-term synchrotron microbeam versus broad-beam radiation damage to mouse skin using a dermatopathological scoring system. *Br. J. Radiol.* **84**(1005), 833–842 (2011).

[88] Ibahim, M. J. *et al.* An Evaluation of Dose Equivalence between Synchrotron Microbeam Radiation Therapy and Conventional Broadbeam Radiation Using Clonogenic and Cell Impedance Assays. *PLoS One* **9**(6), e100547 (2014).

[89] Fernandez-Palomo, C. *et al.* γ-H2AX as a Marker for Dose Deposition in the Brain of Wistar Rats after Synchrotron Microbeam Radiation. *PLoS One* **10**(3), e0119924 (2015).

[90] Ross, C. K. & Klassen, N. V. Water calorimetry for radiation dosimetry. *Phys. Med. Biol.* **41**(1), 1–29 (1996).

[91] Lye, J. E. *et al.* Absolute dosimetry on a dynamically scanned sample for synchrotron radiotherapy using graphite calorimetry and ionization chambers. *Phys. Med. Biol.* **61**(11), 4201–4222 (2016).

[92] Bartzsch, S. *et al.* Micrometer-resolved film dosimetry using a microscope in microbeam radiation therapy. *Med. Phys.* **42**(7), 4069–4079 (2015).

[93] McErlean, C. M., Bräuer-Krisch, E., Adamovics, J. & Doran, S. J. Assessment of optical CT as a future QA tool for synchrotron x-ray microbeam therapy. *Phys. Med. Biol.* **61**(1), 320–337 (2016).

[94] Bräuer-Krisch, E. *et al.* Potential high resolution dosimeters for MRT. *AIP Conf. Proc.* **1266**, 89–97 (2010).

[95] Livingstone, J., Stevenson, A. W., Butler, D. J., Häusermann, D. & Adam, J.-F. Characterization of a synthetic single crystal diamond detector for dosimetry in spatially fractionated synchrotron x-ray fields. *Med. Phys.* **43**(7), 4283–4293 (2016).

[96] Akselrod, G., Akselrod, M., Benton, E. & Yasuda, N. A novel Al2O3 fluorescent nuclear track detector for heavy charged particles and neutrons. *Nucl. Instruments Methods Phys. Res. Sect. B Beam Interact. with Mater. Atoms* **247**(2), 295–306 (2006).

[97] Akselrod, M. S. & Sykora, G. J. Fluorescent nuclear track detector technology – A new way to do passive solid state dosimetry. *Radiat. Meas.* **46**(12), 1671–1679 (2011).

[98] Bartz, J., Sykora, G., Bräuer-Krisch, E. & Akselrod, M. Imaging and dosimetry of synchrotron microbeam with aluminum oxide fluorescent detectors. *Radiat. Meas.* **46**(12), 1936–1939 (2011).

[99] Als-Nielsen, J. & McMorrow, D. *Elements of Modern X-ray Physics* (John Wiley & Sons, Inc., Hoboken, NJ, USA, 2011).

[100] van der Veen, F. & Pfeiffer, F. Coherent x-ray scattering. *J. Phys. Condens. Matter* **16**(28), 5003–5030 (2004).

[101] Schleede, S. *X-ray Phase-Contrast Imaging at a Compact Laser-Driven Synchrotron Source*. Ph.D. thesis, Technical University of Munich (2013).

[102] Black, E. D. An introduction to Pound-Drever-Hall laser frequency stabilization. *Am. J. Phys.* **69**(1), 79–87 (2001).

[103] Hauptner, A. *et al.* Microirradiation of cells with energetic heavy ions. *Radiat Env. Biophys* **42**, 237–245 (2004).

[104] Greubel, C. *et al.* Low LET proton microbeam to understand high-LET RBE by shaping spatial dose distribution. *Nucl. Instruments Methods Phys. Res. Sect. B Beam Interact. with Mater. Atoms* **404**, 155–161 (2017).

[105] Rothkamm, K. & Löbrich, M. Evidence for a lack of DNA double-strand break repair in human cells exposed to very low x-ray doses. *Proc. Natl. Acad. Sci. U. S. A.* **100**(9), 5057–5062 (2003).

[106] Tu, W.-Z. *et al.* γH2AX foci formation in the absence of DNA damage: Mitotic H2AX phosphorylation is mediated by the DNA-PKcs/CHK2 pathway. *FEBS Lett.* **587**(21), 3437–3443 (2013).

[107] Greubel, C. *et al.* Competition effect in DNA damage response. *Radiat. Environ. Biophys.* **47**(4), 423–429 (2008).

[108] Schmid, T. E. *et al.* Differences in the kinetics of γ-H2AX fluorescence decay after exposure to low and high LET radiation. *Int. J. Radiat. Biol.* **86**(8), 682–691 (2010).

[109] Scherer, W. F., Syverton, J. T. & Gey, G. O. Studies on the Propagation in Vitro of Poliomyelitis Viruses: IV. Viral Multiplication in a Stable Strain of Human Malignant Epithelial Cells (Strain Hela) Derived From an Epidermoid Carcinoma of the Cervix. *J. Exp. Med.* **97**(5), 695–710 (1953).

[110] Fertil, B., Reydellet, I. & Deschavanne, P. J. A benchmark of cell survival models using survival curves for human cells after completion of repair of potentially lethal damage. *Radiat. Res.* **138**(1), 61–69 (1994).

[111] INTERNATIONAL ATOMIC ENERGY AGENCY. Cytogenetic Analysis for Radiation Dose Assessment. Technical Reports Series No. 405, IAEA, Vienna (2001).

[112] Romm, H., Oestreicher, U. & Kulka, U. Cytogenetic damage analysed by the dicentric assay. *Ann. Ist. Super. Sanita* **45**(3), 251–259 (2009).

[113] Bonassi, S., El-Zein, R., Bolognesi, C. & Fenech, M. Micronuclei frequency in peripheral blood lymphocytes and cancer risk: evidence from human studies. *Mutagenesis* **26**(1), 93–100 (2011).

[114] Schmid, E., Braselmann, H. & Nahrstedt, U. Comparison of γ-ray induced dicentric yields in human lymphocytes measured by conventional analysis and FISH. *Mutat. Res. Lett.* **348**, 125–130 (1995).

[115] Galloway, S. M. & Tice, R. R. Cytogenetic monitoring of human populations. In Tice, R. R., Costa, D. L. & Schaich, K. M. (eds.) *Genotoxic Effects of Airborne Agents*, chap. C VIII, 463–488 (Plenum Press, New York, 1982), 1st edn.

[116] Anderson, D., Baumgartner, A. & Cemeli, E. Cytogenetics. In *Gen. Appl. Toxicol.* (John Wiley & Sons Ltd, Chichester, UK, 2009).

[117] Gascoigne, K. E. & Cheeseman, I. M. Induced dicentric chromosome formation promotes genomic rearrangements and tumorigenesis. *Chromosome Res.* **21**(4), 407–418 (2013).

[118] Schmid, T. E. *et al.* The effectiveness of 20 MeV protons at nanosecond pulse lengths in producing chromosome aberrations in human-hamster hybrid cells. *Radiat. Res.* **175**(6), 719–727 (2011).

[119] INTERNATIONAL ATOMIC ENERGY AGENCY. Biological Dosimetry: Chromosomal Aberration Analysis for Dose Assessment. Technical Reports Series No. 260, IAEA, Vienna (1986).

[120] Urban, T. *Dosimetric Characterization of Microbeams for Preclinical Experiments in Radiotherapy at the Munich Compact Light Source.* Master's thesis, Technical University of Munich (2017).

[121] Ashland. Gafchromic Radiology, Radiotherapy and Security Radiographic Films, and FilmQA Pro Software (2017), URL `http://www.gafchromic.com/` (Accessed: 2017-05-17).

[122] Student. The probable error of a mean. *Biometrika* **6**(1), 1–25 (1908).

[123] Certified Scientific Software. spec, URL `https://certif.com` (Accessed: 2017-11-07).

[124] Python Software Foundation. Python Language Reference, version 2.7, URL `http://www.python.org/` (Accessed: 2017-11-07).

[125] Oliphant, T. E. Guide to NumPy (2006) (2006), URL `http://www.numpy.org/` (Accessed: 2017-11-07).

[126] Jones, E., Oliphant, T. & Peterson, P. SciPy: Open source scientific tools for Python (2001), URL `http://www.scipy.org/` (Accessed: 2017-11-07).

[127] Hunter, J. D. Matplotlib: A 2D graphics environment. *Comput. Sci. & Eng.* **9**(3), 90–95 (2007).

[128] Carpenter, A. E. *et al.* CellProfiler: image analysis software for identifying and quantifying cell phenotypes. *Genome Biol.* **7**(10), R100 (2006).

[129] Prezado, Y., Renier, M. & Bravin, A. A New Synchrotron Radiotherapy Technique with Future Clinical Potential: Minibeams Radiation Therapy. In Dössel, O. & Schlegel, W. C. (eds.) *World Congr. Med. Phys. Biomed. Eng.*, 29–32 (Springer Berlin Heidelberg, Munich, 2009).

[130] Martínez-Rovira, I., Fois, G. & Prezado, Y. Dosimetric evaluation of new approaches in GRID therapy using nonconventional radiation sources. *Med. Phys.* **42**(2), 685–693 (2015).

[131] Deman, P. *et al.* Monochromatic minibeam radiotherapy: theoretical and experimental dosimetry for preclinical treatment plans. *Phys. Med. Biol.* **56**(14), 4465–4480 (2011).

[132] Amemiya, K. *et al.* Soft X-ray imaging using CR-39 plastics with AFM readout. *Nucl. Instruments Methods Phys. Res. Sect. B Beam Interact. with Mater. Atoms* **187**(3), 361–366 (2002).

[133] Burger, K. *Study of filter design for Filtered Backprojection in Differential Phase-Contrast Computed Tomography.* Master's thesis, Ludwig-Maximilians-Universität München (2013).

[134] Kirby, D. *Radiation Dosimetry of Conventional and Laser-Driven Particle Beams.* Ph.D. thesis, University of Birmingham (2011).

[135] Giaddui, T. *et al.* Characteristics of Gafchromic XRQA2 films for kV image dose measurement. *Med. Phys.* **39**(2), 842–850 (2012).

[136] Brown, T. A. D. *et al.* Dose-response curve of EBT, EBT2, and EBT3 radiochromic films to synchrotron-produced monochromatic x-ray beams. *Med. Phys.* **39**(12), 7412–7417 (2012).

[137] Alnawaf, H., Yu, P. K. & Butson, M. Comparison of Epson scanner quality for radiochromic film evaluation. *J. Appl. Clin. Med. Phys.* **13**(5), 314–321 (2012).

[138] Greilich, S. *et al.* Fluorescent nuclear track detectors as a tool for ion-beam therapy research. *Radiat. Meas.* **56**, 267–272 (2013).

[139] Hegelich, B. M. *Acceleration of heavy Ions to MeV/nucleon Energies by Ultrahigh-Intensity Lasers.* Ph.D. thesis, Ludwig-Maximilians-Universität München (2002).

[140] Martin, T. & Koch, A. Recent developments in X-ray imaging with micrometer spatial resolution. *J. Synchrotron Radiat.* **13**(2), 180–194 (2006).

[141] Beese, L., Feder, R. & Sayre, D. Contact x-ray microscopy. A new technique for imaging cellular fine structure. *Biophys. J.* **49**(1), 259–268 (1986).

[142] Luke, H. The origins of the sampling theorem. *IEEE Commun. Mag.* **37**(4), 106–108 (1999).

[143] Thompson, A. C., Nix, J. C., Achterkirchen, T. G. & Westbrook, E. M. Large Format CMOS-based Detectors for Diffraction Studies. *J. Phys. Conf. Ser.* **425**(1), 012018 (2013).

[144] Bauer, B. B. *Eigenschaften reflektiver und transmittiver CsI-Photokathoden.* Ph.D. thesis, Technical University of Munich (1995).

[145] Kaye & Laby Online. Tables of Physical & Chemical Constants (16th edition 1995). 4. Atomic and nuclear physics. (2005), URL `www.kayelaby.npl.co.uk` (Accessed: 2017-11-07).

[146] Hignette, O., Cloetens, P., Rostaing, G., Bernard, P. & Morawe, C. Efficient sub 100nm focusing of hard x rays. *Rev. Sci. Instrum.* **76**(6), 063709 (2005).

[147] Spiga, J. *Monte Carlo simulation of dose distributions for synchrotron Microbeam Radiation Therapy.* Ph.D. thesis, Università degli Studi di Cagliari (2008).

[148] Mariotti, L. G. *et al.* Use of the γ-H2AX Assay to Investigate DNA Repair Dynamics Following Multiple Radiation Exposures. *PLoS One* **8**(11), e79541 (2013).

[149] Burger, K. *et al.* Increased cell survival and cytogenetic integrity by spatial dose redistribution at a compact synchrotron X-ray source. *PLoS One* **12**(10), e0186005 (2017).

[150] Cont, D. *X-Ray Beam Characterization at the Munich Compact Light Source.* Master's thesis, Technical University of Munich (2016).

[151] Hofmann, A. Characteristics of Synchrotron Radiation. In *CAS - CERN Accelerator School : Synchrotron Radiation and Free Electron Lasers*, chap. Accelerato, 1–44 (CERN-1998-004, Grenoble, 1996), 1998 ed. edn.

[152] Loewen, R. Private communication (2017).

[153] Bidola, P. M. *Characterization and Application of High Resolution Phase-Contrast Laboratory Micro-CT Setups.* Ph.D. thesis, Technical University of Munich (2017).

[154] Hock, K., Adelmann, B. & Hellmann, R. Comparative Study of Remote Fiber Laser and Water-Jet Guided Laser Cutting of Thin Metal Sheets. *Phys. Procedia* **39**, 225–231 (2012).

[155] Richardson, W. H. Bayesian-Based Iterative Method of Image Restoration. *J. Opt. Soc. Am.* **62**(1), 55–59 (1972).

[156] Dey, N. *et al.* Richardson-Lucy algorithm with total variation regularization for 3D confocal microscope deconvolution. *Microsc. Res. Tech.* **69**(4), 260–266 (2006).

[157] Gullikson, E. X-Ray Interactions With Matter (2004), URL `http://henke.lbl.gov` (Accessed: 2017-08-25).

[158] Henke, B., Gullikson, E. & Davis, J. X-ray interactions: photoabsorption, scattering, transmission, and reflection at E=50-30000 eV, Z=1-92. *At. Data Nucl. Data Tables* **54**(2), 181–342 (1993).

[159] Gerward, L. X-ray attenuation coefficients and atomic photoelectric absorption cross sections of silicon. *J. Phys. B At. Mol. Phys.* **14**(18), 3389–3395 (1981).

[160] Mika, J. F., Martin, L. J. & Barnea, Z. X-ray attenuation of silicon in the energy range 25-50 keV. *J. Phys. C Solid State Phys.* **18**(26), 5215–5223 (1985).

[161] Tran, C. Q., Chantler, C. T. & Barnea, Z. X-ray mass attenuation coefficient of silicon: theory versus experiment. *Phys. Rev. Lett.* **90**(25), 257401 (2003).

[162] Andreo, P., Burns, D. T. & Salvat, F. On the uncertainties of photon mass energy-absorption coefficients and their ratios for radiation dosimetry. *Phys. Med. Biol.* **57**(8), 2117–2136 (2012).

[163] Boone, J. M. & Chavez, A. E. Comparison of x-ray cross sections for diagnostic and therapeutic medical physics. *Med. Phys.* **23**(12), 1997–2005 (1996).

[164] Berger, M. J. & Hubbell, J. H. XCOM: photon cross sections on a personal computer. Report NBSIR 87-3597, National Bureau of Standards, Gaithersburg, MD, USA (1987).

[165] Crosbie, J. C. *et al.* Tumor Cell Response to Synchrotron Microbeam Radiation Therapy Differs Markedly From Cells in Normal Tissues. *Int. J. Radiat. Oncol. Biol. Phys.* **77**(3), 886–894 (2010).

[166] Hamada, N. *et al.* Histone H2AX Phosphorylation in Normal Human Cells Irradiated with Focused Ultrasoft X Rays: Evidence for Chromatin Movement during Repair. *Radiat. Res.* **166**(1), 31–38 (2006).

[167] Anderson, D. *et al.* Comparison of two methods for measuring gamma-H2AX nuclear fluorescence as a marker of DNA damage in cultured human cells: applications for microbeam radiation therapy. *J. Instrum.* **8**(6), 6008–6016 (2013).

[168] McNamara, A. L., Oelfke, U. & Kuncic, Z. Revealing the underlying mechanism of microbeam radiation therapy with low energy Monte Carlo simulations. *J. Phys. Conf. Ser.* **489**(012018), 1–4 (2014).

[169] Schmid, T. E. *et al.* Low LET protons focused to submicrometer shows enhanced radiobiological effectiveness. *Phys. Med. Biol.* **57**(19), 5889–5907 (2012).

[170] Greubel, C. & Schmid, T. E. Private Communication (2016).

[171] Schmid, E., Schlegel, D., Krumrey, M. & Stephan, G. RBE of Neutrons at Energies of 36 keV-15 MeV and Photons at Energies of 1.8 keV-40 keV for Induction of Dicentrics in Human Lymphocytes. In *11th Int. Congr. Int. Radiat. Prot. Assoc. 23-28 May 2004*, 1–8 (International Radiation Protection Association (IRPA), Fontenay-aux-Roses, France, 2004).

[172] Speicher, M. R., Ballard, S. G. & Ward, D. C. Karyotyping human chromosomes by combinatorial multi-fluor FISH. *Nat. Genet.* **12**(4), 368–375 (1996).

[173] Rangan, S. R. S. A new human cell line (FaDu) from a hypopharyngeal carcinoma. *Cancer* **29**(1), 117–121 (1972).

[174] Brüchner, K. *et al.* Establishment of a small animal tumour model for in vivo studies with low energy laser accelerated particles. *Radiat. Oncol.* **9**(1), 57 (2014).

[175] Oppelt, M. *et al.* Comparison study of in vivo dose response to laser-driven versus conventional electron beam. *Radiat. Environ. Biophys.* **54**(2), 155–166 (2015).

[176] Beyreuther, E. Private communication (2016).

[177] Girst, S. *Proton Minibeam Radiotherapy.* Ph.D. thesis, Universität der Bundeswehr München (2016).

[178] Schields, P. J. *et al.* Overview of polycapillary X-ray optics. *Powder Diffr.* **17**(2), 70–80 (2002).

[179] Åström, K. J. & Hägglund, T. *PID controllers: Theory, Design, and Tuning, Second Edition* (Instrument Society of America, Research Triangle Park, NC, 1995), 2nd ed. edn.

[180] Tomayko, M. M. & Reynolds, C. P. Determination of subcutaneous tumor size in athymic (nude) mice. *Cancer Chemother. Pharmacol.* **24**(3), 148–154 (1989).

[181] Feldman, J. P. & Goldwasser, R. A mathematical model for tumor volume evaluation using two-dimensions. *J. Appl. Quant. Methods* **4**(4), 455–462 (2009).

[182] Beyreuther, E. *et al.* An optimized small animal tumour model for experimentation with low energy protons. *PLoS One* **12**(5), 1–15 (2017).

[183] Bouchet, A., Serduc, R., Laissue, J. A. & Djonov, V. Effects of microbeam radiation therapy on normal and tumoral blood vessels. *Phys. Medica* **31**, 634–641 (2015).

[184] Uyama, A. *et al.* A narrow microbeam is more effective for tumor growth suppression than a wide microbeam: an in vivo study using implanted human glioma cells. *J. Synchrotron Radiat.* **18**(Pt 4), 671–678 (2011).

[185] Merrem, A., Bartzsch, S., Laissue, J. & Oelfke, U. Computational modelling of the cerebral cortical microvasculature: effect of x-ray microbeams versus broad beam irradiation. *Phys. Med. Biol.* **62**(10), 3902–3922 (2017).

[186] Fernandez-Palomo, C. *et al.* Bystander effects in tumor-free and tumor-bearing rat brains following irradiation by synchrotron X-rays. *Int. J. Radiat. Biol.* **89**(6), 445–453 (2013).

[187] Wouters, B. G. & Skarsgard, L. D. The response of a human tumor cell line to low radiation doses: evidence of enhanced sensitivity. *Radiat. Res.* **138**(1 Suppl), S76–S80 (1994).

[188] Smith, L. G., Miller, R. C., Richards, M., Brenner, D. J. & Hall, E. J. Investigation of hypersensitivity to fractionated low-dose radiation exposure. *Int. J. Radiat. Oncol. Biol. Phys.* **45**(1), 187–191 (1999).

[189] Short, S. C., Kelly, J., Mayes, C. R., Woodcock, M. & Joiner, M. C. Low-dose hypersensitivity after fractionated low-dose irradiation in vitro. *Int. J. Radiat. Biol.* **77**(6), 655–664 (2001).

[190] Prise, K. M., Schettino, G., Folkard, M. & Held, K. D. New insights on cell death from radiation exposure. *Lancet. Oncol.* **6**(7), 520–528 (2005).

[191] Wang, G.-J. & Cai, L. Induction of Cell-Proliferation Hormesis and Cell-Survival Adaptive Response in Mouse Hematopoietic Cells by Whole-Body Low-Dose Radiation. *Toxicol. Sci.* **53**(2), 369–376 (2000).

[192] Yu, H. *et al.* Different responses of tumor and normal cells to low-dose radiation. *Contemp. Oncol.* **17**(4), 356–362 (2013).

[193] Das, S., Singh, R., George, D., Vijaykumar, T. S. & John, S. Radiobiological Response of Cervical Cancer Cell Line in Low Dose Region: Evidence of Low Dose Hypersensitivity (HRS) and Induced Radioresistance (IRR). *J. Clin. Diagn. Res.* **9**(6), XC05–XC08 (2015).

[194] Martins de Souza e Silva, J. *et al.* Three-dimensional non-destructive soft--tissue visualization with X-ray staining micro-tomography. *Sci. Rep.* **5**, 14088 (2015).

[195] Stephenson, R. S. *et al.* Contrast Enhanced Micro-Computed Tomography Resolves the 3-Dimensional Morphology of the Cardiac Conduction System in Mammalian Hearts. *PLoS One* **7**(4), e35299 (2012).

[196] Bartzsch, S., Cummings, C., Eismann, S. & Oelfke, U. A preclinical microbeam facility with a conventional x-ray tube. *Med. Phys.* **43**(12), 6301–6308 (2016).

[197] Thuering, T. *et al.* High resolution, large field of view x-ray differential phase contrast imaging on a compact setup. *Appl. Phys. Lett.* **99**(4), 041111 (2011).

[198] Meyer, P. *et al.* Deep x-ray lithography fabrication of x-ray gratings for grating based interferometry: a review. In *XNPIG 2015 - Final program* (Bethesda, MD, USA, 2015).

[199] Poole, C. M., Day, L. R. J., Rogers, P. A. W. & Crosbie, J. C. Synchrotron microbeam radiotherapy in a commercially available treatment planning system. *Biomed. Phys. Eng. Express* **3**(2), 025001 (2017).

Publications and list of scientific presentations

Peer-reviewed publications

Karin Burger, Katarina Ilicic, Martin Dierolf, Benedikt Günther, Dietrich W. M. Walsh, Ernst Schmid, Elena Eggl, Klaus Achterhold, Bernhard Gleich, Stephanie E. Combs, Michael Molls, Thomas E. Schmid, Franz Pfeiffer, and Jan J. Wilkens: "Increased cell survival and cytogenetic integrity by spatial dose redistribution at a compact synchrotron X-ray source", *PLoS ONE*, **12**(10) e0186005 (2017).

Elena Eggl, Susanne Grandl, Anikó Sztrókay-Gaul, Martin Dierolf, Christoph Jud, Lisa Heck, Karin Burger, Benedikt Günther, Klaus Achterhold, Doris Mayr, Jan J. Wilkens, Sigrid D. Auweter, Bernhard Gleich, Karin Hellerhoff, Maximilian F. Reiser, Franz Pfeiffer, and Julia Herzen: "Dose-compatible grating-based phase-contrast mammography with a compact synchrotron source", *Submitted* (2017).

Karin Burger, Thomas Köhler, Michael Chabior, Sebastian Allner, Mathias Marschner, Andreas Fehringer, Marian Willner, Franz Pfeiffer, and Peter Noël: "Regularized iterative integration combined with non-linear diffusion filtering for phase-contrast x-ray computed tomography", *Optics Express* **22**(26) (2014).

Other publications

Karin Burger, Katarina Ilicic, Carolin Konrad, Gabriele Multhoff, Stephanie E. Combs, Jan J. Wilkens, and Thomas E. Schmid: "Untersuchung des Tumorwachstums nach Mikrokanalbestrahlung im Vergleich zu konventioneller homogener Bestrahlung mit brillanter Röntgenstrahlung am weltweit ersten kompakten Synchrotron für den Einsatz in der Radioonkologie", application for animal experiments, *approved by the ethics committee of the government of Upper Bavaria*, ref. no. 55.2-1-54-2532-62-2016, NTP-ID: 00009166-1-7 (2016).

Conference proceedings

Karin Burger, Katarina Ilicic, Annique Hunger, Martin Dierolf, Benedikt Günther, Ernst Schmid, Dietrich W. M. Walsh, Theresa Urban, Stefan Bartzsch, Amira Radtke, Elena Eggl, Klaus Achterhold, Bernhard Gleich, Stephanie E. Combs, Michael Molls, Thomas E. Schmid, Franz Pfeiffer, and Jan J. Wilkens, "Microbeam radiation therapy at a laser-based compact synchrotron x-ray source", *2017 European Conference on Lasers and Electro-Optics – European Quantum Electronics Conference* in: *Optical Society of America*, paper JSIII-3.4 (2017). (Oral presentation)

Karin Burger, Katarina Ilicic, Annique Hunger, Martin Dierolf, Benedikt Günther, Ernst Schmid, Dietrich W. M. Walsh, Theresa Urban, Stefan Bartzsch, Amira Radtke, Elena Eggl, Klaus Achterhold, Bernhard Gleich, Stephanie E. Combs, Michael Molls, Thomas E. Schmid, Franz Pfeiffer, and Jan J. Wilkens, "Mikrokanal-Strahlentherapie mit Röntgenstrahlung an einem kompakten Synchrotron", *Abstracts DEGRO 2017* 23. Jahrestagung der Deutschen Gesellschaft für Radioonkologie in: *Strahlentherapie & Onkologie*, **193**(Suppl 1) V03-2 (2017). (Oral presentation)

Annique Hunger, Karin Burger, Martin Dierolf, Benedikt Günther, Ann-Kristin Porth, Stefan Bartzsch, Theresa Urban, Klaus Achterhold, Bernhard Gleich, Elke Beyreuther, Franz Pfeiffer, Stephanie E. Combs, Jan J. Wilkens, and Thomas E. Schmid, "Setup for tumor growth delay studies in small animals for low energy x-rays and small irradiation fields", *Abstracts DEGRO 2017* 23. Jahrestagung der Deutschen Gesellschaft für Radioonkologie in: *Strahlentherapie & Onkologie*, **193**(Suppl 1) V18-4-jD (2017). (Oral presentation)

Annique Hunger, Karin Burger, Ann-Kristin Porth, Klaus Achterhold, Bernhard Gleich, Elke Beyreuther, Franz Pfeiffer, Stephanie E. Combs, Jan J. Wilkens, and Thomas E. Schmid, "Setup for tumor growth delay studies in small animals for low energy X-rays and small irradiation fields", *Program and Abstract Book ERRS 2017 GBS 2017* 43rd Annual Meeting of the European Radiation Research Society and 20th Annual Meeting of the Society for Biological Radiation Research, 293-344 (2017). (Poster)

Annique Hunger, Karin Burger, Marlon Stein, Martin Dierolf, Benedikt Günther, Ann-Kristin Porth, Stefan Bartzsch, Theresa Urban, Klaus Achterhold, Bernhard Gleich, Elke Beyreuther, Franz Pfeiffer, Stephanie E. Combs, Jan J. Wilkens, and Thomas E. Schmid, "Setup for tumor growth delay studies in small animals for low energy x-rays and small irradiation fields", *Program and Abstract book ConRad 2017* 22nd Nuclear Medical Defence Conference, 80-86 (2017). (Poster)

Theresa Urban, Stefan Bartzsch, Karin Burger, Benedikt Günther, Martin Dierolf, Bernhard Gleich, Klaus Achterhold, Stephanie E. Combs, Franz Pfeiffer, and Jan J. Wilkens, "Dosimetric characterization of microbeams for radiation therapy at the Munich Compact Light Source", *Abstracts BMTMedPhys 2017* Annual Meeting of the German Society of Biomedical Engineering and Joint Conference in Medical Physics in: *Biomedical Engineering/Biomedizinische Technik*, **62**(s1) 180-189 (2017). (Poster)

Rico Burkhardt, Stephan Umkehrer, Max von Teuffenbach, Karin Burger, Julia Herzen, Peter Noël, Stephanie E. Combs, Franz Pfeiffer, and Jan J. Wilkens, "Optimization of X-Ray dark-field microCT and application in a murine lung model", *Abstracts BMTMedPhys 2017* Annual Meeting of the German Society of Biomedical Engineering and Joint Conference in Medical Physics in: *Biomedical Engineering/Biomedizinische Technik*, **62**(s1) 339-348 (2017). (Poster)

Martin Dierolf, Elena Eggl, Benedikt Günther, Regine Gradl, Christoph Jud, Stephanie Kulpe, Lisa Heck, Jessica Böhm, Eva Braig, Karin Burger, Kaye Morgan, Bernhard Gleich, Klaus Achterhold, and Franz Pfeiffer, "Biomedical X-ray Imaging at the Munich Compact Light Source", *Book of Abstracts XNPIG 2017* 4th Conference on X-ray and Neutron Phase Imaging with Gratings, 180-189 (2017). (Invited talk)

Karin Burger, Katarina Ilicic, Martin Dierolf, Benedikt Günther, Dietrich W. M. Walsh, Ernst Schmid, Klaus Achterhold, Bernhard Gleich, Stephanie E. Combs, Michael Molls, Thomas E. Schmid, Franz Pfeiffer, and Jan J. Wilkens, "In-vitro study of microbeam radiation therapy at a compact and brilliant x-ray source", *Abstract Booklet ERRS 2016* 42nd Conference of the European Radiation Research Society, 125-147 (2016). (Poster)

Benedikt Günther, Martin Dierolf, Karin Burger, Regine Gradl, Lorenz Hehn, Elena Eggl, Klaus Achterhold, Bernhard Gleich, and Franz Pfeiffer, "High-resolution microscopy with a laboratory-sized quasi-monochromatic X-ray source based on inverse Compton scattering", *Abstracts XRM 2016* 13th International X-ray Microscopy Conference, S1-P4-14 (2016). (Poster)

Karin Burger, Elena Eggl, Christoph Jud, Martin Dierolf, Bernhard Gleich, Klaus Achterhold, Katarina Ilicic, Thomas E. Schmid, Jan J. Wilkens, and Franz Pfeiffer "The Munich Compact Light Source – The potential for X-ray microbeam irradiations at a compact synchrotron", *Conference Booklet MASR 2015* 8th conference on Medical Applications of Synchrotron Radiation, 29-95 (2015). (Oral presentation)

Invited talks

"Microbeam irradiations using a compact synchrotron x-ray source – in vitro and in vivo studies at the MuCLS", *COST SYRA3*, 7th Work Group meetings and 8th Management Committee meeting of the COST Action TD1205, 4-5th of March 2017, Grenoble, France.

Other oral presentations

"The potential of the Munich Compact Light Source for X-ray microbeam radiation therapy in-vitro & in-vivo", *MAP C3 Meeting*, Munich Centre for Advanced Photonics – Project meeting C3, 15th November 2016, Munich, Germany.

"The Munich Compact Light Source – X-ray microbeam irradiations in-vitro & in-vivo at a compact synchrotron", *Science at the Munich Compact Light Source*, Workshop, 17th October 2016, Garching, Germany.

"Microbeam radiation therapy at the Munich Compact Light Source – an in-vitro study of cell survival and chromosome aberrations", *Seminar über Spezielle Probleme der Medizinischen Physik*, 30th May 2016, Munich, Germany.

"C.3.5 X-ray Microbeam Radiation Therapy at the Munich compact light source – Cell irradiation with absorption gratings", *MAP C3 Meeting*, Munich Centre for Advanced Photonics – Project meeting C3, 3rd November 2014, Munich, Germany.

Poster presentations and awards

"The Munich Compact Light Source – Towards Microbeam Radiation Therapy with a compact synchrotron", *Tag der Physikerinnen*, 23rd June 2015, Garching, Germany.

"The Munich Compact Light Source – Towards Microbeam Radiation Therapy with a compact synchrotron", *IMPRS-MAP Workshop*, Workshop on ultrafast laser development and applications, 26th-31st July 2015, Wildbad Kreuth, Germany.

"The Munich Compact Light Source – Grating-based x-ray imaging with a compact synchrotron", *ANKA/KNMF Joint Users' Meeting 2014*, 13-14th October 2014, Karlsruhe, Germany.

"The Munich Compact Light Source – Towards Microbeam Radiation Therapy with a compact synchrotron", *COST SYRA3 – Training School on radiation therapy, biology and dosimetry*, 18th-21st May 2014, ESRF, Grenoble, France.

Awards: Best Poster Award, *COST SYRA3 – Training School on radiation therapy, biology and dosimetry*, 18th-21st May 2014 for "The Munich Compact Light Source – Towards Microbeam Radiation Therapy with a compact synchrotron".

Acknowledgments

Thesis Ends – Acknowledgments

For both taking and tackling the task
of a supervisor,
I'm very grateful to Jan Wilkens and
Franz Pfeiffer.
You gave me valuable advice
From paper work to living mice.
Thank you, Jan, for your diplomacy,
Helping me to handle bureaucracy.
It was a pleasure being part of your
group,
Solving problems with a well-focused
loupe.
I learned a lot from you these years,
'bout academic and research spheres.
It is evident
That this is meant
In the positive sense,
From day one to my defense.

As everybody knows – especially when
your project grows –
It's important that money flows:
Thus, I'd like to thank CALA
For its MuCLS supporting thaler.
The DFG, the MAP,
For funding our research on MRT.
The helpful staff at KIT
For important grating delivery.
The Action COST Syra3
That hosted me in each city:
In Grenoble, Krakow, or Rostock.
For pencil, water, battery block,
I'd like to thank the suddenly
vanished,
IMETUM
Consortium,
By MSB now namely polished.
Thanks to Bernhard Gleich, Klaus
Achterhold and team,
Without you, we've had no beam.
Thanks to Josef Hintermair, Sepp,
For helping out with the biolab.

For endless hours without any flours,
Just sometimes cake
If you had a take,
I gratefully acknowledge support
Of the MuCLS board.
Thank you Martin for being there,
Solving problems everywhere,
Explaining physics,
Discussing mystics.
Benedikt helping operation
Of the MuCLS for X-ray creation.
Always ready to save the day,
May it be lost screws in the tray.
Thanks, Theresa, for your helping
hands.
To prepare the setup at a glance.

Thanks, Thomas Schmid, at this place
For explaining the biological case,
Planning studies,
Recruiting doctoral buddies.

Katarina, I'm very glad
For the great motivation you had,
For exchanging bio and physics,
Showing me magic cell mixing tricks.
Annique and Ann-Kristin,
For cooperation and discipline
In the in-vivo experiment,
Following through until the end.
Marlon, Andrea and many others,
Accepting timewise quite bad offers.
Mr. Ernst Schmid for counting chromosomal aberrations,
Under the microscope with extraordinary patience.

I'd like to express my respect and affections
For all the help in paper corrections.
Especially, Elena, Martin, Christian, and Stefan,
Correcting my words – thank you, bar none.

To Rudi and Alen, the precision engineers,
For great work in short time – thanks and cheers!

Eric Parzinger, thanks a lot,
For the silver dot we got.
And I'd like to take the occasion
To thank Tobias Ostermayr as well,
For testing what CR-39 could tell
On the impact of X-ray radiation.

After the tumors were resected,
Iodine staining was effected.
Thanks so much, Juliana, for your interest and aid,
And for the precious friendship we made.

Thanks to the IMETUM girls and guys,
Always keen to make fun and surprise,
Creating a nice atmosphere
I really enjoyed being here.
Thanks to Johannes, Pidassa, Mark, Florian,
Andre, Kaye, Maite, Adrian,
Friedrich, Mathias, Lorenz, Sebastian
Regine, Christoph, Eva and Jonathan.
My apologies to those I did not mention by name,
My gratitude to them stays the same.

Elena, it was nice that we shared
Important details while we cared
About our coffee consumption
With almost daily resumption.

Simone, thanks for enlightening my days,
Entering with me the 'creative phase'.

Thank you, Klaus, for enjoyable runs
In often very hot midday suns,
Even though they got less
(Writing took my time, I guess).
Next time see you in running dress!

I'd like to acknowledge Ulrike and Dieter,
Offering their rooms - yes, every meter
To welcome whole E17,
Providing drinks to global cuisine.
Merci for the dinners with great food,
Spreading laughter and good mood.

Thanks to the people from Radio-oncology,
Especially to the members of ATRT.
Another nice place to drink Cappuccino
Was with Birgit in our little bureau.
Thank you for the good time together
Debating energy consumption or jogging weather.

Finally, I'm very glad,
For the good friends I made and had.
Thank you for so many great hours,
When life and time were truly ours.

My family, thank you so much,
You always kept in touch.
For your belief
That I will achieve
My goals, take it long or short.

Thanks to my mother and father for your endless support.
To my sister, for your loyalty,
Reliable, no royalty.

Last but not least, I send
Many thanks to my best friend,
My beloved husband.
Always right at my side.
With you this story has a bright
And very happy end.

END